Alma Mater Studiorum - Università di Bologna

DOTTORATO DI RICERCA IN

MECCANICA E SCIENZE AVANZATE DELL'INGEGNERIA

Ciclo 34

Settore Concorsuale: 09/C2 - FISICA TECNICA E INGEGNERIA NUCLEARE

Settore Scientifico Disciplinare: ING–IND/10 - FISICA TECNICA INDUSTRIALE

LINEAR AND NONLINEAR THERMAL INSTABILITY OF NEWTONIAN AND NON–NEWTONIAN FLUID SATURATED POROUS MEDIA

Presentata da: Pedro Vayssière Brandão

Coordinatore Dottorato

Marco Carricato

Supervisore

Antonio Barletta

Co–supervisore

Michele Celli

Esame finale anno 2022

Acknowledgements

The present project would not have been possible without the support of many people. First of all, I cannot thank enough my supervisor, professor Antonio Barletta, for all the guidance, the knowledge, the support, the lessons, and the patience. I am also indebted to my co–supervisor, professor Michele Celli, for all his attention, for the support, for the guidance and for the encouragement.

I also recognize the importance of my former supervisor, professor Leonardo Alves, in my academic life, I am very grateful for all he has done for me during this journey. I would like to express also my gratitude for all the lessons, the patience and the support that professor Mohamed Najib Ouarzazi gave me in these years of collaboration. I sincerely thank also professors Silvia Hirata and Andrew Rees for all their support and for all interesting discussion we have had.

I express my gratitude also to my former graduate colleagues from UFF, that even from afar have collaborated and helped me a lot in this journey.

Finally, I thank all my dear friends and my family. Above all, I have to mention my mother Adriana, my father Ricardo and my (step)mother Rita for all their support in these years.

This study was financed in part by the Coordenação de Aperfeiçoamento de Pessoal de Nível Superior - Brazil (CAPES) - Grant n° 88881.174085/2018–01.

Dedication

In recent years, Brazil has been suffering an assault by people that are not interested in science, or any kind of true knowledge. This fact affects the lives of a lot of people, among whom people that have not even had the possibility to study at university neither to be really positively impacted by the knowledge transformed therein. This thesis is dedicated to the Brazilian people that have supported me during these three years.

caminho sim
sem porta de partida
ou de chegada
com um pouco de lama
na estrada
caminho ainda assim
sem saber o paradeiro
ou se chegarei por inteiro
caminho com um pouco de medo
caminho até o fim

Abstract

The present work aims to investigate the influence of different aspects, such as non–standard steady solutions, complex fluid rheologies and non–standard porous–channel geometries, on the stability of a Darcy–Bénard system. In order to do so, both linear and nonlinear stability theories are considered. A linear analysis focuses on studying the dynamics of the single disturbance wave present in the system, while its nonlinear counterpart takes into consideration the interactions among the single modes. The scope of the stability analysis is to obtain information regarding the transition from an equilibrium solution to another one, and also information regarding the transition nature and the emergent solution after the transition. The disturbance governing equations are solved analytically, whenever possible, and numerical by considering different approaches. Among other important results, it is found that a cylinder cross–section does not affect the thermal instability threshold, but just the linear pattern selection for dilatant and pseudoplastic fluid saturated porous media. A new rheological model is proposed as a solution for singular issues involving the power–law model. Also, a generalised class of one parameter basic solutions is proposed as an alternative description of the isoflux Darcy–Bénard problem. Its stability is investigated.

Contents

List of Figures

List of Tables

Nomenclature

0.1 Roman letters

A	surface area; disturbance amplitude
$\mathcal{A}$	surface area
a	void distribution function; Yasuda parameter
b, d	elliptical semi axes
b	Hele–Shaw width
$\mathbf{b}$	vector function
B	hydraulic conductivity
b_1, b_2	roots of the characteristic polynomial
$\mathcal{B}$	matrix of the generalized eigenvalue problem
c	specific heat
C	positive parameter; form coefficient
$\mathcal{C}$	real constant
D	differential operator
$\mathbf{D}^d$	dispersion tensor
∂	derivative; boundaries
$\mathbf{e}_x$	unit vector in the x-direction
$\mathbf{e}_z$	unit vector in the z-direction
f	solution of Helmholtz equation; function of n
F	operator; function of (x, y)
$\mathbf{g}$	gravitational acceleration
g	modulus of $\mathbf{g}$
G	function of (x, y)
h	pressure divided by the specific weight ρg; function of (n, ϕ)
H	porous layer height
$\mathbf{I}$	identity tensor
$\mathcal{I}_n$	expansion coefficient
k	wavenumber
K	permeability of the porous medium
$\mathbf{K}$	permeability tensor, inverse of $\mathbf{K}_0^{-1}$

$\mathbf{K}_0^{-1}$	inverse of permeability tensor
l	side length of a square
L	length of the flow path
$\mathcal{L}$	linear operator
$\mathbf{L}$	linear operators
$\mathbf{L}_t^*$	tortuosity tensor
$\mathbf{m}$	transformation vector
m, n	integers
$\mathbf{M}$	velocity transformation tensor,
$m_1, \ldots, m_4$	coefficients
$M_1, \ldots, M_4$	coefficients,
n	power–law index
$\mathbf{n}$	unitary directional vector
N	number of collocation points and polynomial order
$\mathbf{N}$	nonlinear operator
NL	nonlinear term
Nu	Nusselt number
p	difference between the pressure and the hydrostatic pressure
$\mathcal{P}$	piezometric head
$\mathbf{q}$	quantities vector
Q	volumetric flow rate
q_0	uniform wall heat flux
$\mathbf{r}$	position vector
$\mathbf{RH}$	right–hand side operator
Ra	Rayleigh number
Ra^*	Rayleigh number as defined in [110]
Re_K	permeability based Reynolds number
s	curvilinear coordinate; disturbance growth rate
t	time
$\mathbf{t}$	curve tangent
T_0	reference temperature
T	temperature
$\mathbf{u}$	velocity vector, (u, v, w); seepage velocity
$\mathbf{u}^*$	local velocity
$\mathbf{U}^*$	intrinsic velocity
$\mathcal{V}$	total volume of solid matrix
Wi	Weissemberg number
$\mathbf{x}$	position vector, (x, y, z)

0.2 Greek letters

α	constant; eigenvalue
β	constant; volumetric thermal expansion coefficient
χ	average thermal diffusivity; ratio between elliptical semi–axes
γ	thermal expansion coefficient
δ	positive parameter; numerical solver step–size
ΔT	temperature difference
η	consistency factor
η_{ef}	effective consistency factor
ϵ	small parameter
ε	small parameter
γ	shear rate
μ	dynamic viscosity; generic control parameter; distance to criticality
κ	tortuosity factor
$\varkappa$	thermal conductivity
$\varkappa_f, \varkappa_s, \varkappa_m$	thermal conductivity of the solid, fluid and the average of both
λ	eigenvalue; dimensionless characteristic time of the non–Newtonian fluid
λ^*	dimensional characteristic time of the non–Newtonian fluid
λ, η	elliptical coordinates
Λ	diagonal eigenvalues matrix; parameter
ω	angular frequency
Ω	parameter $\Omega = Ra^*/Ra$
ϕ	inclination between the x axis and the wave vector
Φ	porosity
ρ	density of the fluid
ρ_0	density of the fluid for $T = T_0$
σ	volumetric heat capacity ratio
Υ	generic quantity

0.3 Superscripts, subscripts

$1, 2$	upstream and downstream positions
a	apparent
b	basic state
c	critical value
eff	effective
f	fluid
hs	Hele–Shaw

l	lower
T	longitudinal
max	maximum
N	Newtonian
pl	power–law
s	solid; stationary
th	threshold
tr	tricritical
T	transpose; transverse
u	upper
$'$	derivative with respect to z
$\tilde{}$	disturbances eigenfunctions; coefficients of series expansions
$\hat{}$	fourier quantity transformation; coefficients of series expansions
$*$	microscopic–scale variables; complex conjugate

0.4 Acronyms

DB	Darcy–Bénard
HRL	Horton–Rogers–Lapwood
RB	Rayleigh–Bénard
REV	Representative Elementary Volume

Chapter 1

Introduction

In this chapter the class of physical problems to be analysed will be introduced in order to motivate the present study and clearly illustrate the objectives. First of all I will briefly introduce the physical phenomenon, nowadays known as Rayleigh–Bénard convection, as well as its modified version for fluid saturated porous media, *i.e.* the Darcy–Bénard convection. In parallel, I will indicate some real systems where these phenomena emerge, which can be useful to figure out possible applications. A bibliography review of the main studies dealing with the concepts used in this thesis will also be presented.

1.1 Motivation

The phenomenon of natural convection, either in clear fluids and in porous media, is well known nowadays. Its study began with the experiments developed by the French physicist Henri Bénard [20], who was the first to carried out the detailed experiment on the appearance of convective cells in a layer of fluid heated from bellow. Figure 1.1 shows the pattern similar to those observed by Bénard in his experiments [83]. Some years after the experiments of Bénard, Lord Rayleigh [114] presented an attempt to examine how the interesting experimental results obtained by Bénard could be explained theoretically. Rayleigh used concepts of stability theory in his theoretical investigations. The idea behind the use of stability theory to investigate the appearance of convective cells relies on the hypothesis that it is related to the growth of disturbances present in the equilibrium state. In the case of the onset of convection, the conductive state would be the equilibrium state, while the transition to the convective state would be related to the transition to instability, caused by the density stratification. The conceptualization of the stability theory will be rigorously presented later on in Chapter 3.

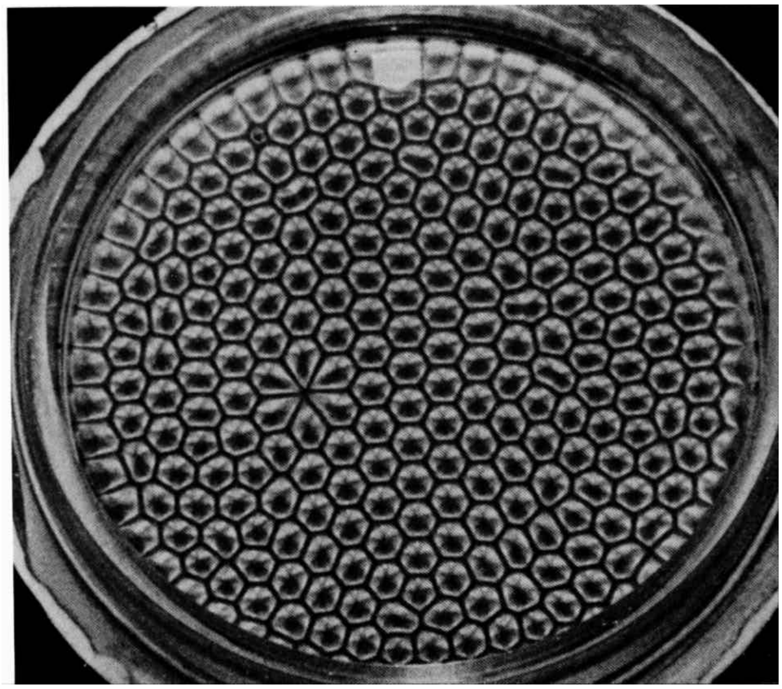

Figure 1.1: Hexagonal Bénard convection pattern, from Koschmieder [83]

Block [22] proposed a series of experiments to investigate the surface tension as a possible cause to the convective cells observed by Bénard. He argued that for really small thickness layer, as those used in some experiments carried out by Bénard, the mechanism inducing the instability would not be the convection but the change of the surface tension due to temperature variation. Later on, Pearson [109] investigated theoretically the effects of the surface tension variation with temperature as an important mechanism to trigger instabilities in thin liquid films. By using small disturbances analysis he concluded that, in fact, some of the results observed by Bénard were caused by surface tension forces. In any case, the instabilities caused by buoyancy effects are nowadays known as Rayleigh–Bénard (RB) instability. For a more exhaustive review of Rayleigh–Bénard convection problems, I refer the reader to the works by Kelly [77] and Nicolas [96] as well as to the books by Koschmieder [84], Getling [56] and Zeytounian [137].

The counterpart of RB convection for a porous medium saturated by a fluid is known as Darcy–Bénard (DB) convection. The phenomenon takes this name because of the French engineer Henry Darcy, which authored the pioneering study on the empirical law for fluid flows in porous media [45].

Until the 1970s, the bulk of the studies involving porous media flows were related to geophysical applications. Among the possible applications in this field, one can cite, for instance, the oil recovery by thermal methods, the design of aquifers as energy storage systems, drainage and irrigation, underground spreading of chemical waste and the storage of carbon dioxide in aquifers [39, 129, 106]. More recently, other kinds of applications can be seen in a wide variety of industrial areas. Among others, one can mention different kinds of devices, such as electronic equipments and heat exchangers. For the latter class of devices, porous media are often considered in order to enhance the heat transfer [91].

There has been a recent dramatic increase of attention for heat transfer in non–Newtonian fluid saturated porous media. In particular, the enhancement of oil recovery processes and ceramic processing can be mentioned [120]. Table I of Shenoy [120] presents an extensive list of possible applications in a wide range of scientific and engineering applications, such as biomechanics, food technology, chemical engineering, geophysics, groundwater hydrology and industrial engineering.

The study of thermal instabilities in porous media came out to be of great interest given the important applications cited so far. Stability analysis is able to give us important information and insights about the onset of convection, changes in the qualitative and quantitative behaviour of the flow, changes in the patterns observed and the enhancement of heat transfer.

1.2 General literature review

The pioneering studies which deal with the onset of DB convection by employing the stability analysis are those by Horton and Rogers [67] and by Lapwood [87]. In fact, nowadays it is called Horton–Rogers–Lapwood (HRL) problem. In these studies, the vertical unstable temperature gradient, originated by the temperature difference between the horizontal walls, is the possible source of instability. The stability of the conductive state of a saturated horizontal porous layer was investigated through small disturbances analysis. The parameter that controls the problem is the dimensionless parameter called Darcy–Rayleigh number (here denoted by Ra). It was found that the threshold of instability is $Ra = 4\pi^2$ and the wavenumber associated to the onset of convection is equal to π. In addition, it is known that the disturbance waves are non–travelling.

The effect of horizontal fluid flow at the onset of instability was investigated some years later by Prats [111]. In his study, he concluded that the instability threshold is not affected by the presence of a throughflow, but the latter can influence only the phase velocity of the wave disturbances. Some years later, Sutton [126] investigated the effect of vertical throughflow in closed channels, taking into account also the effects of the lateral confinement on the onset of convection. He showed that, for moderate and high values of aspect ratio, a vertical throughflow plays a stabilizing role at the transition to instability in a horizontal porous channel. Later on, Jones and Persichetti [71] studied the effect of vertical flows in infinitely wide channels, which coincides with the infinite aspect ratio from the work of Sutton [126]. Jones and Persichetti [71] showed the effect of throughflow with different combinations of boundary conditions in the upper and lower boundaries. The effect of vertical flows in horizontal porous channels was further investigated by Homsy and Sherwood [66] and by Nield [98].

Gill [57] studied the convection in a vertical channel rigorously proving that this kind of flow, in a vertical impermeable porous channel whose walls are kept at different temperatures, is always stable. More recently, by relaxing the impermeability on the wall of boundaries employed in Gill's problem, Barletta [10] demonstrated that convection in a porous slab can be unstable. He extended the original problem by considering permeable walls, instead of impermeable ones, and compared both models. He demonstrated, by using linear stability theory, that the flow system examined could be destabilized. Barletta [10] also simulated numerically the fully nonlinear problem confirming the linear predictions.

Although the literature deals with the boundary conditions of impermeability and uniform temperature, it is not always the case. It is worth investigating other ways of modelling real problems as well as different applications. From a practical point of view, it is not always realistic or even feasible to deal with prescribed temperatures. It may be necessary to deal with more complex ways of modelling the velocity and temperature boundary conditions.

Nield [97] investigated the effects of different boundary conditions on the onset of thermohaline convection in porous media. Table I of his work presents the values of critical Rayleigh number and the corresponding critical wave number for various boundary conditions. Such results are in agreement with those presented by Jones and Persichetti [71] considering the case without throughflow. In these cases, although different boundary conditions are considered, the same equilibrium solution applies. It can be concluded that, for the same basic solution, switch from a prescribed temperature boundary condition to a prescribed heat flux has a destabilizing effect.

Another type of thermal boundary condition which influences the stability involves not only a vertical temperature gradient, but also a horizontal one. In that case, a unicellular flow is formed due to an inclined temperature gradient. Such a flow is also called Hadley flow. Weber [131] investigated the effect of inclined temperature gradient on the stability of convective flows in porous media considering just small horizontal temperature gradients. Nield [100, 101] relaxes this restriction on the magnitude of the horizontal temperature gradient and studies a more general case. Finally, Kaloni and Qiao [74], extended the former analyses by investigating the nonlinear stability. They concluded that the transition to instability may be subcritical when the horizontal temperature gradient is non–zero.

There are many practical situations in which the fluid presents a complex non–Newtonian rheology. Kim et al. [80] studied the stability of viscoelastic fluids saturating porous media from the linear and the nonlinear point of view. They showed that the elastic parameters of the fluid have a destabilizing effect and that the heat transfer rate, given by the averaged Nusselt number, is enhanced by the non–Newtonian nature of the fluid.

Barletta and Nield [12] were the first to examine the stability of a Rayleigh–Bénard system involving a purely viscous non–Newtonian fluid saturating a porous medium. In their study, they used the Otswald–de–Waele power–law model. They showed that the selection of the preferred modes for the onset of instability, namely longitudinal or transverse, depend on the magnitude of the basic flow and on the power–law index which is associated with the rheological behaviour of the fluid. A particularity of the power–law model is that it presents a singularity in the limiting case of vanishing shear rate, giving zero or infinite apparent viscosity for shear–thickening and shear–thinning fluids, respectively. However, this is not an issue in the non–Newtonian fluid dynamics if one is dealing with high values of shear rates. On the other hand, since the stability analysis often deals with transition and onset of flows and secondary flows, the singular behaviour of the apparent viscosity can be a significant issue. Barletta and Nield [12] find that the critical Rayleigh number is zero for dilatant fluids and infinite for pseudoplastic ones.

Linear stability analysis is meant to determine the threshold beyond which infinitesimal wave disturbances grow in time. In the framework of linear analysis it is necessary to make a distinction between two kinds of instability, namely convective and absolute instabilities. Such a distinction was first introduced in the fluid mechanics world by Huerre and Monkewitz [68]. The convective instability concept is focused on finding when a single disturbance mode starts growing in time. It means that, if we are dealing with spatially localized disturbances, it is advected downstream by the basic flow, when it is present, and eventually goes out of the domain of interest. On the other hand, the absolute instability is about the onset of growth in time of spatially localized disturbances. In an absolutely unstable regime disturbances grow both in the downstream and in the upstream directions.

Experimental and numerical studies have provided evidence that support this distinction as well as confirm the theoretical predictions. The experimental work by Combarnous and Bia [43] confirms the threshold of instability and show some interesting results about the physical characteristics of the convective structures in the unstable regime. In addition, a more recent study by Dufour and Neel [52] confirmed numerically the theoretical predictions for small flow rates. They showed also that oscillation frequency and wavelength are also in a good agreement with theoretical predictions. Delache et al. [47] performed a spatio–temporal stability analysis by taking into account the effects of inertia on the momentum balance equation and made a comparison with some experimental results. They found that both qualitatively and quantitatively the theoretical results are in good agreement with the experimental ones, arguing that the qualitative change in the preferred mode observed experimentally should be related to a transition from convective to absolute instability. Regarding non–Newtonian fluids, Hirata and Ouarzazi [61] studied the effect of the throughflow in the spatiotemporal dynamics of linear disturbances in viscoelastic saturated porous media convection by using the concepts of convective and absolute instability. Alves and Barletta [4] did the same for power–law fluids.

In some cases, the results of the linear stability analysis do not correspond to the behaviour of real–world systems. Moreover, even when the transition is dictated by linear mechanisms, small disturbances analysis might fail in the supercritical domain, especially far from the critical point. In those cases, it is necessary to carry out nonlinear studies. To avoid the solution of the fully nonlinear equations, the weakly nonlinear technique has been employed to study the nonlinear dynamics close to the critical point. Weakly nonlinear analysis is able to give us information about the transition point and also about the nature of the bifurcation as well as the disturbances evolution in the supercritical domain. Delache and Ouarzazi [46] have investigated the nonlinear interaction of mixed convection patterns in porous media by using the weakly nonlinear theory. Among other important results, they investigated the preferred modes that appear in the supercritical region and found that the average heat transfer given by the weakly nonlinear calculations are in a good agreement with experiments for Rayleigh numbers up to three times its critical values.

The linear concepts of convective and absolute instability have their nonlinear counterparts. If one thinks about spatially localized disturbances, which can be thought of as wavepackets, it is possible to define the front velocities at the borders of the wavepacket. In general, for small disturbance amplitudes, the linear dynamics of the single infinitesimal wave should dominate over the nonlinear interactions between them. However, there are some cases in which the nonlinear dynamics may dominate when the disturbance modes achieve finite amplitudes. In this case, if the nonlinear front velocities are greater than the linear ones, the transition to absolute instability may be driven by the nonlinear dynamics. Ouarzazi et al. [107] investigated the mixed convection in porous media together with the Soret effect and studied the nature of the transition to instability, having also determined the velocity and wavenumbers of the linear and nonlinear fronts. These concepts will be better discussed later on. Further investigations on this subject can be found in the works by Chomaz [41] and by Delbende and Chomaz [48]. An exhaustive survey regarding the dynamics of front propagation into unstable states can be found in Saarlos [130].

1.3 Objectives

The main objective of this thesis is the investigation of the diverse effects which influence the transition to instability for convection in porous media. In order to do so, the stability theory is considered. In particular, I have analysed the effects of vertical throughflow in both a horizontal porous channel and a vertical porous cylinder with arbitrary cross–section saturated by non–Newtonian fluids of power–law type. Furthermore, I proposed a modified version of Darcy's law for Carreau–Yasuda fluids and studied the linear and non–linear stability of a horizontal porous channel, saturated by this kind of fluids, both in the presence and in the absence of a throughflow. Finally, I proposed a generalized basic solution for the convective flow in a porous channel heated from the bottom and cooled from the top by a uniform heat flux. The stability of this class of basic states is also investigated.

Before entering in the study of the particular cases, I will present the basic concepts necessary to do it. In particular, I will present an overview of the theory of fluid dynamics and heat transfer in porous media. The theory of stability will also be presented here together with the numerical methods used to solve the mathematical problems of instability. Specifically, I will present in Chapter 2 the physical–mathematical models for convection in porous media. In Chapter 3, I will describe the stability theory at the basis of the present study, and also the linear and nonlinear types of analysis. Finally, in Chapter 4, I will present the numerical methods used to solve the differential equations which come out from the stability analysis.

In Chapter 5, I will present the study of the effect of vertical pressure gradient in a horizontal porous layer saturated by a power–law fluid. In Chapter 6, I will present the study of the throughfow in a vertical porous cylinder with arbitrary cross–section saturated by a power–law fluid. In Chapter 7, I will present the Darcy–Carreau model and investigate the linear and nonlinear stability of the natural convection of non–Newtonian fluids in porous channels. In Chapter 8, I will present the Darcy–Carreau–Yasuda model and investigate the linear stability of the non–Newtonian mixed convection in porous media; a comparison with some theoretical and experimental results available in the literature is also presented. Finally, in Chapter 9, I will present a generalised basic state for the isoflux Darcy–Bénard problem as well as its stability analysis.

Chapter 2

Mathematical modelling

In this chapter, I will introduce the mathematical modelling of fluid dynamics and heat transfer for incompressible fluid flow through porous media. In a first moment, I will define a porous medium and I will present some examples, important properties and characteristic information. Then, I will introduce the conservation laws such as the balance of mass, balance of linear momentum and finally the balance of energy. For the momentum balance equations I will present also the variations for non–Newtonian fluids. Concerning the energy balance equation, I remark that I consider here just the local thermal equilibrium model.

2.1 Porous media

The understanding of fluid flow phenomena in porous media is closely related to a combination of empirical investigation and theoretical knowledge. A porous medium can be defined as a heterogeneous system composed partly by a solid phase and partly by voids. In this thesis, I will assume that the porous matrix is perfectly rigid. When the voids (pores) are interconnected, different flow regimes can occur. In the present thesis I consider just single–phase flows.

Examples of porous media can be found both in nature and in industrial applications. In the case of natural porous media the pores are distributed irregularly and their shape and size are usually irregular. Examples of natural porous media include soil, sand, wood, limestone and biological tissues. On the other hand, among the manufactured porous media I can mention metal foams, cigarette filters, ceramic materials, concrete, fiberglass, which can be more or less irregular. The additive manufacturing technique yielded, in the recent years, the opportunity of designing the structure of the porous matrix.

The pioneering study of fluid flow in porous media was authored by Henry Philibert Gaspard Darcy. In 1856, he published a report about the design of the water system in the city of Dijon, France [45]. Darcy was the first scientist which investigated this topic proposing a relationship for the fluid flow in porous media, specifically water and sand beds in his case. Before entering in the specific aspects of the flow modelling in porous media, we define some properties such as the porosity and the filtration velocity. For a more complete survey of fluid dynamics and heat transfer in porous media, I refer the reader to the books by Bear [19], Nield et al. [106] and Kaviany [76].

2.2 Local volume average

At a microscopic scale, the variables of interest for the flow, such as the velocity field, display considerable irregularities. However, in real problems the variables are often measured in macro–regions containing several pores. Usually, in these cases, such variables behave from the macroscopic point of view in a steady and regular way. This is always the case for every macro–region if we assume that the solid phase is distributed homogeneously through the porous domain. This macro–region is called Representative Elementary Volume (REV), which must be larger than the single pore volume but much smaller than the total volume of the porous matrix. The REV is the smallest differential volume whose extension would not influence the local average properties calculations.

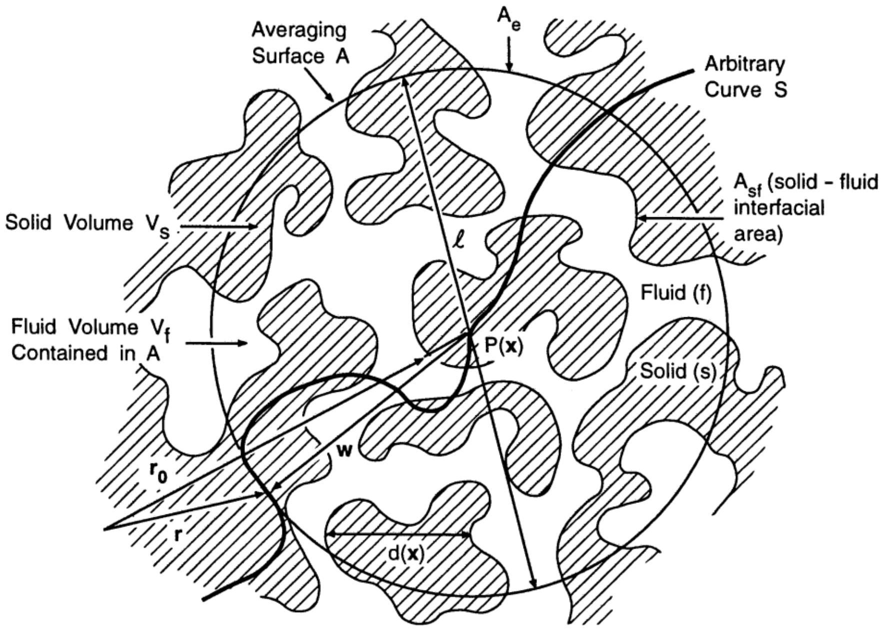

Figure 2.1: Representative Elementary Volume, from Kaviany [76]

The models for the conservation laws that will be treated in the present work usually take into consideration average variables that are based on the existence of the REV. The local volume average method presented here is based on the work by Whitaker [133] and this method is also presented in Kaviany [76]. Let $\mathcal{V}$ be the total volume of a solid matrix contained in a surface $\mathcal{A}$, as can be seen in Figure 2.1. A void distribution function $a(x)$ inside $\mathcal{V}$ can be written as

$$a(x) = \begin{cases} 1, & \text{if } x \in f \\ 0, & \text{if } x \in s, \end{cases} \tag{2.1}$$

with s representing the solid region and f the void one, occupied by the fluid. Thus, the local porosity is defined as

$$\Phi(x) = \frac{1}{\mathcal{V}} \int_{\mathcal{V}} a(x) \mathrm{d}V = \frac{\mathcal{V}_f}{\mathcal{V}}, \tag{2.2}$$

where $\mathcal{V} = \mathcal{V}_f + \mathcal{V}_s$. The porosity is the ratio between the void volume and the total volume occupied by the solid matrix and the void. There can be basically three classes of connections between the pores, namely interconnected, dead end and isolated. The first one refers to the case where each void connected to more than one pore, the second one is when the voids are connected only to another pore while the last one refers to voids not connected at all.

The local volume average of any quantity Υ is then defined as

$$\langle \Upsilon \rangle = \frac{1}{\mathcal{V}} \int_{\mathcal{V}} \Upsilon \mathrm{d}V. \tag{2.3}$$

By considering a quantity Υ related to the fluid, the local volume average and its relation with the intrinsic average is

$$\langle \Upsilon \rangle = \frac{1}{\mathcal{V}} \int_{\mathcal{V}_f} \Upsilon \mathrm{d}V = \Phi \langle \Upsilon \rangle^f = \Phi \frac{1}{\mathcal{V}_f} \int_{\mathcal{V}_f} \Upsilon \mathrm{d}V \tag{2.4}$$

For the velocity, we might use these two ways of taking this average. When the averaging process is done by considering just the void space, or the region occupied by the fluid ($\mathcal{V}_f$), it is called intrinsic velocity

$$\textbf{Intrinsic Velocity:} \quad \mathbf{U} = \langle \mathbf{u}^* \rangle^f = \frac{1}{\mathcal{V}_f} \int_{\mathcal{V}_f} \mathbf{u}^* \mathrm{d}V, \tag{2.5}$$

while, when the average is taken with respect to the whole REV, we have the well–known seepage, or filtration, velocity

$$\textbf{Seepage Velocity:} \quad \mathbf{u} = \langle \mathbf{u}^* \rangle = \frac{1}{\mathcal{V}} \int_{\mathcal{V}_f} \mathbf{u}^* \mathrm{d}V. \tag{2.6}$$

By confirming the relation given by Equation (2.4), we have that the integrals at the right–hand sides of Equations (2.5) and (2.6) are identical, as $\mathbf{u}^*$ is zero in the solid part of $\mathcal{V}$. In this case, it is possible to obtain a relation between such velocities

$$\mathbf{u} = \Phi \mathbf{U}. \tag{2.7}$$

In order to locally average the equations of mass, momentum and energy balance, it is necessary to introduce the mathematical identity which allows one to write the average of a gradient or divergence as a gradient or divergence of an average. It is well developed in the work by Slattery [122] and a detailed version can be found also in the work by Whitaker [132]. We follow here the derivations present in the book by Kaviany [76]. After some algebraic manipulations and by considering the Reynolds Transport theorem, as well as the Green transformation, it has been proved that [122, 132]

$$\boldsymbol{\nabla} \int_{\mathcal{V}_f} \Upsilon \mathrm{d}V = \int_{\mathcal{A}_e} \Upsilon \mathbf{n} \, \mathrm{d}A, \tag{2.8}$$

where $\mathcal{A}_e$ is the limiting surface of $\mathcal{V}$ and $\mathbf{n}$ is the outward pointing normal vector on the control surface. Then, the identity for a scalar quantity Υ, according to Kaviany [76], is

$$\langle \boldsymbol{\nabla} \Upsilon \rangle = \boldsymbol{\nabla} \langle \Upsilon \rangle + \frac{1}{\mathcal{V}} \int_{\mathcal{A}_{sf}} \Upsilon \mathbf{n} \, \mathrm{d}A, \tag{2.9}$$

while for a vector quantity, $\boldsymbol{\Upsilon}$,

$$\langle \boldsymbol{\nabla} \cdot \boldsymbol{\Upsilon} \rangle = \boldsymbol{\nabla} \cdot \langle \boldsymbol{\Upsilon} \rangle + \frac{1}{\mathcal{V}} \int_{\mathcal{A}_{sf}} \boldsymbol{\Upsilon} \cdot \mathbf{n} \, \mathrm{d}A. \tag{2.10}$$

where $\mathcal{A}_{sf}$ is the solid–fluid interface area, as it is displayed in Figure 2.1.

2.3 Mass balance

The continuity equation for clear fluids is

$$\frac{\partial \rho}{\partial t} + \boldsymbol{\nabla} \cdot (\rho \, \mathbf{u}^*) = 0, \tag{2.11}$$

where ρ is the fluid density. By applying the volume average technique, it becomes

$$\frac{\partial \langle \rho \rangle}{\partial t} + \langle \boldsymbol{\nabla} \cdot (\rho \, \mathbf{u}^*) \rangle = 0, \tag{2.12}$$

which, by using Equation (2.10) and taking into consideration that the velocity is zero at the solid–fluid interfaces, becomes

$$\frac{\partial \langle \rho \rangle}{\partial t} + \boldsymbol{\nabla} \cdot \langle \rho \, \mathbf{u}^* \rangle = 0. \tag{2.13}$$

By considering an incompressible flow, it is simply written as

$$\boldsymbol{\nabla} \cdot \langle\, \mathbf{u}^* \rangle = 0, \tag{2.14}$$

or

$$\boldsymbol{\nabla} \cdot\, \mathbf{u} = 0. \tag{2.15}$$

2.4 Momentum balance

In a slightly different way from its modern version, the original Darcy's law was given by

$$Q = A\, B\, \frac{(h_1 + z_1) - (h_2 + z_2)}{L}, \tag{2.16}$$

where Q is the volume flow rate, A is the area of the porous medium normal to the flow, $B = \rho g K/\mu$ is the hydraulic conductivity with K, μ and g denoting the permeability, the fluid dynamic viscosity and the modulus of the gravitational acceleration, respectively. Moreover, h is the pressure divided by the specific weight ρg, z is the elevation, L is the length of the flow path and the subscripts 1 and 2 are relative to the upstream and downstream positions, respectively [33]. Nowadays, the widely used differential version of Darcy's law is

$$\mathbf{u} = \frac{K}{\mu} \left(-\boldsymbol{\nabla} p + \mathbf{f} \right), \tag{2.17}$$

where p is the fluid pressure and $\mathbf{f}$ is the external body force applied to the fluid per unit of volume, which in the case of the gravitational force, becomes

$$\mathbf{u} = \frac{K}{\mu} \left(-\boldsymbol{\nabla} p + \rho \mathbf{g} \right), \tag{2.18}$$

with $\mathbf{g}$ being the gravitational acceleration vector.

2.4.1 Theoretical deduction

A wide discussion can be found in the literature about the theoretical derivation of Darcy's law. I recommend the works by Slattery [122], Whitaker [132], Gray and O'Neill [58], Whitaker [133] and Kaviany [76] for the details of the derivation. By considering the stationary Navier–Stokes equation for creeping flows,

$$0 = -\boldsymbol{\nabla} \mathcal{P} + \mu \nabla^2 \mathbf{u}^*, \tag{2.19}$$

where $\mathcal{P}$ is the piezometric head, namely

$$\mathcal{P} = p - \rho\,\mathbf{g}\cdot\mathbf{r}. \tag{2.20}$$

By taking the divergence of Equation (2.19), we show that $\mathcal{P}$ must satisfy the Laplace equation

$$\nabla^2\mathcal{P} = 0, \tag{2.21}$$

which implies, from Equation (2.19), that the velocity must satisfy the biharmonic equation

$$\nabla^4\mathbf{u}^* = 0. \tag{2.22}$$

The velocity must satisfy the no–slip condition at the solid–fluid interface

$$\mathbf{u}^* = 0 \quad \text{at} \quad \mathcal{A}_{sf}, \tag{2.23}$$

in addition, if we define the boundary conditions for $\mathbf{u}^*$ at the entrance and exit of the REV $\mathcal{V}$, it is possible to demonstrate that $\mathbf{u}$ and $\mathbf{u}^*$ are continuous and that the transformation of the average velocity into the pore–scale velocity is possible via [132, 76]

$$\mathbf{u}^* = \mathbf{M}(\mathbf{r})\cdot\mathbf{u}, \tag{2.24}$$

with $\mathbf{r}$ being the position vector showed in Figure 2.1.

It can be shown also that [132]

$$\nabla^4\mathbf{M} = 0, \tag{2.25}$$

and that the velocity transformation tensor $\mathbf{M}$ is dependent on the porous medium geometry, can vary only spatially within the pore, and it is independent of $\mathbf{u}$. Therefore, $\mathbf{u}^*$ is a linear vector function of $\mathbf{u}$. An interesting discussion about the closure of this problem can be found in Whitaker [133] and Barrere et al. [18].

By considering an arbitrary curve, whose tangent is $\mathbf{t}$, we define the curvilinear coordinate s as

$$\mathbf{t}\cdot\boldsymbol{\nabla} = \frac{\mathrm{d}}{\mathrm{d}s}. \tag{2.26}$$

On account of Equations (2.19) and (2.24), the scalar product of $\mathbf{t}$ and $\boldsymbol{\nabla}\mathcal{P}$ can be evaluated as

$$\mathbf{t}\cdot\boldsymbol{\nabla}\mathcal{P} = \frac{\mathrm{d}\mathcal{P}}{\mathrm{d}s} = \mu\mathbf{t}\cdot\nabla^2\mathbf{u}^* = \mu\mathbf{t}\cdot\nabla^2\mathbf{M}\cdot\mathbf{u}, \tag{2.27}$$

after some simplifications, that are reported with more details in Whitaker [132] and Slattery [122], one obtains

$$\mathcal{P}(s) = \mathcal{P}_0 + \mu \left[\int_0^s \left(\mathbf{t} \cdot \nabla^2 \mathbf{M} \right) \mathrm{d}s \right] \cdot \mathbf{u}. \tag{2.28}$$

The term in square brackets depends only on s and on the geometry. At this point we can define a transformation vector $\mathbf{m}$, which, in addition to the geometry, depends on the position $\mathbf{r}$,

$$\mathbf{m} = \int_0^s \left(\tau \cdot \nabla^2 \mathbf{M} \right) \mathrm{d}s, \tag{2.29}$$

which allows us to determine $\mathcal{P}$ up to an arbitrary constant

$$\mathcal{P} = -\mu \, \mathbf{m} \cdot \mathbf{u}. \tag{2.30}$$

From Equation (2.8) we can say that

$$\boldsymbol{\nabla} \int_{\mathcal{V}_f} \mathcal{P} \mathrm{d}V = -\int_{\mathcal{A}_e} \left(\mu \, \mathbf{m} \cdot \mathbf{u} \right) \mathbf{n} \, \mathrm{d}A, \tag{2.31}$$

after multiplying both sides by $1/\mathcal{V}$, we have

$$\boldsymbol{\nabla} \langle \mathcal{P} \rangle = -\mu \, \mathbf{K}_0 \cdot \mathbf{u} \tag{2.32}$$

with

$$\mathbf{K}_0 = -\frac{1}{\mathcal{V}} \int_{\mathcal{A}_e} \mathbf{n} \int_0^s \left(\tau \cdot \nabla^2 \mathbf{M} \right) \mathrm{d}s \, \mathrm{d}A. \tag{2.33}$$

If $\mathbf{K}_0$ has an inverse, one can define $\mathbf{K} = \Phi \mathbf{K}_0^{-1}$, then

$$\mathbf{u} = -\frac{\mathbf{K}}{\mu \Phi} \cdot \boldsymbol{\nabla} \langle \mathcal{P} \rangle. \tag{2.34}$$

By remembering that that $\mathcal{P} = p - \rho \mathbf{g} \cdot \mathbf{r}$, we have,

$$\mathbf{u} = -\frac{\mathbf{K}}{\mu \Phi} \cdot \boldsymbol{\nabla} \left(\langle p - p_0 \rangle - \rho \langle \mathbf{g} \cdot \mathbf{r} \rangle \right). \tag{2.35}$$

where,

$$\langle \mathbf{g} \cdot \mathbf{r} \rangle = \langle \mathbf{r} \cdot \mathbf{g} \rangle = \frac{1}{\mathcal{V}} \int_{\mathcal{V}_f} \left(\mathbf{r} \cdot \mathbf{g} \right) \mathrm{d}V = -\Phi \, \mathbf{r}_0 \cdot \mathbf{g} \tag{2.36}$$

where $\mathbf{r}_0$ is the position vector locating the centroid of the averaging volume [132]. Since the pore pressure is given by

$$\langle p - p_0 \rangle^f = \frac{1}{\mathcal{V}_f} \int_{\mathcal{V}_f} \left(p - p_0 \right) \mathrm{d}V = \frac{1}{\Phi} \langle p - p_0 \rangle, \tag{2.37}$$

we have

$$\mathbf{u} = -\frac{\mathbf{K}}{\mu \Phi} \cdot \boldsymbol{\nabla} \left[\Phi \left(\langle p - p_0 \rangle^f - \rho \mathbf{r}_0 \cdot \mathbf{g} \right) \right]. \tag{2.38}$$

We can simplify the gravitational term by considering

$$\boldsymbol{\nabla}\left[\Phi(\rho\mathbf{r}_0\cdot\mathbf{g})\right]=\boldsymbol{\nabla}(\rho\mathbf{r}_0\cdot\Phi\mathbf{g})=\rho\boldsymbol{\nabla}\mathbf{r}_0\cdot\Phi\mathbf{g}+\rho\mathbf{r}_0\cdot\mathbf{g}\boldsymbol{\nabla}\Phi \tag{2.39}$$

with $\boldsymbol{\nabla}\mathbf{r}_0$ being the unit tensor,

$$\boldsymbol{\nabla}\left[\Phi(\rho\mathbf{r}_0\cdot\mathbf{g})\right]=\rho\Phi\mathbf{g}+\rho\mathbf{r}_0\cdot\mathbf{g}\boldsymbol{\nabla}\Phi, \tag{2.40}$$

which, by assuming a nearly uniform porous medium ($\boldsymbol{\nabla}\Phi\sim 0$), becomes

$$\boldsymbol{\nabla}\left[\Phi(\rho\mathbf{r}_0\cdot\mathbf{g})\right]=\rho\Phi\mathbf{g}. \tag{2.41}$$

Equation (2.38) then becomes

$$\mathbf{u}=-\frac{\mathbf{K}}{\mu}\cdot\left(\boldsymbol{\nabla}\langle p-p_0\rangle^f-\rho\mathbf{g}\right), \tag{2.42}$$

or,

$$\frac{\mu}{\mathbf{K}}\mathbf{u}=-\boldsymbol{\nabla}\langle p-p_0\rangle^f+\rho\mathbf{g}. \tag{2.43}$$

2.4.2 Non–Newtonian fluids

A Newtonian fluid is one that reflects the linear relationship between the shear rate and shear stress, and the parameter that defines the shear stress as a function of the shear rate is called viscosity. A non–Newtonian fluid usually exhibits a nonlinear relationship between shear rate and shear stress.

There are different ways of classifying the different kinds of non–Newtonian behaviour. Metzner [94] considers that the non–Newtonian fluids may be divided into three categories, namely purely viscous, viscoelastic and time–dependent. On the other hand, Shenoy and Mashelkar [121] distinguish first between inelastic and viscoelastic, with the inelastic being divided then into time–dependent and time–independent. The time–dependent fluids are subdivided into tixotropic and rheopectic. The time–independent fluids can be divided into pseudoplastic, dilatant, Bingham plastic and pseudoplastic with yield stress.

In the present thesis, we will deal only with time–independent non–Newtonian fluids, specifically with pseudoplastic and dilatant fluids. The apparent viscosity of a fluid is defined as the ratio between the shear stress and the shear rate. For a Newtonian fluid it is constant and equal to the viscosity of the fluid. Pseudoplastic fluids, also called shear–thinning fluids, decrease their apparent viscosity with increasing shear rate. Dilatant fluids, also called shear–thickening fluids, increase the apparent viscosity with increasing shear rate [120]. One of the most used models to deal with this kind of non–Newtonian fluid is the power–law model, namely

$$\tau = \eta \dot{\gamma}^n, \tag{2.44}$$

where τ is the shear stress, η is the consistency factor, $\dot{\gamma}$ is the shear rate and n is the power–law index.

Figure 2.2 shows the different qualitative behaviour of the types of fluid that will be considered here.

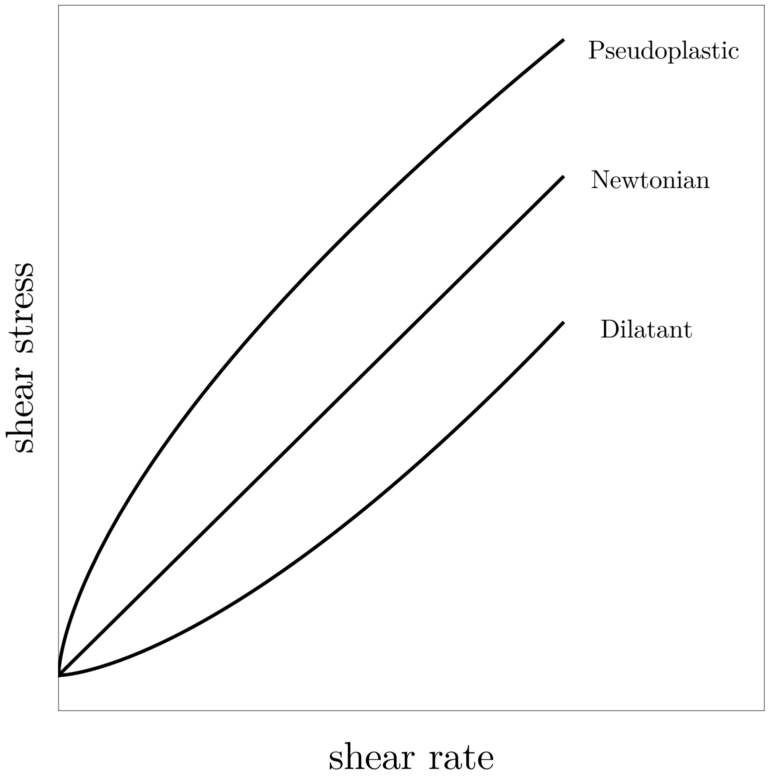

Figure 2.2: Qualitative behaviour of different types of non–Newtonian fluid.

In his review, Shenoy [120] presented and discussed different models to deal with non–Newtonian fluids in porous media. Christopher and Middleman [42] were the first to propose a modified Darcy's law that is useful for shear–thinning and shear–thickening fluids of power–law type. Such a model is given by

$$\frac{\eta_{ef}}{K} |\mathbf{u}|^{n-1} \mathbf{u} = -\boldsymbol{\nabla} p + \rho \mathbf{g}, \tag{2.45}$$

where η_{ef}/K coincides with μ/K when the fluid is Newtonian, $n = 1$, and it is given by

$$\frac{\eta_{ef}}{K} = 2\kappa\mu \left(\frac{3\Phi}{50K}\right)^{\frac{n+1}{2}} \left(\frac{3n+1}{n\Phi}\right). \tag{2.46}$$

Here, η_{ef} is the effective consistency factor of the fluid, K is the permeability, p is the dynamic pressure, μ is the consistency factor, n is the power–law index and κ is the tortuosity. The tortuosity factor can be defined in different ways. For instance, Christopher and Middleman [42], Kemblowski and Michniewicz [78] and Dharmadhikari and Kale [49] proposed, respectively

$$\kappa = \begin{cases} 25/12 \\ (2.5)^n 2^{(1-n)/2} \\ \frac{2}{3}\left(\frac{8n}{9n+3}\right)^n \left(\frac{10n-3}{6n+1}\right)\left(\frac{75}{16}\right)^{(3(10n-3))/(10n+11)} \end{cases} \tag{2.47}$$

It is worth to note here that Equation (2.46) may be written as

$$\frac{\mu_a}{K}\mathbf{u} = -\boldsymbol{\nabla} p + \rho \mathbf{g}, \tag{2.48}$$

where μ_a is the apparent viscosity and it is given by

$$\mu_a = \eta_{ef}|\mathbf{u}|^{n-1}. \tag{2.49}$$

It is easy to observe a sensible issue in this model. In the limit of vanishing shear rate, here represented by a vanishing seepage velocity, Equation (2.49) gives a zero apparent viscosity for shear–thickening fluids ($n > 1$) and infinite apparent viscosity for shear–thinning fluids ($n < 1$). Attempting to deal with this singularities, Nield [103, 104] proposed a modification on the original power–law model, yielding to an apparent viscosity

$$\mu_a = \mu_0 \left(1 + \mathcal{C}|\mathbf{u}|^{n-1}\right), \tag{2.50}$$

where $\mathcal{C}$ is a constant and μ_0 is the apparent viscosity at zero shear rate. This proposed model is able to deal with the singularities just for shear–thickhening fluids. For $n > 1$ and vanishing shear rate, the model yields the classical Darcy's model. On the other hand, for $n < 1$ the problem persists.

2.4.3 Limits of Darcy's law validity

The Darcy's equation (2.18) is known to be valid for incompressible creeping flows (low velocities). At high velocities, microscopic scale effects are manifested macroscopically in the failure of Darcy's law to relate linearly the velocity with the pressure–drop. The onset of the non–Darcian regime was, in the past, associated with the transition to the turbulence while, nowadays, we know that this is not correct. Many attempts have been done in order to deal with this problem in the second half of the 19th century. Dupuit [53] was the first to propose a correction by trying to include the flow contribution of the single pores to the global flow characteristics [86]. What Dupuit [53] proposed was an additional quadratic velocity term on the Darcy equation, namely

$$\alpha\mathbf{u} + \beta|\mathbf{u}|\mathbf{u} = -\boldsymbol{\nabla} p. \tag{2.51}$$

By the end of the 19th century, there was a discussion between a group of scientists that defended the linear Darcy's equation and another one defending the quadratic form proposed by Dupuit [86]. After the defence made by Forchheimer [55] of the quadratic version, Equation (2.51) took his name. The physical reason for the additional quadratic term, according to Lage [86], is the form force imposed to a fluid by a solid surface. Newton proposed that this resistive force should be proportional to the average fluid velocity square. Taking this concept into account, Equation (2.51) may be rewritten as

$$\frac{\mu}{K}\mathbf{u} + C\rho|\mathbf{u}|\mathbf{u} = -\boldsymbol{\nabla} p \tag{2.52}$$

where C is the form coefficient.

At this point, it is worth to discuss the limit of validity of the Darcy equation as well as the transition to a non–Darcian regime. There are different strategies adopted in the literature to investigate this transition. Some studies have considered the modified Reynolds number as the control parameter that must be used to estimate the transition from viscous dominated flow to form dominated regime, as presented, for instance, by Hlushkou and Tallarek [64]. The permeability based Reynolds number is given by

$$Re_K = \frac{\rho U K^{1/2}}{\mu}, \tag{2.53}$$

where K is the permeability. The reason why the modified Reynolds number should be used is argued to be the same reason why it is used to identify a creeping flow in clear fluids. They argue that in the Darcy regime viscous forces dominate over inertia, so the Reynolds number should be the adequate parameter to control this transition.

Nevertheless, according to Lage [86] the reason why the modified Reynolds number should not be used with this purpose is that the quadratic term is not related to the inertia, as it is commonly said, but it is related to the form forces. He argues that the correct control parameter should be instead a ratio between form forces and viscous forces, namely

$$\frac{C\rho U^2}{\frac{\mu}{K}U} = \frac{\rho C K}{\mu}U. \tag{2.54}$$

Zeng and Grigg [136] have reached the same conclusion of Lage [86]. In their study, they compared the criterion employed to identify the transition between the two regimes based on the modified Reynolds number and the one based on the Forchheimer number. The conclusion is that the one based on the Forchheimer number is the more adequate. They defined the Forchheimer number as the ratio between the pressure drop caused by liquid–solid interactions with the pressure drop due to viscous resistance. The Forchheimer number has exactly the same definition of (2.54) and it is called Fo in their work. It is worth to mention here that there are other extensions of Darcy's law with different purposes, but it is out of the scope for the present thesis the presentation and discussion of all of them. For a good review on this subject I suggest the works by Lage [86], Nield et al. [106] and Kaviany [76].

2.5 Energy balance

The application of the first law of thermodynamics for a porous medium saturated by a fluid is not so direct as it is for a continuous single–phase medium. In the case of saturated porous media, we have to take into consideration two important aspects. The first one is that we are dealing with REV averaged quantities. The second one is that in a first instance we have two different media that may interact thermodynamically.

In a first moment, the well known model for energy balance in porous media will be presented. In a second moment, the equations for the energy balance will be derived by applying the same local average technique as used before for mass and momentum balance. It is assumed that the solid is rigid, isotropic, that there is no internal heat production and that viscous dissipation and radiative effects are negligible.

In parallel, it can be said that at the pore scale there can be a temperature difference between the fluid and solid phases, ΔT_d. In the same way, inside the REV there exists a maximum temperature difference ΔT_l. Finally, over the macroscopic scale of the system the temperature differences are of order of ΔT_L. At this point, it is assumed that

$$\Delta T_d < \Delta T_l \ll \Delta T_L. \tag{2.55}$$

Such an inequality allows us to assume that within the REV ($\mathcal{V} = \mathcal{V}_f + \mathcal{V}_s$) the solid and fluid phases are in local thermal equilibrium (LTE), that is,

$$\frac{1}{\mathcal{V}_f}\int_{\mathcal{V}_f} T_f^* \mathrm{d}V = \frac{1}{\mathcal{V}_s}\int_{\mathcal{V}_s} T_s^* \mathrm{d}V = \frac{1}{\mathcal{V}}\int_{\mathcal{V}} T^* \mathrm{d}V, \tag{2.56}$$

with the superscript star (*) indicating the microscopic–scale variables. If we consider the local averages

$$T_f = \langle T_f^* \rangle^f = \frac{1}{\mathcal{V}_f}\int_{\mathcal{V}_f} T_f^* \mathrm{d}V, \tag{2.57a}$$

$$T_s = \langle T_s^* \rangle^s = \frac{1}{\mathcal{V}_s}\int_{\mathcal{V}_s} T_s^* \mathrm{d}V, \tag{2.57b}$$

$$T = \langle T^* \rangle = \frac{1}{\mathcal{V}}\int_{\mathcal{V}} T^* \mathrm{d}V, \tag{2.57c}$$

we can say that

$$T_f = T_s = T. \tag{2.58}$$

The energy balance equation for the solid phase can be then written as

$$(1-\Phi)(\rho c)_s \frac{\partial T_s}{\partial t} = (1-\Phi)\boldsymbol{\nabla}\cdot(\varkappa_s \nabla T_s), \tag{2.59}$$

while the one for the fluid phase is

$$\Phi(\rho c_p)_f \frac{\partial T_f}{\partial t} + (\rho c_p)_f \mathbf{u}\cdot\boldsymbol{\nabla} T_f = \Phi\boldsymbol{\nabla}\cdot(\varkappa_f \boldsymbol{\nabla} T_f), \tag{2.60}$$

where c is the specifc heat of the solid, c_p is the specific heat at constant pressure of the fluid and $\varkappa$ is the thermal conductivity. The subscripts s and f are relative to the solid and the fluid, respectively. If we use Equation (2.58), we have

$$\Phi(\rho c_p)_m \frac{\partial T}{\partial t} + (\rho c_p)_f \mathbf{u}\cdot\boldsymbol{\nabla} T = \boldsymbol{\nabla}\cdot(\varkappa_m \boldsymbol{\nabla} T), \tag{2.61}$$

where

$$(\rho c_p)_m = (1-\Phi)(\rho c)_s + \Phi(\rho c_p)_f, \tag{2.62}$$

$$\varkappa_m = (1-\Phi)\varkappa_s + \Phi\varkappa_f, \tag{2.63}$$

represents, respectively, the overall heat capacity per unit volume and the overall thermal conductivity. I remark that if very fast transients are present in the system, the inequality (2.55) cannot be satisfied and in this case a local thermal non–equilibrium model should be considered.

2.5.1 Theoretical deduction

In this section, I will follow the derivations made by Kaviany [76], Slattery [123] and Quintard [112]. It is assumed that the medium is rigid, isotropic, there is no internal heat production and that viscous dissipation and radiative effects are negligible. To simplify the treatment, following Kaviany [76], I start with the energy balance equation for the fluid medium (with $\varkappa_s = 0$)

$$\frac{\partial T_f^*}{\partial t} + \boldsymbol{\nabla}\cdot(T_f^* \mathbf{u}^*) = \boldsymbol{\nabla}\cdot\chi_f \boldsymbol{\nabla} T_f^*, \tag{2.64}$$

where $\chi_f = \varkappa_f/(\rho c_p)_f$. Impermeability is considered at the fluid–solid interface. By applying the local volume average

$$\frac{\partial\langle T_f^*\rangle}{\partial t} + \langle\boldsymbol{\nabla}\cdot(T_f^* \mathbf{u}^*)\rangle = \langle\boldsymbol{\nabla}\cdot\chi_f \boldsymbol{\nabla} T_f^*\rangle, \tag{2.65}$$

which after applying the relation (2.9) and the boundary conditions, we have

$$\frac{\partial \langle T_f^* \rangle}{\partial t} + \boldsymbol{\nabla} \cdot \langle (T_f^* \mathbf{u}^*) \rangle = \boldsymbol{\nabla} \cdot \left(\chi_f \boldsymbol{\nabla} \langle T_f^* \rangle + \frac{\chi_f}{\mathcal{V}} \int_{\mathcal{A}_{fs}} \mathbf{n} T_f^* \mathrm{d}A. \right). \tag{2.66}$$

Now, based on the intrinsic average, the following definitions are introduced

$$T_f^* = T_f + T_f' \tag{2.67}$$

$$\mathbf{u}^* = \mathbf{U} + \mathbf{U}' \tag{2.68}$$

where the variables with the primes are relative to the spatial deviation, and we have $\langle T_f' \rangle = 0$. The convective term can be rewritten as

$$\frac{1}{\mathcal{V}} \int_{\mathcal{V}} \mathbf{u}^* T_f^* \mathrm{d}V = \Phi \frac{1}{\mathcal{V}_f} \int_{\mathcal{V}_f} \mathbf{u}^* T_f^* \mathrm{d}V = \Phi \mathbf{U} T_f + \Phi \langle \mathbf{U}' T_f' \rangle, \tag{2.69}$$

yielding

$$\frac{\partial \Phi T_f}{\partial t} + \boldsymbol{\nabla} \cdot (\Phi T_f \mathbf{U}) = \boldsymbol{\nabla} \cdot \left(\Phi \chi_f \boldsymbol{\nabla} T_f + \frac{\chi_f}{\mathcal{V}} \int_{\mathcal{A}_{fs}} \mathbf{n} T_f' \mathrm{d}A \right) - \boldsymbol{\nabla} \cdot \left(\Phi \langle \mathbf{U}' T_f' \rangle^f \right). \tag{2.70}$$

Similar to what was already done for the velocity, we introduce a closure constitutive equation,

$$T_f' = \mathbf{b} \cdot \boldsymbol{\nabla} T_f, \tag{2.71}$$

with $\mathbf{b}$ being the vector function that maps the gradient of the intrinsic phase–averaged temperature into the local fluctuation temperature field (in analogy with the treatment of turbulence). Again, $\boldsymbol{\nabla}\Phi$ is assumed to be small, and consequently Φ can be locally approximated as a constant.

$$\frac{\partial T_f}{\partial t} + \mathbf{U} \cdot \boldsymbol{\nabla} T_f = \boldsymbol{\nabla} \cdot \left[\chi_f \left(\mathbf{I} + \frac{1}{\mathcal{V}_f} \int_{\mathcal{A}_{fs}} \mathbf{n}\mathbf{b} \mathrm{d}A \right) \cdot \boldsymbol{\nabla} T_f \right] - \boldsymbol{\nabla} \cdot \left(\langle \mathbf{U}' \mathbf{b} \rangle^f \cdot \boldsymbol{\nabla} T_f \right), \tag{2.72}$$

where we consider that

$$\langle \mathbf{U}' T_f' \rangle^f = \langle \mathbf{U}' \mathbf{b} \cdot \boldsymbol{\nabla} T_f \rangle^f = \langle \mathbf{U}' \mathbf{b} \rangle^f \cdot \boldsymbol{\nabla} T_f, \tag{2.73}$$

because $\boldsymbol{\nabla} T_f$ is constant inside the REV. Now, following Carbonell and Whitaker [35], we define the tortuosity tensor as

$$\mathbf{L}_t^* = \frac{1}{\mathcal{V}_f} \int_{\mathcal{A}_{fs}} \mathbf{n}\mathbf{b} \mathrm{d}A, \tag{2.74}$$

while the dispersion tensor is

$$\mathbf{D}^d = -\frac{1}{\mathcal{V}_f}\int_{\mathcal{V}_f} \mathbf{U}'\mathbf{b}\mathrm{d}V. \tag{2.75}$$

Then, we can finally write the equation for the fluid phase for the case $\varkappa_s = 0$.

$$\frac{\partial T_f}{\partial t} + \mathbf{U}\cdot\boldsymbol{\nabla}T_f = \boldsymbol{\nabla}\cdot\left(\boldsymbol{\chi}^f_{eff}\cdot\boldsymbol{\nabla}T_f\right), \tag{2.76}$$

where $\boldsymbol{\chi}^f_{eff}$ is defined as the total effective thermal diffusivity tensor of the fluid phase, which for the case $\varkappa_s = 0$ is given by

$$\boldsymbol{\chi}^f_{eff} = \chi_f\left(\mathbf{I} + \mathbf{L}^*_t\right) + \mathbf{D}^d, \tag{2.77}$$

with $\mathbf{I}$ being the identity tensor.

A generalization of Equation (2.76) is possible for the generic case with $\varkappa_s \neq 0$. Under the assumption of local thermal equilibrium, if we add the equations of energy balance for the fluid and solid phases, we obtain

$$\sigma\frac{\partial T}{\partial t} + \mathbf{u}\cdot\boldsymbol{\nabla}T = \boldsymbol{\nabla}\cdot\left(\boldsymbol{\chi}_{eff}\cdot\boldsymbol{\nabla}T\right), \tag{2.78}$$

where

$$\sigma = \frac{(\rho c_p)_m}{(\rho c_p)_f}, \tag{2.79}$$

$$(\rho c_p)_m = (1-\Phi)(\rho c)_s + \Phi(\rho c_p)_f, \tag{2.80}$$

and

$$\boldsymbol{\chi}_{eff} = \frac{\boldsymbol{\varkappa}_{eff}}{(\rho c_p)_f}, \tag{2.81}$$

with $\boldsymbol{\varkappa}_{eff}$ being the effective thermal conductivity given by

$$\boldsymbol{\varkappa}_{eff} = \left[(1-\Phi)\varkappa_s + \Phi\varkappa_f\right]\mathbf{I} + \frac{1}{\mathcal{V}}(\varkappa_f - \varkappa_s)\int_{\mathcal{A}_{fs}}\mathbf{n}\mathbf{b}\mathrm{d}A - (\rho c_p)_f\langle\mathbf{U}'\mathbf{b}\rangle^f. \tag{2.82}$$

In the expression for the effective thermal conductivity tensor, we can see three different contributions: a simple average of the thermal conductivity, a correction to the average due to the tortuosity and finally a contribution due to the dispersion mechanisms. It is not unusual to see in the literature some works that consider just a simple average between both thermal conductivities. For an interesting discussion about effective properties in porous media, please see the work by Quintard et al. [113].

Chapter 3

Stability theory

In this chapter, the stability theory will be described and discussed. Specifically, one of the possible definitions of *stability* of a dynamical system will be presented. Next, the particularities of the linear stability theory usually considered in the stability analysis of fluid systems will be described. Finally, the weakly nonlinear approach will be presented and discussed.

3.1 General description of stability

The stability analysis of a dynamical system aims to identify if, considering a given equilibrium solution of such a system, it will remain in equilibrium when subject to small disturbances. It is worth to point out that the equilibrium solution, in a first instance, can be a steady solution or even a time–periodic one. In the present thesis, just steady equilibrium solutions are considered.

If a given equilibrium solution is stable, small disturbances are damped in such a way that the original equilibrium solution is always recovered in an asymptotic limit. On the other hand, if it is unstable, the disturbances are amplified in such a way that the original equilibrium state cannot be recovered again. The study of the possible new states that may arise after breaking the original equilibrium concerns the bifurcation theory which will be treated later. For a more exhaustive review on the theory of dynamical systems as well as on the theory of bifurcation I refer the reader to the books by Kuznetsov [85] and Strogatz [125]. For a systematic review on the stability theory, focused on fluid dynamics and heat transfer problems, I mention the books by Drazin and Reid [51], Schmid et al. [118] and Chandrasekhar [38].

Among the different concepts of stability, the one proposed by Lyapunov [90] is certainly one of the most used in the theory of dynamical systems. Namely, it states that if $x(t)$ is a dynamical variable and x_0 is an equilibrium condition of a given dynamical system, x_0 is said to be stable, in the Lyapunov sense, if for an instant of time $t = t_0$, for all $\epsilon > 0$, there exists a $\delta(t_0, \epsilon) > 0$ such that

$$||x(t_0) - x_0|| < \delta \quad \Rightarrow \quad ||x(t) - x_0|| < \epsilon, \quad \forall t \geq t_0. \tag{3.1}$$

3.2 Linear analysis

Linear stability analysis is the branch of stability theory dealing with infinitesimal disturbances. In general, the disturbances behave as plane waves and can be modelled by Fourier modes. Once this assumption is made, the original problem can be reduced to an eigenvalue problem (EVP) and two different approaches can be considered: one based on the eigenvalues and the other one based on the eigenvectors. The latter one is called by some authors as "stability without eigenvalue" [128] or "nonmodal stability" [117]. Traditionally the study of linear stability has been made through the eigenvalue approach, usually called modal analysis [73].

If one is interested in investigating the short–time dynamic behaviour of the disturbances, the eigenvector analysis is the most suitable choice. The stability analysis without eigenvalues is based on the loss of orthogonality of the eigenvectors [117] of the linear operator, that may take place only if the linear operator is a non–normal one, which means that it does not commute with its adjoint. On the other hand, considering that the loss of orthogonality of the eigenvectors is due to a linear disturbance growth mechanism, large amplitudes should be observed. This phenomenon is expected to be uncommon.

The eigenvalue analysis, instead, provides information about the asymptotic linear growth of the single plane waves, or the single Fourier modes. In general, the particular mode that becomes of interest is the most unstable one, or the one with the largest growth rate. This kind of analysis can be interpreted as the upper parametric limit, above which the infinitesimal disturbances present in the system start to grow asymptotically. In the present study, just the eigenvalue approach is considered. In order to illustrate such an analysis, consider the following generic dynamical system,

$$\frac{\partial q(x,t)}{\partial t} = F_\mu(x, t, q(x,t)), \tag{3.2}$$

where q is the vector formed by the physical quantities of the problem, x is the spatial position, t is the time, F is the operator that characterizes the specific problem and μ is the vector formed by the control parameters. We suppose that such a system has a stationary solution, called "basic solution" q_0,

$$\frac{\partial q_0}{\partial t} = F_\mu(x, t, q_0) = 0. \tag{3.3}$$

Such a basic solution, is observable if it is stable in relation to the disturbances. In order to investigate the stability of such a solution, we consider that the physical quantities can be decomposed in two parts, namely the one relative to the basic solution and another one relative to the perturbations,

$$q(x,t) = q_0 + \tilde{q}(x,t), \tag{3.4}$$

with $\tilde{q} \ll q_0$. After substituting in Equation (3.2), we have that the dynamics of $\tilde{q}$ is given by

$$\frac{\partial \tilde{q}(x,t)}{\partial t} = F_\mu(x,t,q_0 + \tilde{q}(x,t)). \tag{3.5}$$

The right–hand side of Equation (3.5) can be expanded in a Taylor series, yielding

$$F_\mu(x,t,q_0 + \tilde{q}(x,t)) = F_\mu(x,t,q_0) + \tilde{q}\left(\frac{\partial F_\mu}{\partial q}\right)_{q_0} + \mathcal{O}(\tilde{q}^2), \tag{3.6}$$

what allows one to write

$$\frac{\partial \tilde{q}(x,t)}{\partial t} = \left(\frac{\partial F_\mu}{\partial q}\right)_{q_0} \tilde{q}(x,t) = \mathcal{L}_\mu \tilde{q}(x,t) \tag{3.7}$$

with

$$\mathcal{L}_\mu = \left(\frac{\partial F_\mu}{\partial q}\right)_{q_0} \tag{3.8}$$

being the linear operator of the specific problem. The linearised problem then becomes

$$\frac{\partial \tilde{q}(x,t)}{\partial t} = \mathcal{L}_\mu(x,t,q_0)\tilde{q}(x,t). \tag{3.9}$$

At this point, we assume that the disturbances are periodic in space what allow us to apply a Fourier transform on the disturbance quantities $\tilde{q}(x,t)$ [8]

$$\hat{q}(k,t) = \frac{1}{\sqrt{2\pi}} \int_{-\infty}^{+\infty} \tilde{q}(x,t) e^{-ikx} \mathrm{d}x, \tag{3.10}$$

with its inverse transform given by

$$\tilde{q}(x,t) = \frac{1}{\sqrt{2\pi}} \int_{-\infty}^{+\infty} \hat{q}(k,t) e^{ikx} \mathrm{d}k. \tag{3.11}$$

Once the transformation is applied, we turn the dependence on x into a dependence on k, a parameter with the physical meaning of a wave number. By looking at Equation (3.11) it is clear that the disturbance is represented by a linear combination of spatially–periodic wavelike signals. Physically, that means that the disturbances are a plane waves infinitely wide in space. When applied to Equation (3.9), it yields

$$\frac{\partial \hat{q}(k,t)}{\partial t} = \hat{\mathcal{L}}_\mu(k,t,q_0)\hat{q}(k,t), \tag{3.12}$$

whose solution is given by

$$\hat{q}(k,t) = \sum_n e^{\lambda_n t}\overline{q}_n(k), \tag{3.13}$$

whenever λ and $\overline{q}$ solve the eigenvalue problem

$$\hat{\mathcal{L}}_\mu Q = Q\Lambda \tag{3.14}$$

where Λ is the diagonal matrix with the eigenvalues λ_n of $\hat{\mathcal{L}}_\mu$ and Q is the eigenvector matrix with $\overline{q}_n$ being the eigenvectors. Alternatively, we may assume that the disturbance solution is an arbitrary superposition of the disturbances, in which each one of the disturbances may have different amplitudes,

$$\hat{q}(k,t) = \sum_n^\infty A_n\overline{q}_n(k), \tag{3.15}$$

where A_n is the solution of

$$\frac{\mathrm{d}A_n}{\mathrm{d}t} = \lambda_n A_n, \tag{3.16}$$

that is,

$$A_n = A_n(0)e^{\lambda_n t}. \tag{3.17}$$

The solution of the disturbances linearised equations is then given by

$$\hat{q}(k,t) = \sum_n^\infty A_n(0)e^{\lambda_n t}\overline{q}_n(k), \tag{3.18}$$

where λ_n is in general complex $\lambda_n = s_n + i\omega$

$$\hat{q}(k,t) = \sum_n^\infty A_n(0)e^{s_n t}e^{i\omega_n t}\overline{q}_n(k), \tag{3.19}$$

with s being the growth rate of the disturbances and ω the frequency.

Let s_i be the maximum of all s_n for a given k, then we have

$$\text{If} \quad \begin{cases} s_i < 0 & \Rightarrow \text{Stable} \\ s_i = 0 & \Rightarrow \text{Neutrally stable} \\ s_i > 0 & \Rightarrow \text{Unstable} \end{cases}$$

Similarly, the maximum of all s_i for all values of k is called s_1, and occurs when $\partial s_i/\partial k = 0$, where

$$\mu(k_c) = \mu_c$$

with k_c being the critical wavenumber and μ_c is the critical value of μ.

3.2.1 Convective and absolute instabilities

Once the problem becomes unstable, it is necessary to distinguish between the nature of the instability. From the point of view of the linear stability theory, it is possible to classify the unstable state as convectively unstable or absolutely unstable. The distinction between both types of instability may be done by looking at the way that a given equilibrium solution responds to an impulse. If the impulse decays asymptotically to zero all around the domain, it is said to be stable. However, if it is amplified, the solution is said to be unstable.

In the case of fluid dynamics, if the disturbances amplify as they are advected away by the basic flow, they are said to be convectively unstable [68]. That means that by observing at a fixed point in space, the impulse response decays asymptotically to zero. On the other hand, if the problem is absolutely unstable, the disturbances grow in time for a fixed point in space, so that the impulse response eventually starts to affect all the domain [68].

In his book, Barletta [8] presents a thorough discussion about absolute instabilities for convective flows in porous media. According to this author, a single normal mode with a given wavenumber k is convectively unstable if $s > 0$. On the other hand, a perturbation $\mathcal{F}(x, t)$ is absolutely unstable if it is absolutely integrable over all the real x-axis and if

$$\lim_{t \to +\infty} |\mathcal{F}(x, t)| = +\infty, \quad \forall x \in \mathbb{R}. \tag{3.20}$$

3.3 Weakly nonlinear analysis

The linear stability analysis provides information about the threshold to the instability, as well as information about the wave disturbance modes, but it does not take into account the interaction between the wave disturbances. As the problem becomes unstable from the linear point of view, that is when $\mu > \mu_c$, the equilibrium solution is not observed any more and the system displays a bifurcation to a different state. Informations regarding the new equilibrium solution can be determined by tackling the problem in different ways. A numerical simulation of the fully nonlinear system as well as an experimental investigation are two possible choices that can be quite complicated depending on the kind of problem. In this way, the weakly nonlinear analysis can be an interesting way of approaching this problem from a theoretical point of view. The approach described in this section is similar to that used by Newell and Whitehead [95] and in more recent papers by Bouteraa et al. [23] and Requilé et al. [115].

Once the instability threshold is exceeded, the disturbances start to grow with a growth rate that is proportional to the distance from the critical point. In that sense, if $\mu > \mu_c$ we have that $s_1 > 0$. By expanding the growth rate around the critical point, we have

$$s_1(\mu) = s_1(\mu_c) + \left(\frac{\partial s_1}{\partial \mu}\right)_{\mu_c} (\mu - \mu_c) + \mathcal{O}\left((\mu - \mu_c)^2\right), \tag{3.21}$$

where $s_1(\mu_c) = 0$. Here, for simplicity it will be assumed that $\omega_c = 0$ and that no spatial variations take place in the unstable region ($k = k_c$). Thus, the temporal dynamics of the amplitude of the unstable modes, given by Equation (3.16), can be formulated as

$$\frac{\mathrm{d}A_1}{\mathrm{d}t} = \left(\frac{\partial s_1}{\partial \mu}\right)_{\mu_c} (\mu - \mu_c) A_1, \tag{3.22}$$

confirming the previous idea that, in the vicinity of the first bifurcation point, the growth rate varies proportionally to $(\mu - \mu_c)$. The disturbances now can be expressed as,

$$\hat{q}(k_c, t) = A_1(0) e^{\left(\frac{\partial s_1}{\partial \mu}\right)_{\mu_c} (\mu - \mu_c) t} \overline{q}_1(k_c). \tag{3.23}$$

The linear dynamics suggests that, around the critical point, the time scale is a different one, that is called slow time $t_2 \sim \mathcal{O}\left((\mu - \mu_c)t\right)$. The disturbances solution around the critical point then become,

$$\hat{q}(k_c, t) = A_1(t_2) \overline{q}_1(k_c), \tag{3.24}$$

or

$$\tilde{q}(x, t) = A_1(t_2) \overline{q}_1(k_c) e^{i k_c x} + \text{c.c}, \tag{3.25}$$

with c.c representing the complex conjugate.

The aim of the present analysis is to determine the temporal evolution of $A_1(t_2)$ in the vicinity of the instability threshold. When a system bifurcates the first time, the disturbances start to grow up to the saturation due to the nonlinear terms. If the nonlinearities are not present, the disturbances grow infinitely in time. Since the study of the interaction between the disturbances is out of the scope of a linear analysis, it cannot give any kind of information about the saturation. The weakly non linear analysis consists in developing the disturbances $\tilde{q}$ as a linear combination of all possible interaction between the disturbance modes and their complex conjugate. Considering that the amplitude of $A_1(t_2)$ is small, we have that at $\mathcal{O}(A_1(t_2))$ the linear problem is recovered. At $\mathcal{O}(A_1(t_2)^2)$ there is the interaction between the fundamental mode and itself, yielding a harmonic mode and the fundamental mode and its complex conjugate, yielding a nonlinear correction to the basic state. At $\mathcal{O}(A_1(t_2)^3)$ there are more complex interactions. The interaction between the complex conjugate of the fundamental mode with the harmonic of second order cause resonance with the fundamental mode that must be eliminated. Similarly, the fundamental mode with the nonlinear correction, originating another resonant term that must be eliminated as well. The elimination of these terms means that linear growth is balanced by the resonant nonlinear terms. If these nonlinear terms are not able to balance the linear growth, that means that it is necessary to go beyond in the expansion around the criticality. This fact lead us to scale the amplitude based on the distance to the criticality, namely

$$A(\mu - \mu_c) \sim A^3, \tag{3.26}$$

which implies that

$$A \sim (\mu - \mu_c)^{1/2}. \tag{3.27}$$

From the practical point of view, the analysis consists in applying an asymptotic series for the disturbances,

$$\tilde{q} = \varepsilon\tilde{q}_1 + \varepsilon^2\tilde{q}_2 + \varepsilon^3\tilde{q}_3 + \mathcal{O}(\varepsilon^4), \tag{3.28}$$

and after substituting in the original equations, one can solve the problem for each order. Then, if we assume that $(\mu - \mu_c) \sim \mathcal{O}(\varepsilon^2)$, we have that $A \sim \mathcal{O}(\varepsilon)$. Such an assumption implies that the new time scale may be defined as

$$t_2 = \varepsilon^2 t, \tag{3.29}$$

and also that the distance to criticality is given by

$$\mu = \mu_c + \varepsilon^2\mu_2. \tag{3.30}$$

After substituting all these definitions in the original equations, one can finally solve the problem at first and second order. At third order, in order to determine the first nonlinear correction to the linear growth, one applies the mathematical condition known as the Fredholm alternative. It is worth to emphasize that, if the first nonlinear correction to the linear growth is not enough, it is necessary to go beyond on the expansions, at least up to the fifth order.

Chapter 4

Numerical methodology

In this chapter, I will briefly describe the two main approaches employed for the solution of the eigenvalue problems that are considered in the present thesis, namely the shooting method and the matrix forming approach.

4.1 Shooting method

In the last chapter, the fundamentals of the linear theory was presented by considering an auxiliary system in which physical quantities depended just on time (t) and on a homogeneous direction (x). In this section, I will treat the dependence on t and x as a dependence on λ and k, that are the complex frequency and the wavenumber, respectively. In addition, a dependence on a non–homogeneous direction z will be introduced. Usually, the linear differential problem that comes from the stability analysis is a boundary value problem, which means that the physical problem is bounded in one or more direction. The linear eigenvalue problem can be solved by employing different techniques, depending on the information that in sought. If the aim is to understand the threshold values of the governing parameters for the onset of instability, the shooting method is a suitable choice. For a more complete treatment of the shooting method, I refer the reader to the books by Burden and Faires [34] and Hoffman and Frankel [65].

The shooting method consists in transforming a boundary value problem into a double initial value problem. Then, by using the boundary conditions as target conditions for a root finding method, one obtains the threshold values of the governing parameters. Consider a generic linear differential equation like

$$\frac{\partial^2 \mathbf{q}}{\partial z^2} = \mathbf{G}(\lambda, k, \mu, \mathbf{q}), \tag{4.1}$$

where $\mathbf{q}$ is a vector formed by the generic quantities q_1 and q_2, where $\mathbf{q} = (q_1, q_2)^T$ and $\mathbf{G}$ is a linear function of λ, k, μ and $\mathbf{q}$. The other quantities λ, k and μ are the same quantities defined in Chapter 3. Considering that the boundaries are defined two, namely $z = 0$ and $z = H$, for each variable two boundary conditions are necessary. For this generic problem, the boundary conditions are given by

$$z = 0: \quad q_1 = q_{01}, \quad q_2 = q_{02} \tag{4.2a}$$

$$z = H: \quad q_1 = q_{H1}, \quad q_2 = q_{H2}, \tag{4.2b}$$

where q_{01}, q_{02}, q_{H1} and q_{H2} are, in a first instance, complex quantities. Here, the boundary conditions are considered as the first type for simplicity, but it could be any kind of boundary condition.

The shooting method consists in getting rid of the original boundary conditions in one boundary, creating new unknown initial conditions on the other boundary, and then solving the initial value problem. The initial value problem must have the same number of initial values that had before of boundary conditions. That means that for the present problem two new initial values must be imposed. Since in a first instance the quantities are allowed to be complex, then the new initial conditions may be written as

$$z = 0: \quad \frac{\partial q_1}{\partial z} = c_1 = c_{r,1} + ic_{i,1}, \quad \frac{\partial q_2}{\partial z} = c_2 = c_{r,2} + ic_{i,2}. \tag{4.3}$$

Since the problem is homogeneous, the solution can be found up to a constant. For this reason, one of the conditions can be rescaled, reducing the boundary conditions to

$$z = 0: \quad \frac{\partial q_1}{\partial z} = 1, \quad \frac{\partial q_2}{\partial z} = c_{21} = c_{r,21} + ic_{i,21}. \tag{4.4}$$

Now, it is possible to solve the initial value problem formed by Equation (4.1) together with Equations (4.2a) and (4.4). The result of $\mathbf{q}$ depends on the control parameters. If one is interested on the instability threshold, has to impose that $s = 0$, and that $\lambda = i\omega$. For each value of k, μ, ω, $c_{r,21}$ and $c_{i,21}$ the solution of $\mathbf{q}$ changes and return a different value of $\mathbf{q}(z = H)$. In the present case, lets consider that for each assigned value of k we want to know the values of μ, ω, $c_{r,21}$ and $c_{i,21}$ that satisfies the neutral stability condition as well as the original boundary conditions. In practice, we have to solve four real equations:

$$\begin{split}\{\mathrm{Re}\left[q_1(H) - q_{H1}\right], \mathrm{Im}\left[q_1(H) - q_{H1}\right], \mathrm{Re}\left[q_2(H) - q_{H2}\right], \mathrm{Im}\left[q_2(H) - q_{H2}\right]\} \\ = \{0, 0, 0, 0\}\end{split} \tag{4.5}$$

and four unknown real variables to recover, namely

$$\{\mu, \omega, c_{r,21}, c_{i,21}\}. \tag{4.6}$$

The initial value problem can be solved by any numerical method that solves ordinary differential equations with a given initial condition. Then, to find the exact values of (4.6) that satisfies (4.5), a root–finding method is applied. In the present work, the symbolic computation software *Mathematica* [69], and their built–in functions, are employed. The initial value problem is solved by using a fourth order Runge–Kutta method and the root–finding procedure is carried out by using a Newton–Raphson method.

4.1.1 Critical condition

For each assigned values of k there is at least one correspondent value of μ that is relative to the neutral stability condition. Once the neutral stability conditions are determined, one may seek for the absolute minimum of μ over all values of $\mu(k)$ that identifies μ_c, k_c and ω_c, *i.e.* the critical values of μ, k and ω respectively. A method employed to obtain directly these critical values is by taking the derivative of Equations (4.2) with respect to the wave number, k, and then by imposing the constraint $\mathrm{d}\mu/\mathrm{d}k = 0$, leading to

$$\frac{\partial^2 \mathbf{q}_k}{\partial z^2} = \mathbf{G}_k(\lambda, k, \mu, \mathbf{q}, \lambda_k, \mathbf{q}_k), \tag{4.7}$$

where the subscript k means a parametric derivative with respect to k. The boundary condition of this new system are given by

$$z = 0: \quad q_{k,1} = q_{k,01}, \quad q_{k,2} = q_{k,02} \tag{4.8a}$$

$$z = H: \quad q_{k,1} = q_{k,H1}, \quad q_{k,2} = q_{k,H2}, \tag{4.8b}$$

where $q_{k,01}$, $q_{k,02}$, $q_{k,H1}$ and $q_{k,H2}$ are complex quantities correspondent to the derivative of the original quantities given by (4.2) with respect to k.

The extended system made of Equations (4.1) and (4.7) is solved by using the same procedure as described in Section 4.1.

4.2 Matrix forming

As explained in the last section, when using the shooting method, the solution is given point–by–point, that is for each value of k. The impracticality of building an automatic routine to detect all possible eigenvalue branches when solving Equation (4.1) is evident. An alternative methodology that gives more control on the different eigenvalue branches is the matrix forming one, which consists in reformulating the differential problem given by Equation (4.1), and the subsequent transformation of it in an algebraic matrix eigenvalue problem. Equation (4.1) can be rewritten as a generalized eigenvalue problem

$$\mathbf{L}_1\mathbf{q} = \lambda\mathbf{L}_2\mathbf{q}, \tag{4.9}$$

where $\mathbf{L}_1$ and $\mathbf{L}_2$ are the linear operators which depends on k and μ and contain already the information regarding the boundary conditions (4.2a) and (4.4). As in the previous section, λ is the eigenvalue.

In the matrix–forming approach, for each assigned value of k and μ the whole eigenvalue spectrum is calculated, not just specific modes. In the present work the differential operators are transformed in algebraic ones by adopting the Chebyshev–Gauss–Lobatto pseudo–spectral method described in Boyd [24], Juniper et al. [73] and El-Baghdady and El-Azab [54] is used. The differential eigenvalue problem then becomes an algebraic eigenvalue problem which can be solved in different ways. In this study, the QZ algorithm from the Fortran library *Linear Algebra PACKage* (LAPACK) [7] is used.

Chapter 5

A horizontal porous layer with vertical pressure gradient saturated by a power–law fluid

5.1 Introduction

An important variant of the Horton–Rogers–Lapwood problem concerns a vertical, instead of horizontal, throughflow in a porous channel. This phenomenon is usually found in geophysical applications. Zhao et al. [138] approached in their book the convective heat transfer in geological systems. They pointed out the importance of convection on the comprehension of different natural phenomena such as mineralization, and how some natural geological flows are caused by a vertical pressure difference. Among the pioneering studies that dealt with the onset of convection in horizontal porous channels with vertical throughflow, those by Sutton [126] and by Homsy and Sherwood [66] deserve to be mentioned.

Barletta et al. [16] extended the work carried out by Homsy and Sherwood [66] by tanking into considerations the effects of viscous dissipation. Subsequently, Barletta and Storesletten [15] took into account the role of the non–Newtonian rheology described by a power–law model on the onset of instability in a porous channel with vertical throughflow. Jones and Persichetti [71] investigated the effect of vertical throughflow under different configurations.

The present study focuses on the investigation of the effect of the vertical throughflow caused by a pressure gradient on the onset of convection in a porous channel saturated by a non–Newtonian fluid whose rheology is described by a power–law model. The linear stability theory is applied and the resulting mathematical problem is solved numerically. For some specific cases, analytical solutions can be found.

The contents of this chapter is based on the paper by Brandão, P. V., Celli, M., Barletta, A. and Alves, L. S. de B., Convection in a horizontal porous layer with vertical pressure gradient saturated by a power–law fluid, Transport in Porous Media, doi:10.1007/s11242-019-01328-5 [27].

5.2 Mathematical model

A porous channel with permeable walls saturated by a power–law fluid is considered here. A local thermal equilibrium between the solid and fluid phases is assumed. The Oberbeck–Boussinesq approximation is considered as valid and Darcy's law is generalised to model the non–Newtonian behaviour of the power–law fluid [120]. The governing equations, namely the mass balance, the momentum balance and the energy balance equations, may be written in their dimensional form as

$$\boldsymbol{\nabla} \cdot \mathbf{u} = 0, \tag{5.1a}$$

$$\frac{\eta_{ef}}{K} |\mathbf{u}|^{n-1} \mathbf{u} = -\boldsymbol{\nabla} p - \rho_0 \mathbf{g} \beta (T - T_0), \tag{5.1b}$$

$$\sigma \frac{\partial T}{\partial t} + \mathbf{u} \cdot \boldsymbol{\nabla} T = \chi \nabla^2 T, \tag{5.1c}$$

where η_{ef}/K coincides with μ/K when $n = 1$, *i.e.*, the Newtonian case, and it can be written as in Equation (2.46)

$$\frac{\eta_{ef}}{K} = 2\kappa\mu \left(\frac{3\Phi}{50K} \right)^{(n+1)/2} \left(\frac{3n+1}{n\Phi} \right)^{n}. \tag{5.2}$$

Here, η_{ef} is the effective consistency factor of the power–law fluid, κ is the tortuosity. Christopher and Middleman [42] assumed that κ is a constant equal to $25/12$. Moreover, K is the permeability, p is the dynamic pressure, ρ_0 is the fluid density at the reference temperature T_0, β is the thermal expansion coefficient of the fluid, $\mathbf{g}$ is the gravity acceleration with modulus g, n is the power–law index, t is the time, σ is the ratio between the average volumetric heat capacity of the saturated porous medium and the volumetric heat capacity of the fluid, χ is the effective thermal diffusivity of the porous medium, μ is the consistency factor and Φ is the porosity.

The horizontal porous channel is limited by isothermal and isobaric permeable walls, in such way that a vertical throughflow is present and the boundary conditions are given by

$$z = 0: \quad p = p_0 + \Delta p, \quad T = T_0 + \Delta T, \tag{5.3a}$$

$$z = H: \quad p = p_0, \quad T = T_0. \tag{5.3b}$$

5.2.1 Dimensionless formulation

The following dimensionless quantities can be introduced,

$$\frac{1}{H}(x,y,z) \to (x,y,z), \qquad \frac{H}{\chi}\mathbf{u} \to \mathbf{u}, \qquad \frac{\chi}{\sigma H^2}t \to t,$$
$$\frac{T-T_0}{\Delta T} \to T, \qquad \frac{p-p_0}{\Delta p} \to p, \tag{5.4}$$

as well as the dimensionless parameters

$$Ra = \frac{\rho_0 g \beta \Delta T K H^n}{\eta_{ef}\chi^n}, \qquad \Lambda = \frac{H^{n-1}K\Delta p}{\eta_{ef}\chi^n}, \tag{5.5}$$

with Ra being the non–Newtonian Darcy–Rayleigh number and Λ a control parameter based on quantities relative to the fluid and the flow. At this point, one can write the dimensionless governing equations as

$$\boldsymbol{\nabla}\cdot\mathbf{u} = 0, \tag{5.6a}$$
$$|\mathbf{u}|^{n-1}\mathbf{u} = -\Lambda\boldsymbol{\nabla}p + Ra\,T\mathbf{e}_z, \tag{5.6b}$$
$$\frac{\partial T}{\partial t} + \mathbf{u}\cdot\boldsymbol{\nabla}T = \nabla^2 T, \tag{5.6c}$$

where $\mathbf{e}_z$ is the unit vector in the z direction. The dimensionless formulation of the boundary conditions is given by

$$z = 0: \quad p = 1, \quad T = 1, \tag{5.7a}$$
$$z = 1: \quad p = 0, \quad T = 0. \tag{5.7b}$$

5.2.2 Steady state

The onset of convection is understood as the modification of a basic equilibrium solution and the emergence of a different state. The basic state is a steady solution of the problem where the pressure difference between the boundaries creates a vertical throughflow. From the local mass balance equation, one can conclude that such a vertical throughflow is uniform and its dimensionless form involves the Péclet number,

$$\mathbf{u}_b = \{0, 0, Pe\}, \tag{5.8}$$

where the subscript b stands for basic solution and Pe the Péclet number based on the dimensional vertical velocity due to the pressure difference on the boundaries. The basic temperature is expressed as

$$T_b(z) = \frac{\mathrm{e}^{Pe} - \mathrm{e}^{Pez}}{\mathrm{e}^{Pe} - 1}. \tag{5.9}$$

From Equation (5.6b), one obtains

$$Pe^n = -\Lambda \frac{\mathrm{d}p_b}{\mathrm{d}z} + RaT_b. \tag{5.10}$$

On account of Equation (5.9), one obtains an expression for $\mathrm{d}p_b/\mathrm{d}z$,

$$\frac{\mathrm{d}p_b}{\mathrm{d}z} = \frac{Pe^{1+n} - \mathrm{e}^{Pe}Pe^{1+n} + \mathrm{e}^{Pe}PeRa - \mathrm{e}^{Pez}PeRa}{(\mathrm{e}^{Pe} - 1)Pe\Lambda}. \tag{5.11}$$

Finally, by integrating Equation (5.11), the parameter Λ can be written as

$$\Lambda = Pe^n + \left(\frac{1}{1 - \mathrm{e}^{Pe}} + \frac{1}{Pe} - 1\right) Ra. \tag{5.12}$$

5.3 Linear stability analysis

The x and y components of Equation (5.6b) are

$$|\mathbf{u}|^{n-1}u = -\Lambda \frac{\partial p}{\partial x} \tag{5.13a}$$

$$|\mathbf{u}|^{n-1}v = -\Lambda \frac{\partial p}{\partial y} \tag{5.13b}$$

which means $u = v = 0$ at the both upper and the lower boundaries where the pressure is uniform. Moreover, from Equation (5.6a) one obtains $\partial w/\partial z = 0$ at the boundaries.

In order to reduce the number of variables and simplify the analysis, one can get rid of the dependence on the pressure by taking the curl of Equation (5.6b). In this way, the governing equations are expressed as a function of the velocity and temperature fields

$$\boldsymbol{\nabla} \cdot \mathbf{u} = 0, \tag{5.14a}$$

$$\boldsymbol{\nabla} \times \left(|\mathbf{u}|^{n-1}\mathbf{u}\right) = \boldsymbol{\nabla} \times \left(Ra\, T\mathbf{e}_z\right), \tag{5.14b}$$

$$\frac{\partial T}{\partial t} + \mathbf{u} \cdot \boldsymbol{\nabla} T = \nabla^2 T. \tag{5.14c}$$

For the linear stability analysis, it is assumed that the physical quantities can be decomposed into a basic part and another one relative to the disturbances, as explained in Section 3.2,

$$\mathbf{u} = \mathbf{u}_b + \epsilon\tilde{\mathbf{u}}, \qquad T = T_b + \epsilon\tilde{T}. \tag{5.15}$$

Here, $\epsilon \ll 1$ represents the order of magnitude of the disturbances. By substituting Equation (5.15) into Equations (5.14), and by neglecting terms of $\mathcal{O}(\epsilon^2)$, the linearised equations are achieved

$$\frac{\partial \tilde{u}}{\partial x} + \frac{\partial \tilde{v}}{\partial y} + \frac{\partial \tilde{w}}{\partial z} = 0, \tag{5.16a}$$

$$n\frac{\partial \tilde{w}}{\partial y} - \frac{\partial \tilde{v}}{\partial z} = \frac{Ra}{|Pe|^{n-1}}\frac{\partial \tilde{T}}{\partial y}, \tag{5.16b}$$

$$n\frac{\partial \tilde{w}}{\partial x} - \frac{\partial \tilde{u}}{\partial z} = \frac{Ra}{|Pe|^{n-1}}\frac{\partial \tilde{T}}{\partial x}, \tag{5.16c}$$

$$\frac{\partial \tilde{u}}{\partial y} - \frac{\partial \tilde{v}}{\partial x} = 0, \tag{5.16d}$$

$$\frac{\partial \tilde{T}}{\partial t} + \tilde{w}\frac{\mathrm{d}T_b}{\mathrm{d}z} + Pe\frac{\partial \tilde{T}}{\partial z} = \frac{\partial^2 \tilde{T}}{\partial x^2} + \frac{\partial^2 \tilde{T}}{\partial y^2} + \frac{\partial^2 \tilde{T}}{\partial z^2}, \tag{5.16e}$$

$$z = 0, 1: \quad \frac{\partial \tilde{w}}{\partial z} = 0, \quad \tilde{T} = 0. \tag{5.16f}$$

After some algebraic manipulations, it is possible to reduce Equations (5.16) to a formulation involving only the temperature and the vertical component of the velocity, for the disturbances

$$n\left(\frac{\partial^2 \tilde{w}}{\partial x^2} + \frac{\partial^2 \tilde{w}}{\partial y^2}\right) + \frac{\partial^2 \tilde{w}}{\partial z^2} = \frac{Ra}{|Pe|^{n-1}}\left(\frac{\partial^2 \tilde{T}}{\partial x^2} + \frac{\partial^2 \tilde{T}}{\partial y^2}\right), \tag{5.17a}$$

$$\frac{\partial \tilde{T}}{\partial t} + \tilde{w}\frac{\mathrm{d}T_b}{\mathrm{d}z} + Pe\frac{\partial \tilde{T}}{\partial z} = \frac{\partial^2 \tilde{T}}{\partial x^2} + \frac{\partial^2 \tilde{T}}{\partial y^2} + \frac{\partial^2 \tilde{T}}{\partial z^2}, \tag{5.17b}$$

$$z = 0, 1: \quad \frac{\partial \tilde{w}}{\partial z} = 0, \quad \tilde{T} = 0. \tag{5.17c}$$

It is assumed that the disturbances can be represented as a superposition of normal modes as already discussed in Section 3.2. Such modes are given by

$$\tilde{w}(x, y, z, t) = \hat{w}(z)\, \mathrm{e}^{i(k_x x + k_y y - \omega t)}, \tag{5.18a}$$

$$\tilde{T}(x, y, z, t) = \hat{T}(z)\, \mathrm{e}^{i(k_x x + k_y y - \omega t)}, \tag{5.18b}$$

where k_x and k_y are the complex wave numbers in the x and y directions, respectively, and ω is the complex frequency. By substituting Equations (5.18) into Equations (5.17), one obtains the differential eigenvalue problem,

$$\hat{w}'' - (k_x^2 + k_y^2)(n\,\hat{w} - \frac{Ra}{|Pe|^{n-1}}\hat{T}) = 0, \tag{5.19a}$$

$$\hat{T}'' - Pe\,\hat{T}' - (k_x^2 + k_y^2 - i\omega)\hat{T} + \frac{\mathrm{e}^{Pe z}}{\mathrm{e}^{Pe} - 1}Pe\,\hat{w} = 0, \tag{5.19b}$$

$$z = 0, 1: \quad \hat{w}' = 0, \quad \hat{T} = 0, \tag{5.19c}$$

where the primes denote derivatives with respect to z. Here, in Equations (5.19a) and (5.19b) the Squire transformation $k^2 = k_x^2 + k_y^2$ is applied. This yields a two–dimensional modal stability analysis.

The differential eigenvalue problem represented by Equations (5.19) is solved numerically by means of the shooting–method as described in Section 4.1. Once the neutral stability conditions are established, one may identify the critical values, k_c, Ra_c, and ω_c by seeking for the absolute minimum of Ra on the neutral stability curve. A method to obtain directly these critical values is described in Section 4.1.1

5.4 Results and discussion

5.4.1 Validation

In order to verify the correctness of the present numerical calculations, the results for a Newtonian fluid are considered and they are compared with the results available in the literature. In particular, Jones and Persichetti [71] present the value of Ra_c as a function of Pe for different types of boundary conditions, including the ones used in the present study. In Figure 5.1, a good agreement between the data evaluated by Jones and Persichetti [71] and those obtained here is displayed. The vertical dashed line represents the value of Pe beyond which the critical wave number shifts from zero to a positive value. This situation will be discussed better later on. It is important to remark that small deviations that can be observed in Figure 5.1 are attributed to the process of reading the data from the plot.

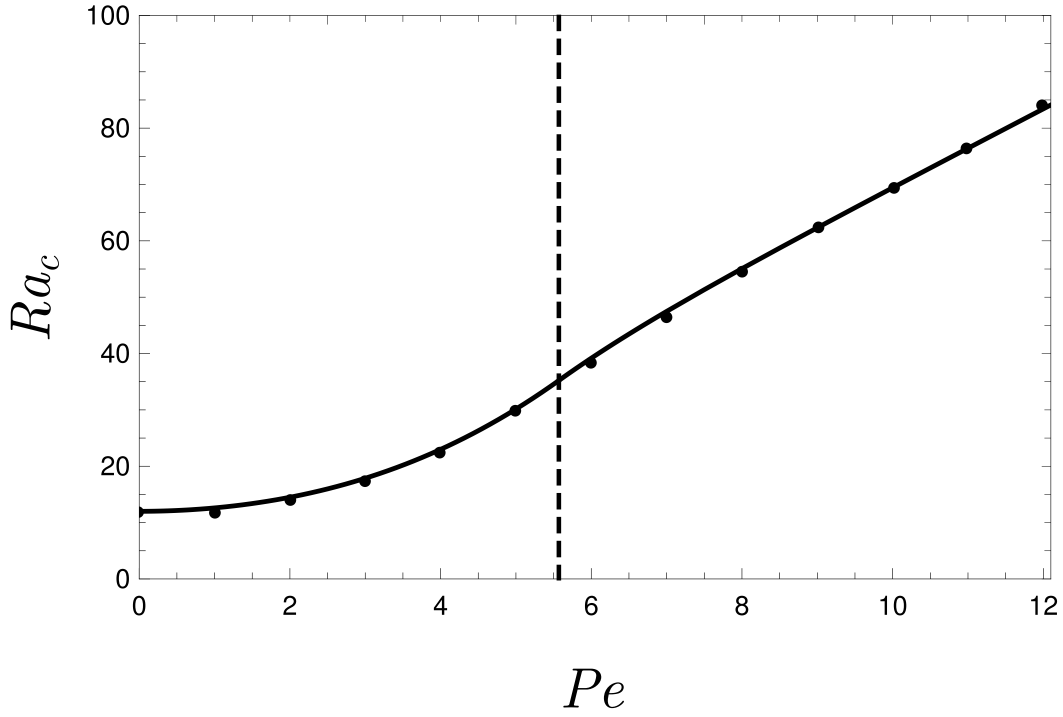

Figure 5.1: Critical Rayleigh number as a function of Pe for $n = 1$: comparison between present results (continuous line) and those obtained by Jones and Persichetti [71] (dots)

5.4.2 Neutral stability condition

In the present section, the neutral stability condition is presented in the form of neutral stability curves in the parametric plane (k, Ra). For a given value of the power–law index n and of the Péclet number Pe, a single neutral stability curve is shown. Figure 5.2 shows the instability threshold for different values of the power–law index. Different frames are considered with $Pe = 0.1, 1, 2, 5$.

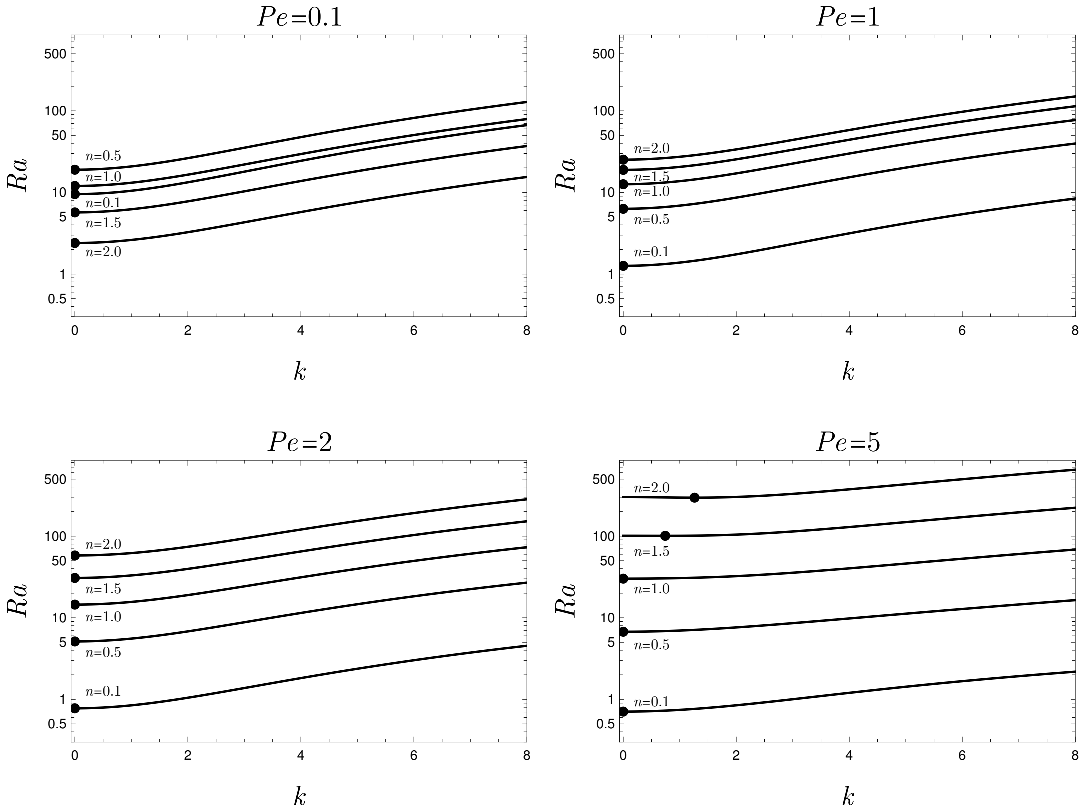

Figure 5.2: Neutral stability curves for $Pe = 0.1$, $Pe = 1$, $Pe = 2$ and $Pe = 5$ in a semi-logarithmic scale; dots identify the critical conditions for the onset of convection.

These figures reveal that, for $k \to 0$, the Rayleigh number approaches a finite limit, Ra_0, under all the parametric conditions examined. Moreover, for small Pe, the minimum value of Ra along these curves, *i.e.*, the critical Rayleigh number, Ra_c, is located at $k = 0$ in such a way that $Ra_c = Ra_0$. However, this condition is not true for all cases. For instance, one may note that, for $Pe = 5$, the neutral stability curves relative to $n = 1.5$ and $n = 2$ display the critical condition with $k_c > 0$. Furthermore, it is worth to mention that all the modes pertinent to neutral stability are stationary, *i.e.*, the real part of the frequency is zero, $\omega_r = 0$. Such a result is expected since the throughflow along the vertical direction implies an invariance by rotations around the z axis. This symmetry holds also in the classical Darcy–Bénard problem.

5.4.3 Asymptotic analysis for small values of k

The numerical results suggests that an asymptotic analysis can be developed in order to obtain analytically the neutral stability condition in the limiting case $k \to 0$. The power series expansions with respect to k are given by

$$\hat{w} = \hat{w}_0 + k\hat{w}_1 + k^2\hat{w}_2 + \ldots + k^n\hat{w}_n + \ldots \ , \tag{5.20a}$$

$$\hat{T} = \hat{T}_0 + k\hat{T}_1 + k^2\hat{T}_2 + \ldots + k^n\hat{T}_n + \ldots \ , \tag{5.20b}$$

$$Ra = Ra_0 + kRa_1 + k^2 Ra_2 + \ldots + k^n Ra_n + \ldots \ . \tag{5.20c}$$

By substituting Equation (5.20) into Equations (5.19), one obtains a sequence of boundary value problems to be solved iteratively. Again, the the scale fixing condition $\hat{w}(0) = 1$ is used, meaning $\hat{w}_0(0) = 1$ and $\hat{w}_n(0) = 0$ for every $n > 0$. To zero order in k we have

$$\hat{w}_0'' = 0, \tag{5.21a}$$

$$\hat{T}_0'' - Pe\,\hat{T}_0' + \frac{e^{Pe z}}{e^{Pe} - 1} Pe\,\hat{w}_0 = 0, \tag{5.21b}$$

$$\begin{aligned} z = 0: \quad & \hat{w}_0 = 1, \quad \hat{w}_0' = 0, \quad \hat{T}_0 = 0, \\ z = 1: \quad & \hat{w}_0' = 0, \quad \hat{T}_0 = 0, \end{aligned} \tag{5.21c}$$

which yields

$$\hat{w}_0(z) = 1, \tag{5.22a}$$

$$\hat{T}_0(z) = -\frac{e^{Pe} + e^{Pe + Pe z}(z-1) - e^{Pe z} z}{(e^{Pe} - 1)^2}. \tag{5.22b}$$

At first order in k, the resulting equations are given by

$$\hat{w}_1'' = 0, \tag{5.23a}$$

$$\hat{T}_1'' - Pe\,\hat{T}_1' + \frac{e^{Pe z}}{e^{Pe} - 1} Pe\,\hat{w}_1 = 0, \tag{5.23b}$$

$$\begin{aligned} z = 0: \quad & \hat{w}_1 = 0, \quad \hat{w}_1' = 0, \quad \hat{T}_1 = 0, \\ z = 1: \quad & \hat{w}_1' = 0, \quad \hat{T}_1 = 0, \end{aligned} \tag{5.23c}$$

whose solution is $\hat{w}_1 = \hat{T}_1 = 0$. At the second order in k, one has

$$\hat{w}_2'' - n\,\hat{w}_0 + \frac{Ra_0}{|Pe|^{n-1}} \hat{T}_0 = 0, \tag{5.24a}$$

$$\hat{T}_2'' - Pe\,\hat{T}_2' - \hat{T}_0 + \frac{e^{Pe z}}{e^{Pe} - 1} Pe\,\hat{w}_2 = 0, \tag{5.24b}$$

$$
\begin{aligned}
z = 0: \quad & \hat{w}_2 = 0, \quad \hat{w}_2' = 0, \quad \hat{T}_2 = 0, \\
z = 1: \quad & \hat{w}_2' = 0, \quad \hat{T}_2 = 0.
\end{aligned}
\tag{5.24c}
$$

The expressions for $\hat{w}_2$ and $\hat{T}_2$ are omitted in the interest of brevity. Moreover, the boundary conditions (5.24) allow one to obtain Ra_0 analytically as a function of Pe and n, namely

$$
Ra_0 = \frac{4n\, Pe^{n+1}}{4 - Pe^2 \cosh{(Pe/2)}^2}. \tag{5.25}
$$

Higher order solutions allow one to determine analytical expressions for Ra_1 and Ra_2. One finds that $Ra_1 = 0$ while Ra_2 is a function of Pe and n whose signal changes from positive to negative as Pe increases. Table 5.1 compares the values of Ra_0 obtained numerically and those obtained analytically. Numerical data are provided for $k = 10^{-2}, 10^{-4}, 10^{-6}, 10^{-8}$ as an approximation of the limiting case $k \to 0$. It is worth noting that, for $k = 10^{-4}$, the numerical and the analytical results in the limit $k \to 0$ are in agreement within eight significant.

Table 5.1: Comparison between numerical and analytical results for Ra considering the case of vanishing wave number for $Pe = 0.1$. Subscripts N and A stand for numerical and analytical, respectively.

n	$Ra_{0,N}$				$Ra_{0,A}$
	$k = 10^{-2}$	$k = 10^{-4}$	$k = 10^{-6}$	$k = 10^{-8}$	$k \to 0$
0.1	9.5368002	9.5367053	9.5367053	9.5367053	9.5367053
0.2	15.150699	15.150549	15.150549	15.150549	15.150549
0.3	18.051941	18.051763	18.051763	18.051763	18.051763
0.4	19.118887	19.118700	19.118700	19.118700	19.118700
0.5	18.983339	18.983154	18.983154	18.983154	18.983154
0.6	18.094802	18.094626	18.094626	18.094626	18.094626
0.7	16.768746	16.768584	16.768584	16.768584	16.768584
0.8	15.222729	15.222583	15.222583	15.222583	15.222583
0.9	13.603322	13.603193	13.603193	13.603193	13.603193
1.0	12.006115	12.006001	12.006001	12.006001	12.006001
1.1	10.490475	10.490376	10.490376	10.490376	10.490376
1.2	9.0904148	9.0903291	9.0903291	9.0903291	9.0903291
1.3	7.8225039	7.8224305	7.8224305	7.8224305	7.8224305
1.4	6.6916073	6.6915449	6.6915449	6.6915449	6.6915449
1.5	5.6949990	5.6949461	5.6949461	5.6949461	5.6949461
1.6	4.8252782	4.8252336	4.8252336	4.8252336	4.8252336
1.7	4.0724079	4.0723705	4.0723705	4.0723705	4.0723705
1.8	3.4251125	3.4250812	3.4250812	3.4250812	3.4250812
1.9	2.8718114	2.8717853	2.8717853	2.8717853	2.8717853
2.0	2.4012218	2.4012001	2.4012001	2.4012001	2.4012001

For a given value of n, it is important to evaluate the threshold value, Pe_{th}, of the Péclet number such that $Ra_c = Ra_0$ for $Pe \leqslant Pe_{th}$. These values can be determined by imposing $Ra_2 = 0$. Indeed, this condition remarks a change in the concavity of the function $Ra(k)$ in the vicinity of $k = 0$. The values of Pe_{th} are reported in Table 5.2.

Table 5.2: Threshold values of Pe, for different values of n, where the critical value of Ra switches from a vanishing to a finite wave number.

n	Pe_{th}
0.1	11.776849
0.2	9.3823306
0.3	8.2475072
0.4	7.5280494
0.5	7.0096499
0.6	6.6081057
0.7	6.2822806
0.8	6.0092045
0.9	5.7748272
1.0	5.5699654
1.1	5.3883060
1.2	5.2253331
1.3	5.0777104
1.4	4.9429072
1.5	4.8189603
1.6	4.7043179
1.7	4.5977330
1.8	4.4981891
1.9	4.4048472
2.0	4.3170075

A wider range of values of n, is considered in Figure 5.3 where a plot of Pe_{th} versus n is reported. The results reported in this figure suggest that for $n \to 0$ the threshold value of Pe tends to infinity, while for $n \to \infty$ the threshold value of Pe tends to zero.

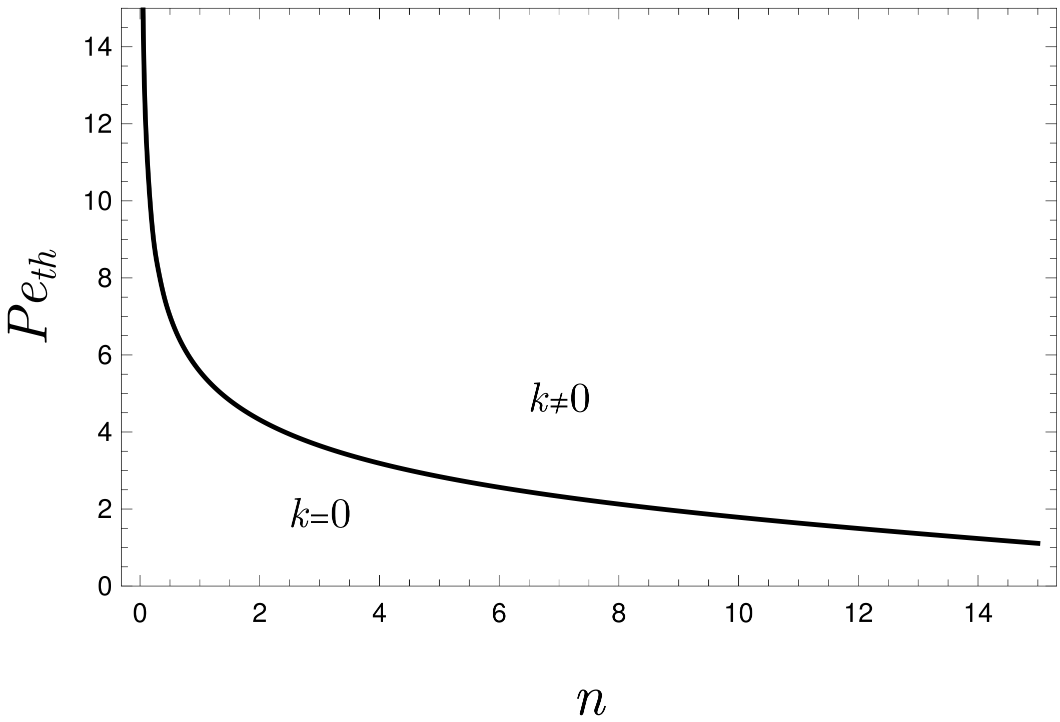

Figure 5.3: Critical Pe as a function of n separating the parametric region where the onset of instability occurs due to uniform disturbances or not

Figure 5.4 shows Ra_c as a function of Pe for different values of n. These results show that the relaxation of the constraint of Newtonian behaviour has either a stabilising or a destabilising effect depending on the value of the Péclet number. For a given $n \neq 1$, there exists a Péclet number such that Ra_c coincides with the critical Rayleigh number of a Newtonian fluid ($n = 1$). This behaviour is illustrated in Figure 5.5, where the vertical dashed line marks the transition from pseudoplastic to dilatant rheology. The right–hand frame of Figure 5.4 shows that Ra_c for the Newtonian case with $Pe > 0$ is always larger than its limit for vanishing Pe, *i.e.* $Ra_c = 12$. It is worth to mention that the range explored in Figure 5.4 is one where $k_c = 0$, so that $Ra_c = Ra_0$.

A general overview of the critical values of Ra and k is presented in Figure 5.6. The dotted line in the left–hand frame marks the transition from a low–Pe regime where $k_c = 0$ to a high–Pe regime where $k_c > 0$. The dashed lines are relative to the values of Ra_0. This transition is highlighted also in the right–hand frame where the plots of k_c versus Pe are shown.

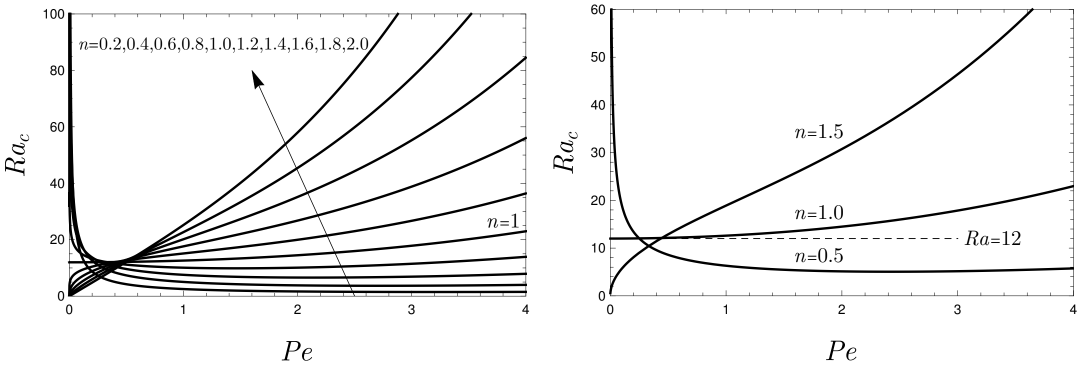

Figure 5.4: Plots of Ra_c versus Pe for different values of n.

On account of Eq (5.25), when $Pe \to 0$, three cases can be considered depending on the pseudoplastic, Newtonian, or dilatant behaviour of the fluid, namely

$$\lim_{Pe \to 0} Ra_c = \lim_{Pe \to 0} Ra_0 = \begin{cases} \infty & \text{if } n < 1 \\ 12 & \text{if } n = 1 \\ 0 & \text{if } n > 1 \end{cases} . \tag{5.26}$$

The result agrees with the behaviour displayed in Figure 5.4 and Figure 5.6. In the absence of vertical throughflow, $Pe = 0$, the base flow is unstable for dilatant fluids and stable for pseudoplastic fluids. While for Newtonian fluids the onset of instability occurs for $Ra_c = 12$, which coincides with the result reported by Nield [97] and Jones and Persichetti [71].

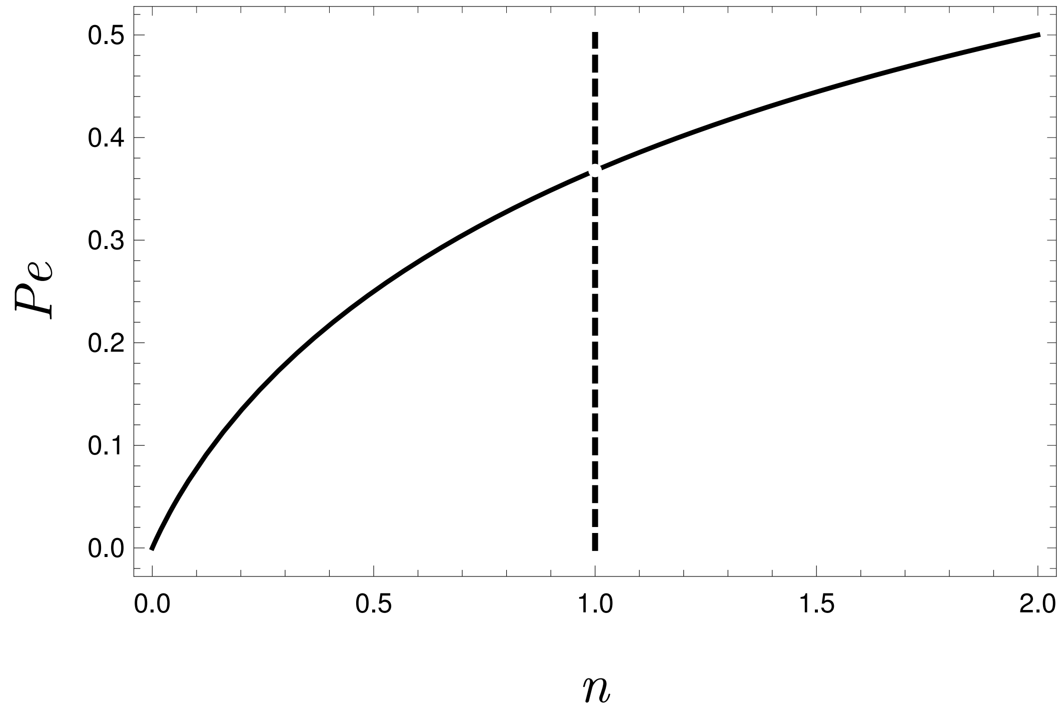

Figure 5.5: Value of Pe versus n where the non–Newtonian and the Newtonian values of Ra_c coincide.

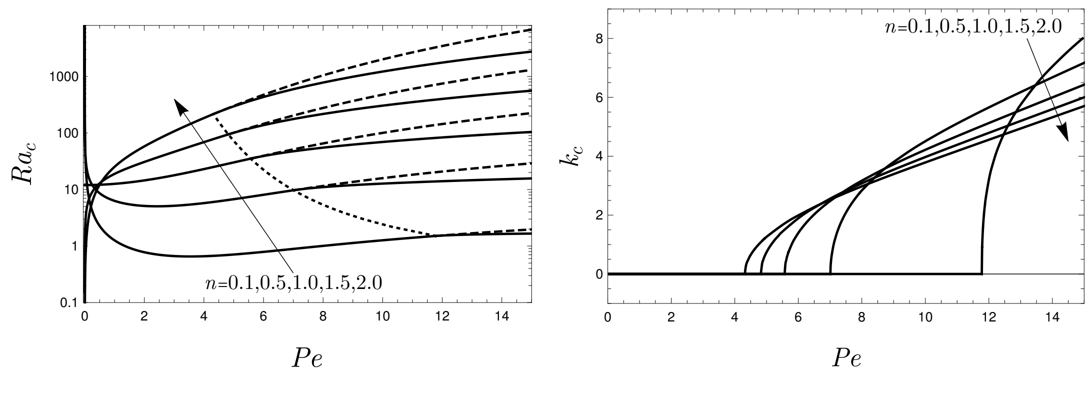

Figure 5.6: Ra_c (solid) and Ra_0 (dashed) versus Pe for different values of n (left–hand frame); k_c versus Pe for different values of n (right–hand frame).

5.5 Conclusions

The vertical throughflow in a horizontal porous layer with permeable boundaries saturated by a power–law fluid has been investigated in this chapter. The onset of the buoyancy–driven instability has been studied by means of a linear analysis and the results have been reported through the neutral stability curves and the critical values of the Rayleigh number, Ra, and of the perturbation wave number, k. Governing parameters influencing the onset conditions are the power–law index, n, and the dimensionless flow rate, represented by the Péclet number, Pe. It has been shown that the neutral stability condition for a vanishing wave number always corresponds to a finite value of Ra, denoted as Ra_0. This regime of infinite wavelength perturbations has been investigated by employing an asymptotic analysis. A good agreement between the asymptotic solutions and the numerical solution for $k \to 0$ has been found. Furthermore, for small values of Pe the neutral stability condition for $k \to 0$ yields the critical Darcy–Rayleigh number, *i.e.* $Ra_c = Ra_0$.

The linear stability analysis evidenced that, for sufficiently small values of Pe, the pseudoplastic fluids turn out to be more stable than the Newtonian fluids, while the dilatant fluids are less stable. An opposite conclusion can be made for larger values of Péclet, where the most stable behaviour is observed for dilatant fluids. Moreover, the linear instability arises with infinite wavelength perturbations once that Pe is below a threshold which depends on the power–law index, n. In particular, the threshold value of Pe is a monotonic decreasing function of n.

Chapter 6

A vertical throughflow of a power–law fluid saturating a porous cylinder with arbitrary cross–section

6.1 Introduction

As commented by Shenoy [120] in his book and pointed out in Chapter 5, convection heat transfer may be of interest also when non–Newtonian fluids saturate porous media. Processes involving oil recovery and its enhancement, ceramic processing and filtration are some examples of non–Newtonian fluid flows in porous media. For these processes, it can be interesting to deal with vertical throughflows in confined spaces.

As mentioned in the previous chapter, Sutton [126] and Homsy and Sherwood [66] were two of the pioneers in extending the classical HRL problem by considering the horizontal walls as permeable and consequently allowing the presence of a vertical throughflow.

More recently, different studies have been done in this direction including more complex effects. Barletta et al. [16] studied the effect of a vertical throughflow on the onset of convection in a horizontal porous channel, by taking into consideration the effect of heat generated by viscous dissipation inside the channel. Alves and Barletta [3] investigated the role of a non–Newtonian behaviour on the transition to instability, but yet considering horizontal throughflow. Barletta and Storesletten [15] investigated the effect of vertical throughflow on the onset of instability for power–law fluids.

The present chapter presents a study of the effect of the lateral confinement on the transition to instability for vertical throughflow in a horizontal porous channel saturated by a non–Newtonian fluid of power–law type. In their paper, Barletta and Storesletten [14] have already concluded, for the special case of a Newtonian fluid, that the geometry of a vertical permeable and conducting cylinder does not affect the eigenvalue problem solution and, consequently, the onset of instability. Although this conclusion can be expected to hold also for a more complex fluid rheology, this topic is worth to be investigated. In order to carry out such an investigation, a linear stability analysis is employed.

The contents of this chapter are based on the paper by Brandão, P. V., Celli, M., Barletta, A. and Storesletten, L., Thermally unstable throughflow of a power–law fluid in a vertical porous cylinder with arbitrary cross–section, International Journal of Thermal Sciences, doi:10.1016/j.ijthermalsci.2020.106616, [25].

6.2 Mathematical model

A vertical porous cylinder saturated by an Ostwald–de Waele (power–law) fluid is considered. The cylinder with arbitrary cross–section is bounded by two horizontal permeable planes, which allow the presence of a vertical troughflow. Let the vertical z axis be parallel to the gravitational acceleration $\mathbf{g}$, but with opposite direction (see Figure 6.1). The sidewall boundary is impermeable and adiabatic, while the horizontal boundary planes, at $z = 0$ and $z = H$, are permeable and isothermal with temperatures $T = T_0 + \Delta T$ and $T = T_0$, respectively. Here, T is the temperature field, T_0 is a reference temperature and ΔT is a positive temperature difference.

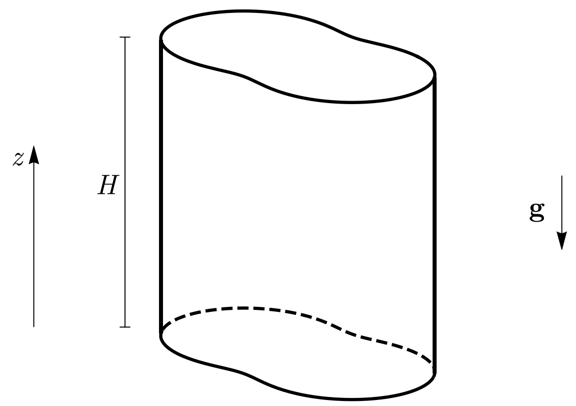

Figure 6.1: Sketch of the porous cylinder laterally confined by an arbitrarily shaped sidewall

6.2.1 Governing equations

When a power–law fluid saturates a porous medium and the flow is driven by the thermal buoyancy force, the appropriate model can be based on the Oberbeck–Boussinesq approximation and on the generalized Darcy's law showed in Equation (2.46). The generalised Darcy's law, together with the equations for local mass balance and energy balance, yield

$$\boldsymbol{\nabla} \cdot \mathbf{u} = 0, \tag{6.1a}$$

$$\frac{\eta_{ef}}{K} |\mathbf{u}|^{n-1} \mathbf{u} = -\boldsymbol{\nabla} p - \rho_0 \mathbf{g} \beta (T - T_0), \tag{6.1b}$$

$$\sigma \frac{\partial T}{\partial t} + \mathbf{u} \cdot \boldsymbol{\nabla} T = \chi \nabla^2 T, \tag{6.1c}$$

where $\mathbf{u}$ is the velocity with Cartesian components (u, v, w), η_{ef} is the effective consistency factor, K is the permeability and p is the local difference between the pressure and the hydrostatic pressure, ρ_0 is the density of the fluid at temperature T_0, while β is the thermal expansion coefficient of the fluid. Time is denoted by t, σ is the ratio between the average volumetric heat capacity of the saturated porous medium and the volumetric heat capacity of the fluid and χ is the effective thermal diffusivity of the porous medium. The effective consistency factor η_{ef} depends on the power–law index n, on the consistency factor of the power–law fluid, on the permeability K, as well as on the porosity and on the tortuosity as it can be seen in the Section 2.4.2.

The lateral sidewall of the vertical cylinder, with cross–section A, is bounded by a closed, piecewise differentiable curve ∂A in the (x, y) plane. The curve ∂A is defined by the equation

$$F(x, y) = 0. \tag{6.2}$$

A vertical throughflow in the porous cylinder is induced by the following boundary conditions:

$$z = 0, \quad x, y \in A : \quad w = w_0, \quad T = T_0 + \Delta T, \tag{6.3a}$$

$$z = H, \quad x, y \in A : \quad w = w_0, \quad T = T_0, \tag{6.3b}$$

$$F(x, y) = 0, \quad 0 < z < H : \quad \mathbf{n} \cdot \mathbf{u} = \mathbf{n} \cdot \boldsymbol{\nabla} T = 0, \tag{6.3c}$$

where w_0 is the prescribed vertical fluid velocity and $\mathbf{n}$ is the unit outward normal to the cylinder sidewall. Thus, $\mathbf{n}$ lies on the (x, y) plane.

6.2.2 Dimensionless quantities

Now, the dimensional quantities and operators are scaled in order to define a dimensionless formulation

$$\begin{aligned} &\frac{1}{H}\mathbf{x} \to \mathbf{x}, \quad \frac{H}{\chi}\mathbf{u} \to \mathbf{u}, \quad \frac{\chi}{\sigma H^2} t \to t, \\ &\frac{T - T_0}{\Delta T} \to T, \quad H\boldsymbol{\nabla} \to \boldsymbol{\nabla}, \quad H^2 \nabla^2 \to \nabla^2. \end{aligned} \tag{6.4}$$

The dimensionless parameters Ra and Pe are defined as

$$Ra = \frac{\rho_0 g \beta \Delta T K H^n}{\eta_{ef} \chi^n}, \quad Pe = \frac{w_0 H}{\chi}, \tag{6.5}$$

where g is the modulus of $\mathbf{g}$. The dimensionless parameter Ra is the non–Newtonian Darcy–Rayleigh number, while Pe is the Péclet number. The instability is possible only if Ra is positive. On the other hand, Pe may assume both positive and negative values. A positive Pe means an upward throughflow and a negative Pe means a downward throughflow.

By employing the dimensionless quantities defined by Equations (6.4) and (6.5), Equations (6.1) can be written as

$$\boldsymbol{\nabla} \cdot \mathbf{u} = 0, \tag{6.6a}$$

$$\boldsymbol{\nabla} \times (|\mathbf{u}|^{n-1}\mathbf{u}) = Ra \boldsymbol{\nabla} \times (T\mathbf{e}_z), \tag{6.6b}$$

$$\frac{\partial T}{\partial t} + \mathbf{u} \cdot \boldsymbol{\nabla} T = \nabla^2 T, \tag{6.6c}$$

where $\mathbf{e}_z$ is the unit vector in the z direction. Equation (6.6b) is obtained by applying the curl operator to both sides of Equation (6.1b), so that the dynamic pressure field is eliminated from the original governing equations.

The dimensionless boundary conditions (6.3) can be rewritten in a dimensionless form as

$$z = 0, \quad x, y \in A: \quad w = Pe, \quad T = 1, \tag{6.7a}$$

$$z = 1, \quad x, y \in A: \quad w = Pe, \quad T = 0, \tag{6.7b}$$

$$F(x, y) = 0, \quad 0 < z < 1: \quad \mathbf{n} \cdot \mathbf{u} = \mathbf{n} \cdot \boldsymbol{\nabla} T = 0. \tag{6.7c}$$

It is interesting to note that, in the interest of simplicity, the same notation for the dimensionless equation, $F(x, y) = 0$, is adopted to characterise the dimensional boundary in the (x, y) plane. In the former case we deal with dimensionless coordinates. Moreover, the function F itself is different from that employed with dimensional coordinates, unless F is homogeneous, which is a special case. In the following, A and ∂A are considered as the dimensionless cross–section of the cylinder and its boundary, respectively.

6.2.3 Base flow state

A stationary solution of Equations (6.6) and (6.7) is given by a uniform vertical throughflow with a purely vertical temperature gradient $\mathrm{d}T_b/\mathrm{d}z$, namely

$$u_b = 0, \quad v_b = 0, \quad w_b = Pe, \quad T_b(z) = \frac{e^{Pe} - e^{Pe z}}{e^{Pe} - 1}. \tag{6.8}$$

where the subscript “b” stands for basic state.

6.3 Small–amplitude perturbations

A stability analysis of the vertical base flow is now carried out under the assumption of small–amplitude perturbations, as presented in the Section 3.2.

6.3.1 Disturbance equations

The stability of the system is studied by decomposing the flow quantities into a basic part (6.8) and another one relative to the disturbances. The velocity and temperature fields are then expressed as

$$\mathbf{u} = Pe\,\mathbf{e}_z + \epsilon\tilde{\mathbf{u}}, \quad T = T_b(z) + \epsilon\tilde{T}, \tag{6.9}$$

where $\tilde{\mathbf{u}} = (\tilde{u}, \tilde{v}, \tilde{w})$ and $\tilde{T}$ are the perturbation fields and $\epsilon \ll 1$ is an infinitesimal perturbation parameter such that, hereafter, terms $O(\epsilon^2)$ are considered as negligible.

Thus, substituting Equation (6.9) into Equations (6.6) yields a linearised system of governing equations for the disturbances given by

$$\frac{\partial \tilde{u}}{\partial x} + \frac{\partial \tilde{v}}{\partial y} + \frac{\partial \tilde{w}}{\partial z} = 0, \tag{6.10a}$$

$$n\frac{\partial \tilde{w}}{\partial y} - \frac{\partial \tilde{v}}{\partial z} = \frac{Ra}{|Pe|^{n-1}}\frac{\partial \tilde{T}}{\partial y}, \tag{6.10b}$$

$$n\frac{\partial \tilde{w}}{\partial x} - \frac{\partial \tilde{u}}{\partial z} = \frac{Ra}{|Pe|^{n-1}}\frac{\partial \tilde{T}}{\partial x}, \tag{6.10c}$$

$$\frac{\partial \tilde{v}}{\partial x} - \frac{\partial \tilde{u}}{\partial y} = 0, \tag{6.10d}$$

$$\frac{\partial \tilde{T}}{\partial t} + \tilde{w}\frac{\partial T_b}{\partial z} + Pe\frac{\partial \tilde{T}}{\partial z} = \nabla^2\tilde{T}, \tag{6.10e}$$

which are subject to the boundary conditions

$$z = 0, 1, \quad x, y \in A: \quad \tilde{w} = \tilde{T} = 0, \tag{6.11a}$$

$$F(x, y) = 0, \quad 0 < z < 1: \quad \mathbf{n}\cdot\tilde{\mathbf{u}} = \mathbf{n}\cdot\boldsymbol{\nabla}\tilde{T} = 0. \tag{6.11b}$$

For practical reasons, it can be convenient to rewrite the linearised equations according to a $\tilde{w}$–$\tilde{T}$ formulation. Thus, by rearranging Equations (6.10) and (6.11), one has

$$n\left(\frac{\partial^2 \tilde{w}}{\partial x^2} + \frac{\partial^2 \tilde{w}}{\partial y^2}\right) + \frac{\partial^2 \tilde{w}}{\partial z^2} = \frac{Ra}{|Pe|^{n-1}}\left(\frac{\partial^2 \tilde{T}}{\partial x^2} + \frac{\partial^2 \tilde{T}}{\partial y^2}\right), \tag{6.12a}$$

$$\frac{\partial \tilde{T}}{\partial t} + \tilde{w}\frac{\mathrm{d}T_b}{\mathrm{d}z} + Pe\frac{\partial \tilde{T}}{\partial z} = \frac{\partial^2 \tilde{T}}{\partial x^2} + \frac{\partial^2 \tilde{T}}{\partial y^2} + \frac{\partial^2 \tilde{T}}{\partial z^2}. \tag{6.12b}$$

$$z = 0, 1, \quad x, y \in A: \quad \tilde{w} = \tilde{T} = 0, \tag{6.12c}$$

$$F(x, y) = 0, \quad 0 < z < 1: \quad \mathbf{n} \cdot \boldsymbol{\nabla}\tilde{w} = \mathbf{n} \cdot \boldsymbol{\nabla}\tilde{T} = 0. \tag{6.12d}$$

With the new formulation, all the boundary conditions must be expressed in terms of $\tilde{w}$ and $\tilde{T}$, as in Equation (6.12d). In particular, the boundary conditions for $\tilde{w}$ in Equation (6.12d) can be derived by evaluating the scalar product of the momentum balance equation in the (x, y) plane, expressed by Equations (6.10b) and (6.10c), with the unit normal $\mathbf{n}$ to the curve ∂A, namely

$$n\, \mathbf{n} \cdot \boldsymbol{\nabla}\tilde{w} - \frac{\partial\,(\mathbf{n} \cdot \tilde{\mathbf{u}})}{\partial z} = \frac{Ra}{|Pe|^{n-1}}\, \mathbf{n} \cdot \boldsymbol{\nabla}\tilde{T}. \tag{6.13}$$

Then, by employing Equation (6.13) for $(x, y) \in \partial A$, and by taking into account Equation (6.11b), it is obtained

$$\mathbf{n} \cdot \boldsymbol{\nabla}\tilde{w} = 0, \tag{6.14}$$

which is the boundary condition for $\tilde{w}$ reported in Equation (6.12d).

6.3.2 Eigenvalue problem

In order to determine the instability threshold, *i.e.* the neutral stability condition, the disturbances are expressed as normal modes periodic in time,

$$\tilde{T} = \hat{T}(z)\, f(x, y)\, e^{i\,\omega\, t}, \tag{6.15a}$$

$$\tilde{w} = \hat{w}(z)\, f(x, y)\, e^{i\,\omega\, t}, \tag{6.15b}$$

where ω is the angular frequency and $f(x, y)$ is a solution of the two–dimensional Helmholtz equation with Neumann boundary conditions at $F(x, y) = 0$, namely

$$\nabla_2^2\, f(x, y) = -\alpha^2\, f(x, y), \tag{6.16a}$$

$$F(x, y) = 0: \quad \mathbf{n} \cdot \boldsymbol{\nabla} f(x, y) = 0, \tag{6.16b}$$

where α is the wavenumber.

Due to the symmetry under rotations around the z axis, observed both in the governing equations and in the basic flow state, the principle of exchange of stabilities is expected to hold (see, for instance, Alves and Barletta [3] and Barletta and Storesletten [15]). Thus, the condition $\omega = 0$ can be set. Although this result cannot be proved theoretically for the present problem, the validity of the principle is verified numerically for every case examined in the following. By employing Equations (6.15) and (6.16), Equations (6.12) yield

$$\hat{w}'' - n\,\alpha^2\,\hat{w} + \frac{Ra}{|Pe|^{n-1}}\,\alpha^2\,\hat{T} = 0, \tag{6.17a}$$

$$\hat{T}'' - Pe\,\hat{T}' - (\alpha^2 + i\omega)\,\hat{T} + Pe\,G(z)\,\hat{w} = 0, \tag{6.17b}$$

$$z = 0, 1: \quad \hat{w} = \hat{T} = 0, \tag{6.17c}$$

Here, the primes denote differentiation with respect to z and $G(z)$ is defined as

$$G(z) = -\frac{1}{Pe}\frac{\mathrm{d}T_b}{\mathrm{d}z} = \frac{e^{Pe\,z}}{e^{Pe} - 1}. \tag{6.18}$$

By looking at the eigenvalue problem defined by Equations (6.17), some conclusions can be made regarding the role played by the sign of Pe. In principle, Pe may assume either positive or negative values, which corresponds to upward or downward flow, respectively. From Equations (6.17) one may observe that just Equation (6.17b) is affected by a signal change of Pe, while in Equation (6.17a) Pe appears with its absolute value. For a downward flow, by applying a simple coordinate transformation, it can be seen that the eigenvalue problem is mapped onto one with a positive Pe. In fact, in view of Equation (6.18), the eigenvalue problem (6.17) remains invariant under the transformation

$$Pe \to -Pe, \qquad z \to 1 - z. \tag{6.19}$$

As already pointed out by Barletta and Storesletten [15], the practical effect of this symmetry is that the eigenvalues, in the present case the pair (ω, Ra), does not depend on the sign of Pe, while the eigenfunctions $(\hat{w}, \hat{T})$ experience a reflection with respect to the mid–plane $z = 1/2$. Thus, from now, only positive values of Pe will be considered without any loss of generality.

6.3.3 Three special cases

Three different cases for the lateral confinement are considered here, namely

1. A is a square, with dimensionless side length ℓ;
2. A is a circle with dimensionless radius s. In other terms, ∂A is defined by the equation $F(x, y) = x^2 + y^2 - s^2 = 0$;
3. A is an ellipse with dimensionless semiaxes b and d, with $b > d$. In this case, ∂A is given by $F(x, y) = x^2/b^2 + y^2/d^2 - 1 = 0$.

Case I: Square cross–section

If we consider the case of a square cross–section, the boundary conditions are

$$z = 0, 1;\ 0 < x < \ell;\ 0 < y < \ell : \quad \tilde{w} = \tilde{T} = 0, \tag{6.20a}$$

$$x = 0, \ell;\ 0 < y < \ell;\ 0 < z < 1 : \quad \frac{\partial \tilde{w}}{\partial x} = \frac{\partial \tilde{T}}{\partial x} = 0, \tag{6.20b}$$

$$y = 0, \ell;\ 0 < x < \ell;\ 0 < z < 1 : \quad \frac{\partial \tilde{w}}{\partial y} = \frac{\partial \tilde{T}}{\partial y} = 0. \tag{6.20c}$$

The general form of the function $f(x, y)$, after solving the Helmholtz eigenvalue problem (6.16), is expressed as

$$f(x, y) = \cos\left(\frac{m_1 \pi}{\ell} x\right) \cos\left(\frac{m_2 \pi}{\ell} y\right), \tag{6.21}$$

where m_1 and m_2 are non–negative integers, while the eigenvalues α are obtained analytically by

$$\alpha = \frac{\pi}{\ell} \sqrt{m_1^2 + m_2^2}. \tag{6.22}$$

Therefore, the normal modes are labelled through the pair of integers (m_1, m_2). The symmetry of the square cross–section implies that the modes can be commuted, namely (m_1, m_2) and (m_2, m_1) are equivalent, as it is mathematically evident from Equations (6.21) and (6.22). The ordering of such modes according to the increasing eigenvalues is reported in table 6.1 for the lowest 11 modes.

Table 6.1: Square cross–section: first 11 modes and the corresponding eigenvalues (6.22)

(m_1, m_2)	$\alpha\ell$
(0,0)	0
(1,0)	3.14159
(1,1)	4.44288
(2,0)	6.28319
(2,1)	7.02481
(2,2)	8.88577
(3,0)	9.42478
(3,1)	9.93459
(3,2)	11.3272
(4,0)	12.5664
(4,1)	12.9531

Case II: Circular cross–section

When the cross–section is a circular cylinder, the boundary conditions can be written in cylindrical coordinates in the form

$$z = 0, 1; \quad 0 < r < s : \quad \tilde{w} = \tilde{T} = 0, \tag{6.23a}$$

$$r = s; \quad 0 < z < 1 : \quad \frac{\partial \tilde{w}}{\partial r} = \frac{\partial \tilde{T}}{\partial r} = 0. \tag{6.23b}$$

Consequently, the general modes $f(r, \hat{T})$ obtained by solving the Helmholtz eigenvalue problem (6.16) are given by

$$f(r, \hat{T}) = J_m(\alpha r) \cos\left(m\hat{T}\right), \tag{6.24}$$

where $J_m(\alpha r)$ is the Bessel function of first kind and of order m. In this case, α can be determined by solving the equation

$$J_m'(\xi) = 0, \quad \xi = \alpha s. \tag{6.25}$$

The nonzero values of ξ that satisfy Equation (6.25) form a sequence $\{\xi_{m,k} \,|\, m = 0, 1, 2, 3...; k = 1, 2, 3...\}$ where m is the azimuthal mode number and k the radial mode number. Table 6.2 presents the first 11 roots of Equation (6.25) in increasing order.

Table 6.2: Circular cross–section: first 11 modes and the corresponding eigenvalues (6.25)

(m, k)	$\xi_{m,k} = \alpha s$
(1,1)	1.84118
(2,1)	3.05424
(0,1)	3.83171
(3,1)	4.20119
(4,1)	5.31755
(1,2)	5.33144
(5,1)	6.41562
(2,2)	6.70613
(0,2)	7.01559
(6,1)	7.50127
(3,2)	8.01524

Case III: Elliptical cross–section

Barletta [10] studied the effect of lateral confinement by a cylindrical wall with elliptical cross-section in the case of a Newtonian fluid saturating a porous cylinder. In that study, the authors assumed Dirichlet boundary conditions for the Helmholtz problem (6.16) instead of Neumann boundary conditions. Following the same procedure of Barletta [10], the elliptical coordinates (λ, η) are considered here and are given by

$$x = c \cosh\lambda \cos\eta, \qquad y = c \sinh\lambda \sin\eta, \tag{6.26}$$

where c is the semi–distance between the foci of the ellipse, $0 \leq \lambda < +\infty$ and $0 \leq \eta < 2\pi$. The elliptical boundary is given by $\lambda = \lambda_0$, the ratio between the semi–axes is given by $d/b = \chi = \tanh \lambda_0$ and $c = b/\cosh\lambda_0$. The limiting case of a circular contour is recovered when $\lambda_0 \to \infty$.

The Helmholtz Equation (6.16) can be solved by separation of variables, with f given by [1, 14]

$$f(\lambda, \eta) = \mathrm{ce}_m(i\lambda; C)\ \mathrm{ce}_m(\eta; C)\,, \tag{6.27}$$

or

$$f(\lambda, \eta) = i\,\mathrm{se}_m(i\lambda; C)\ \mathrm{se}_m(\eta; C)\,, \tag{6.28}$$

with $m = 0, 1, 2, \ldots$ and

$$C = \frac{\alpha^2 b^2}{4\ \cosh^2 \lambda_0}. \tag{6.29}$$

Functions ce_m and se_m are the elliptic versions of cosine and sine, respectively, also called even and odd Mathieu functions of order m.

The boundary condition (6.16b) is expressed in elliptical coordinates as

$$\frac{\partial f}{\partial \lambda} = 0, \quad \text{for } \lambda = \lambda_0. \tag{6.30}$$

Thus, Equations (6.28) and (6.30) imply that the eigenvalues αs can be calculated, for a given aspect ratio χ, as the positive roots of either,

$$\frac{\partial}{\partial \lambda}\, \mathrm{ce}_m\!\left(i\lambda; \frac{\alpha^2 b^2}{4\ \cosh^2 \lambda_0} \right)\bigg|_{\lambda=\lambda_0} = 0, \tag{6.31}$$

or

$$\frac{\partial}{\partial \lambda}\, \mathrm{se}_m\!\left(i\lambda; \frac{\alpha^2 b^2}{4\ \cosh^2 \lambda_0} \right)\bigg|_{\lambda=\lambda_0} = 0, \tag{6.32}$$

where $\lambda_0 = \mathrm{arctanh}\chi$ and $m = 0, 1, 2, \ldots$.
The software *Mathematica 12* [69] offers a suitable environment for carrying out this computation, by using the built–in functions `MathieuCPrime`, `MathieuSPrime`, as well as `Mathieu CharacteristicA` and `MathieuCharacteristicB`.

The roots of Equations (6.31) and (6.32) can be ordered so that the eigenvalues α form a monotonic increasing sequence. Analogously to Barletta [10], the modal notation is implemented here: $(\mathrm{e}; m, k)$ and $(\mathrm{o}; m, k)$. In fact, $(\mathrm{e}; m, k)$ denotes the mode associated with the kth root of Equation (6.31), for $m, k = 0, 1, 2, \ldots$. Similarly, $(\mathrm{o}; m, k)$ is for the kth root of Equation (6.32), with $m - 1, k = 0, 1, 2, \ldots$. This ordering of the normal modes, $(\mathrm{e}; m, k)$ and $(\mathrm{o}; m, k)$, and the associated eigenvalues $\alpha\, b$ are listed in table 6.3, for two values of aspect ratio, namely $\chi = 9/10$ and $\chi = 1/4$.

Table 6.3: Elliptical cross–section: first 11 eigenvalues αb in increasing order, with the corresponding even (e) or odd (o) normal modes: $(\mathrm{e}; m, k)$, $(\mathrm{o}; m, k)$

$\chi = 9/10$		$\chi = 1/4$	
modes	αb	modes	αb
$(\mathrm{e}; 0, 0)$	0	$(\mathrm{e}; 0, 0)$	0
$(\mathrm{e}; 1, 0)$	1.8485646	$(\mathrm{e}; 1, 0)$	1.8832257
$(\mathrm{o}; 1, 0)$	2.0363607	$(\mathrm{e}; 2, 0)$	3.4701287
$(\mathrm{e}; 2, 0)$	3.1870665	$(\mathrm{e}; 3, 0)$	5.0364174
$(\mathrm{o}; 2, 0)$	3.2253344	$(\mathrm{e}; 4, 0)$	6.5946258
$(\mathrm{e}; 0, 1)$	4.0785718	$(\mathrm{o}; 1, 0)$	6.7389286
$(\mathrm{e}; 3, 0)$	4.4108506	$(\mathrm{o}; 2, 0)$	7.8062030
$(\mathrm{o}; 3, 0)$	4.4170182	$(\mathrm{e}; 5, 0)$	8.1482947
$(\mathrm{e}; 1, 1)$	5.4919288	$(\mathrm{o}; 3, 0)$	8.9350656
$(\mathrm{e}; 4, 0)$	5.5884622	$(\mathrm{e}; 6, 0)$	9.6988909
$(\mathrm{o}; 4, 0)$	5.5893372	$(\mathrm{o}; 4, 0)$	10.116229

6.4 Critical conditions

By solving Equations (6.17), the instability threshold can be determined. That means that, for each pair (n, Pe), one is able to find the neutral stability condition in the form of a neutral stability curve in the plane (α, Ra) by using the shooting–method described in Section 4.1. The minimum value of Ra along the neutral stability curve is its critical value, Ra_c. A direct numerical evaluation of Ra_c is possible by deriving Equations (6.17) with respect to α. Thus, one obtains additional equations which lead to an extended eigenvalue problem that is solved in the same way as explained in the Section 4.1.1.

When one takes the limit $Pe \to 0$ in the Newtonian case ($n = 1$), the classical Horton–Rogers–Lapwood (HRL) problem is recovered [106]. This case can be thus employed as a benchmark to verify the numerical calculations. The analytical solution of the HRL problem yields $Ra_c = 4\pi^2$ and $\alpha_c = \pi$ [106]. A comparison between the numerical data obtained for extremely small Péclet numbers and $n = 1$ and the analytical solution of the HRL problem is reported in table 6.4. The numerical data are presented with 12 significant figures and a good agreement, with 9 coincident figures, can be observed already for $Pe = 10^{-4}$. Figure 6.2 shows the influence of the power–law index n on the critical values of α and Ra for fixed values of Pe.

Table 6.4: Verification of the numerical values of (Ra_c, α_c) when $Pe \to 0$

Pe	Ra_c	α_c
10^{-2}	39.4785571021	3.14159634429
10^{-3}	39.4784190030	3.14159269064
10^{-4}	39.4784176220	3.14159265411
10^{-5}	39.4784176082	3.14159265374
0	39.4784176044	3.14159265359

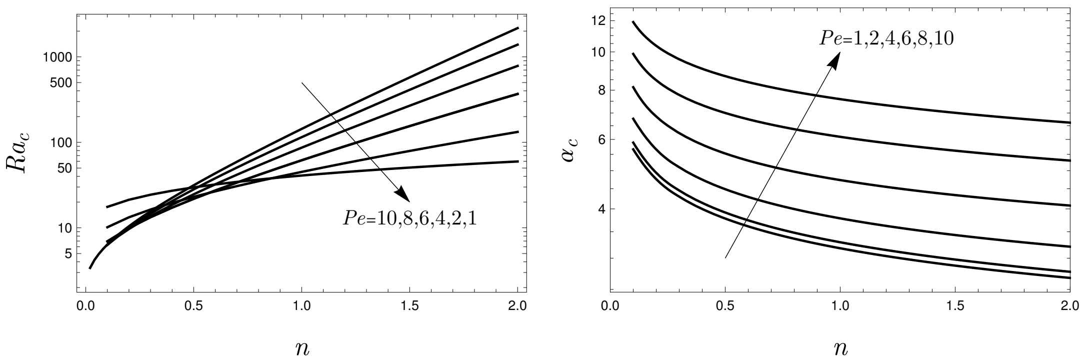

Figure 6.2: Values of α_c and Ra_c versus n for different Péclet numbers

All the numerical calculations are carried out by using the Software *Mathematica 12* [69]. By using the built-in function called `NDSolve` one can solve a wide class of differential equations. In order to ensure the accuracy of the computations, a convergence analysis is made by choosing decreasing step sizes inside `NDSolve`, as well as the adaptive step size method used as a default in `NDSolve`. Such a convergence analysis is presented in Table 6.5 through the values of critical wavenumber and critical Rayleigh number.

Table 6.5: Values of Ra_c and α_c obtained numerically by considering different step sizes for $Pe = 4$ and $n = 0.6$

Step size	$\hat{\alpha}_c$	$\hat{Ra}_c$
0.5	4.28837700268	27.3297991218
0.1	4.28837700268	27.3297991218
0.05	4.28884531862	27.3274560424
0.01	4.28892463671	27.3269209309
0.005	4.28892480058	27.3269197435
0.001	4.28892481182	27.3269196613
Adaptive	4.28892481183	27.3269196613

In order to illustrate the critical temperature difference leading to the instability for a specific fluid, the properties of the fluid and of the porous medium used in the Experiment 5 described in Petrolo et al. [110] is considered here. In particular, a porous medium with porosity 0.5 and $H = 0.5$ m is considered. In this case, a temperature difference of 5.60 K must be employed for the onset of the instability.

In Figure 6.3, the most unstable modes for the elliptic case with $\xi = 9/10$ are showed as well. This case presents a lower geometrical symmetry with respect to the circular case, while it allows an analytical expression of the eigenmodes in terms of nontrivial special functions.

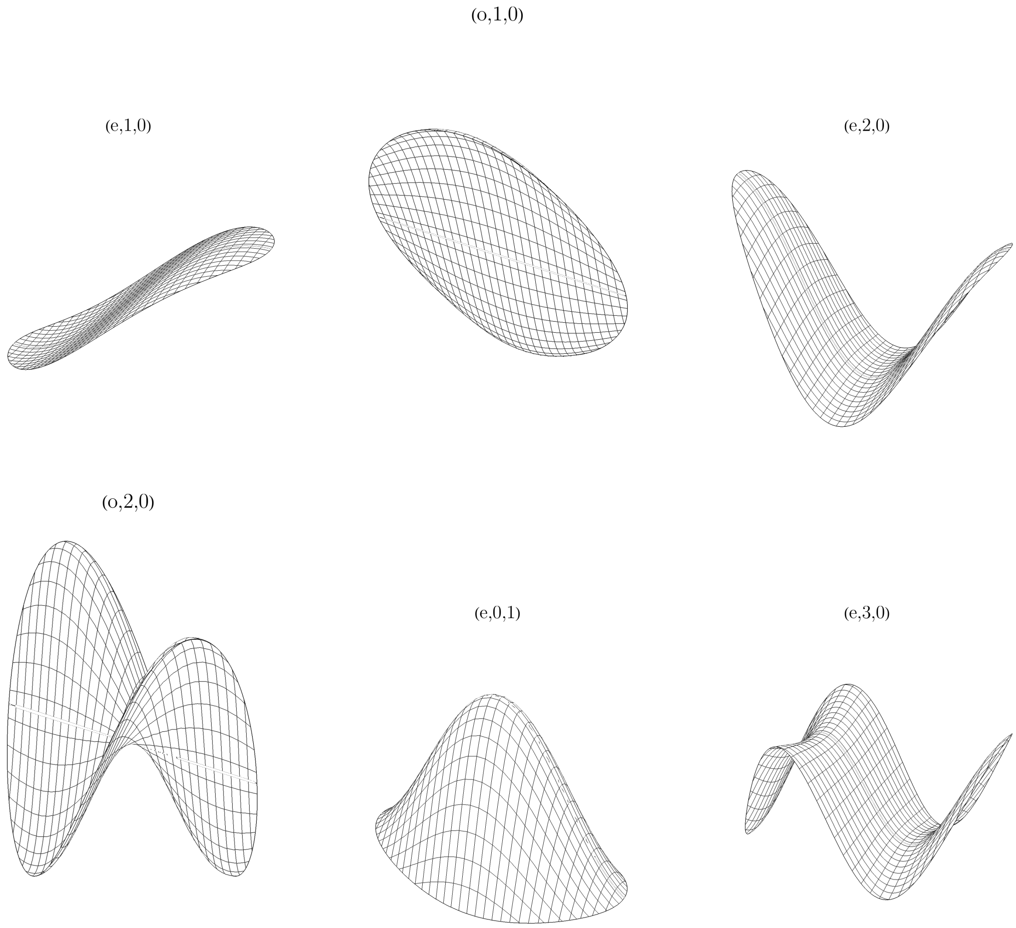

Figure 6.3: Plots of the eigenfunctions for an elliptic cylinder with $\xi = 9/10$ relative to the first 6 normal modes

6.5 Neutral stability condition

Figures 6.4 and 6.5 show the neutral stability curves for the Newtonian case ($n = 1$), with $Pe = 2$ and $Pe = 6$ respectively. The curves are presented for each one of the three cases defined in Section 6.3.3. For the case of elliptical cross–section, two different aspect ratios between the two semi–axis are considered. The numbers above the curves denote the modes corresponding to each branch. All these curves are generated considering the lower six modes of perturbation. The critical values of Ra shown in these plots coincide with those reported by Homsy and Sherwood [66] as well as by Barletta [9].

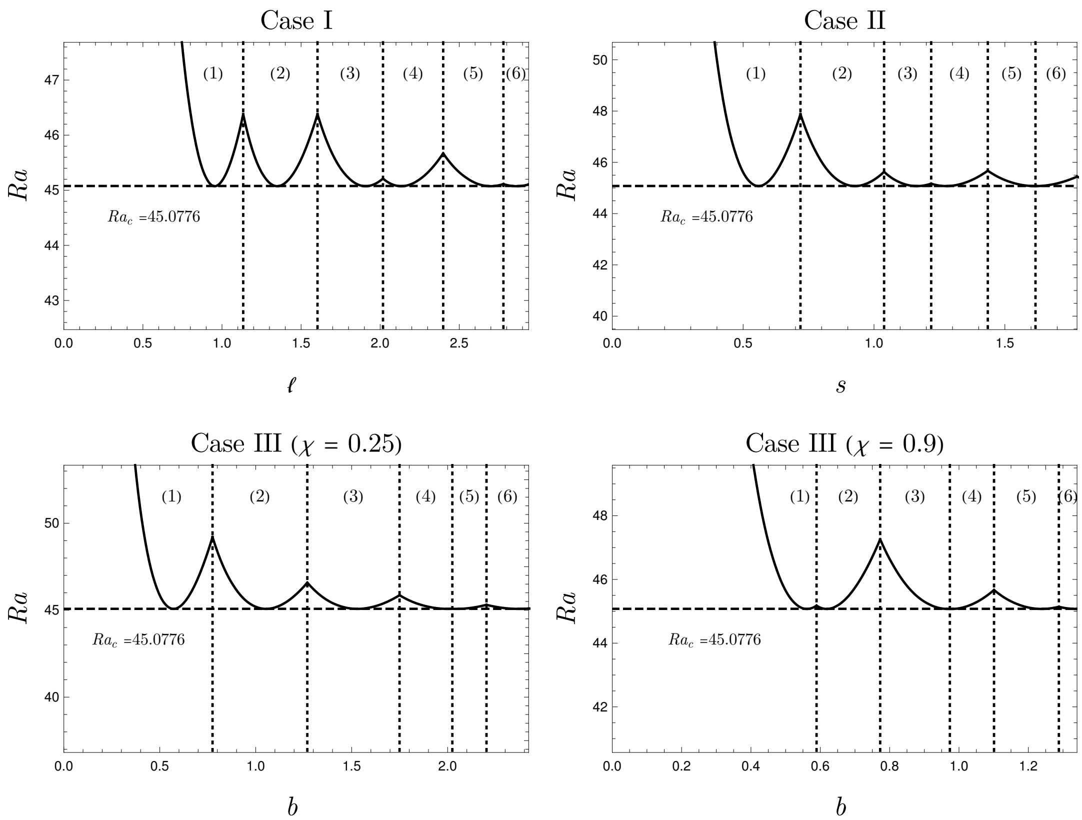

Figure 6.4: Marginal stability curves for $n = 1$ and $Pe = 2$; different modes $(1), (2), \ldots$ are labelled according to the ordering defined in tables 6.1–6.3

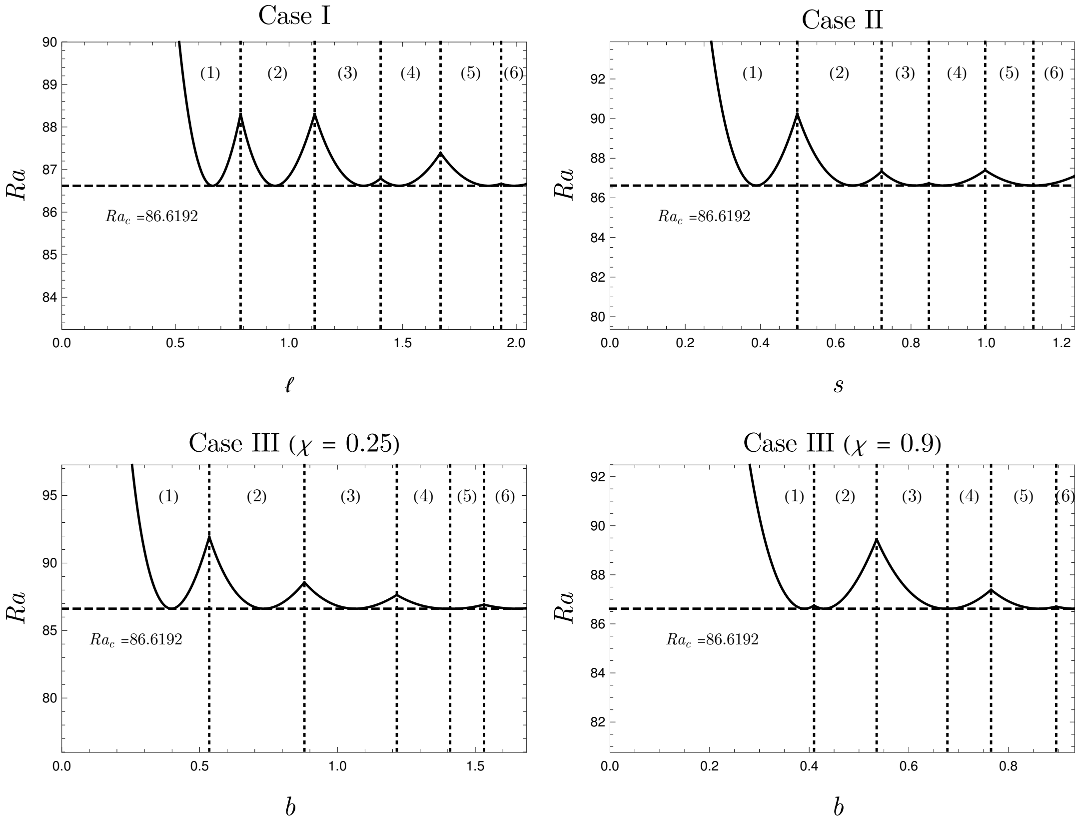

Figure 6.5: Marginal stability curves for $n = 1$ and $Pe = 6$; different modes $(1), (2), \ldots$ are labelled according to the ordering defined in tables 6.1–6.3

Figures 6.6 and 6.7 show the neutral stability curves for non–Newtonian fluid flows ($n \neq 1$). In particular, Figures 6.6 and 6.7 are relative to a pseudoplastic fluid, while Figures 6.8 and 6.9 are drawn for a dilatant fluid. Again the results are presented for fixed Pe and n and for three different geometries of the cylinder cross–section. The critical values of Ra displayed in these figures are in agreement with those reported in Barletta and Storesletten [15].

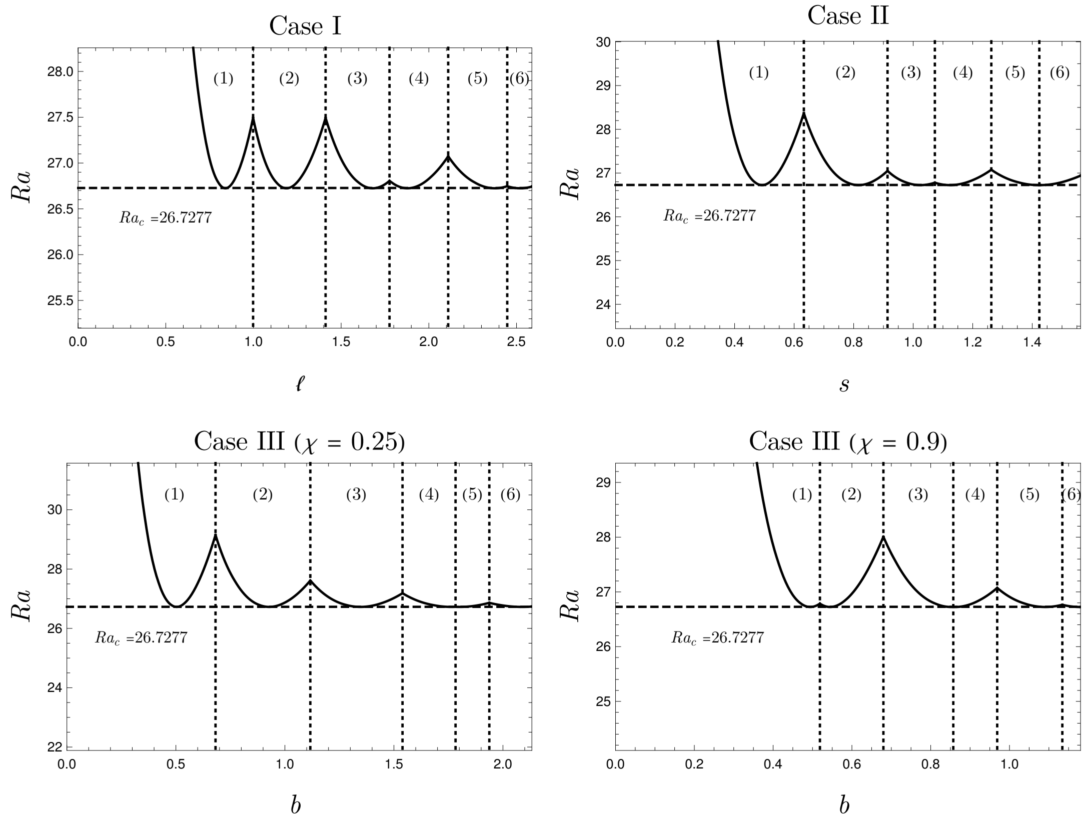

Figure 6.6: Marginal stability curves for $n = 0.6$ and $Pe = 2$; different modes $(1), (2), \ldots$ are labelled according to the ordering defined in tables 6.1–6.3

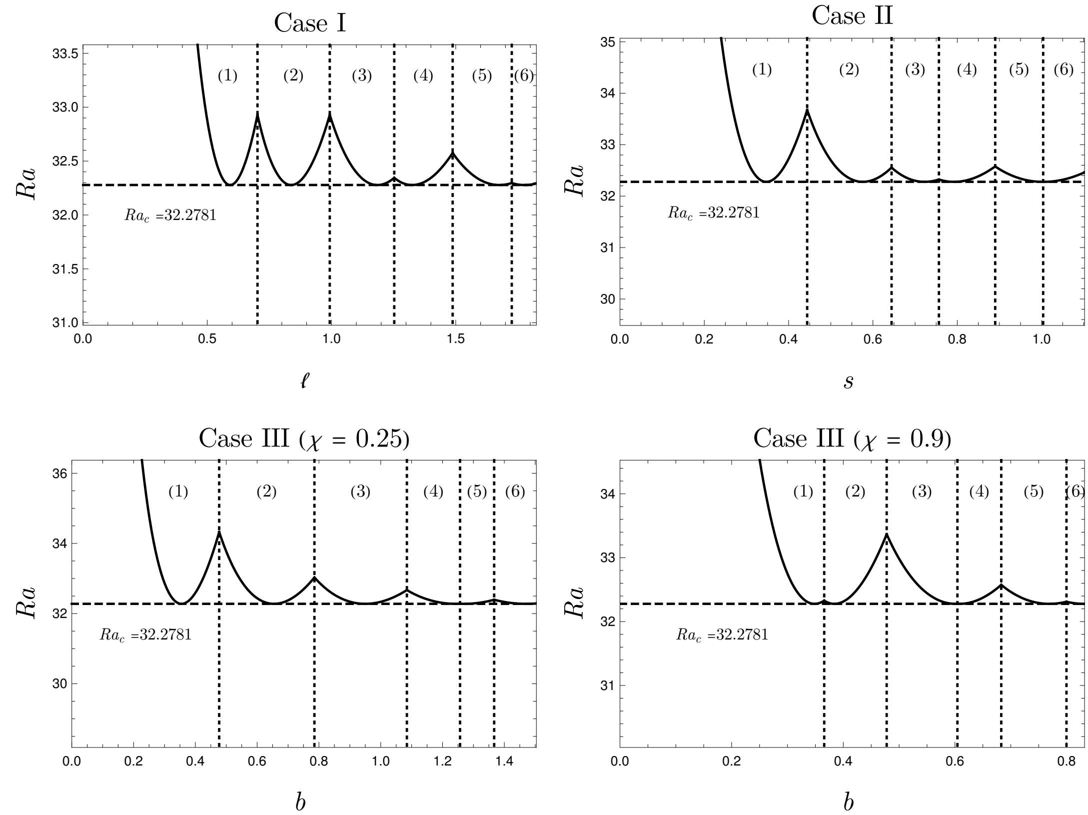

Figure 6.7: Marginal stability curves for $n = 0.6$ and $Pe = 6$; different modes $(1), (2), \ldots$ are labelled according to the ordering defined in tables 6.1–6.3

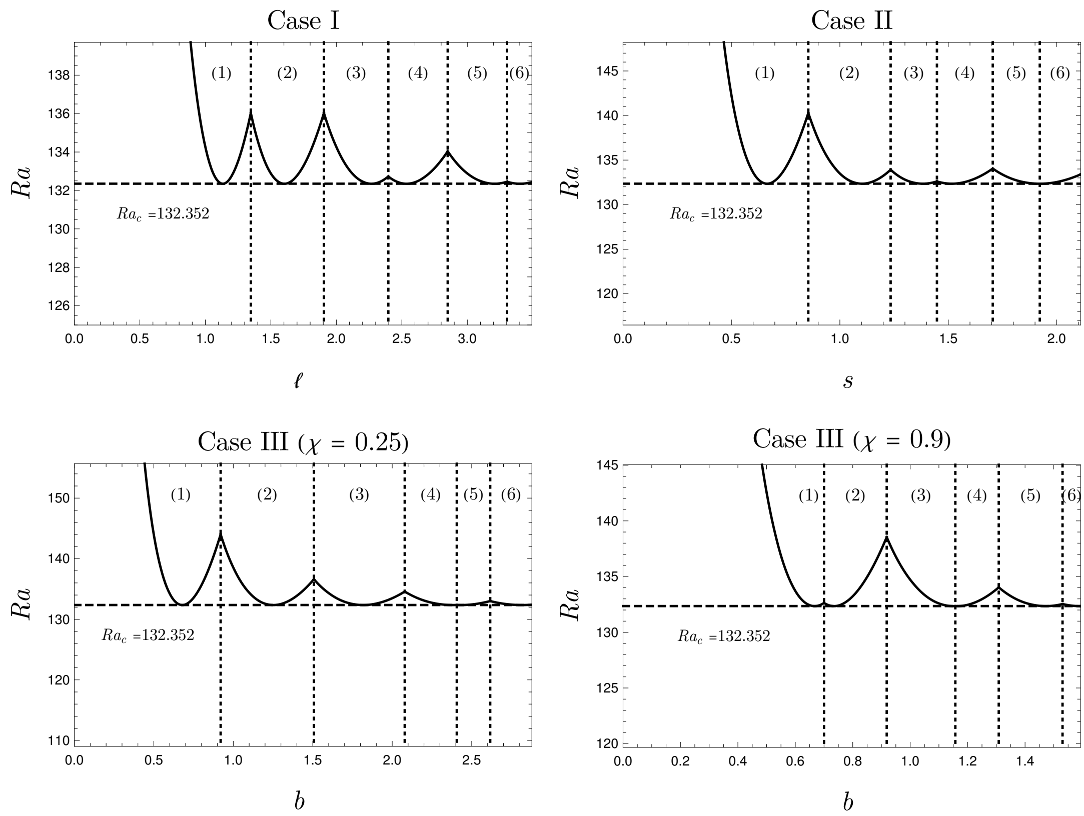

Figure 6.8: Marginal stability curves for $n = 2$ and $Pe = 2$; different modes $(1), (2), \ldots$ are labelled according to the ordering defined in tables 6.1–6.3

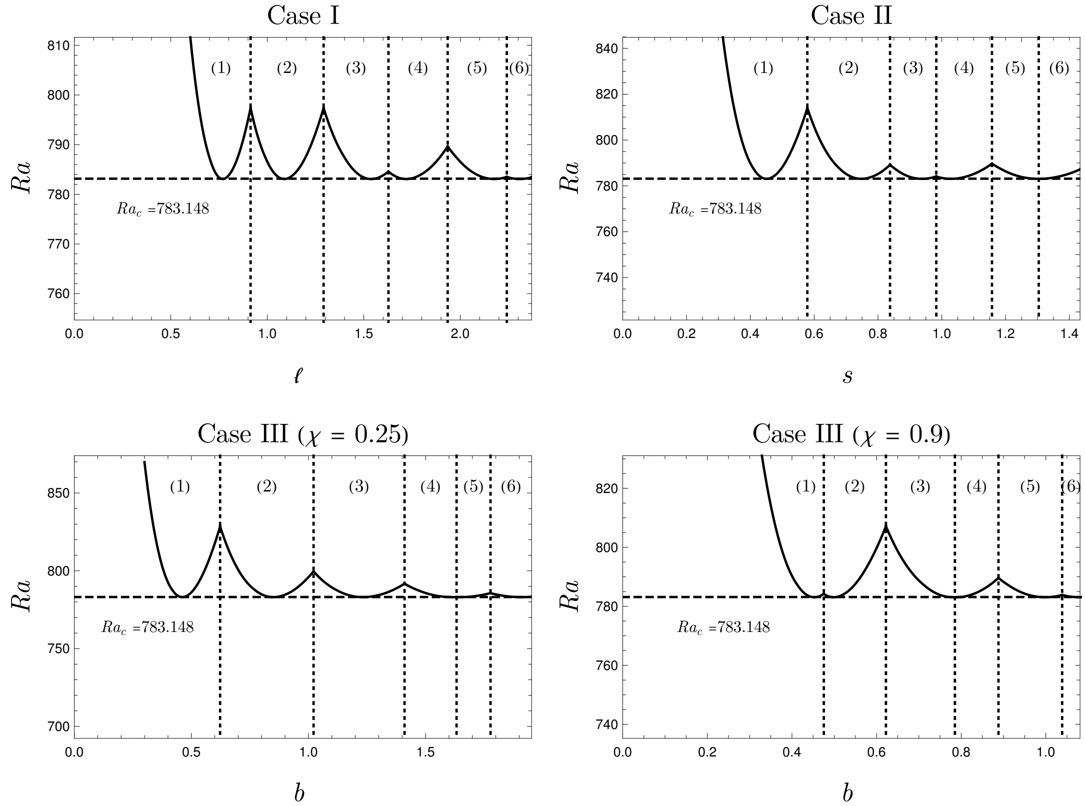

Figure 6.9: Marginal stability curves for $n = 2$ and $Pe = 6$; different modes $(1), (2), \ldots$ are labelled according to the ordering defined in tables 6.1–6.3

The lateral confinement changes significantly the selection of the modes and consequently the pattern selection at the onset of instability. However, the critical values of Ra and α just depend on n and Pe, while they are not influenced by the geometry of the sidewall. Therefore, in the interest of conciseness, the reader is referred to Barletta and Storesletten [15] for a thorough discussion of the critical values of Ra and α and of their dependence on n and Pe.

6.6 The asymptotic solution for large Péclet numbers

When $|Pe|$ becomes very large, the convection cells at the onset of instability gradually tend to display a boundary layer structure, as they tend to be confined to a small region close to either the lower or the upper boundary, depending on the sign of Pe.

It was already noted in Section 6.3.2 that the eigenvalue problem (6.17) is symmetric under flow reversal $Pe \to -Pe$. In the following analysis, the Péclet number Pe is assumed as negative, thus relying on the above mentioned symmetry to infer the behaviour when Pe is positive. For $Pe < 0$ and $|Pe| \gg 1$, the convective cells concentrate in the region of to the lower boundary, $z = 0$. First of all, the quantities z, W, Ra and α are rescaled by defining

$$\hat{z} = z\,|Pe|, \quad \hat{\hat{w}} = \frac{\hat{w}}{|Pe|}, \quad \hat{Ra} = \frac{Ra}{|Pe|^n}, \quad \hat{\alpha} = \frac{\alpha}{|Pe|}. \tag{6.33}$$

Then, by considering $Pe < 0$ and $\omega = 0$, Equations (6.17) can be rewritten as

$$\frac{\mathrm{d}^2\hat{\hat{w}}}{\mathrm{d}\hat{z}^2} - n\,\hat{\alpha}^2\,\hat{\hat{w}} + \hat{Ra}\,\hat{\alpha}^2\,\hat{T} = 0, \tag{6.34a}$$

$$\frac{\mathrm{d}^2\hat{T}}{\mathrm{d}\hat{z}^2} + \frac{\mathrm{d}\hat{T}}{\mathrm{d}\hat{z}} - \hat{\alpha}^2\,\hat{T} - \frac{e^{-\hat{z}}}{e^{-|Pe|} - 1}\,\hat{\hat{w}} = 0, \tag{6.34b}$$

$$\hat{z} = 0, |Pe|: \quad \hat{T} = \hat{\hat{w}} = 0. \tag{6.34c}$$

By taking the limit $|Pe| \to \infty$, Equations (6.34) yield

$$\frac{\mathrm{d}^2\hat{\hat{w}}}{\mathrm{d}\hat{z}^2} - n\,\hat{\alpha}^2\,\hat{\hat{w}} + \hat{Ra}\,\hat{\alpha}^2\,\hat{T} = 0, \tag{6.35a}$$

$$\frac{\mathrm{d}^2\hat{T}}{\mathrm{d}\hat{z}^2} + \frac{\mathrm{d}\hat{T}}{\mathrm{d}\hat{z}} - \hat{\alpha}^2\,\hat{T} + e^{-\hat{z}}\,\hat{\hat{w}} = 0, \tag{6.35b}$$

$$\hat{T}(0) = \hat{\hat{w}}(0) = 0. \tag{6.35c}$$

$$\lim_{\hat{z}\to+\infty} \hat{T} = \lim_{\hat{z}\to+\infty} \hat{\hat{w}} = 0. \tag{6.35d}$$

Now, one may solve Equations (6.35) by adapting the shooting method mentioned in Chapter 4.1 to a situation where the eigenvalue problem is defined over a semi–infinite range, $\hat{z} \geqslant 0$. To this aim, first the numerical solution of the system (6.35) is developed by assuming that the conditions for $\hat{z} \to +\infty$ hold, in fact, for a sufficiently large $\hat{z} = \hat{z}_{\max}$. Then, the sensitivity to the choice of $\hat{z}_{\max}$ is tested by gradually increasing its value. Table 6.6 illustrates the test for a strongly pseudoplastic fluid ($n = 0.1$), as this condition turned to present a very large sensitivity to the choice of $\hat{z}_{\max}$. This table shows that with $\hat{z}_{\max} = 25$ one achieves a 6 figures accuracy in the evaluation of both $\hat{\alpha}_c$ and $\hat{Ra}_c$.

Table 6.6: Sensitivity of $\hat{\alpha}_c$ and $\hat{Ra}_c$ to the choice of $\hat{z}_{\max}$ for $n = 0.1$

$\hat{z}_{\max}$	$\hat{\alpha}_c$	$\hat{Ra}_c$
10	1.19032239700	5.06444512579
11	1.18047438202	5.05575866872
12	1.17489331882	5.05149305271
13	1.17181039419	5.04941766775
14	1.17014306733	5.04841472535
15	1.16925621114	5.04793225624
16	1.16879049859	5.04770083714
17	1.16854834716	5.04759003274
18	1.16842341049	5.04753703493
19	1.16835934958	5.04751170145
20	1.16832667007	5.04749959597
21	1.16831007088	5.04749381254
22	1.16830167066	5.04749104979
23	1.16829743338	5.04748973009
24	1.16829530211	5.04748909972
25	1.16829423286	5.04748879863
26	1.16829369767	5.04748865481
27	1.16829343035	5.04748858611
28	1.16829329708	5.04748855330
29	1.16829323076	5.04748853763
30	1.16829319781	5.04748853015

On account of Equations (6.33) and (6.35), it can be concluded that, when $|Pe| \gg 1$, the neutral stability value of Ra is proportional to $|Pe|^n$, that is

$$Ra = \hat{Ra}\,|Pe|^n. \tag{6.36}$$

Table 6.7 shows the critical values of $\alpha/|Pe|$ and $Ra/|Pe|^n$ with $Pe = 20$. In the same table, these data are compared with the critical values of $\hat{\alpha}$ and $\hat{Ra}$ obtained by the numerical solution of Equations (6.35) for the asymptotic case $|Pe| \gg 1$. The agreement is good especially for $n \geqslant 0.4$. In every case, the data with $Pe = 20$ and $|Pe| \gg 1$ coincide within at least 5 significant figures. An useful comparison is one between the trends of α_c and Ra_c obtained numerically with those obtained by employing the asymptotic solution data given by Table 6.7.

Table 6.7: Comparison between the asymptotic analysis ($|Pe| \gg 1$) and the numerical solutions with $Pe = 20$: critical values of $\hat{\alpha}$ and $\hat{Ra}$

n	$\hat{\alpha}_c$	$\hat{\alpha}_c$ ($\lvert Pe\rvert \gg 1$)	$\hat{Ra}_c$	$\hat{Ra}_c$ ($\lvert Pe\rvert \gg 1$)
0.1	1.16833	1.16829	5.04750	5.04749
0.2	1.02929	1.02929	6.56943	6.56942
0.4	0.904532	0.904532	8.92619	8.92619
0.6	0.837517	0.837517	10.9049	10.9049
0.8	0.792457	0.792457	12.6901	12.6901
1.0	0.758867	0.758867	14.3522	14.3522
1.2	0.732280	0.732280	15.9270	15.9270
1.4	0.710389	0.710389	17.4357	17.4357
1.6	0.691853	0.691853	18.8921	18.8921
1.8	0.675827	0.675827	20.3058	20.3058
2.0	0.661746	0.661746	21.6837	21.6837

Figure 6.10 illustrates such trends, where the solid lines are relative to the numerical solution while the dashed lines denote the asymptotic solution for $|Pe| \gg 1$. An evident coincidence between the solid and the dashed lines is shown for $|Pe| > 10$ meaning that, in this range, the asymptotic solution can be considered as a reliable approximation. It is worth to mention that, for a Newtonian fluid ($n = 1$), Homsy and Sherwood [66] reported the values $\hat{\alpha}_c = 0.759$ and $\hat{Ra}_c = 14.3$, respectively. Indeed, the agreement with the data displayed in Table 6.7 is fair. It is important to mention that Homsy and Sherwood [66] did not describe explicitly the procedure followed to obtain their results.

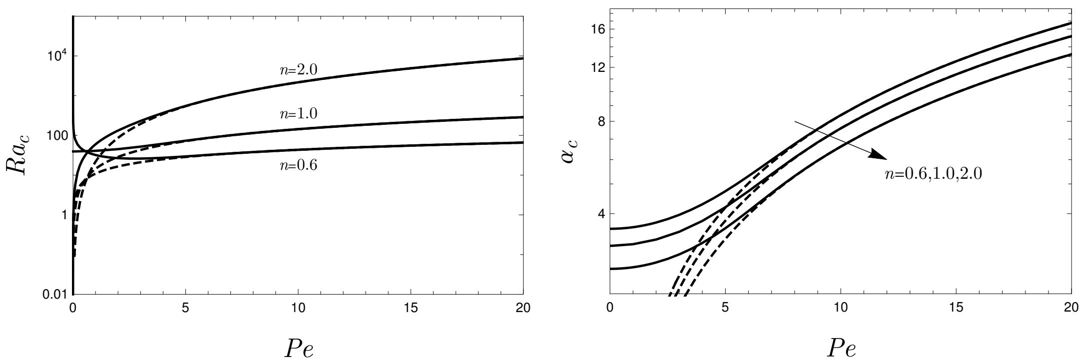

Figure 6.10: Critical values of α_c and Ra_c versus Pe for different values of n. The solid lines are those relative to the numerical solution, while the dashed lines are relative to the asymptotic solution valid for $|Pe| \gg 1$

6.7 Conclusions

The effects of the lateral confinement with impermeable adiabatic sidewalls on the onset of thermoconvective instability in a porous medium have been studied. A porous layer saturated by a power–law fluid has been considered. The layer is laterally bounded by a vertical cylindrical wall with arbitrary cross-section and it is subject to a vertical base throughflow. The permeable horizontal boundaries of the porous cylinder are kept at different uniform temperatures, with heating from below, so that the vertical base throughflow may display an instability of the Darcy–Bénard type. The modified Darcy law for power–law fluid is employed to model the momentum transfer. The dimensionless parameters driving the instability are the power–law index, n, the Péclet number of the base throughflow, Pe, and the Darcy–Rayleigh number, Ra. Normal mode perturbations are identified by the wavenumber, α, whose values are constrained by the geometry of the sidewall boundary. Thus, for a given geometry, only a discrete sequence of wavenumbers is allowed, which depends on the geometry of the sidewall. The main features of the instability reported in this study are the following:

- The rheological behaviour of the saturating fluid, *i.e.* its power–law index n, does not influence the sequence of the allowed wavenumbers, α. This sequence is uniquely determined by solving the two–dimensional Helmholtz eigenvalue problem with Dirichlet boundary conditions defined in the cylinder horizontal cross–section.

- The neutral stability condition is affected only by n and Pe, while the geometry of the sidewall just contribute to the selection of the allowed wavenumbers.

- There exists an asymptotic solution of the neutral stability problem which holds for $|Pe| \gg 1$. In this regime, the convective cells arising at the onset of the instability form a boundary layer structure near one of the boundaries. In practice, numerical data show that such a solution starts to be reliable when Pe is approximately larger than 10.

Chapter 7

A Darcy–Carreau model for nonlinear natural convection of non–Newtonian fluids in porous media

7.1 Introduction

Besides the power–law model used to describe the non–Newtonian behaviour of dilatant and pseudoplastic fluids, there has been an increasing interest for the stability studies involving other kinds of fluids. Kim et al. [79] and Yoon et al. [135] performed a linear stability analysis by using the modified Darcy's law based on the Oldroyd–B model to study the onset of convection in a viscoelastic fluid confined in a porous medium. It was demonstrated that for viscoelastic fluids a Hopf bifurcation, as well as a stationary bifurcation, may occur at the onset of convection depending on the magnitude of the viscoelastic parameters. For a Hopf bifurcation, Hirata et al. [63] investigated the nature of the disturbances waves at the onset of instability. The nonlinear interaction between stationary and oscillatory instabilities is analysed by Taleb et al. [127] by considering both, a fully nonlinear numerical simulation and also the weakly nonlinear theory. The oscillatory nature of the instability at the onset of convection was confirmed experimentally by Kolodner [82], by using DNA suspensions in clear fluids.

The modified Darcy's model for power–law fluids in porous media considers the drag term in Darcy's law as $\frac{\mu_a}{K}\,\mathbf{u}$, where $\mathbf{u}$ is the seepage velocity, K is the permeability of the porous medium and μ_a is the apparent viscosity given by

$$\mu_a = \eta_{ef}\,|\mathbf{u}|^{n-1}, \tag{7.1}$$

where η_{ef} is the effective consistency factor and n is the power–law index. An important singularity of the power–law model is that, in the limit of a vanishing $\mathbf{u}$, the apparent viscosity goes to infinite for shear–thinning fluids ($n < 1$) and to zero for shear–thickening fluids ($n > 1$). To deal with these singularities, Nield [103, 104] proposed a modified drag term, $\frac{\mu_0}{K}\,(1 + C\,|\mathbf{u}|^{n-1})\,\mathbf{u}$, *i.e.* a modified apparent viscosity,

$$\mu_a \;=\; \mu_0\,\left(1 + C\,|\mathbf{u}|^{n-1}\right), \tag{7.2}$$

where C is a constant.

By looking at this suggested model, it is easy to observe that for small values of $\mathbf{u}$ and for dilatant fluids ($n > 1$) one recovers the usual linear Darcy's law with μ_0 being the fluid viscosity at $\mathbf{u} = 0$. Consequently, as pointed out by Nield [103, 104], the critical Rayleigh number at the onset of convection becomes independent of the power–law index and, thus, equal to the classical value for Newtonian fluids, *i.e.* $Ra_c = 4\,\pi^2$. Nonetheless, for pseudoplastic fluids ($n < 1$) in the limit of vanishing v, the apparent viscosity μ_a becomes infinite.

Barletta and Nield [12] investigated the onset of mixed convection in a porous layer heated from below in the presence of a horizontal throughflow, considering both pseudoplastic and dilatant fluids. In this study the throughflow is characterized by a Péclet number Pe in such a way that the classical Darcy–Bénard problem is recovered in the limit of zero Pe. In this limit, the results obtained by employing the linear stability theory showed that Ra_c tends to infinity for shear–thinning fluids and to zero for shear–thickening fluids. It is important to remark that these results were obtained by considering the power–law model, which, as discussed earlier, presents some singularities in the limit of vanishing throughflow.

Thermal instabilities in clear fluids and in saturated porous media can be considered as qualitatively similar in a number of aspects. For this reason, in order to understand qualitatively some phenomena in the field of fluid saturated porous media, it can be interesting to look at some results in the literature obtained for thermal stability analysis of non–Newtonian fluids. Chi et al. [40] stated that the neutral stability condition cannot be determined for shear–thinning fluids described by a power-law model, because of the unphysical infinite viscosity arising for vanishing shear rate.

Bouteraa et al. [23] studied the Rayleigh-Bénard problem, considering pseudoplastic fluids, by using a Carreau rhelogical model. By using the weakly nonlinear analysis, they derived the Landau amplitude equation and found out that the nature of the bifurcation may be supercritical or subcritical depending on the shear-thinning strength. The nature of the bifurcation predicted by the weakly nonlinear theory [23] was confirmed by fully nonlinear two-dimensional numerical simulations by Jenny et al. [70] and by Benouared et al. [21].

Moreover, Darbouli et al. [44] concluded experimentally that the onset of convection for all the cases considered happened for a Rayleigh number around $Ra_c = 1800$, which can be considered as almost equal to the Newtonian case. This results agree well with the linear stability predictions obtained by Liang and Acrivos [88] for the Carreau model.

This chapter aims to present some novel results obtained by a weakly nonlinear stability theory for the onset of Darcy–Bénard convection for pseudoplastic and dilatant fluids. A new model that adapts the Carreau model to porous media is presented as an attempt to bypass the singularities problem presented by the power–law model in the limit of vanishing flow rate.

The contents of this chapter are based on the paper by Brandão, P. V. and Ouarzazi, M. N., Darcy–Carreau model and nonlinear natural convection for pseudoplastic and dilatant fluids in porous media, Transport in Porous Media, doi:10.1007/s11242-020-01523-9 [26].

7.2 Rheological model and dimensionless equations

7.2.1 Rheological model

In order to deal with the singularity for shear–thinning fluids ($n < 1$) at zero shear-rate in a fluid medium, a regularized form of the power–law model can be used. It is called Carreau model [36] and it is given by

$$\frac{\mu - \mu_\infty}{\mu_0 - \mu_\infty} = (1 + (\lambda^* \dot{\gamma})^2)^{\frac{n-1}{2}}, \tag{7.3}$$

where $\dot{\gamma}$ is the shear rate, μ_∞ is the infinite shear rate viscosity and λ^* is a characteristic time for the non–Newtonian fluid, defined as

$$\lambda^* = (\frac{\eta}{\mu_0})^{\frac{1}{n-1}}, \tag{7.4}$$

where η is the consistency factor. Usually, μ_∞ can be considered as negligible and the Carreau model reduces to

$$\frac{\mu}{\mu_0} = \Big(1 + (\lambda^* \dot{\gamma})^2\Big)^{\frac{n-1}{2}}. \tag{7.5}$$

In the same way, the singularities in the limit of vanishing seepage velocity $\mathbf{u}$ of the power–law model for porous media, can be avoided by adopting the following rheological model, called here the Darcy–Carreau model,

$$\frac{\mu_a}{\mu_0} = \left(1 + (\frac{\eta_{ef}}{\mu_0})^{\frac{2}{n-1}} |\mathbf{u}|^2\right)^{\frac{n-1}{2}}, \tag{7.6}$$

noting that, in the limit of high values of $|\mathbf{u}|$, the power–law model (7.1) can be recovered. Also, the apparent viscosity assumes a finite non zero value $\mu_a = \mu_0$ in the limit of a vanishing seepage velocity $|\mathbf{u}|$, independently of n. In the present study, the following expression for η_{ef} is employed [108, 89]

$$\eta_{ef} = \eta\, f_p\, (\Phi\, K)^{\frac{1-n}{2}}, \tag{7.7}$$

where $f_p = 8^{(-\frac{n+1}{2})}\, 2\,(\frac{3n+1}{n})^n$ and Φ is the porosity of the porous medium.

By introducing the characteristic time of the non–Newtonian fluid λ^* defined by (7.4), the Darcy–Carreau model (7.6) then becomes

$$\frac{\mu_a}{\mu_0} = \left[1 + \left(\lambda^* f_p^{\frac{1}{n-1}} (\Phi\, K)^{-\frac{1}{2}} |\mathbf{u}|\right)^2\right]^{\frac{n-1}{2}} . \tag{7.8}$$

Savins [116], in his review on non–Newtonian flows in porous media, studied the effect of the tortuosity of the porous medium on the shear rate $\dot{\gamma}_p^*$, which is proportional to $(\Phi\, K)^{\frac{-1}{2}} |\mathbf{u}|$. Longo et al. [89] investigated non–Newtonian axisymmetric porous gravity currents and demonstrated that it is fundamental to choose a correct range for the shear rate range for the determination of the rheological parameters. Here, the porous shear rate is defined as,

$$\dot{\gamma}_p^* = f_p^{\frac{1}{n-1}} (\Phi\, K)^{-\frac{1}{2}} |\mathbf{u}|, \tag{7.9}$$

and, thus, Equation (7.8) may be written as

$$\frac{\mu_a}{\mu_0} = \left(1 + (\lambda^* \dot{\gamma}_p^*)^2\right)^{\frac{n-1}{2}} . \tag{7.10}$$

The Darcy-Carreau model given by Equation (7.10) looks like the Carreau model for clear fluids (7.5) if the infinite shear rate viscosity μ_∞ is considered to be zero.

7.2.2 Mathematical formulation

An isotropic and homogeneous porous cavity of height H and infinitely wide in the horizontal plane is here considered. The porous channel is saturated by either a pseudo-plastic or a dilatant fluid and it is heated from the bottom and cooled from the top. The horizontal walls are considered impermeable and both the upper and lower walls are kept at constant temperatures, T_1 and T_0, respectively.

The Oberbeck-Boussinesq approximation is considered valid. The apparent viscosity is assumed to obey the Darcy–Carreau rheological model (7.8). The equations for mass balance, apparent viscosity, momentum balance and energy balance can be written as

$$\nabla \cdot \mathbf{u} = 0, \tag{7.11}$$

$$\frac{\mu_a}{\mu_0} = \left(1 + (\lambda^* f_p^{\frac{1}{n-1}} (\Phi\, K)^{-\frac{1}{2}} |\mathbf{u}|)^2\right)^{\frac{n-1}{2}} , \tag{7.12}$$

$$\frac{\mu_a}{K} \mathbf{u} + \nabla p = \rho_0\, \beta\, (T - T_0))\mathbf{g}, \tag{7.13}$$

$$\sigma \frac{\partial T}{\partial t} + \mathbf{u} \cdot \nabla T = \chi\, \nabla^2 T, \tag{7.14}$$

subject to the following boundary conditions at the horizontal walls

$$z = 0: \quad w = 0, \quad T = T_0 + \Delta T, \tag{7.15a}$$

$$z = H: \quad w = 0, \quad T = T_0. \tag{7.15b}$$

with $\mathbf{u} = (u, v, w)$ being the velocity field, T the temperature field, p the hydrostatic pressure field, μ_a the apparent dynamic viscosity, μ_0 the dynamic viscosity at the zero shear rate, χ the effective thermal diffusivity, β the fluid thermal expansion coefficient, K the permeability, ρ_0 the fluid density ate the reference temperature T_0, σ is the ratio between the average volumetric heat capacity of the saturated porous medium and the volumetric heat capacity of the fluid, respectively and $\mathbf{g}$ the gravity acceleration with modulus g.

7.3 Dimensionless equations

The following dimensionless quantities can be introduced

$$\frac{1}{H}(x, y, z) \to (x, y, z), \qquad \frac{H}{\chi}\mathbf{u} \to \mathbf{u}, \qquad \frac{\chi}{\sigma H^2} t \to t,$$
$$\frac{T - T_0}{\Delta T} \to T, \qquad \frac{K}{\chi \mu_0} p \to p, \tag{7.16}$$

which allow one to write the governing equations in their dimensionless form as following

$$\nabla \cdot \mathbf{u} = 0, \tag{7.17}$$

$$\left(1 + \alpha\, |\mathbf{u}|^2\right)^{\frac{n-1}{2}} \mathbf{u} + \nabla P = Ra\, T\, \mathbf{e}_z, \tag{7.18}$$

$$\frac{\partial T}{\partial t} + \mathbf{u} \cdot \nabla T = \nabla^2 T, \tag{7.19}$$

with

$$Ra = \frac{\rho_0 K H g \beta \Delta T}{\chi \mu_0}, \tag{7.20}$$

and

$$\alpha = \lambda^{*2}\, f_p^{\,\frac{2}{n-1}}\, \frac{1}{\Phi\, K}\, (\frac{\chi}{H})^2, \tag{7.21}$$

After introducing the dimensionless characteristic time of the fluid $\lambda = \frac{\lambda^*}{H^2/\chi}$ and the Darcy number $Da = \frac{K}{H^2}$, Equation (7.21) can be written as,

$$\alpha = \lambda^2\, f_p^{\,\frac{2}{n-1}}\, \frac{1}{\Phi\, Da}. \tag{7.22}$$

The dimensionless boundary conditions are

$$z = 0: \quad w = 0, \quad T = 1, \tag{7.23a}$$

$$z = H: \quad w = 0, \quad T = 0. \tag{7.23b}$$

The basic solution for the flow quantities can be written in dimensionless form as

$$\mathbf{u} = \{0, 0, 0\}, \tag{7.24}$$

$$T_b = 1 - z, \tag{7.25}$$

$$\nabla p_b = Ra\, T_b\, \mathbf{e}_z. \tag{7.26}$$

7.4 Weakly nonlinear analysis

7.4.1 Amplitude equation

As explained in the sections 3.2 and 3.3, in order to investigate the stability of the conductive state, the flow quantities are decomposed into a basic part and another one relative to the disturbances

$$\mathbf{u} = \tilde{\mathbf{u}}(x, z, t), \quad T = T_b + \tilde{T}(x, z, t), \quad p = p_b + \tilde{p}(x, z, t). \tag{7.27}$$

After substituting Equations (7.27) into (7.17)-(7.19), eliminating the pressure field by applying the curl on the momentum balance equation, and introducing the disturbance stream function ψ defined by

$$u = \frac{\partial \psi}{\partial z} \;\text{ and }\; w = -\frac{\partial \psi}{\partial x}, \tag{7.28}$$

one is able to have the dimensionless nonlinear governing equations for the disturbances in terms of ψ and $\tilde{T}$

$$\nabla^2 \psi + Ra \frac{\partial \tilde{T}}{\partial x} = NL, \tag{7.29}$$

$$\frac{\partial \tilde{T}}{\partial t} + \frac{\partial \psi}{\partial x} - \nabla^2 \tilde{T} = -(\mathbf{u} \cdot \nabla)\tilde{T}, \tag{7.30}$$

with NL being the nonlinear term

$$\begin{aligned} NL = -\alpha(n-1) \Bigg[& \left(\frac{\partial \psi}{\partial z}\right)^2 \frac{\partial^2 \psi}{\partial z^2} + \left(\frac{\partial \psi}{\partial x}\right)^2 \frac{\partial^2 \psi}{\partial x^2} + \\ & 2 \frac{\partial \psi}{\partial z} \frac{\partial \psi}{\partial x} \frac{\partial^2 \psi}{\partial x \partial z} + \frac{1}{2} \left(\left(\frac{\partial \psi}{\partial z}\right)^2 + \left(\frac{\partial \psi}{\partial x}\right)^2 \right) \left(\frac{\partial^2 \psi}{\partial x^2} + \frac{\partial^2 \psi}{\partial z^2} \right) \Bigg]. \end{aligned} \tag{7.31}$$

The governing equations can be rewritten in a compact matrix notation as

$$(\mathbf{L}'\partial_t + \mathbf{L}(Ra))\mathbf{q} = \mathbf{N}. \tag{7.32}$$

where the vector $\mathbf{q} = (\psi, \tilde{T})^T$ contains the disturbance stream function and temperature. Here, $\mathbf{L}'$ and $\mathbf{L}$ are the linear operators

$$\mathbf{L}' = \begin{pmatrix} 0 & 0 \\ 0 & 1 \end{pmatrix}, \tag{7.33}$$

and

$$\mathbf{L} = \begin{pmatrix} \left(\frac{\partial^2}{\partial x^2} + \frac{\partial^2}{\partial z^2}\right) & Ra\frac{\partial}{\partial x} \\ \frac{\partial}{\partial x} & -\left(\frac{\partial^2}{\partial x^2} + \frac{\partial^2}{\partial z^2}\right) \end{pmatrix}, \tag{7.34}$$

with $\mathbf{N}$ being the nonlinear operator. In the vicinity to the linear threshold, a small parameter ε, which measures the distance to criticality, is introduced by setting $Ra = Ra_c + \varepsilon^2 R_2$, where R_2 is of order of unity. In this way, the temporal scale is fixed as

$$t_2 = \varepsilon^2 t, \tag{7.35}$$

allowing the derivative with respect to time to be replaced by

$$\frac{\partial}{\partial t} \to \frac{\partial}{\partial t} + \varepsilon^2 \frac{\partial}{\partial t_2}, \tag{7.36}$$

and the evolution equations are obtained by expanding the vector $\mathbf{q}$ in power series of ε, *i.e.*

$$\mathbf{q} = \varepsilon q_1 + \varepsilon^2 q_2 + \mathcal{O}(\varepsilon^3) \tag{7.37}$$

where the functions $\mathbf{q}_i$ depend on the slow variable t_2. By substituting Equation (7.37) into the system (7.32), and by collecting coefficients of each order of ε, the following equations are obtained for each order

$$(\mathbf{L}'\partial_t + \mathbf{L}_0)\mathbf{q}_1 = 0, \tag{7.38}$$

$$(\mathbf{L}'\partial_t + \mathbf{L}_0)\mathbf{q}_2 = \mathbf{N}_{(2)} = \mathbf{RH}_2, \tag{7.39}$$

$$(\mathbf{L}'\partial_t + \mathbf{L}_0)\mathbf{q}_3 = -\mathbf{L}_2\mathbf{q}_1 - \mathbf{L}'\partial_{t_2}\mathbf{q}_1 + \mathbf{N}_{(3)} = \mathbf{RH}_3, \tag{7.40}$$

with $\mathbf{L}_0$ being as the linear operator for $Ra = Ra_c$, and $\mathbf{RH}_n$ representing the final righ–hand side terms. While $\mathbf{L}_2$ is given by

$$\mathbf{L}_2 = \begin{pmatrix} 0 & R_2\frac{\partial}{\partial x} \\ 0 & 0 \end{pmatrix}. \tag{7.41}$$

At first order, the linear problem is recovered and the first–order variables $\mathbf{q}_1 = \left(\psi_1, \tilde{T}_1\right)^T$ are considered to behave as normal modes,

$$\left(\psi_1, \tilde{T}_1\right) = A(t_2)\ (\Psi_1, \Theta_1)\, e^{ik_c\, x + s\, t} \sin(\pi z) +\ c.\,c, \tag{7.42}$$

where A is the disturbance amplitude, which depends on the slow time t_2, s is the temporal growth rate of the disturbances and c. c stands for complex conjugate. Substituting (7.42) into (7.38) leads to the linear dispersion relation,

$$s\ =\ -(k^2 + \pi^2)\ +\ \frac{k^2}{(k^2\ +\ \pi^2)}\, Ra. \tag{7.43}$$

The neutral stability condition can be found by setting $s\ =\ 0$ leading to $Ra = (k^2\ +\ \pi^2)^2/k^2$. The critical values, that are the minimum values of the curve (Ra, k) are those expected for the Darcy–Bénard problem, *i.e.* $Ra_c = 4\pi^2$ and $k_c = \pi$. Such a result means that the non–Newtonian behaviour of the fluid does not affect the linear characteristics of the instability, as it was predicted by Nield [104, 103] for dilatant fluids, for instance. For the present study, this result holds for both dilatant and pseudoplastic fluids.

By taking into account that $\partial s/\partial Ra = 1/2$ at (Ra_c, k_c), and by assuming that the wavenumber remain constant in the present analysis $k = k_c$, the Taylor series expansion in the neighbourhood of criticality for s can be written as

$$s(Ra)\ =\ s(Ra = Ra_c)\ + (1/2)\,(Ra - Ra_c)\ +\ ... \tag{7.44}$$

with $s(Ra\ =\ Ra_c)\ = 0$. This relation states that the linear disturbance growth rate in the vicinity of the criticality is $(1/2)\,(Ra - Ra_c)$, which justifies the introduction of the slow time scale t_2 defined by (7.35).

The eigenfunctions at $\mathcal{O}(\varepsilon)$ and $\mathcal{O}(\varepsilon^2)$ are, respectively,

$$\left(\tilde{T}_1, \psi_1\right)\ =\ (1, 2\pi i)\ A(t_2)\, e^{ik_c x}\ \sin(\pi z)\ +\ c.\,c, \tag{7.45}$$

$$\tilde{T}_2\ =\ -\,\pi\ \mid A\mid^2\ \sin(2\pi z) \quad \text{and} \quad \psi_2\ =\ 0, \tag{7.46}$$

with the quantity $\tilde{T}_2$ representing a nonlinear correction to the conductive basic of the temperature and it is due to the interaction of the fundamental mode with its complex conjugate.

The solutions at first and second order are obtaining by solving the respective equations for q_1 and q_2. At third order, on the other hand, there is no need to solve the equation. Instead, one projects the whole equation onto $q^\dagger$, where $q^\dagger$ is the solution of the adjoint linear problem. Such a procedure yields a solvability condition, known as the Fredholm alternative as already explained in Section 3.3. The solvability condition is then applied by considering the following inner product,

$$\langle q_i, q_j\rangle\ =\ \frac{1}{2\pi/k_c}\int_0^{2\pi/k_c}\int_0^1 q_i\cdot q_j^*\mathrm{d}z\,\mathrm{d}y, \tag{7.47}$$

where q_j^* is the complex conjugate of q_j. Then, one may reintroduce the original variables $t = t_2/\varepsilon^2$, which yields the amplitude equation

$$\frac{dA}{dt} = \beta A - \delta\, A\, |A|^2, \tag{7.48}$$

where the explicit expressions for β and δ are given by

$$\beta = \frac{R_a - Ra_c}{2} \quad \text{and} \quad \delta = 2\,\pi^4 + 10\,\pi^6\,\alpha\,(n-1), \tag{7.49}$$

where β represents the linear disturbance growth rate, determined by the linear stability analysis, and δ is the Landau constant.

7.4.2 Nature of bifurcations

The Landau coefficient δ in the amplitude equation (7.48) presents two different nonlinear contributions for the current problem. The first one, *i.e.* $2\,\pi^4$, is relative to the nonlinear thermal advection, while the second one, *i.e.* $10\,\pi^6\,\alpha\,(n-1)$, is relative to the non–Newtonian character of the fluid. From a physical point of view, the latter can be related to the variation of the apparent viscosity $\mu_a = (1 + (\alpha\,|\mathbf{u}|)^2)^{(n-1)/2}$ in the vicinity of the onset of convection, which is given by

$$\frac{d\mu_a}{d|\mathbf{u}|^2}\,(|\mathbf{u}|^2 = 0) = \alpha\,\frac{n-1}{2}. \tag{7.50}$$

Equation (7.50) shows that in the vicinity of the convection threshold, where $|\mathbf{u}|$ may assume small values, the nonlinear correction reduces the apparent viscosity for pseudoplastic fluids ($n < 1$), while it enhances the apparent viscosity for dilatant fluids ($n > 1$). By introducing the parameter

$$\alpha_p = \alpha\,|\frac{n-1}{2}| = |\frac{n-1}{2}|\, f_p^{\,\frac{2}{n-1}}\, \lambda^2\, \frac{1}{\Phi\, Da}, \tag{7.51}$$

which may be assumed as a measure of the non–Newtonian effects, the Landau constant may be written as $\delta = 2\,\pi^4 \pm 20\,\pi^6\,\alpha_p$, where the positive and negative signs correspond, respectively, to dilatant and pseudoplastic fluids.

The sign of the Landau constant δ determines the nature of the bifurcation. The nonlinear coefficient δ is always positive for Newtonian fluids ($n = 1$) as well as for dilatant fluids ($n > 1$). On the other hand, it can be both positive or negative for pseudoplastic fluids ($n < 1$). For Newtonian fluids, the classical results of the Darcy–Bénard convection are recovered. For non–Newtonian fluids, the bifurcation is always supercritical for dilatant fluids. For the case of pseudoplastic fluids, the nature of the bifurcation depends on the value of α_p. There exists a particular value of $\alpha_p = \alpha_p^{tr}$ related to a tricritical bifurcation point,

$$\alpha_p^{tr} = \frac{1}{10\pi^2}, \tag{7.52}$$

such that the bifurcation to the unstable state is supercritical when $\alpha_p < \alpha_p^{tr}$ and subcritical otherwise.

Bouteraa et al. [23] investigated the nonlinear stability of the Rayleigh–Bénard problem considering pseudoplastic fluids. In that case, the nature of the bifurcation is related to the shear–thinning characteristics of the fluid. In contrast, for the porous medium case, the nature of the bifurcation is determined by the intrinsic properties of the medium (here represented by the Darcy number Da) together with the fluid properties. In fact, by considering the definition of α given by (7.22), the condition required for subcritical bifurcation can be written as

$$\frac{\lambda^2}{\Phi Da}(1-n)\, f_p{}^{\frac{2}{n-1}} > \frac{1}{5\pi^2} \quad . \tag{7.53}$$

Figure 7.1 shows the bifurcation curves, defined by $\lambda^2/(\Phi Da)\,(1-n)\, f_p{}^{2/(n-1)} = 1/(5\pi^2)$, where the transition from supercritical to subcritical bifurcation may occur, in the plane (n, λ) for different values of ΦDa. For a given value of ΦDa, the bifurcation is said to be supercritical below the curve and supercritical above the curve. It can be seen in Figure 7.1 that when the n approaches $n = 1$, all the curves go to infinity, certifying a supercritical bifurcation for all values of ΦDa as it occurs for the Newtonian case. In the same figure, it can be seen also that decreasing the value of n favours a subcritical bifurcation. The same can be concluded by looking at the characteristic time of the fluid λ. If it increases, the transition becomes subcritical and the contrary is true if it decreases. These results also indicate that the more permeable are the porous materials the more the bifurcation is likely to be supercritical.

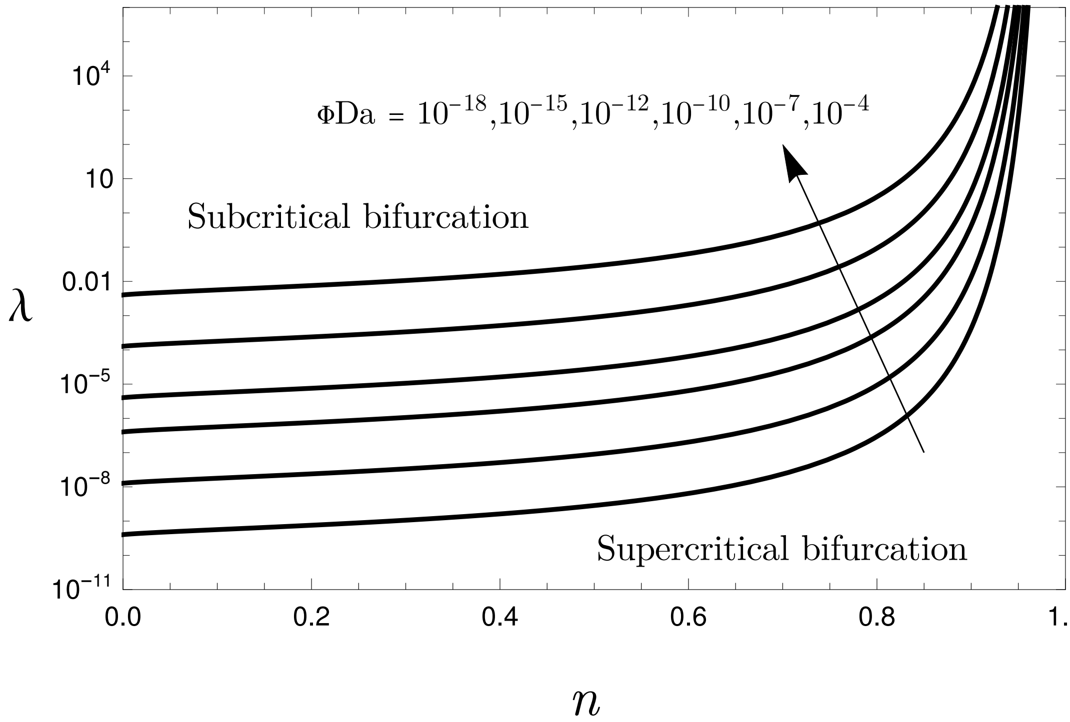

Figure 7.1: Tricritical bifurcation curves separating regions of subcritical and supercritial bifurcation in (n, λ) plane at different values of ΦDa corresponding to pseudoplastic fluids.

7.4.3 Equilibrium amplitude, isocontours and average heat transfer

From the amplitude equation (7.48) it is easy to see that the bifurcation is always supercritical for dilatant fluids, independently of α_p. On the other hand, for pseudoplastic fluids this is true just for $\alpha_p < \alpha_p^{tr}$. In both cases, when the transition is supercritical, the stable stationary nonlinear equilibrium solution can be written as

$$\begin{aligned} |A_s| &= \left[\frac{Ra - Ra_c}{Ra_c}\right]^{1/2} \frac{1}{\pi} \frac{1}{\left(1 \pm 10\,\pi^2\,\alpha_p\right)^{1/2}} \\ &= \frac{|A_s^N|}{\left(1 \pm 10\,\pi^2\,\alpha_p\right)^{1/2}}, \end{aligned} \tag{7.54}$$

where the positive and negative signs correspond to dilatant and pseudoplastic fluids, respectively, and A_s^N is the equilibrium amplitude for Newtonian fluids, which is defined by,

$$|A_s^N| = \frac{1}{\pi}\left[\frac{Ra - Ra_c}{Ra_c}\right]^{1/2}. \tag{7.55}$$

Figure 7.2 presents the supercritical bifurcation diagram showing the equilibrium amplitude for dilatant and pseudoplastic fluids. The equilibrium amplitude is presented as a function of the relative distance to criticality for different values of α_p. The dashed curve represent the Newtonian case, the continuous curves the pseudoplastic case and the dotted curves the dilatant case. This figure shows the pseudoplastic fluid convection amplitude behaviour when α_p increases and approaches the tricritical point $\alpha_p = \alpha_p^{tr}$. From this figure it il clear also that convection in pseudoplastic fluids is stronger when compared to both Newtonian and dilatant fluids. On the other hand, the dilatant fluid convection amplitude decreases with the bifurcation parameter α_p.

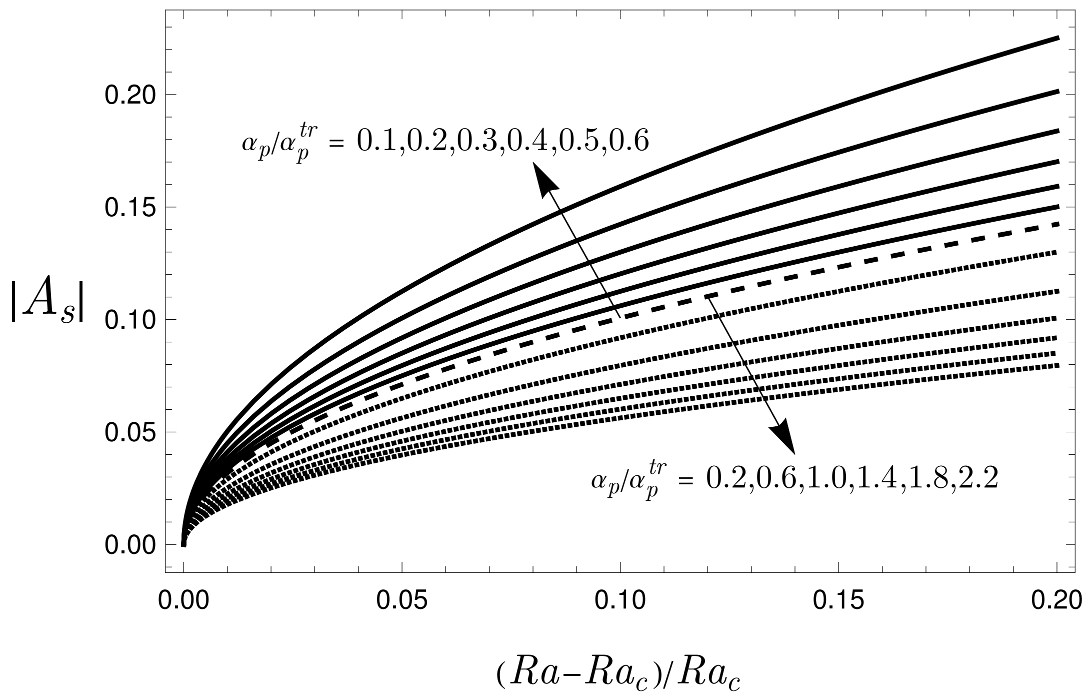

Figure 7.2: Finite amplitude of supercritical instability versus the relative distance to criticality. Continuous curves correspond to pseudoplastic fluids, the single dashed curve corresponds to the Newtonian case while the dotted curves below correspond to the dilatant fluids. The arrows indicate the direction in which α_p grows.

For pseudoplastic fluids, when $\alpha_p > \alpha_p^{tr}$, the bifurcation is subcritical and the cubic amplitude Equation (7.48) is not able to provide any stable finite amplitude equilibrium.

Therefore, in order to obtain such an equilibrium solution it would be necessary to extend the analysis up to higher orders.

The Nusselt number represents the total heat transfer through the fluid layer induced by convection and conduction normalised by its conductive contribution. The mean Nusselt number N evaluated at $z = 0$ can be given by

$$Nu \,=\, 1- < \left(\frac{\partial \tilde{T}}{\partial z}\right)_{z=0} >, \tag{7.56}$$

where $< \cdot >$ stands for the horizontal average over one wavelength of the quantity being averaged. By applying this definition, one has

$$\begin{aligned} Nu - 1 \,&=\, \left[\frac{Ra \,-\, Ra_c}{Ra_c}\right] \frac{2}{(1 \,\pm\, 10\,\pi^2\,\alpha_p)} \\ &=\, \frac{(Nu^N - 1)}{(1 \,\pm\, 10\,\pi^2\,\alpha_p)}, \end{aligned} \tag{7.57}$$

where Nu^N represents the Nusselt number for Newtonian fluids,

$$Nu^N - 1 \,=\, 2\left[\frac{Ra \,-\, Ra_c}{Ra_c}\right], \tag{7.58}$$

which is the same as that derived by Joseph [72].

In analogy with Figure 7.2, Figure 7.3 shows the Nusselt number for Newtonian, pseudoplastic and dilatant fluids as a function of the relative distance to criticality for different values of α_p. The Newtonian case is presented for comparison purposes. The dashed, continuous and dotted curves correspond to the Newtonian, pseudoplastic and dilatant fluids, respectively. It is to be noted that the heat transfer is always stronger in a pseudoplastic fluid convection, compared to both the Newtonian and the dilatant fluids. This was expected from the convection amplitude results. Following the definition (7.51) for α_p, one can say that heat transfer is quite intense for strongly shear–thinning fluids and for weakly permeable porous media. The opposite trend holds for dilatant fluids.

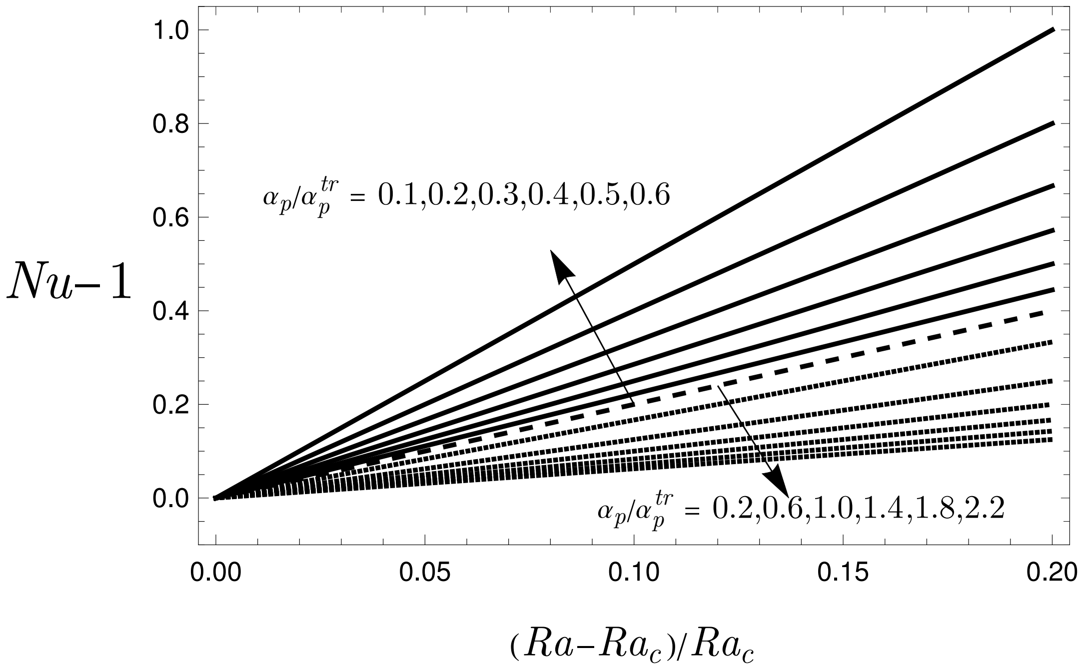

Figure 7.3: Convective Nusselt number versus the relative distance to criticality. Continuous curves correspond to pseudoplastic fluids, the single dashed curve in the center corresponds to the Newtonian fluid and the dotted curves below correspond to the dilatant fluids. The arrows indicate the direction in which α_p grows.

Figure 7.4 presents the disturbance isotherms for pseudoplastic fluids, considering a single convective cell in the spatial domain. The results are relative to the linear disturbance solution (a), the nonlinear correction, computed from the nonlinear stability analysis (b) and the total temperature field (c), including the basic solution. The magnitude of the streamfunction and temperature fields depend on the relative distance to criticality and on the value of α_p. Here, the prescribed values of these two parameters are, respectively, $\frac{Ra-Ra_c}{Ra_c} = 0.1$ and $\alpha_p = 0.5\alpha_p^{tr}$. From Figure 7.4 (b), it can be seen that the nonlinear interaction distorts the linear fundamental mode and breaks the symmetry with respect to the vertical and horizontal midplanes.

Figure 7.5 shows the convective cell pattern in terms of streamfunction (continuous curves) and the total temperature field (dashed curves) isocontours. The results are shown for both pseudoplastic (a) and dilatant (b) fluids. In this figure, the streamlines are seen to be equally spaced between $\psi = 0$, at the horizontal boundaries, and the maximum value which lies at the center of the cell. The isotherms are qualitatively similar to the Newtonian case and consist of hot ascending and cold descending plumes. The results for dilatant fluids are qualitatively similar.

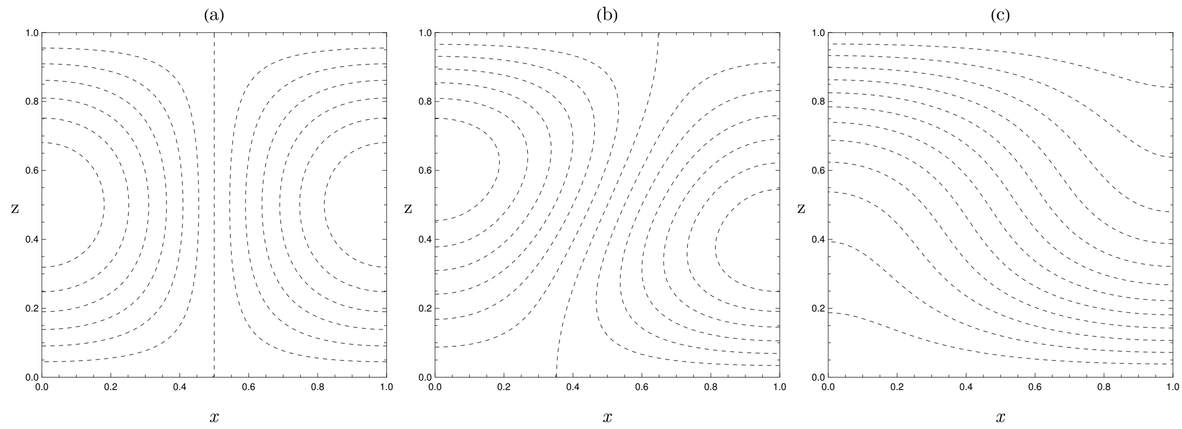

Figure 7.4: Disturbance isotherm patterns for pseudoplastic fluids obtaianed by linear stability (a) and nonlinear stability (b). The total temperature field including the conductive state is represented in (c). The prescribed parameters are $\frac{Ra-Ra_c}{Ra_c} = 0.1$ and $\alpha_p = 0.5\alpha_p^{tr}$.

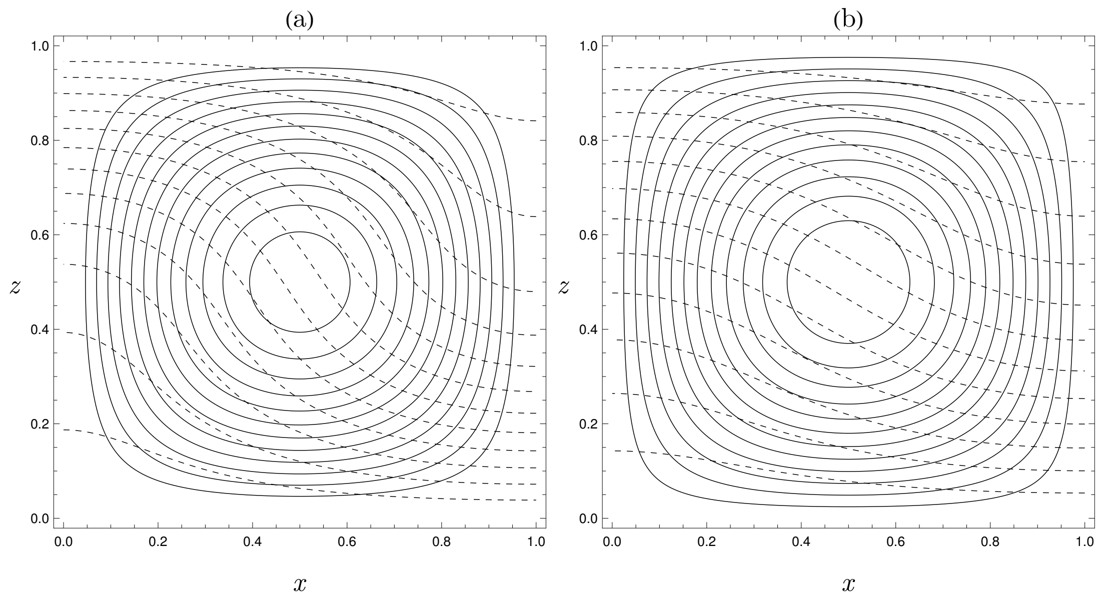

Figure 7.5: Streamline and isotherm patterns obtained for pseudoplastic (a) and dilatant (b) fluids at $\frac{Ra-Ra_c}{Ra_c} = 0.1$ and $\alpha_p = 0.5\alpha_p^{tr}$.

For non–Newtonian fluids, the dimensionless apparent viscosity is modified spatially when convection takes place, in contrast to the Newtonian case, where it is uniform and equal to one. Figures 7.6 show the isolines of apparent viscosity for pseudoplastic (a) and dilatant (b) fluids. As expected, the local apparent viscosity μ_a in the presence of convection is smaller for pseudoplastic fluids and higher for dilatant fluids, when compared to the Newtonian fluids. Both figures indicate that $\mu_a \sim 1$ near the the center of the cell and near the corners, which is a consequence of small convective velocities at these regions. It can be seen also that the minimum of the apparent viscosity for pseudoplastic fluids is observed at both the middle of the horizontal and of the vertical boundaries of the cell. The opposite is true for dilatant fluids.

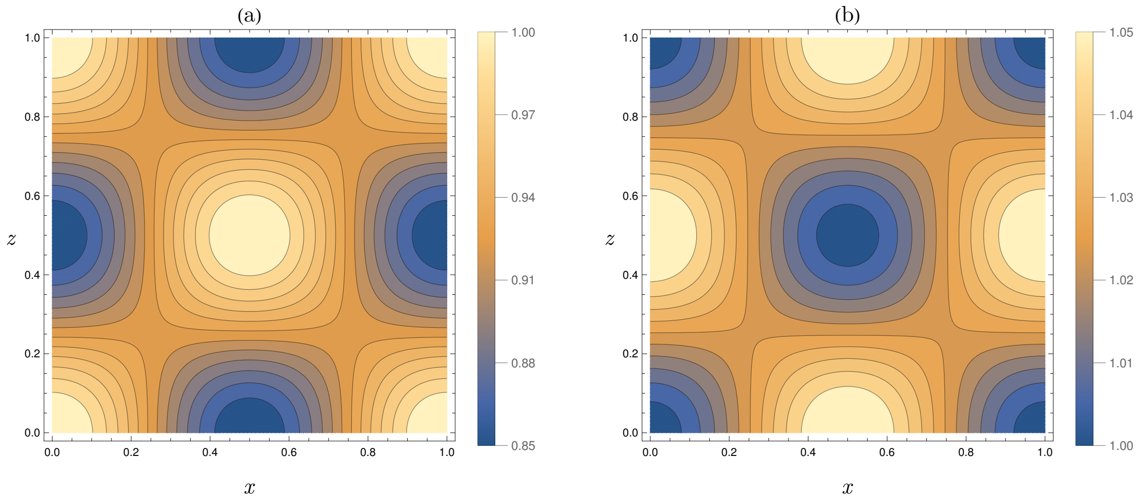

Figure 7.6: Apparent viscosity isolines for pseudoplastic (a) and dilatant (b) fluids at $\frac{Ra-Ra_c}{Ra_c} = 0.1$ and $\alpha_p = 0.5\alpha_p^{tr}$

7.5 Conclusions

A novel rheological model for the apparent viscosity of non–Newtonian inelastic fluids saturating porous media was proposed here. This model can be seen as an extension of the well known Carreau model for clear fluids to porous media, thus it is called Darcy–Carreau model. Compared with the model which is usually considered in the literature, namely the power–law model, the present model displays substantial differences especially in the limit of small seepage velocities. Since the stability investigations are often focused on the onset of convection, such a difference may have important implications.

Linear stability results pointed out that the instability threshold for non–Newtonian fluids considered here is exactly the same as the instability threshold for Newtonian fluids. Although this result is not new for dilatant fluids, as it was already pointed out by Nield [104], the present Darcy–Carreau model is able to conclude the same thing for pseudoplastic fluids.

The nonlinear disturbances behaviour has been investigated by using the weakly nonlinear theory. The effect of the two nonlinear terms in the governing equations, namely the advection and non–Newtonian apparent viscosity terms, have been determined. It is shown that the nonlinear effects depend on a single dimensionless parameter $\alpha_p(n, \lambda, Da, \Phi)$, which is proportional to the characteristic time of the fluid λ and is inversely proportional to the properties of the porous medium, Da and Φ.

Considering that increasing the bifurcation parameter α_p means physically making stronger the non–Newtonian nature of the fluids or decreasing the permeability of the porous medium, the main results obtained from this analysis may be summarized in the following way:

- For dilatant fluids, the bifurcation from the conductive state to the convective state is always supercritical and it does not depend on α_p. The amplitude of the convective rolls and the average convective heat flux decrease as α_p increases.

- For pseudoplastic fluids, the nature of the bifurcation depends on the parameter α_p, in such a way that when $\alpha_p < \alpha_p^{tr}$ the bifurcation is supercritical and if $\alpha_p > \alpha_p^{tr}$ it is subcritical. Such a result can be interpreted physically as competition between the nonlinear advective term and the nonlinear non–Newtonian apparent viscosity term. While the former tends to induce a supercritical bifurcation, the latter one promotes a subcritical bifurcation. In the case of a supercritical bifurcation, it has been found that, by increasing α_p, the amplitude of the convective rolls increases and the average heat flux is enhanced.

Chapter 8

A Darcy–Carreau–Yasuda model for non–Newtonian mixed convection in porous media

8.1 Introduction

As already commented in the last chapter, there has been a substantial increase in the interest for the study of thermal instabilities in non–Newtonian fluid saturated porous media. Either viscous or viscoelastic rheology has been taken into account in the last years [12, 4, 62, 127, 5, 37]. By considering non–Newtonian viscous fluids, one can say that the simplest rheological model is the power–law model.

Again, one can mention that, in the limit of vanishing throughflow, the power–law model presents a singularity which emerges in the stability analysis. By considering the Darcy-Bénard problem without throughflow, the linear stability results show that the problem is always stable for shear–thinning fluids and always unstable for shear–thickening fluids. The limitations of the power–law model for the analysis of the onset of the Darcy-Bénard convection were already pointed out by Nield [103, 104]. In order to overcome these limitations, Brandão and Ouarzazi proposed in a recent paper [26] a novel Darcy–Carreau rheological model for the apparent viscosity of non-Newtonian inelastic fluids flowing through a porous medium.

Recently, Petrolo et al. [110] performed a set of experiments in a Hele–Shaw cell to investigate both the instability threshold as well as the convective patterns considering pseudoplastic fluids with non–zero flow rates. The experiments were conducted considering Xanthan Gum mixtures with different concentrations as working fluids. Moreover, a two–dimensional linear stability analysis is proposed in that study. The fluid is considered to be of power–law type with a temperature dependent consistency index. Comparison between linear stability analysis and experiments pointed out a good agreement between theory and experiments concerning the critical wavenumber of the instability and a not so good agreement between theory and experiments for the critical Rayleigh number.

The objective of the present study is to revisit the Rayleigh-Bénard problem with non–zero flow rates in porous media as well as in a Hele-Shaw cell. Here, the Darcy–Carreau model considered in the last Chapter, as well in the paper by Brandão and Ouarzazi [26], is extended to a Darcy–Carreau–Yasuda model, which is the application of the Carreau–Yasuda model [134] to saturated porous media. Such a model includes the power–law behaviour in the limit of sufficiently high values of shear rate and the Newtonian behaviour in the limit of small values of shear rate. The Carreau–Yasuda model contains five parameters that allow the interpretation of the fluid rheology from the experimental results (see Section 8.4.2). Figure 8.1 shows the viscosity distribution as a function of the shear rate predicted by both the Carreau–Yasuda and the power-law models with the measured viscosity data [110]. It can be seen from this figure that the power law model overestimates the apparent viscosity in the limit of small shear rate, that is the region where the thermal instability is observed experimentally.

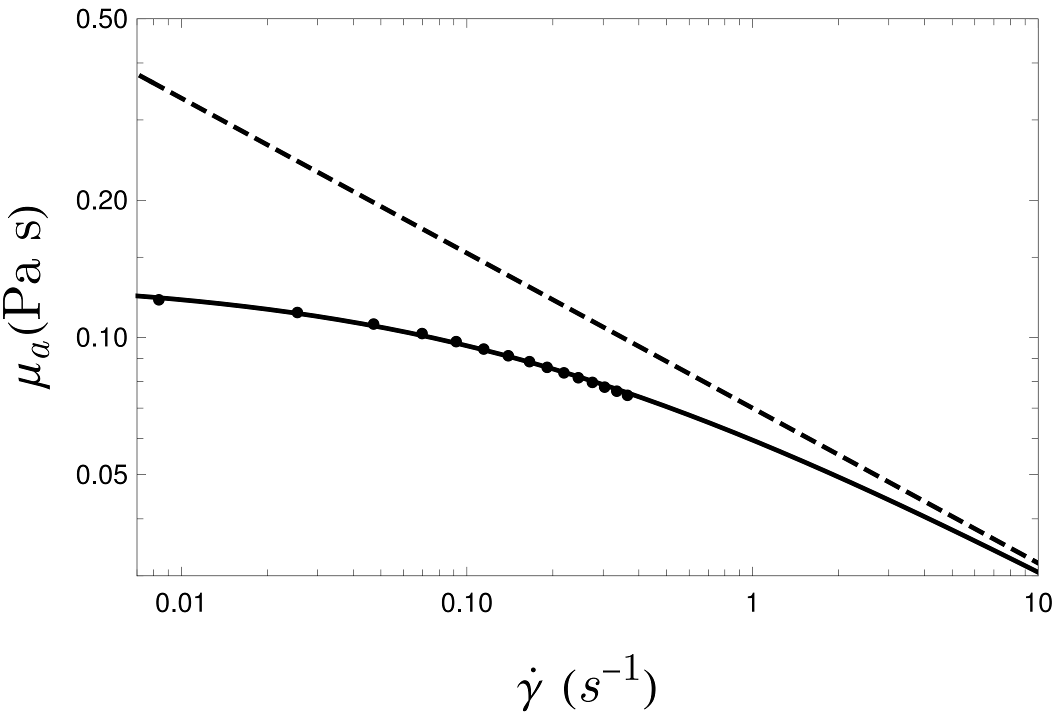

Figure 8.1: Measured data (points) of Experiment 4 extracted from [110] and fitted Carreau–Yasuda rheological model (continuous line). The dashed line represents the power–law predictions.

The contents of this chapter are based on the paper by Brandão, P. V., Ouarzazi,

M. N., Hirata, S. da C. and Barletta, A., Darcy–Carreau–Yasuda rheological model and onset of inelastic non–Newtonian mixed convection in porous media, Physics of Fluids, doi:10.1063/5.0048143 [29].

8.1.1 Darcy–Carreau–Yasuda rheological model

In the previous Chapter, the issues involving the power–law model in the limit of small shear rate were already discussed. For porous media, the apparent viscosity of the fluid can be written as in Equation (7.1). For clear fluids, the apparent fluid viscosity is given by

$$\mu_a \,=\, \eta\,\dot{\gamma}^{n-1}. \tag{8.1}$$

For fluid saturated porous media, after integrating over a representative elementary volume, the power–law model introduces the apparent viscosity as given by Equation (7.1)

$$\mu_a \,=\, \eta_{ef}\,|\mathbf{u}|^{n-1}, \tag{8.2}$$

where η_{ef} is the effective consistency factor and $\mathbf{u}$ is the seepage velocity.

From the expressions (8.1) and (8.2) of the apparent viscosity μ_a, it is possible to define the shear rate $\dot{\gamma}_p^*$ for porous media flows as

$$\dot{\gamma}_p^* \,=\, \left(\frac{\eta_{ef}}{\eta}\right)^{\frac{1}{n-1}}\,|\mathbf{u}|. \tag{8.3}$$

The ratio $\frac{\eta_{ef}}{\eta}$, in general, depends on the permeability of the medium K, the power–law index n and on the porosity of the medium Φ. An expression of this ratio was already used by many authors as, for instance, Pascal et al. [108] and Longo et al. [89]. It is given by,

$$\frac{\eta_{ef}}{\eta} \,=\, f_p\,(\Phi\,K)^{\frac{1-n}{2}}, \tag{8.4}$$

where $f_p \,=\, 8^{(-\frac{n+1}{2})}\,2\,(\frac{3n+1}{n})^n$.

Thus, the porous shear rate (8.3) can be written as

$$\dot{\gamma}_p \,=\, f_p^{\frac{1}{n-1}}\,(\Phi\,K)^{-\frac{1}{2}}\,|\mathbf{u}|. \tag{8.5}$$

The power–law model gives singular values of the apparent viscosity for zero shear rates. Namely, it gives infinite for shear–thinning ($n < 1$) fluids and zero for shear–thickening ($n > 1$) fluids. To deal with these singularities in clear fluids, a regularized form of the power–law model may be used, namely the Carreau–Yasuda model, which is given by

$$\frac{\mu - \mu_\infty}{\mu_0 - \mu_\infty} \,=\, (1 \,+\, (\lambda^*\dot{\gamma})^a)^{\frac{n-1}{a}}, \tag{8.6}$$

which reduces to (7.3) in the case of $a = 2$, where the positive constant a is the Yasuda parameter that represents the transition between the region of small values of shear rate and the power-law region. The constant μ_∞ is the infinite shear rate viscosity and λ^* is the characteristic time of the non-Newtonian fluid defined as in Equation (7.4),

$$\lambda^* = (\frac{\eta}{\mu_0})^{\frac{1}{n-1}}. \tag{8.7}$$

Usually, μ_∞ can be neglected [2] and then the Carreau–Yasuda model reduces to

$$\frac{\mu}{\mu_0} = (1 + (\lambda^* \dot{\gamma})^a)^{\frac{n-1}{a}}. \tag{8.8}$$

Similarly, the singularities of the power–law model for porous media may be avoided in the limit of zero seepage velocity $\mathbf{u}$ by adopting the so–called Darcy–Carreau–Yasuda model

$$\frac{\mu}{\mu_0} = \left(1 + \left(\frac{\eta_{ef}}{\mu_0}\right)^{\frac{a}{n-1}} |\mathbf{u}|^a\right)^{\frac{n-1}{a}}. \tag{8.9}$$

Similar to the Darcy–Carreau model presented in the last Section, given by (7.6), in the limit of high values of seepage velocities the power–law model (8.2) is recovered. Also, in the limit of vanishing seepage velocities the fluid behaves as a Newtonian one and the viscosity takes a finite non-zero value $\mu = \mu_0$ independently of n.

By taking into consideration the characteristic time of the fluid λ^* defined by (7.4), and reproduced in (8.7), and the ratio $\frac{\eta_{ef}}{\eta}$ defined by (7.7), and reproduced in (8.4), the Darcy–Carreau–Yasuda model (8.9) may be written as

$$\frac{\mu_a}{\mu_0} = \left(1 + (\lambda^* \dot{\gamma}_p^*)^a\right)^{\frac{n-1}{a}}. \tag{8.10}$$

For practical reasons, it can be of interest to write the Darcy–Carreau–Yasuda model as a function of the fluid and the porous medium properties. The generalized Darcy–Carreau–Yasuda model (8.10) is given by

$$\frac{\mu_a}{\mu_0} = \left(1 + (\lambda^* f_p^{\frac{1}{n-1}} (\Phi K)^{-\frac{1}{2}} |\mathbf{u}|)^a\right)^{\frac{n-1}{a}}. \tag{8.11}$$

8.1.2 Governing equations

An isotropic and homogeneous porous channel of height H and infinite extension in the horizontal direction is considered. The porous matrix is saturated by a shear–thinning or shear–thickening fluid and it is moving at a constant velocity u_0 in the x direction. The system is heated from below and cooled from above. The upper and lower horizontal walls are considered impermeable and are kept at constant temperatures

$T_0 + \Delta T$ and T_0, respectively. The Oberbeck-Boussinesq approximation is considered to hold here. The apparent viscosity is modelled by the Darcy–Carreau–Yasuda model (8.11). The mass balance, momentum balance and energy balance equations, as well as the Darcy–Carreau–Yasuda rheological model, can thus be written as

$$\nabla \cdot \mathbf{u} = 0, \tag{8.12}$$

$$\frac{\mu_a}{K}\,\mathbf{u} + \nabla p - \rho_0\,\beta\,(T - T_0)\mathbf{g} = 0, \tag{8.13}$$

$$\sigma\,\frac{\partial T}{\partial t} + \mathbf{u}\cdot\nabla T = \chi\,\nabla^2 T, \tag{8.14}$$

$$\frac{\mu_a}{\mu_0} = \left(1 + (\lambda^*\, f_p^{\frac{1}{n-1}}\,(\Phi\, K)^{-\frac{1}{2}}\,|\mathbf{u}|)^a\right)^{\frac{n-1}{a}}, \tag{8.15}$$

subject to the following boundary conditions at the horizontal walls

$$z = 0: \quad w = 0, \quad T = T_0 + \Delta T, \tag{8.16a}$$

$$z = H: \quad w = 0, \quad T = T_0. \tag{8.16b}$$

with $\mathbf{u} = (u, v, w)$ being the velocity field, T the temperature field, p the hydrostatic pressure field, μ_a the apparent dynamic viscosity, μ_0 the dynamic viscosity at the zero shear rate, χ the effective thermal diffusivity, β the fluid thermal expansion coefficient, K the permeability, ρ_0 the fluid density ate the reference temperature T_0, σ is the ratio between the average volumetric heat capacity of the saturated porous medium and the volumetric heat capacity of the fluid, respectively and $\mathbf{g}$ the gravity acceleration with modulus g.

Considering the energy equation (8.14) and the boundary conditions (8.16), a possible basic solution for the temperature is one that leads to a linear vertical thermal stratification:

$$T_b - T_1 = (1 - z/H)(T_0 - T_1), \tag{8.17}$$

A horizontal throughflow is imposed,

$$\mathbf{u}_b = u_0\,\mathbf{e}_x, \tag{8.18}$$

which implies, according to (8.15), a variation of the basic apparent viscosity of the form,

$$\frac{\mu_{a(b)}}{\mu_0} = \left(1 + \left(\lambda^*\, f_p^{\frac{1}{n-1}}\,(\Phi\, K)^{-\frac{1}{2}}\,u_0\right)^a\right)^{\frac{n-1}{a}}. \tag{8.19}$$

According to the definition of the porous shear rate, given by (8.5), the basic shear rate for porous media is $\dot\gamma_{p_b} = f_p^{\frac{1}{n-1}}\,(\Phi\, K)^{-\frac{1}{2}}\,u_0$. Hence, the term $\lambda^*\, f_p^{\frac{1}{n-1}}\,(\Phi\, K)^{-\frac{1}{2}}\,u_0$ is the product of the basic porous shear rate $\dot\gamma_{p_b}$ and the characteristic time λ^* of the fluid. This product, is known as the Weissenberg number in the literature about non–Newtonian clear fluids. Since we consider here that the non–Newtonian fluid is saturating a porous medium, a Darcy-Weissenberg number can be defined as,

$$Wi = \lambda^* \dot{\gamma}_{p_b}, \tag{8.20}$$

which may be seen as a measure of the influence of non-Newtonian forces on the fluid flow. By introducing this number, Equation (8.19) can be reduced to,

$$\frac{\mu_{a(b)}}{\mu_0} = (1 + Wi^a)^{\frac{n-1}{a}}. \tag{8.21}$$

The influence of the non–Newtonian character of the fluid on the apparent viscosity depends on Wi, n and a. The special cases of $n = 1$ or $\lambda^* = 0$, which implies $Wi = 0$, is correspondent to a Newtonian fluid with viscosity μ_0, independently of u_0. Prats [111] has demonstrated that, in this case, the instability threshold, as well as the instability pattern, do not depend on the flow–rate..

In the limit of zero flow–rate, the Darcy-Weissenberg number is zero, and according to (8.21), the viscosity is constant and equal to the viscosity μ_0 as well. Therefore, we can expect that, in this limit, the non–Newtonian fluid behaves as a Newtonian fluid.

Figures 8.2 and 8.3 show the variation of $\frac{\mu_{a(b)}}{\mu_0}$ as a function of Wi for $a = 2$ (*i.e.* Darcy–Carreau model (7.6)). Different values of n are considered, for both pseudoplastic and dilatant fluids. Figure 8.2 shows that an increase in the Darcy-Weissenberg number, for a fixed value of n, means a decrease in the apparent viscosity. Such a decrease is more effective for small values of n, that is when the fluid is more shear–thinning. The opposite is true for dilatant fluids.

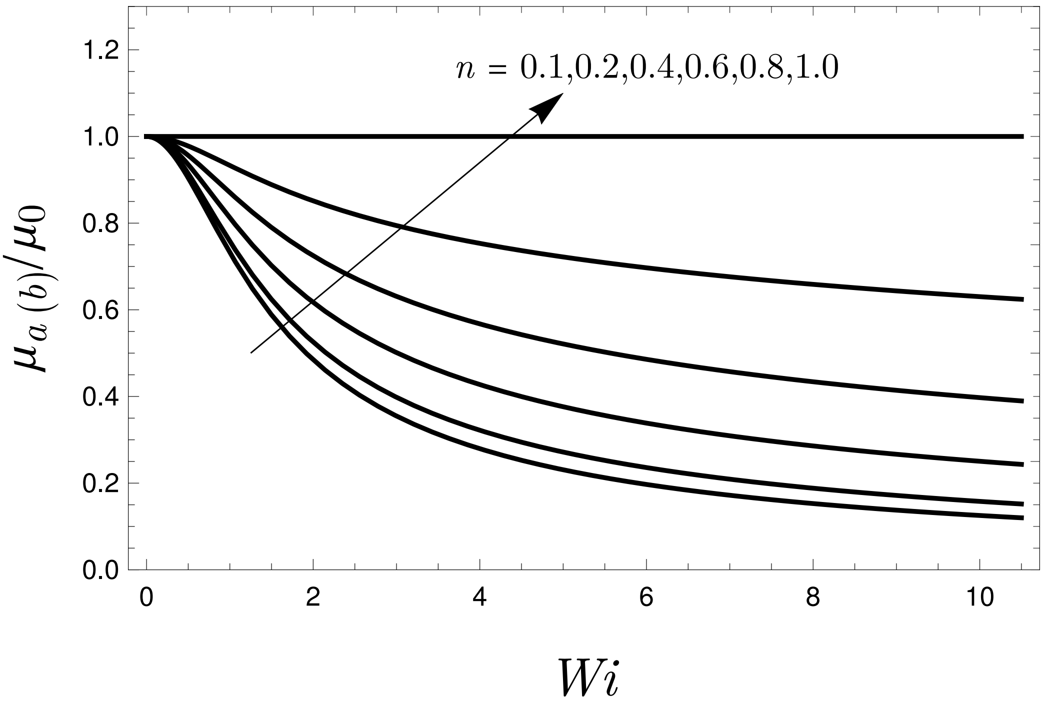

Figure 8.2: Apparent viscosity normalised by the viscosity at zero shear rate μ_0 versus Darcy-Weissenberg number for $a = 2$ and different values of n: pseudoplastic fluids.

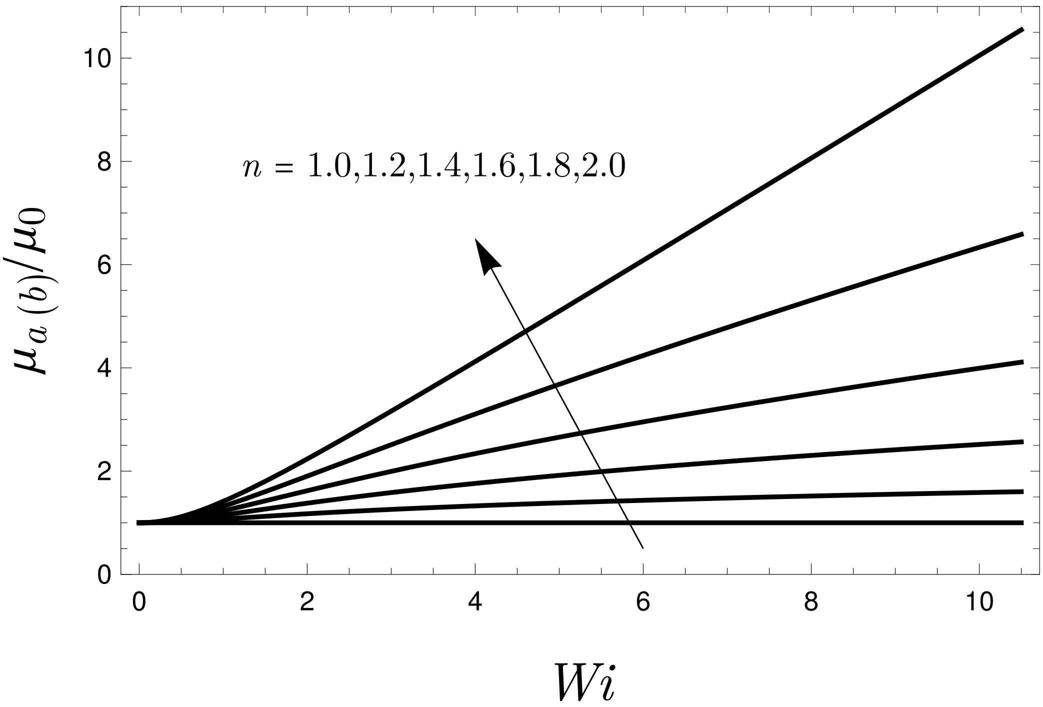

Figure 8.3: Apparent viscosity normalised by the viscosity at zero shear rate μ_0 versus Darcy-Weissenberg number for $a = 2$ and different values of n: dilatant fluids

The influence of the Yasuda parameter a on the apparent viscosity may be significant when $Wi \to 0$ or $Wi = \mathcal{O}(1)$. When $Wi \gg 1$, Equation (8.21) yields,

$$\frac{\mu_{a(b)}}{\mu_0} = Wi^{\,n-1}. \tag{8.22}$$

In this limit, the apparent viscosity is given by the power-law model and it does not depend on the Yasuda parameter a.

From Eq.(8.13), it is possible to observe that also the horizontal basic pressure gradient is influenced by the non–Newtonian nature of the fluid,

$$-\frac{\partial p_b}{\partial x} = \frac{\mu_0}{K}\,(1 + Wi^a)^{\frac{n-1}{a}}\,u_0. \tag{8.23}$$

Moreover, the buoyancy force generates a vertical pressure gradient,

$$\frac{\partial p_b}{\partial z} = -\rho_0\,\beta\,(1 - z/H)\,(T_0 - T_1). \tag{8.24}$$

8.2 Dimensionless equations and linear stability analysis

8.2.1 Dimensionless equations

The following dimensionless quantities are introduced

$$\frac{1}{H}(x,y,z) \to (x,y,z), \qquad \frac{H}{\chi}\mathbf{u} \to \mathbf{u}, \qquad \frac{\chi}{\sigma H^2}t \to t,$$
$$\frac{T-T_0}{\Delta T} \to T, \qquad \frac{K}{\chi \mu_0}p \to p, \tag{8.25}$$

which allow one to write the governing equations in their dimensionless form as follows

$$\nabla \cdot \mathbf{u} = 0, \tag{8.26}$$

$$(1 + (\alpha\,|\mathbf{u}|)^a)^{\frac{n-1}{a}}\,\mathbf{u} + \nabla p = Ra\,T\,\mathbf{e}_z, \tag{8.27}$$

$$\frac{\partial T}{\partial t} + \mathbf{u}\cdot\nabla T = \nabla^2 T, \tag{8.28}$$

where $\alpha = \lambda^* f_p^{\frac{1}{n-1}}\,(\Phi\,K)^{\frac{-1}{2}}\,\chi/H$. For a finite Pe, one can write

$$\alpha = \frac{Wi}{Pe}. \tag{8.29}$$

The dimensionless version of the boundary conditions is given by

$$z = 0: \quad w = 0, \quad T = 1, \tag{8.30a}$$

$$z = H: \quad w = 0, \quad T = 0. \tag{8.30b}$$

The basic solution may be written in dimensionless form as

$$T_b = 1 - z, \tag{8.31}$$

$$\mathbf{u}_b = \{Pe, 0, 0\}, \tag{8.32}$$

$$\nabla p_b = -\,(1 + Wi^a)^{\frac{n-1}{a}}\,Pe\,\mathbf{e}_x + Ra\,T_b\,\mathbf{e}_z. \tag{8.33}$$

The Rayleigh Ra and the Péclet Pe number are introduced, and their definitions are given by

$$Ra = \frac{\rho_0 K H g \beta \Delta T}{\chi \mu_0}, \tag{8.34}$$

and

$$Pe = \frac{u_0\,H}{\chi}. \tag{8.35}$$

8.2.2 Linearised equations

To investigate the stability of the present equilibrium solution, the physical quantities are split into a basic part and another one relative to the infinitesimal disturbances (see Section 3.2),

$$\mathbf{u} = \mathbf{u}_b + \tilde{\mathbf{u}}(x, y, z, t),$$
$$T = T_b + \tilde{T}(x, y, z, t), \quad p = p_b + \tilde{p}(x, y, z, t). \tag{8.36}$$

By substituting the decomposed quantities (8.36) into (8.26)–(8.28), and by neglecting nonlinear terms for the disturbances, one has the linearised governing equations for the disturbances. In order to simplify the analysis, one may apply the curl operator to get rid of the pressure field in the equations. Thus, by manipulating the equations, it is possible to obtain the linearised governing equations for the disturbances in terms of the vertical disturbance velocity and the disturbance temperature, namely

$$(1 + Wi^a)^{\frac{n-1}{a}} \left[\nabla^2 - \frac{(n-1)\,Wi^a}{1 + n\,Wi^a}\frac{\partial^2}{\partial x^2}\right]\tilde{w} - Ra\left[\nabla_2^2 - \frac{(n-1)\,Wi^a}{1 + n\,Wi^a}\frac{\partial^2}{\partial x^2}\right]\tilde{T} = 0, \tag{8.37a}$$

$$\frac{\partial \tilde{T}}{\partial t} + Pe\frac{\partial \tilde{T}}{\partial x} - \tilde{w} - \nabla^2\tilde{T} = 0, \tag{8.37b}$$

with ∇_2^2 being the two–dimensional Laplacian in the (x, y) plane. The equations are subject to the boundary conditions

$$z = 0, 1: \quad \tilde{w} = 0 = \tilde{T}. \tag{8.38}$$

8.2.3 Dominant modes

The three-dimensional disturbance quantities $\tilde{w}(x, y, z, t)$ and $\tilde{T}(x, y, z, t)$, satisfying the boundary conditions (8.30), can be expressed as

$$[\tilde{w}, \tilde{T}] = \left[\hat{w}, \hat{T}\right] \exp(ik_x x + ik_y y - i\,\omega t)\sin(\pi z) \tag{8.39}$$

where k_x and k_y are the wavenumbers in the streamwise and spanwise direction, respectively, and ω is the complex frequency. Its imaginary part $\mathrm{Im}[\omega]$ and real part $\mathrm{Re}[\omega]$ represent, respectively, the temporal growth rate and the oscillation frequency of the disturbance modes.

The neutral stability condition is obtained by imposing $\mathrm{Im}[\omega] = 0$, which selects the most unstable modes at the onset of convection, that is the first ones to experiment the transition to instability. By substituting Equations (8.39) into (8.37), the dispersion relation of the disturbances are obtained

$$\mathcal{D}\left(k_x, k^2, Ra, \mathrm{Re}\left[\omega\right], Wi, n, a\right) = 0, \tag{8.40}$$

where $k^2 = k_x^2 + k_y^2$. From the imaginary part of the dispersion relation is obtained that the exchange of instability holds, that is $\mathrm{Re}[\omega] = k_x\, Pe$. By considering this result, the real part of the dispersion relation yields

$$\left(k^2 + \pi^2\right)\left(1 + Wi^a\right)^{\frac{n-1}{a}}\left[-\left(k^2 + \pi^2\right) + \frac{(n-1)\, Wi^a}{1 + n\, Wi^a} k_x^2\right] - Ra\left[-k^2 + \frac{(n-1)\, Wi^a}{1 + n\, Wi^a} k_x^2\right] = 0 \tag{8.41}$$

From (8.41) it is possible to recover an explicit expression for Ra in the threshold of instability, namely

$$Ra = \left(k^2 + \pi^2\right)\left(1 + Wi^a\right)^{\frac{n-1}{a}}\left(1 + \frac{\pi^2\left(1 + n\, Wi^a\right)}{k^2\left(1 + n\, Wi^a\right) - (n-1)k_x^2 Wi^a}\right) \tag{8.42}$$

It is also possible to rewrite Equation (8.42) by adopting the relation $k_x = k\cos(\phi)$. In that case, $\phi = 0$ represents the transverse instability rolls, while $\phi = \pi/2$ represents the longitudinal ones. If $0 < \phi < \pi/2$ one has the oblique rolls. For an assigned parametric combination, (Wi, n, a), the neutral stability condition is represented by computing the value of Ra that satisfies the condition, for each value of k and ϕ. For each value of k there is a corresponding value of Ra relative to the neutral stability condition. The minimum value of Ra over all values of k is known as the critical value of Ra or Ra_c. Mathematically, this means that the derivative of (8.42) with respect to k must be zero. The critical value of the wavenumber is given by

$$k_c = \pi\left[\frac{1 + nWi^a}{1 + Wi^a\left(n + (1-n)\cos^2(\phi)\right)}\right]^{\frac{1}{4}}, \tag{8.43}$$

while Ra_c is given by

$$Ra_c = \pi^2\left(1 + Wi^a\right)^{\frac{n-1}{a}}\left[1 + \left(\frac{1 + nWi^a}{1 + Wi^a\left(n + (1-n)\cos^2(\phi)\right)}\right)^{\frac{1}{2}}\right]^2. \tag{8.44}$$

In addition to the dependence on n and Wi, Ra_c depends also on the angle ϕ. The linear pattern selection is the determination of the must unstable type of rolls, that is the value of ϕ that returns the lowest value of Ra. From Equation (8.44), it can be seen that the dependence of the neutral condition on ϕ appears just in one term. The role of its dependence changes depending on the value of n. Equation (8.44) can be rewritten as

$$Ra_c = \pi^2 (1 + Wi^a)^{\frac{n-1}{a}} \left[1 + \left(\frac{1 + nWi^a}{1 + Wi^a\, h(n,\phi)} \right)^{\frac{1}{2}} \right]^2, \tag{8.45}$$

where

$$h(n,\phi) = n + (1-n)\cos^2(\phi). \tag{8.46}$$

By looking at Equation (8.46), one can study the linear pattern selection of the problem. If $n = 1$, the results are independent of ϕ and thus $h(1,\phi) = 1$. For $n \neq 1$, the maximum of $h(n,\phi)$ represents the minimum of Ra_c. Figure 8.4 shows the dependence of the function $h(n,\phi)$ on n, considering transverse ($\phi = 0$), oblique ($\phi = \pi/4$) and longitudinal rolls $\phi = \pi/2$. It is clear that transverse rolls are the most unstable modes for $n < 1$, while for $n > 1$ longitudinal rolls become the dominant ones. Oblique rolls, represented here by $\phi = \pi/4$, are always intermediate.

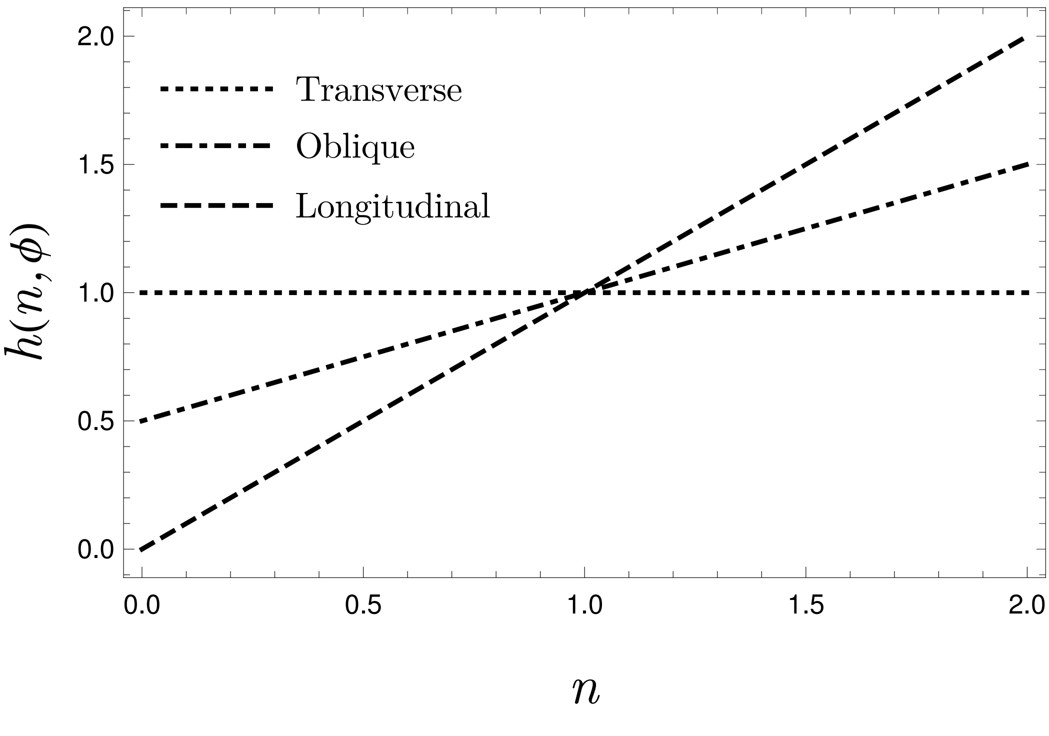

Figure 8.4: Function $h(n,\phi)$ as a function of n for transverse, oblique and longitudinal rolls

.

Thus, the expressions for Ra_c and k_c can be simplified considering the specific cases of transverse and longitudinal cases. They are given, respectively, by

$$Ra_c^T = \pi^2 \left(1 + Wi^a\right)^{\frac{n-1}{a}} \left[1 + \left(\frac{1 + nWi^a}{1 + Wi^a}\right)^{\frac{1}{2}}\right]^2, \tag{8.47a}$$

$$k_c^T = \pi \left[\frac{1 + nWi^a}{1 + Wi^a}\right]^{\frac{1}{4}}, \tag{8.47b}$$

and

$$Ra_c^L = 4\pi^2 \left(1 + Wi^a\right)^{\frac{n-1}{a}}, \tag{8.48a}$$

$$k_c^L = \pi. \tag{8.48b}$$

It can be useful to look at the the critical values of Ra and k in the limit of large Darcy-Weissenberg number ($Wi \gg 1$). In the limit of very large values of Wi, Equations (8.47a), (8.47b) and (8.48a) become

$$Ra_c^T = \pi^2 \left(1 + n^{\frac{1}{2}}\right)^2 (Wi)^{n-1}, \tag{8.49a}$$

$$k_c^T = \pi\, n^{\frac{1}{4}}, \tag{8.49b}$$

$$Ra_c^L = 4\pi^2 (Wi)^{n-1}. \tag{8.49c}$$

By replacing Wi in Equations (8.49a) and (8.49c) by its expression,

$$Wi = \lambda^* f_p^{\frac{1}{n-1}} (\Phi\, K)^{\frac{-1}{2}} u_0 = \left(\frac{\eta_{ef}}{\mu_0}\right)^{\frac{1}{n-1}} \frac{\chi}{H} Pe, \tag{8.50}$$

and by defining a Rayleigh number based on the power–law model Ra^{pl}, as it is usually employed by many authors in the literature (see, for instance, Barletta and Nield [12] and Petrolo et al. [110]),

$$Ra^{pl} = \frac{\beta\, g\, K\, H^n\, \Delta T}{\eta_{ef}\, \chi^n}. \tag{8.51}$$

Equations (8.49a) and (8.49c) can be rewritten as

$$Ra_c^{pl\,T} = \pi^2 \left(1 + n^{\frac{1}{2}}\right)^2 (Pe)^{n-1}, \tag{8.52a}$$

and

$$Ra_c^{pl\,L} = 4\pi^2 (Pe)^{n-1}. \tag{8.52b}$$

The critical value of Rayleigh number based on the definition (8.51), and the corresponding critical wavenumbers (8.49b) and (8.48b), correspond exactly with the results obtained by Barletta and Nield [12]. Such a result demonstrates that the theoretical results coming from the power–law rheological model are recovered by using the Darcy–Carreau–Yasuda model in the limit of large values of Darcy-Weissenberg number. In this limit, the flow behaviour can be said to be strongly non–Newtonian. For this reason, the instability regime will be considered as strongly non–Newtonian as well.

In the limit of small values of Darcy-Weissenberg number, the weakly non–Newtonian regime, a Taylor expansion of Ra_c^T and Ra_c^L yields

$$Ra_c^T \;=\; 4\pi^2 \left(1 \,+\, (n-1)(\frac{1}{2} \,+\, \frac{1}{a})\, Wi^a\right), \tag{8.53a}$$

$$Ra_c^L \;=\; 4\pi^2 \left(1 \,+\, \frac{n-1}{a}\, Wi^a\right). \tag{8.53b}$$

In the case of $Wi = 0$, the classical critical results associated with the HRL problem are recovered, namely $Ra_c \;=\; 4\pi^2$ and $k_c \;=\; \pi$. Such results mean that, for the zero flow–rate case and according to the linear stability predictions, the onset of convection for a non–Newtonian fluid emerges under the same conditions as for a Newtonian one.

Considering the non–Newtonian version of classical Rayleigh–Bénard problem for clear fluids, the study carried out by Darbouli et al. [44] can be be cited. They conducted experiments with Xanthan–gum solutions at different concentrations. They concluded that the onset of convection is observed for all concentrations cases around $Ra_c = 1800$, which corresponds approximately to the Newtonian case. Since the thermal instabilities in both clear fluids and fluid saturated porous media are qualitatively similar, it is not surprising that the onset of non–Newtonian convection in porous media corresponds to the Newtonian results $Ra_c \;=\; 4\pi^2$. This result is different from that observed by Barletta and Nield [12] in the limit of zero Péclet number. Namely, $Ra_c^{pl\,T}$ tends to infinity for shear–thinning fluids and $Ra_c^{pl\,L}$ goes to zero for shear–thickening fluids.

For the general case, the dependence on Wi of Ra_c and k_c at the onset of convection is presented for different values of n associated to pseudoplastic and dilatant fluids. Different values of the Yasuda parameter a are considered. Figure 8.5 shows the critical Rayleigh number for pseudoplastic fluids as a function of Wi for different values of n. The Yasuda parameter is set here $a = 2$ and the results are relative to the transverse rolls. Dashed lines represents the results relative to the power–law model, it can be seen that in the limit of high values of Wi both results coincide

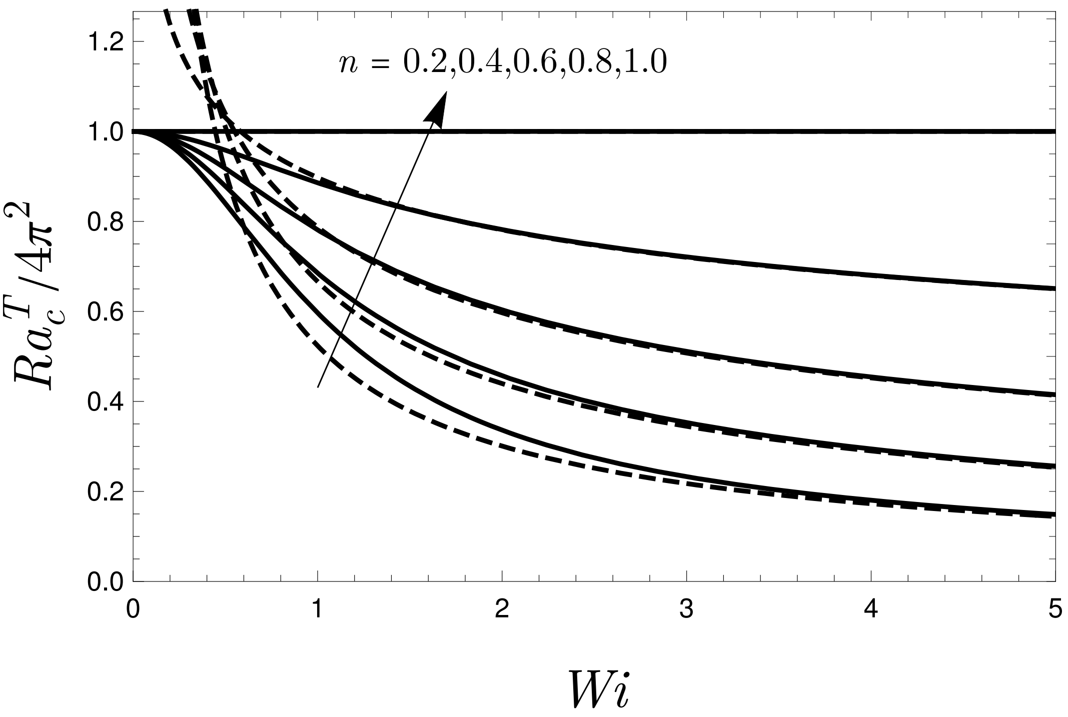

Figure 8.5: Critical Rayleigh number for pseudoplastic fluids, normalized by the critical one for Newtonian fluids ($4\pi^2$), versus the Darcy–Weissenberg number. Results obtained for transverse rolls with $a = 2$ and different values of n. The dashed lines in this figure are relative to the power-law model.

The critical Rayleigh number is normalized by the classical results for Newtonian fluids $Ra_c = 4\pi^2$, in such a way that the departure from the Newtonian case for $n \neq 1$ can be observed clearly when Wi increases. Figure 8.5 shows that Wi has a destabilizing effect. The observed destabilizing effect is stronger for small values of n. A physical interpretation may be related to the reduction of the apparent viscosity with increasing shear–thinning effects, making the fluid less able to resist to thermal buoyancy forces.

As already observed, in the limit of high Wi both results coincide. It can be said that there exists a special value Wi_t, which depends on n, above which the results start to coincide. Here, one can approximate this value by $Wi_t \approx 1$. It is worth to remark also that for $Wi < Wi_t$ the dashed curves tend to infinity, showing the singularity of the power–law model for weakly non–Newtonian fluids, in agreement with the results present in the literature [12]. Consequently, we can state that the power–law model and the Darcy–Carreau model lead to similar results in the strongly non-Newtonian regime (*i.e.* $Wi > Wi_t \approx 1$) while a significant qualitative and quantitative difference between the two models is observed in the weakly non–Newtonian regime (*i.e.* $Wi < Wi_t$).

Figure 8.6 shows that the critical wavenumber for pseudoplastic fluids is always smaller than the classical $k_c = \pi$. This implies that emerging transverse convection rolls have a larger cross–section for pseudoplastic fluids than for Newtonian fluids.

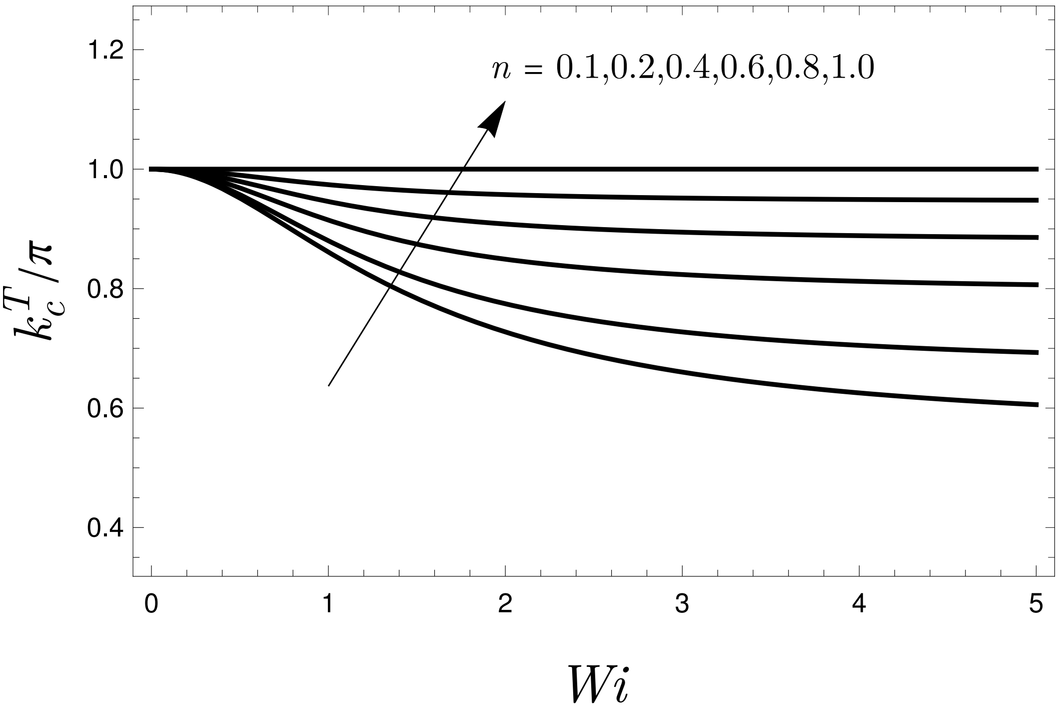

Figure 8.6: Critical wave number for pseudoplastic fluids versus the Darcy-Weissenberg number. Results obtained for transverse rolls with $a = 2$ and different values of n.

Figure 8.7 shows the critical results for dilatant fluids. The critical Rayleigh number is again normalized by the Newtonian result $Ra_c = 4\pi^2$. In this case, increasing Wi generates a stabilizing effect. Such a result is also expected, since for dilatant fluids the apparent viscosity increases with Wi, making the fluid to be more resistant to the thermal buoyancy forces. Dashed curves represent the results obtained by considering the power–law model, for comparison, which qualitatively are similar to those obtained from the present model considering that $Wi > Wi_t \approx 1$. On the other hand, for $Wi < Wi_t$, the critical Rayleigh number predicted by the Darcy–Carreau model (8.49c) tends to classical result $Ra_c = 4\pi^2$, while it goes to zero with the power–law model, as predicted by Barletta and Nield [12]. For the dilatant fluids, the critical wavenumber for longitudinal rolls is constant.

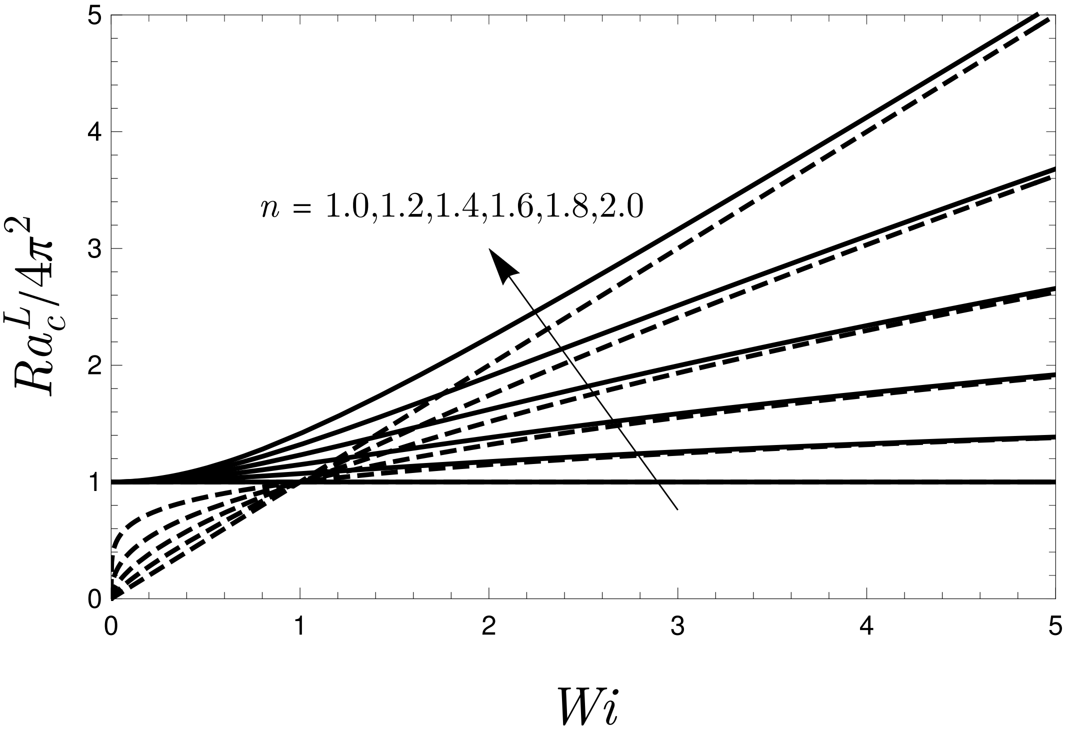

Figure 8.7: Critical Rayleigh number for dilatant fluids, normalized by the critical one for Newtonian fluids ($4\pi^2$), versus the Darcy–Weissenberg number. Results obtained for longitudinal rolls with $a = 2$ and different values of n. The dashed lines in this figure are relative to the power–law model.

The effect of the Yasuda parameter a on Ra_c is illustrated in Figures 8.8 and 8.9, respectively, for a fixed value of n. These two figures show that, as a decreases the critical Rayleigh number for pseudoplastic fluids decreases as well, while it increases for dilatant fluids. The parameter a has then a stabilizing effect for pseudoplastic fluids and a destabilizing effect for dilatant fluids. It is worth to note also that, for a high value of Wi, the critical Rayleigh number becomes less dependent on a meaning that, in this limit, there is no significant difference between the Darcy–Carreau–Yasuda model and the Darcy–Carreau model.

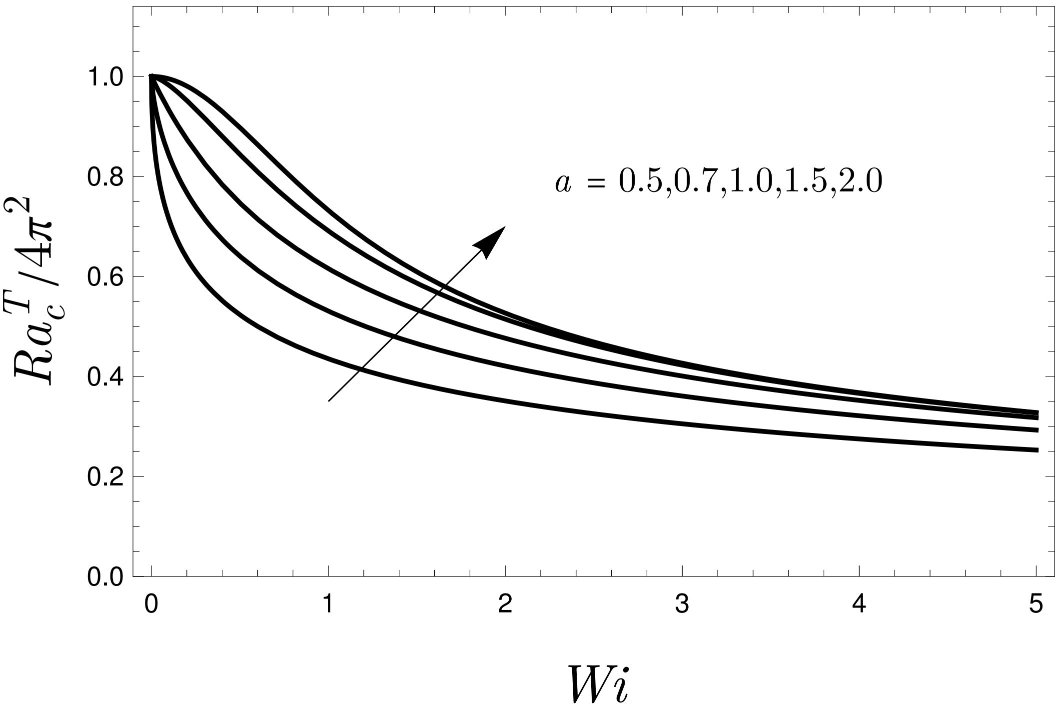

Figure 8.8: Critical Rayleigh number for pseudoplastic fluids, normalized by the Newtonian one ($4\pi^2$), as a function of the Darcy-Weissenberg number. Results are obtained for transverse rolls with $n = 0.5$ and different values of a.

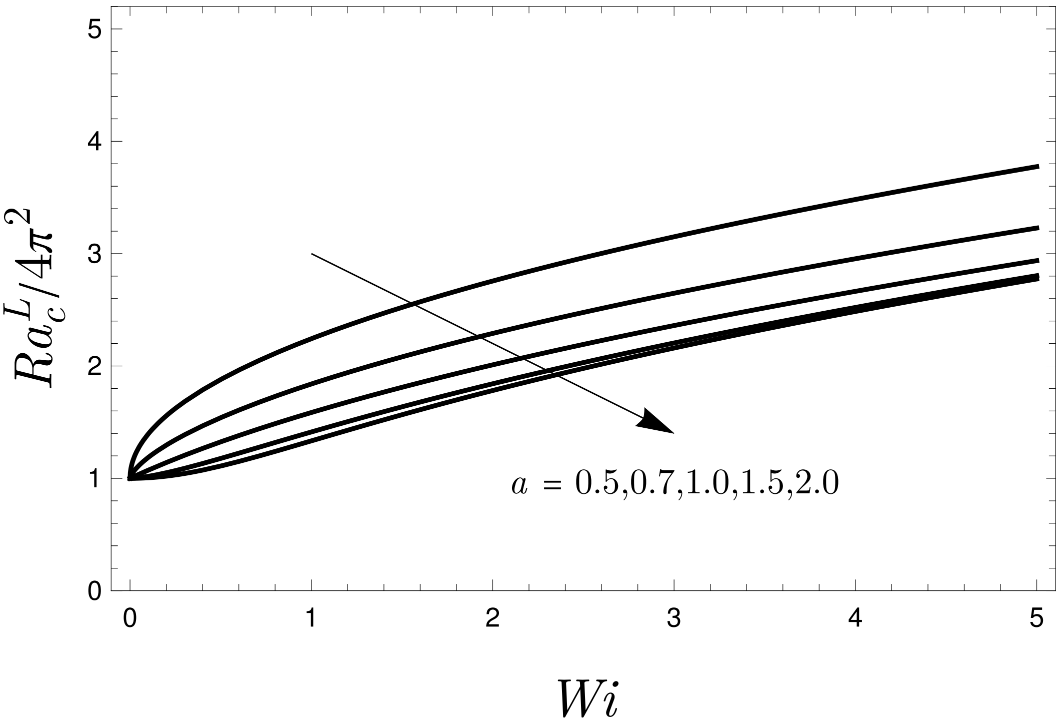

Figure 8.9: Critical Rayleigh number for dilatant fluids, normalized by the Newtonian one ($4\pi^2$), as a function of the Darcy-Weissenberg number. Results are obtained for longitudinal rolls with $n = 1.5$ and different values of a.

8.3 Energy budget analysis

In order to better understand the physical mechanisms involved in the thermal instability of shear–thinning and shear–thickening fluids saturating porous media, an energy budget analysis is here proposed. In a first instance, the momentum equations are written for the most unstable modes, namely transverse rolls for pseudoplastic fluids and longitudinal rolls for dilatant fluids. For the sake of conciseness, the procedure is illustrated here just for pseudoplastic fluids,

$$(1 + Wi^a)^{\frac{n-1}{a}} \left[1 + \frac{(n-1)\,Wi^a}{1 + Wi^a}\right] \tilde{u} = -\frac{\partial \tilde{p}}{\partial x}, \tag{8.54}$$

$$(1 + Wi^a)^{\frac{n-1}{a}} \; \tilde{w} = -\frac{\partial \tilde{p}}{\partial z} + Ra\,\tilde{T}. \tag{8.55}$$

By multiplying Equations (8.54) and (8.55) by the complex conjugate of $\tilde{u}$ and $\tilde{w}$, respectively, and by subsequently adding the two resulting equations, one obtains

$$(1\,+\,Wi^a)^{\frac{n-1}{a}}\left[|\tilde{u}|^2+|\tilde{w}|^2+\frac{(n-1)\,Wi^a}{1\,+\,Wi^a}\,|\tilde{u}|^2\right]\;=-\,\tilde{u}^*\,\frac{\partial\tilde{p}}{\partial x}\,-\,\tilde{w}^*\frac{\partial p}{\partial z}\,+\,Ra\,\tilde{w}^*\,\tilde{T},\quad(8.56)$$

where $\tilde{u}^*$ and $\tilde{w}^*$ are the complex conjugate of $\tilde{u}$ and $\tilde{w}$ respectively.

Equation (8.56) is integrated over a closed convective cell in the xz plane, where the presence of impermeable boundaries is assumed in x =constant. By integrating by parts, applying the Gauss-Green theorem and considering the mass balance equation, a relationship for the fluctuating energy at the instability threshold is obtained

$$\mathrm{e_{th}}+\mathrm{e_{nN}}+\mathrm{e_{d}}=0,\tag{8.57}$$

where each one of the contributions are given by

$$\begin{aligned}\mathrm{e_{th}}\;&=\;Ra_c\int_0^1(\tilde{w}^*\,\tilde{T})\,\mathrm{d}z,\\ \mathrm{e_{nN}}\;&=(1\,+\,Wi^a)^{\frac{n-1}{a}}\,\frac{(1-n)\,Wi^a}{1\,+\,Wi^a}\,\int_0^1|\tilde{u}|^2\,\mathrm{d}z,\\ \mathrm{e_{d}}\;&=\;-\,(1\,+\,Wi^a)^{\frac{n-1}{a}}\int_0^1(|\tilde{u}|^2+|\tilde{w}|^2)\,\mathrm{d}z.\end{aligned}\tag{8.58}$$

The single contributions $\mathrm{e_{th}}$, $\mathrm{e_{nN}}$ and $\mathrm{e_d}$ corresponds to the thermal buoyancy contribution due to the imposed temperature gradient, the non-Newtonian hydrodynamic energy production generated by the interaction of the basic flow with the horizontal perturbation velocity u and the viscous dissipation energy, respectively.

Sice $\mathrm{e_d}$ is negative, the dissipation contribution produces a stabilization effect for the present case. The contribution $\mathrm{e_{nN}}$ is positive for shear–thinning fluids, indicating the destabilizing effect of the non-Newtonian character of the fluid. The same is true for the thermal buoyancy contribution. Such a destabilizing effect is due to the coupling between the throughflow and the non-Newtonian nature of the fluid.

By normalizing the energy contributions by the absolute value of the dissipation contribution $|\mathrm{e_d}|$, the momentum energy budget then becomes,

$$\mathrm{E_{th}}\;+\;\mathrm{E_{nN}}\;=\;1,\tag{8.59}$$

with $\mathrm{E_{th}}\;=\;\frac{\mathrm{e_{th}}}{|\mathrm{e_d}|}$ and $\mathrm{E_{nN}}\;=\;\frac{\mathrm{e_{nN}}}{|\mathrm{e_d}|}$. The expressions of the perturbations u, w and $\tilde{T}$ can be given by

$$\tilde{T}\;=\;\hat{T}\,\exp\!\Big(ik_c^T\,x\;-\;i\,k_c^T\,Pe\,t\Big)\,\sin(\pi z),\tag{8.60}$$

$$\tilde{w}\;=\;((k_c^T)^2\;+\;\pi^2)\,\hat{T}\,\exp\!\Big(ik_c^T\,x\;-\;i\,k_c^T\,Pe\,t\Big)\,\sin(\pi z),\tag{8.61}$$

$$\tilde{u}\;=\;\frac{i\pi}{k_c^T}\,((k_c^T)^2\;+\;\pi^2)\,\hat{T}\,\exp\!\Big(ik_c^T\,x\;-\;i\,k_c^T\,Pe\,t\Big)\,\cos(\pi z).\tag{8.62}$$

Analytical expressions for $\mathrm{E_{th}}$ and $\mathrm{E_{nN}}$ can be obtained by taking into consideration the expressions for $\tilde{T}, \tilde{u}$ and $\tilde{w}$ together with the expressions for Ra_c and k_c, and it is given by

$$\begin{aligned}
\mathrm{E_{th}} &= \frac{(k_c^T)^2\pi^2}{((k_c^T)^2 + \pi^2)^2}\left[1 + \left(\frac{1 + n\,Wi^a}{1 + Wi^a}\right)^{\frac{1}{2}}\right]^2, \\
\mathrm{E_{nN}} &= \frac{\pi^2(1 - n)\,Wi^a}{(1 + Wi^a)((k_c^T)^2 + \pi^2)}.
\end{aligned} \tag{8.63}$$

The contributions $\mathrm{E_{nN}}$ and $\mathrm{E_{th}}$ in the limit of large values of Wi, the so–called strongly non-Newtonian regime, can be simplified to

$$\mathrm{E_{th}} = \sqrt{n}, \tag{8.64}$$

$$\mathrm{E_{nN}} = 1 - \sqrt{n}, \tag{8.65}$$

while it becomes, for the weakly non–Newtonian regime,

$$\mathrm{E_{th}} = 1 - \frac{1}{2}(1 - n)Wi^a, \tag{8.66}$$

$$\mathrm{E_{nN}} = \frac{1}{2}(1 - n)Wi^a. \tag{8.67}$$

In these two limits, the non–Newtonian hydrodynamic energy $\mathrm{E_{nN}}$ increases when the power–law index n decreases from $n = 1$ to $n = 0$. While the opposite is true for $\mathrm{E_{th}}$. The reason is that n is related to the non–Newtonian nature of the fluid, in such a way that decreasing n means that the shear–thinning nature of the fluid becomes predominant.

Figures 8.10 and 8.11 show the thermal and non–Newtonian energy variation as a function of Wi for two cases, namely $a = 0.5$ and $a = 2$, respectively. Different cases of n are considered. It is possible to observe that the non–Newtonian energy $\mathrm{E_{nN}}$ increases as Wi increases, while $\mathrm{E_{th}}$ decreases, indicating that less thermal energy is needed to trigger the instability. In the limit of high values of Wi, the two energies tend asymptotically to constant values. The asymptotic value of $\mathrm{E_{nN}}$ may be explained physically by invoking the characteristic time of the fluid λ^* and the characteristic time of the flow, which is given by the inverse of the porous shear rate $\dot{\gamma}_p^*$. The ratio between these two characteristic times yields the Darcy–Wiessemberg number. Since the linear dynamics occurs at small times, it is ruled by the characteristic time of the flow for large values of Wi. Hence, at this time scale, no interaction between the non-Newtonian characteristics of the fluid and the basic throughflow is expected, leading to a constant non–Newtonian contribution.

Figures 8.10 and 8.11 also show that for small values of n the curves of thermal and non–Newtonian contributions switch their role, that is the dominant disturbance energy changes. In order to evaluate the precise value of Wi in which the curves intersect, one may solve the equation $\mathrm{E_{th}} = \mathrm{E_{nN}}$ for each values of a and n,

$$Wi^a = \frac{3}{1-4n}, \tag{8.68}$$

considering that Wi^a is always positive, this intersection may be observed just for $n < 1/4$, or even for $n = 1/4$ if $Wi \to \infty$.

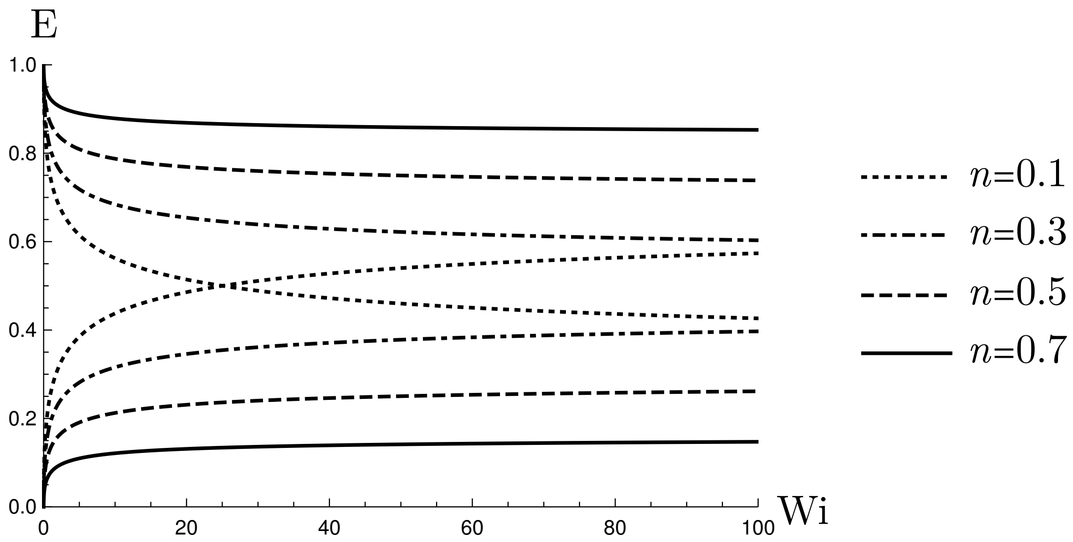

Figure 8.10: Energy budget analysis for $a = 0.5$. Upper curves represent the thermal energy $\mathrm{E_{th}}$ and lower curves the non–Newtonian energy $\mathrm{E_{nN}}$.

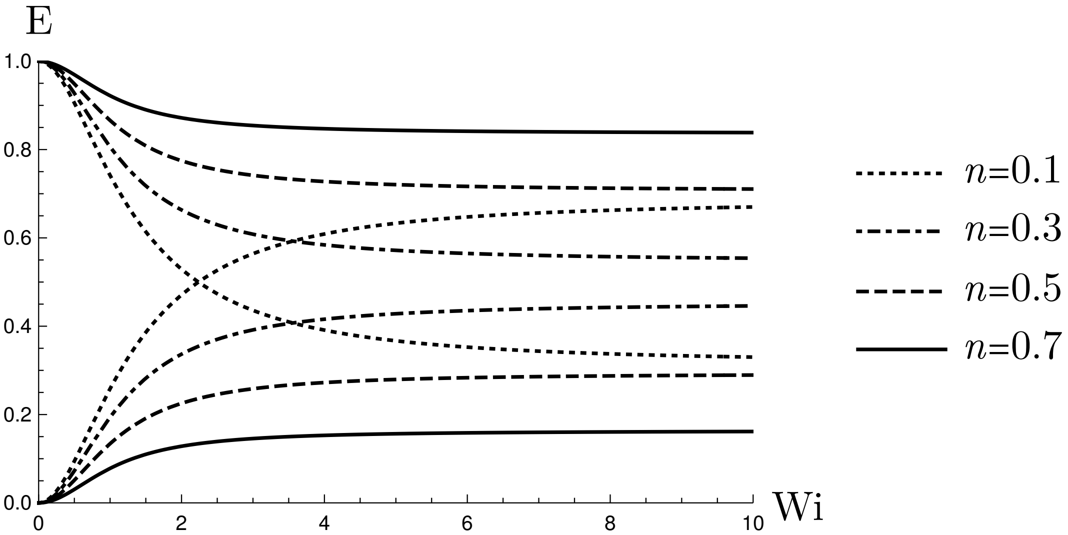

Figure 8.11: Energy budget analysis for $a = 2$. Upper curves represent the thermal energy $\mathrm{E_{th}}$ and lower curves the non–Newtonian energy $\mathrm{E_{nN}}$.

8.4 Discussion of the results in relation to common porous media and to experiments in Hele-Shaw cell

8.4.1 Application to common porous media

In this section, the interaction between the non–Newtonian nature of the fluid and the intrinsic characteristics of the porous medium at the onset of mixed convection is analysed. It is shown that the instability threshold depends on the dimensionless parameters n, a and Wi. An expression for Wi can be given by

$$Wi \,=\, \lambda^* \, f_p{}^{\frac{1}{n-1}} \, (\Phi \, K)^{-\frac{1}{2}} \, u_0, \tag{8.69}$$

where

$$f_p \,=\, 8^{-\frac{n+1}{2}} \, 2 \left(\frac{3n+1}{n} \right)^n . \tag{8.70}$$

By introducing the dimensionless time characteristic of the fluid $\lambda \,=\, \frac{\lambda^*}{H^2/\chi}$, the Darcy number $Da \,=\, \frac{K}{H^2}$ and the Péclet number Pe, Equation (8.69) may be written as

$$Wi \,=\, \lambda \, \dot{\gamma}_p, \tag{8.71}$$

with $\dot{\gamma}_p$ being the dimensionless porous shear rate given by

$$\dot{\gamma}_p = f_p^{\frac{1}{n-1}} (\Phi\, Da)^{-\frac{1}{2}}\, Pe. \tag{8.72}$$

For shear–thinning fluids, the characteristic time of the fluid, λ^*, commonly varies from $0.1\,s$ to $100\,s$. For common porous media the permeability K may vary from $10^{-20}\,m^2$ to $10^{-7}\,m^2$ [106], the filtration velocity u_0 is usually smaller than $4\times10^{-4}\,m\,s^{-1}$ while a typical value for the porosity ϕ is 0.35. By setting $H = 4\times10^{-2}\,m$ and $\chi = 10^{-7}\,m^2\,s^{-1}$, the dimensionless characteristic time of the fluid λ can vary approximately from 10^{-5} to 10^{-2}, while the product of Darcy number Da and the porosity Φ may vary approximately from 10^{-5} to 10^{-18}. The impact of the porous properties on the instability threshold may be investigated by setting the values for λ, n and Pe and by varying the product $(\Phi\, Da)$. On the other hand, the effect of the throughflow on the instability threshold may be studied by assigning values to λ, n and $(\Phi\, Da)$ and by varying the value of Pe. Figure 8.12 shows the dependence on $\Phi\, Da$ of Ra_c for pseudoplastic fluids. Péclet number is set $Pe = 4$ which corresponds to $u_0 = 4\times10^{-5}\,m\,s^{-1}$. The effect of ΦDa is then observed to be a stabilizing one. Instead, for a fixed value of ΦDa, decreasing n has a destabilizing effect, confirming that the shear–thinning characteristic of the fluid enhances the onset of convection.

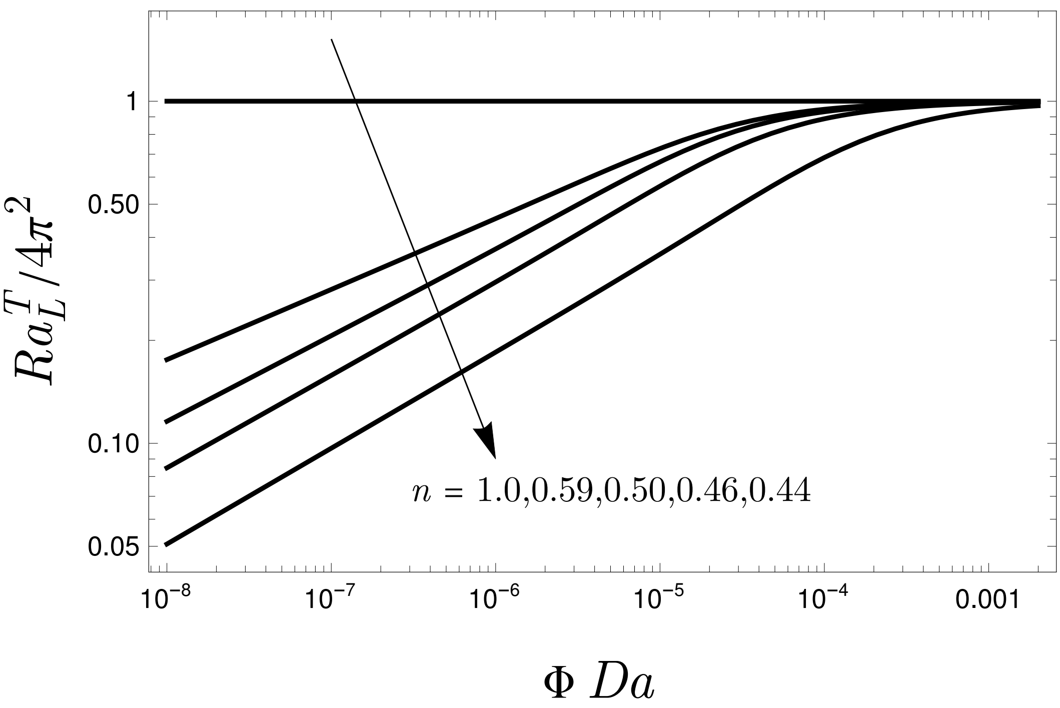

Figure 8.12: Critical Rayleigh number for pseudoplastic fluids as a function of ΦDa. Results obtained for transverse rolls with $a = 2$ and different values of n.

The effect of Pe on the instability threshold can be seen in Figure 8.13 for $\Phi\, Da = 10^{-5}$. The effect of varying Pe for a fixed ΦDa is qualitatively similar to that of varying Wi. For both figures, the data for n and λ^* were extracted from Darbouli et al. [44].

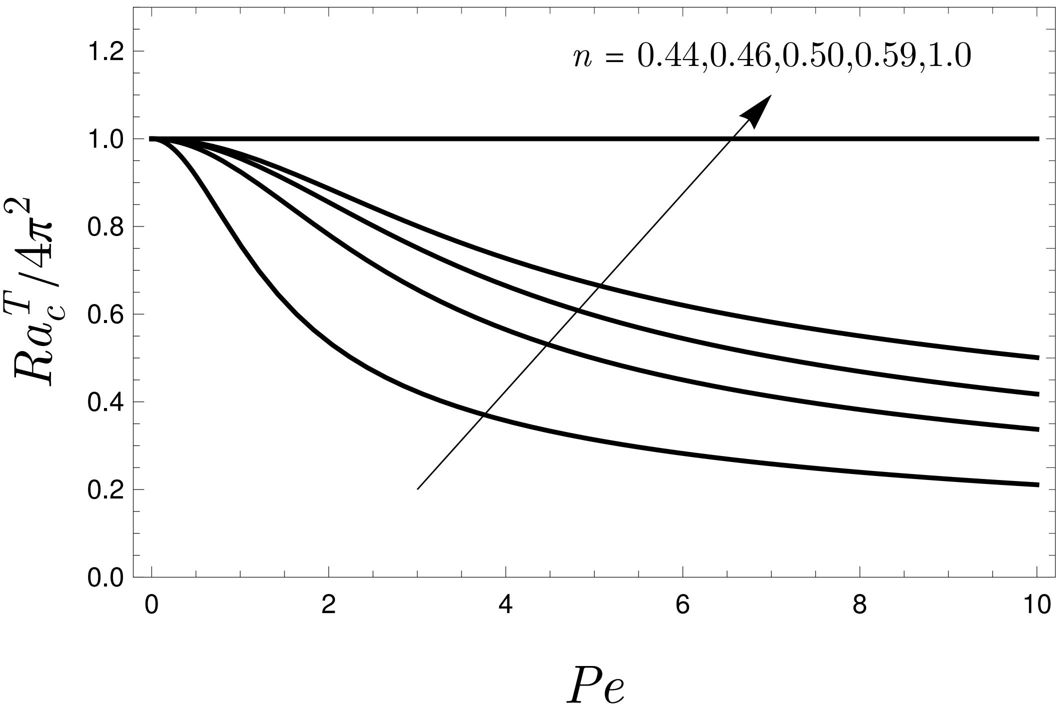

Figure 8.13: Critical Rayleigh number for pseudoplastic fluids as a function of Pe. Results obtained for transverse rolls with $a = 2$ and different values of n.

As discussed before, two regimes of instability can be identified at the instability threshold, namely a strongly and a weakly non–Newtonian regime. In the first one the power–law and the Carreau model almost coincide, while in the second one both models disagree significantly. The condition $Wi \sim 1$ is assumed here as an approximative value of the transitional value of Wi, in which the transition between the two regimes is observed. From Equation (8.71) it is possible to compute the value of λ in which this transition should be observed for each value of $\dot{\gamma}_p$, and it is given by

$$\lambda = \frac{1}{\dot{\gamma}_p}. \tag{8.73}$$

Figure 8.14 shows the characteristic time of the fluid as a function of the porous shear rate representing the transition between both regimes.

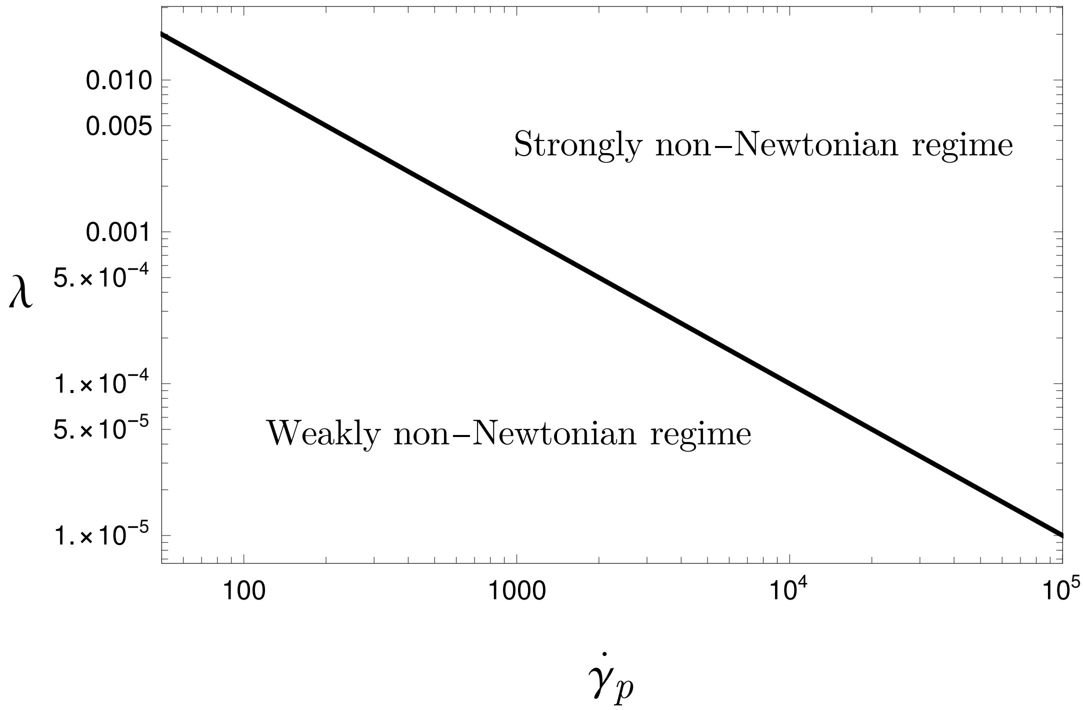

Figure 8.14: Transition map between the weakly and the strongly non-Newtonian regimes of instability.

8.4.2 Comparison with experiments in Hele-Shaw cell

In this section, the present theoretical results for the instability threshold are compared with some experimental data. Petrolo et al. [110] investigated the onset of mixed–convection of pseudoplastic fluids in a Hele–Shaw cell. They investigated the onset of pseudoplastic convection in Hele–Shaw cell by both an experimental and a theoretical approach, namely they investigated the linear stability of the forced convective state. Contrary to the present investigation, they considered a power–law model as the rheological model. For this reason, if a comparison is sought it is necessary to reformulate the present results in terms of the Rayleigh number used by Petrolo et al. [110], denoted here as Ra^* and defined by

$$Ra^* = \frac{\beta\, g\, K^*\, H^n\, \Delta T}{\eta\, \chi^n}, \tag{8.74}$$

where $K^* = (\frac{b}{2})^{n+1}(\frac{n}{2n+1})^n$ is the permeability used in experiments to evaluate the Rayleigh number and b is the width of the Hele–Shaw cell. The relation between Ra^* and the present Ra may be written as,

$$Ra^* = \Omega\, Ra, \tag{8.75}$$

with

$$\Omega = 12 \left(\frac{H}{\chi}\right)^{n-1} \frac{\mu_0}{\eta} \frac{b^{n-1}}{2^{n+1}} \left(\frac{n}{2n+1}\right)^n . \tag{8.76}$$

Almost all data necessary to evaluate Ω and Wi are reported in Table 1 of the work by Petrolo et al. [110]. The data related to μ_0, on the other hand, are not documented in the paper by Petrolo et al.[110]. Nonetheles, considering that in the supplementary material of Petrolo et al.[110] the apparent viscosity μ_a is given as a function of the average shear rate, for the Experiments 4 and 7, it is possible to estimate μ_0 by fitting the experimental data. The expressions of μ_a presented here for both Darcy–Carreau and Darcy–Carreau–Yasuda are considered.

Considering the expression (8.8) of the apparent viscosity given by the Carreau–Yasuda model, where λ^* and $\dot\gamma_p$ are given by (8.7) and (8.3), the following relation is obtained

$$\frac{\eta_{ef}}{\eta} = f_{hs} \, K^{\frac{1-n}{2}} , \tag{8.77}$$

with $f_{hs} = 3^{(-\frac{n+1}{2})} (\frac{2n+1}{n})^n$, $K = b^2/12$. At this point, one may recover μ_0 and the Yasuda parameter a based on the experimental data.

For the Experiment 4, $n = 0.66$ and $\eta = 0.07$. Figure 8.1 in Section 8.1 shows the experimental data (dots) and the Carreau–Yasuda model fit (continuous line) for the best–fitted a, that is the a with the smaller standard error

Table 8.1 show the parameters recovered from the nonlinear regression of the experimental data. Since the fluid properties for both Experiments 4 and 6 in Petrolo et al.[110] are similar, the estimated value of μ_0 is assumed to be the same for both Experiments 4 and 6.

Table 8.1: Estimated coefficients of the Carreau–Yasuda model using data for experiment 4 in Petrolo et al.[110].

	Estimate	Standard Error
μ_0	0.135022	0.001362
a	0.586851	0.00920399

For experiments 7 and 2, the fluid characteristics are $n = 0.55$ and $\eta = 0.1$. Figure 8.15 shows the adjustment of the Carreau–Yasuda model over the experimental data. Table 8.2 shows the result for μ_0 and the best–fitted a. In this case, it is observed that a have no significant effects on the final adjustment or on the value of μ_0. For this reason, the parameter a was fixed to $a = 2$, reducing the Carreau–Yasuda model to the Carreau model.

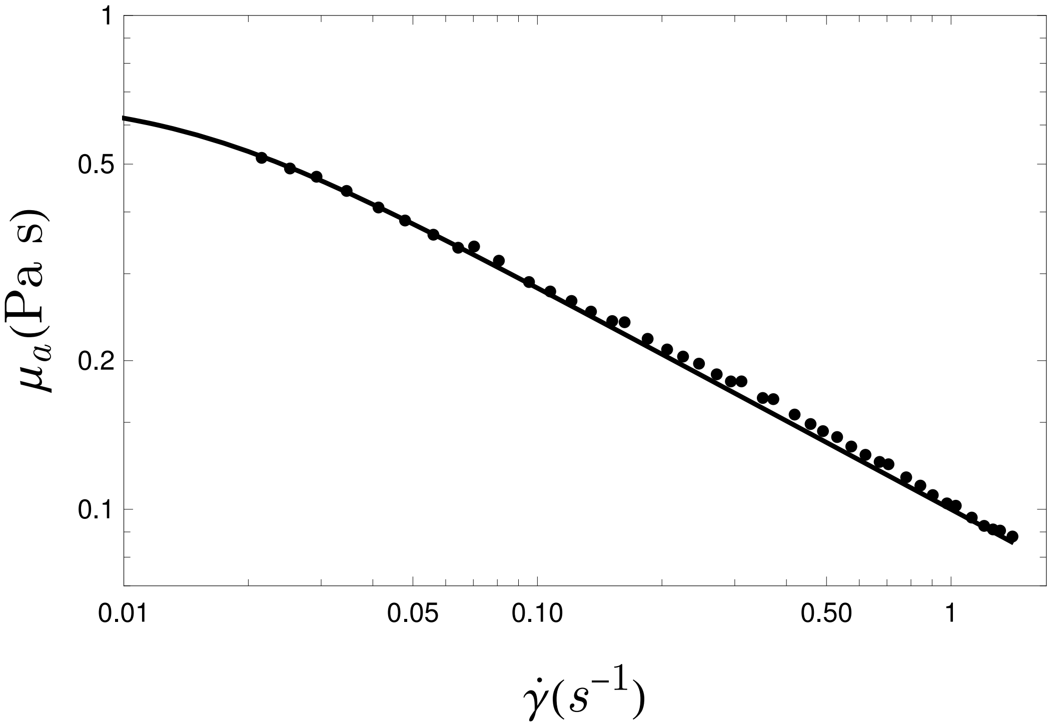

Figure 8.15: Data from experiment 7 of [110] and fitted model, for $a = 2$.

Table 8.2: Coefficients of the Carreau–Yasuda model estimated from experimental data of experiment 7 [110].

	Estimate	Standard Error
μ_0	0.583125	0.050362
a	2.89781	0.83957

In table 8.3, the measured values of critical Rayleigh number $Ra_c^{*,E}$ from the experiments are presented and compared with the present theoretical predictions $Ra_c^{*,T}$. The values of Wi were calculated here considering the definition (8.20) together with the experimental data.

Table 8.3: Critical Rayleigh number $Ra_c^{*,E}$, index n and Pe as determined experimentally in [110] and the corresponding Darcy-Weissenberg number Wi estimated by considering the experimental data. $Ra_c^{*,T}$ is the critical Rayleigh number determined in the present work.

Exp.	n	Pe	Wi	$Ra_c^{*,E}$	$Ra_c^{*,T}$	$\frac{Ra_c^{*,T}-Ra_c^{*,E}}{Ra_c^{*,E}}$
2	0.55	52	14.96	6.2 ± 0.6	5.06	- 18%
4	0.66	52	2.03	8.3 ± 0.8	8.52	2.6%
6	0.66	34	0.88	6.3 ± 0.4	7.14	13%
7	0.55	34	6.52	4.7 ± 0.6	6.13	30.4%

Table 8.3 shows that the disagreement between theoretical and experimental results for the Experiments 2 and 7 is considerable. It is important to note that in such cases the regime is a strongly non–Newtonian one, considering the high values of Wi. In this regime, the theoretical instability threshold given by the power–law model is almost the same as the one given by the present model, namely $Ra_c^{*,T}$ reported in Table 8.3. Therefore, the theoretical predictions given by both rheological models display almost the same discrepancy with experiments for relatively high values of Wi. On the other hand, Table 8.3 shows that the discrepancy between theory and experiments is significantly reduced for Experiments 4 and 6. These cases are both relative to a moderate and a small value of Wi. For these cases, theory overestimated the experimental results by 2.6% and 13%, respectively.

Table 8.4 shows a good agreement between the critical wavenumber of both experimental and theoretical predictions.

Table 8.4: Critical wave number from experimental results (k_c^E) and theory (k_c^T).

Exp.	k_c^E	k_c^T
2	2.99 ± 0.07	2.71
4	2.85 ± 0.06	2.71
6	3.05 ± 0.07	2.97
7	2.78 ± 0.06	3.01

Among the reasons that may cause the disagreement between theoretical and experimental results, it is possible to mention the possibility of a subcritical bifurcation, the need to classify the nature of the transition into convective or absolute and the fact that the present model does not take into account the influence of the yield stress effects, as observed by Petrolo et al. [110].

It may be necessary to investigate the contribution of the nonlinear interactions between the disturbance modes, by employing at least a weakly nonlinear stability analysis, in order to classify the nature of the bifurcation. In addition, since an open flow configuration is considered here, the instability nature must be distinguish between absolute and convective. Unfortunately, there is no information regarding the frequency spectrum of the convective rolls in Petrolo et al. [110], which makes impracticable such a kind of study.

8.5 Conclusion

The present study aimed to extend the work of Petrolo et al. [110] by introducing a new rheological model able to avoid the issues of the power–law model. The Darcy–Carreau–Yasuda model is, in fact, able to describe in a regular way the behaviour of the apparent fluid viscosity at both regions of small and high values of shear rate. A temporal stability analysis indicated that the distinction between stationary and oscillatory disturbance modes depends on the non–Newtonian nature of the fluid. For shear–thinning fluids, the oscillatory transverse rolls are favoured, while for shear–thickening fluids the preferred are the stationary longitudinal rolls.

In the strogly non–Newtonian regime, *i.e.* in the limit of high values of Wi, the present rheological model is reduced asymptotically to a power–law one. In such a regime, a comparison betewen the present and the power–law model predictions are in a very good agreement. On the other hand, in the weakly non–Newtonian regime, i.e. in the limit of small values of Wi, a significant difference between the Darcy–Carreau–Yasuda and the power–law model is observed. In the limit of zero flow–rate, the power–law model predicts that pseudoplastic fluids are unconditionally stable, while dilatant fluids are always unstable. Nevertheless, the results when considering the Darcy–Carreau–Yasuda model demonstrated that the classical critical value for Newtonian fluids $Ra_c = 4\pi^2$ is recovered in the limit of zero Wi. For $Wi < 1$, it is observed that Ra_c decreases for pseudoplastic fluids as Wi increases. This destabilizing effect is more effective for small values of n and a.

An energy budget analysis has been employed and clarified that, in addition to the dissipation contribution to the total disturbance energy, there is a thermal buoyancy contribution and also a non–Newtonian hydrodynamic energy production. For small values of Wi, the thermal buoyancy contribution is demonstrated to be the dominant effect, meaning that the transition has similar characteristics to the Newtonian fluids. For high values of Wi, instead, the non-Newtonian hydrodynamic energy production dominates, indicating that the instability is mainly related to the shear–thinning effects. For moderate values of Wi, it is observed a competition between the two mechanisms.

In addition, a discussion of the results in comparison with some results available in the literature has been made. Some experimental data available in Petrolo et al. [110] and its supplementary material allowed an evaluation and a comparison between the present results, the theoretical results considering a power–law model, and the experimental results. The discrepancy found between theory and experiments is relatively large for both models in the limit of high Wi while the Darcy–Carreau–Yasuda model turned out to be a more adequate framework for small and moderate values of Wi.

Chapter 9

A stability study of a generalised basic state for the isoflux Darcy–Bénard problem

9.1 Introduction

Different types of boundary conditions for the Darcy–Bénard system have been considered in the literature, including, for instance, uniform heat flux boundary conditions instead of the classical isothermal boundary conditions on the horizontal walls [97, 13, 106]. The instability threshold of a Darcy–Bénard problem with isoflux boundary conditions is characterised by infinite wavelength disturbances at the onset and a critical Rayleigh number equal to 12 [97, 106].

Another type of thermal instability occurring in a porous layer emerges when the basic flow is composed by a cellular flow, the so–called Hadley circulation [106]. The Hadley flow is due to the prescribed boundary temperature distributions with a uniform gradient in a given horizontal direction. Such a concept comes from the study of the physics of the atmosphere [60, 50]. The fundamental mechanism is explained by the horizontal temperature gradient that induces the appearance of the convective cells. This concept started to be investigated in the physics of atmosphere, thus in fluid dynamics of clear media, but its application in the fluid dynamics of saturated porous media has also been investigated in several papers [131, 99, 100, 105, 101, 93, 92, 75, 102, 31, 32, 30, 11, 17, 106]. The Hadley flow is a buoyant flow, that emerges in a bidimensional regime, parametrised by a given horizontal temperature gradient. Weber [131] was one of the pioneers to investigate the instability of a basic Hadley flow in a saturated porous medium. The Hadley flow in a porous medium is usually caused by a temperature gradient that is inclined to the horizontal, in such a way that the Darcy–Bénard instability also arises. Among the different studies dealing with Hadfley flow in porous media, it can be cited that by

Nield [99], in which he considered the presence of a horizontal pressure gradient acting on the Hadley cell flow. Important results about the convective or absolute nature of the instabilities are discussed by Brevdo and Ruderman [31, 32], Brevdo [30] as well as by Schuabb et al. [119] for the one– and two–dimensional wavepacket dynamics. The effect of viscous dissipation is taken into consideration in the analysis carried out by Barletta and Nield [11], while the heterogeneity of the porous medium was considered by Barletta et al. [17].

The aim of the present study is to revisit the classical Darcy–Bénard problem with uniform heat flux boundary conditions. A one–parameter class of basic cellular flows is proposed, which can be reduced to the classical conduction state with the fluid at rest as a special case. In particular, it will be demonstrated that the isoflux boundary conditions are compatible with a convective cellular flow of Hadley type with an arbitrary horizontal temperature gradient. Such a horizontal temperature gradient controls the magnitude of the circulation, when it tends to zero the classical conduction state of the isoflux Darcy–Bénard problem is recovered. This generalised single–cell basic flow is parametrised by the horizontal temperature gradient parameter as well as by a Rayleigh number proportional to the imposed boundary heat flux. In the present study, they are independent parameters, in contrast to what happens with the cellular flows described by Kimura et al. [81].

The stability of such basic states is analysed by considering a small–disturbance analysis. The instability threshold is investigated by employing a normal mode analysis and it is displayed in terms of the Rayleigh number and of the horizontal temperature gradient parameter. The must unstable cases and their nature are discussed. The investigation is carried out numerically by employing the shooting method [124, 8] and the Chebyshev–Gauss–Lobatto pseudo–spectral method [24, 73, 54] for the solution of the stability eigenvalue problem.

The contents of this chapter are based on the paper by Brandão, P. V., Barletta, A., Celli, M., Alves, L. de B. and Rees, D. A. S., On the stability of the isoflux Darcy–Bénard problem with a generalised basic state. International Journal of Heat and Mass Transfer, doi:10.1016/j.ijheatmasstransfer.2021.121538 [28].

9.2 Mathematical Model

A horizontal porous layer with thickness H is considered. Coordinate axes are chosen so that the x and y axes are horizontal and the z axis is vertical and directed upward.

The horizontal boundaries are impermeable and subject to the same thermal boundary conditions, that is an upward uniform wall heat flux at the bottom ($z = 0$) and at the top ($z = H$). That means that the incoming thermal power at the lower boundary is considered to be entirely removed from the upper boundary at all given (x, y) position.

9.2.1 Governing equations

Darcy's law is employed to model the momentum balance and the Oberbeck–Boussinesq approximation is assumed. The viscous dissipation effects are considered to be negligible. The velocity field is denoted by $\mathbf{u} = (u, v, w)$, p is the difference between the pressure and the hydrostatic pressure, T is the temperature field, and t is the time. Hence, the mass balance, the momentum balance and the energy balance equations are written as

$$\boldsymbol{\nabla} \cdot \mathbf{u} = 0, \tag{9.1a}$$

$$\frac{\mu}{K}\mathbf{u} = -\boldsymbol{\nabla} p - \rho\, \mathbf{g}\, \beta\, (T - T_0), \tag{9.1b}$$

$$\sigma \frac{\partial T}{\partial t} + \mathbf{u} \cdot \boldsymbol{\nabla} T = \chi \nabla^2 T. \tag{9.1c}$$

The dimensional boundary conditions are given by

$$z = 0, H: \quad w = 0 \quad \text{and} \quad -\varkappa \frac{\partial T}{\partial z} = q_0, \tag{9.2}$$

with β being the coefficient of thermal expansion of the fluid, $\mathbf{g}$ the gravity acceleration with modulus g, K the permeability of the porous medium, μ the dynamic viscosity of the fluid, χ the average thermal diffusivity of the saturated porous medium, $\varkappa$ the average thermal conductivity of the saturated porous medium, ρ the fluid density, T_0 the reference temperature, q_0 the uniform wall heat flux and σ the ratio between the average heat capacities per unit volume of the saturated porous medium and of the fluid.

The following dimensionless quantities are considered as reference quantities

$$\frac{x}{H} \to x, \quad t\,\frac{\chi}{\sigma H^2} \to t, \quad \mathbf{u}\frac{H}{\chi} \to \mathbf{u}, \quad \frac{T - T_0}{\Delta T} \to T, \quad p\frac{K}{\mu\chi} \to p, \tag{9.3}$$

where

$$\Delta T = \frac{q_0 H}{\varkappa}. \tag{9.4}$$

By considering the last reference quantities, a dimensionless formulation of the governing equations (9.1) can be written as

$$\boldsymbol{\nabla} \cdot \mathbf{u} = 0, \tag{9.5a}$$

$$\mathbf{u} = -\boldsymbol{\nabla} p + Ra T \mathbf{e}_z, \tag{9.5b}$$

$$\frac{\partial T}{\partial t} + \mathbf{u} \cdot \boldsymbol{\nabla} T = \nabla^2 T, \tag{9.5c}$$

with the boundary conditions in their dimensionless form given by

$$z = 0, 1: \quad w = 0 \quad \text{and} \quad -\frac{\partial T}{\partial z} = 1, \tag{9.6}$$

with $\mathbf{e}_z$ being the unit vector along the z axis. The modified Rayleigh number Ra can defined as

$$Ra = \frac{\rho \beta g \Delta T K H}{\mu \chi}. \tag{9.7}$$

9.2.2 Basic solution

A generalised stationary solution of Equations (9.5) subject to the boundary conditions (9.6) is proposed here and it is given by

$$u_b = -Ra\, C \left(z - \frac{1}{2} \right), \quad v_b = 0, \quad w_b = 0, \tag{9.8a}$$

$$T_b = C\, x - \frac{1}{12}\, z \left[12 - Ra\, C^2 (3 - 2\, z)\, z \right] + \text{constant}, \tag{9.8b}$$

$$\frac{\partial p_b}{\partial x} = -u_b, \quad \frac{\partial p_b}{\partial y} = 0, \quad \frac{\partial p_b}{\partial z} = Ra\, T_b. \tag{9.8c}$$

The subscript b stands for basic solution, while C is an arbitrary constant that controls the magnitude of the temperature gradient in the x direction and, consequently, the intensity of the horizontal flow. It is worth that the horizontal flow rate is zero independently of C. Indeed, for every assigned value of Ra, Equations (9.8) define a class of solutions of the governing equations by varying the value of the arbitrary constant C. In the limit of vanishing C, the basic state considered in the classical isoflux Darcy–Bénard problem analysed by Nield [97] is recovered.

In a first instance, the constant C may assume either positive or negative values without any significant change in the physical meaning of the solution, since it can be compensated by simply reflecting the x axis. For the sake of simplicity, the analysis will focus on the non–negative values of C.

The temperature T_b is defined up to an arbitrary additive constant due to the boundary conditions of Dirichlet type. However, such an additive constant has no impact on the stability analysis. Figure 9.1 shows plot frames of the isotherms $T_b = \text{constant}$ for a particular case of $Ra = 100$ with different values of C in order to illustrate the effect of varying C on the temperature profile. When $C = 0$ straight horizontal isotherms may be observed, meaning that the temperature gradient is purely vertical, as already expected since this is the special case where the basic state corresponds to the classical Darcy–Bénard problem solution. On the other hand, when C starts to increase, the temperature gradient gradually becomes less uniform. From Equations (9.8) it is possible to see that in the limit of high values of C, the x component of the temperature gradient becomes the dominant one close to the boundaries, while the z component of the temperature gradient is dominant close to the midplane $z = 1/2$.

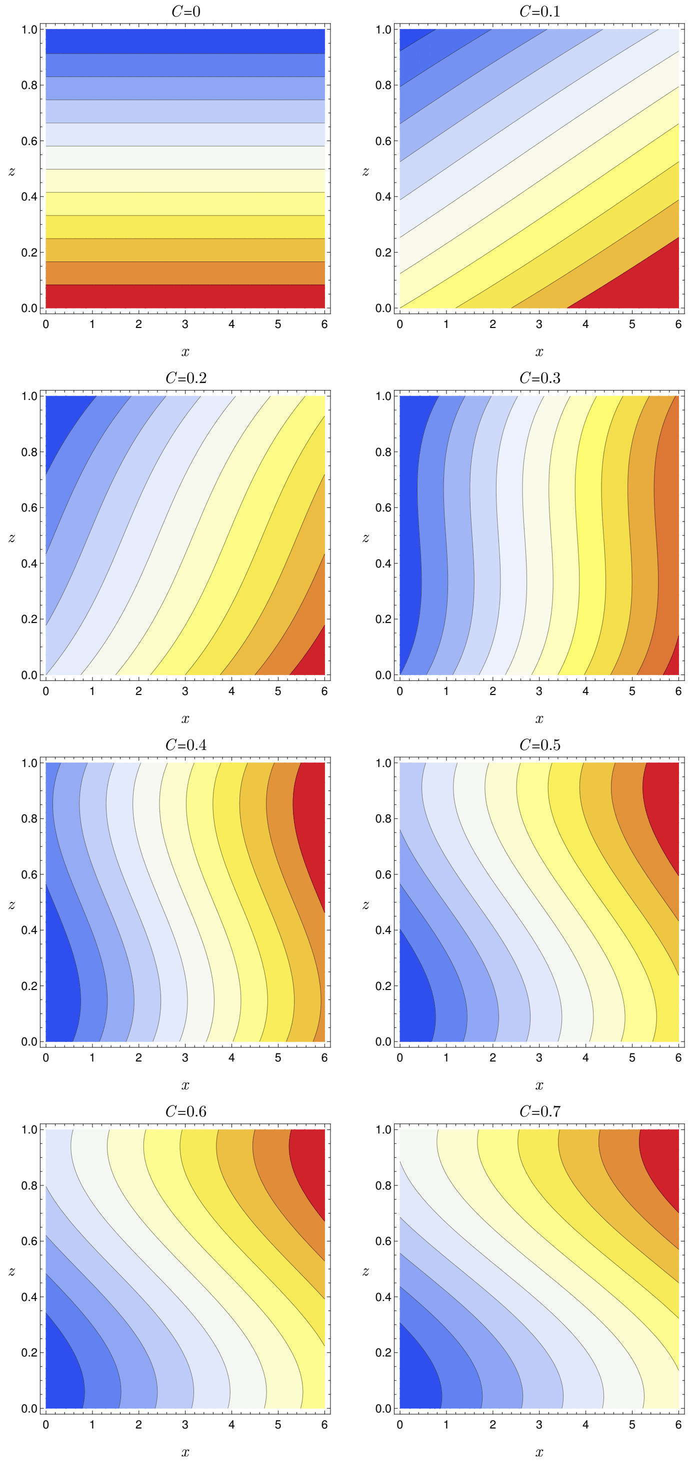

Figure 9.1: Temperature distribution of the basic solutions characterised by $Ra = 100$: each frame is drawn for different values of C.

It is important to remark that, altough the solution (9.8) formally coincides with that presented by Kimura et al. [81] and Gueye et al. [59], their physical meaning is different. In fact, both Kimura et al. [81] and Gueye et al. [59] considered the vertical sidewalls of the cavity, placed at suitable $x = constant$ positions, as adiabatic walls. The adiabaticity constraint induces an interconnection between the parameters C and Ra. In the present analysis, no constraints are assumed for the sidewalls, which implies the independence between C and Ra.

9.3 Linear stability analysis

In order to investigate the stability of the present system a small disturbance analysis is considered. Such an analysis consists in decomposing the original quantities into a basic term and another term relative to the infinitesimal disturbances, as explained in Section 3.2. Such disturbances are considered to behave as normal modes, namely

$$\begin{aligned} \mathbf{u}(x, y, z, t) &= \mathbf{u}_b(z) + \epsilon\, \hat{\mathbf{u}}(z)\, e^{i(k_x x + k_y y - \omega t)}, \\ p(x, y, z, t) &= p_b(x, z) + \epsilon\, \hat{p}(z)\, e^{i(k_x x + k_y y - \omega t)}, \\ T(x, y, z, t) &= T_b(x, z) + \epsilon\, \hat{T}(z)\, e^{i(k_x x + k_y y - \omega t)}, \end{aligned} \tag{9.9}$$

with ϵ being a small perturbation parameter, k_x and k_y the real components of the wave vector in the streamwise and spanwise directions, respectively, ω the complex frequency and $\hat{u}(z)$, $\hat{v}(z)$, $\hat{w}(z)$ and $\hat{T}(z)$ the eigenfunctions. After linearising the resulting equations, and by applying the curl operator to the momentum balance equation, it is possible to get rid of the pressure field. In this way, after some algebraic manipulation, the linearised disturbance equations can be written in terms of the vertical disturbance velocity and the disturbance temperature, namely

$$\hat{w}'' - k^2\, (\hat{w} - Ra\, \hat{T}) = 0, \tag{9.10a}$$

$$\begin{aligned} &\hat{T}'' - \left[k^2 - ik\cos\phi\, Ra\, C\left(z - \frac{1}{2}\right) - i\omega\right] \hat{T} \\ &\quad + \left[1 - \frac{1}{2}\, Ra\, C^2\, (1 - z)\, z\right] \hat{w} - \frac{iC\cos\phi}{k}\, \hat{w}' = 0, \end{aligned} \tag{9.10b}$$

$$z = 0, 1: \quad \hat{w} = 0 = \hat{T}', \tag{9.10c}$$

where the wavenumber k and the components of the wave vector may be written as

$$k = \sqrt{k_x^2 + k_y^2}, \qquad k_x = k\cos\phi, \qquad k_y = k\sin\phi. \tag{9.11}$$

The angle ϕ indicates the inclination between the x axis and the direction of the wave vector, with $0 \le \phi \le \pi/2$. In a first instance, the problem is solved for the marginal stability condition for each assigned value of C and ϕ. Each assigned value of k corresponds to a value of Ra that satisfies the zero growth rate condition . The critical condition is given by the minimum value of Ra along the neutral stability curve. Hence, for each assigned value of the pair (C, ϕ), one can determine the critical values (k_c, Ra_c). For this purpose, the problem is solved by using the shooting method, as explained in Sections 4.1 and 4.1.1.

9.3.1 Matrix formulation

The shooting method may be the most convenient numerical approach if one is seeking for the neutral stability condition, or even the critical conditions. However, there are different ways to approach numerically the differential eigenvalue problem. A possible alternative approach is the one based on the matrix formulation of the differential problem, namely the matrix–form approach (see Section 4.2). The main difference of the matrix–form approach is that it aims to obtain the entire (truncated) spectrum of the linear operator for each assigned value of (k, Ra). In fact, the differential eigenvalue problem can be rewritten as

$$\mathcal{L}q = \omega \mathcal{B} q, \tag{9.12}$$

where $\mathcal{L}$ and $\mathcal{B}$ are linear operators, q is a vector formed by $\hat{w}$ and $\hat{T}$ and ω is the complex frequency, here the complex eigenvalue. Equation (9.12) can be reformulated as

$$\begin{bmatrix} \mathcal{L}_{11} & \mathcal{L}_{12} \\ \mathcal{L}_{21} & \mathcal{L}_{22} \end{bmatrix} \begin{bmatrix} \hat{w} \\ \hat{T} \end{bmatrix} = \omega \begin{bmatrix} \mathcal{B}_{11} & \mathcal{B}_{12} \\ \mathcal{B}_{21} & \mathcal{B}_{22} \end{bmatrix} \begin{bmatrix} \hat{w} \\ \hat{T} \end{bmatrix}, \tag{9.13}$$

where

$$\mathcal{L}_{11} = D^2 - k^2 I \hat{q} \mathcal{L}_{12} = k^2 Ra\, I,$$
$$\mathcal{L}_{21} = \left[1 - \frac{1}{2}\, Ra\, C^2\,(1-z)\, z\right] I - \frac{iC\cos\phi}{k} D,$$
$$\mathcal{L}_{22} = D^2 - \left[k^2 - ik\cos\phi\, Ra\, C\left(z - \frac{1}{2}\right)\right] I, \tag{9.14}$$

with I being the identity matrix, D being the matrix corresponding to the differential operator d/dz, which is given by the Chebyshev–Gauss–Lobatto pseudo–spectral method and

$$\mathcal{B}_{11} = 0 \hat{q} \mathcal{B}_{12} = 0 \hat{q} \mathcal{B}_{21} = 0 \hat{q} \mathcal{B}_{22} = -i\, I. \tag{9.15}$$

9.4 Asymptotic analysis for small values of C

As already mentioned, when $C = 0$ the classical basic state is recovered. It can be of interest to investigate the problem behaviour in the vicinity of this condition, that is in the limit of small values of C. When C vanishes, it is possible to obtain an analytical solution.

By considering just longitudinal modes ($\phi = \pi/2$), Equations. (9.10) show that the eigenvalue problem depends just on C^2, which allows one to write the expansions

$$\hat{w} = \sum_{n=0}^{\infty} \tilde{\hat{w}}_n \, C^{2n}, \quad \hat{T} = \sum_{n=0}^{\infty} \tilde{\hat{T}}_n \, C^{2n}, \quad Ra = \sum_{n=0}^{\infty} \tilde{Ra}_n \, C^{2n}. \tag{9.16}$$

By substituting Equation (9.16) into Equation. (9.10) at each order j, one has

$$\tilde{\hat{w}}_n'' - k^2 \tilde{\hat{w}}_n + k^2 \sum_{m=0}^{n} \tilde{Ra}_m \tilde{\hat{T}}_{n-m} = 0,$$

$$\tilde{\hat{T}}_n'' - k^2 \tilde{\hat{T}}_n + \tilde{\hat{w}}_n - \mathcal{I}_n = 0, \tag{9.17}$$

where $\mathcal{I}_0 = 0$ and

$$\mathcal{I}_n = -\frac{1}{2} z(1-z) \sum_{m=0}^{n-1} \tilde{Ra}_m \, \hat{w}_{n-m-1}, \tag{9.18}$$

for $n > 1$.

One may reduce Equations (9.17) to a single equation of fourth order for $\tilde{\hat{T}}$. Given that such a single equation for $\tilde{\hat{T}}_0(z)$ is of linear constant-coefficient type, a substitution of

$$\tilde{\hat{T}}_0(z) = e^{bz}, \tag{9.19}$$

leads to the characteristic equation

$$k^4 + b^4 - k^2(\tilde{Ra}_0 + 2b^2) = 0, \tag{9.20}$$

for which solutions are given by $b = \pm b_1$ and $b = \pm b_2$, with

$$b_1 = \left(k^2 - k\tilde{Ra}_0^{1/2}\right)^{1/2}, \tag{9.21}$$

and

$$b_2 = \left(k^2 + k\tilde{Ra}_0^{1/2}\right)^{1/2}, \tag{9.22}$$

and the general solution for $\hat{T}_0$ is written as

$$\tilde{\hat{T}}_0(z) = m_1 e^{-b_1 z} + m_2 e^{b_1 z} + m_3 e^{-b_2 z} + m_4 e^{b_2 z}. \tag{9.23}$$

By applying the appropriate boundary conditions, which can be derived from Equations (9.10), the values of the coefficients m_1 to m_4, must satisfy the matrix/vector equation,

$$
\begin{bmatrix}
-b_1 & b_1 & -b_2 & b_2 \\
-b_1 e^{-b_1} & b_1 e^{b_1} & -b_2 e^{-b_2} & b_2 e^{b_2} \\
b_1^2 - k^2 & b_1^2 - k^2 & b_2^2 - k^2 & b_2^2 - k^2 \\
b_1^2 e^{-b_1} - e^{-b_1} k^2 & b_1^2 e^{b_1} - e^{b_1} k^2 & b_2^2 e^{-b_2} - e^{-b_2} k^2 & b_2^2 e^{b_2} - e^{b_2} k^2
\end{bmatrix}
\begin{bmatrix} m_1 \\ m_2 \\ m_3 \\ m_4 \end{bmatrix} = 0. \tag{9.24}
$$

Nonzero solutions are found by imposing that the determinant of the matrix must be equal to zero.

For the higher order equations, the general solution should have the same form as the one at zero order, and it is considered a particular solution of the form

$$
\tilde{\hat{T}}_j^{(p)}(z) = M_1\, m_1\, z\, e^{-b_1 z} + M_2\, m_2\, z\, e^{b_1 z} + M_3\, m_3\, z\, e^{-b_2 z} + M_4\, m_4\, z\, e^{b_2 z}, \tag{9.25}
$$

which, by applying to the equation of j-th order, it is possible to recover the expressions for the M coefficients.

The implicit expression for the solution of $\tilde{Ra}_0$ is given by

$$
k^2 \sinh(b_1) \sinh(b_2) + b_1\, b_2 \left[\cosh(b_1)\cosh(b_2) - 1\right] = 0, \tag{9.26}
$$

which depends on k. At second and fourth orders, it is possible to obtain explicit solutions for both $\tilde{Ra}_1$ and $\tilde{Ra}_2$. They are, however, omitted here for the sake of conciseness.

9.5 Asymptotic analysis for small values of k

As already mentioned, the case $C = 0$ corresponds to the classical DB problem, which critical condition is relative to infinite wavelength disturbances, namely $k_c = 0$. For this reason, an asymptotic analysis for $k \to 0$ can be useful in order to understand how the critical conditions are affected by small variations in C. Expanding the variables in a power series in terms of k, leads to

$$
\hat{w} = \sum_{n=0}^{\infty} \hat{\hat{w}}_n\, k^n, \quad \hat{T} = \sum_{n=0}^{\infty} \hat{\hat{T}}_n\, k^n, \quad Ra = \sum_{n=0}^{\infty} \hat{Ra}_n\, k^n. \tag{9.27}
$$

The solutions at each order are given by,

$$
\hat{\hat{w}}_0 = 0, \tag{9.28a}
$$

$$
\hat{\hat{T}}_0 = 1, \tag{9.28b}
$$

$$
\hat{\hat{w}}_1 = 0, \tag{9.28c}
$$

$$
\hat{\hat{T}}_1 = \mathcal{C}_1 - \frac{1}{6} i\, C\, \hat{Ra}_0 z^2 (2z - 3)\cos(\phi), \tag{9.28d}
$$

$$\hat{\hat{w}}_2 = -\frac{1}{2}\hat{Ra}_0(z-1)z, \tag{9.28e}$$

$$\hat{w}_3 = \frac{1}{120}iz(z-1)[60i(\mathcal{C}_1\hat{Ra}_0 + \hat{Ra}_1) + C\hat{Ra}_0^2(2z^3 - 3z^2 - 3z - 3)\cos(\phi)], \tag{9.28f}$$

which allow one to find the solution of $\hat{\hat{T}}_2$ up to an additional integration constant,

$$\begin{aligned}\hat{\hat{T}}_2 = \frac{1}{1440}\Big[&720z^2 - 9C^2\hat{Ra}_0^2z^2 - 120\hat{Ra}_0z^3 + 60\hat{Ra}_0z^4 + \\ &15C^2\hat{Ra}_0^2z^4 - 6C^2\hat{Ra}_0^2z^5 + 2C^2\hat{Ra}_0^2z^6 + 1440\mathcal{C}_2 - \\ &C^2\hat{Ra}_0^2z^2(9 + 15z^2 - 30z^3 + 10z^4)\cos(2\phi) - \\ &240iC(\mathcal{C}_1\hat{Ra}_0 + \hat{Ra}_1)z^2(2z-3)\cos(\phi)\Big].\end{aligned} \tag{9.29}$$

After applying the boundary conditions, the resulting quadratic equation for $\hat{Ra}_0$ provides the following solutions,

$$\hat{Ra}_0^l = \frac{120}{\sqrt{5}\sqrt{5 - 24C^2\cos(2\phi) - 48C^2} + 5}, \tag{9.30}$$

$$\hat{Ra}_0^u = -\frac{120}{\sqrt{5}\sqrt{5 - 24C^2\cos(2\phi) - 48C^2} - 5}, \tag{9.31}$$

with the superscripts, l and u, referring to lower and upper, respectively.

It is important to note that, in the limit $C \to 0$, the solutions $\hat{Ra}_0^l \to 12$ and $\hat{Ra}_0^u \to \infty$ are in accordance with the classical results for $C = 0$. In addition, in order to obtain physically meaningful results the solution must correspond to positive values of the square roots argument. This means that C have to satisfy the inequalities

$$-\frac{\sqrt{5}}{2\sqrt{6(2+\cos(2\phi))}} < C < \frac{\sqrt{5}}{2\sqrt{6(2+\cos(2\phi))}}. \tag{9.32}$$

Since for the present problem a signal change in C does not imply any important physical change, the analysis may be restrict to positive values of C here. Therefore, C must satisfy

$$C < \frac{\sqrt{5}}{2\sqrt{6(2+\cos(2\phi))}}. \tag{9.33}$$

If this condition is not respected, it means that there is no solution for $k = 0$. This limit represents for instance

$$C < \frac{\sqrt{5}}{6\sqrt{2}} \sim 0.263523, \tag{9.34}$$

for $\phi = 0$, and

$$C < \frac{\sqrt{5}}{2\sqrt{6}} \sim 0.456435, \tag{9.35}$$

for $\phi = \pi/2$.

9.6 Discussion of the results

9.6.1 Verification

In this section the convergence analysis as well as a verification of the numerical calculations are presented. Table 9.1 and 9.2 present the convergence of the calculation performed in the *Mathematica* environment for the first and second most unstable modes. The built–in function `NDSolve` works with an adaptive step–size mesh by default. So different fixed step–size mesh results were obtained and compared with those obtained from the adaptive one in order to ensure the convergence of the computations. The results shown in Tables 9.1 and 9.2 consider ω as the unknown variable. It can be seen that the adaptive mesh returns accurate results with at least 9 converged figures.

Figures 9.2 and 9.3, show the convergence of the numerical calculations performed by considering the matrix–forming approach, that is by using the pseudo–spectral Chebyshev–Gauss–Lobatto method. As expected for pseudo–spectral methods, the convergence can be achieved rapidly, for small values of N, and the absolute error reaches a minimum for a small number of mesh points. The absolute error was calculated by using as reference solutions the adaptive mesh shooting method results.

Table 9.1: Shooting method convergence: a comparison of the results obtained for different values of the fixed step–size δ employed for the domain discretization. The values of the angular frequency ω are obtained for $C = 0.1$, $\phi = 0$, $Ra = 600$, $k = 5$ and for the most unstable mode.

δ	Re[ω]	Im[ω]
0.1	76.1301413428	71.3389808444
0.05	76.3608999828	71.5537897173
0.025	76.3759942723	71.5688304389
0.0125	76.3768763616	71.5698331905
0.01	76.3769093734	71.5698737008
0.005	76.3769304117	71.5699002616
0.0025	76.3769316885	71.5699019385
0.00125	76.3769317671	71.5699020438
Adaptive	76.3769317723	71.5699020508

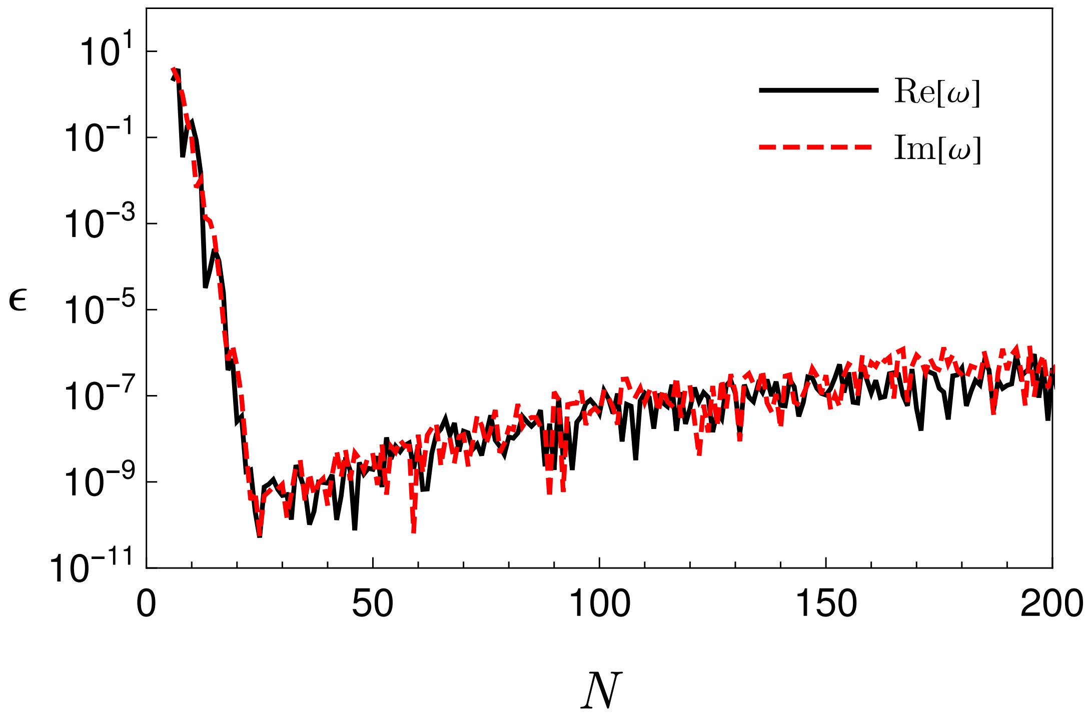

Figure 9.2: Absolute value ϵ of the difference between the results obtained by employing the pseudo–spectral method and the shooting method with adaptive step–size mesh. The parameter ϵ is plotted for different values of the number of collocation points N as well as the order of the Chebyshev polynomial. The values of the angular frequency ω are obtained for $C = 0.1$, $\phi = 0$, $Ra = 600$, $k = 5$ and for the first most unstable mode.

Table 9.2: Same as Table 9.1 but for the second most unstable mode.

δ	Re[ω]	Im[ω]
0.1	38.2012727048	-43.2049433605
0.05	38.5648973811	-43.5971821585
0.025	38.5954461409	-43.6186157267
0.0125	38.5975837099	-43.6197805121
0.01	38.5976713085	-43.6198220187
0.005	38.5977289672	-43.6198479227
0.0025	38.5977326243	-43.6198494454
0.00125	38.5977328544	-43.6198495374
Adaptive	38.5977328698	-43.6198495434

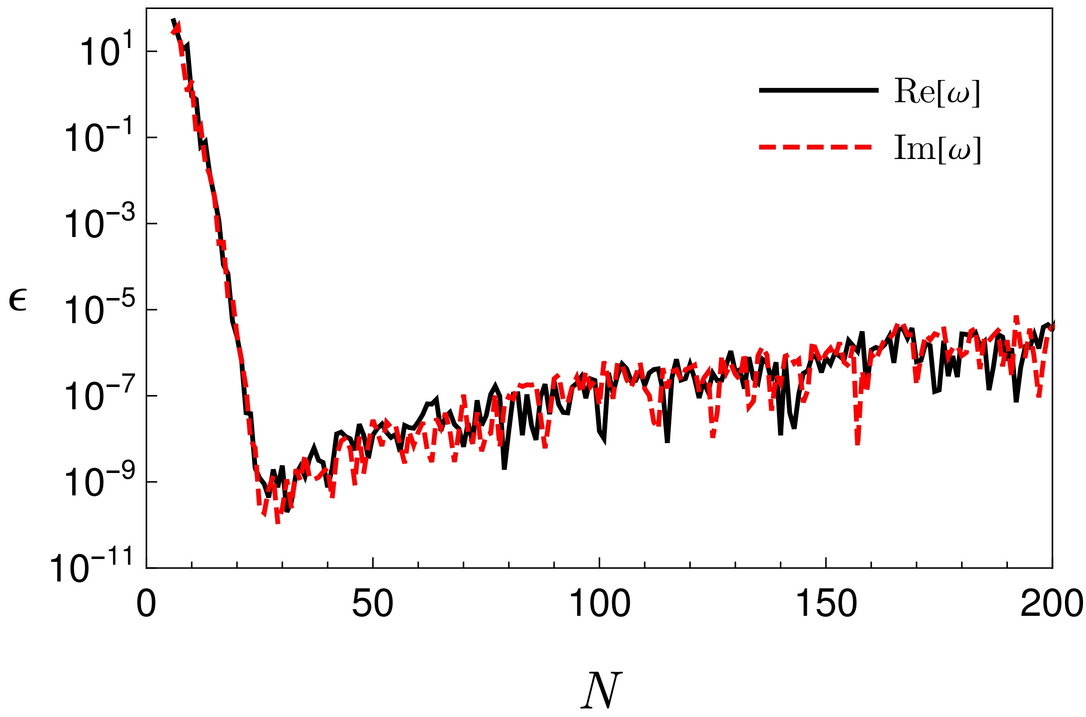

Figure 9.3: Same as Figure 9.2 but for the second most unstable mode.

From now on, the adaptive step–size mesh shooting method and the pseudo–spectral method with $N = 21$ will be considered. Figure 9.4 shows a good agreement between the results obtained by both methods.

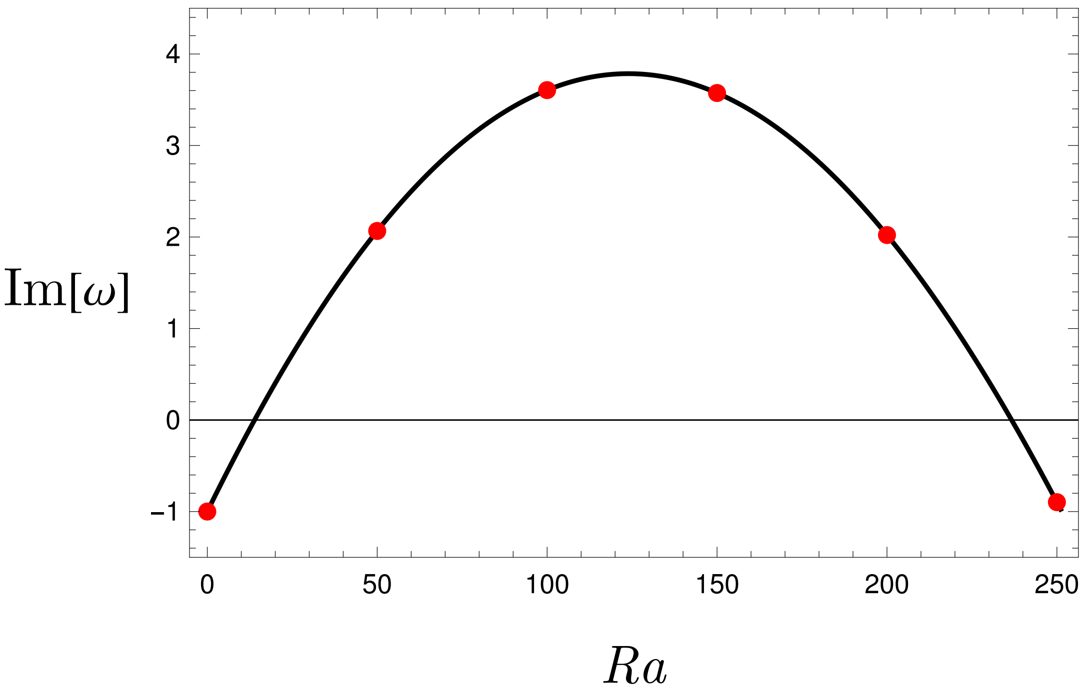

Figure 9.4: Growth rate as a function of Ra for $C = 0.2$, $\phi = \pi/2$ and $k = 1$: comparison between shooting method (continuous line) and matrix forming (red dots) results.

Once the accuracy of the numerical calculations were verified, it is possible to compare the numerical results with those from the asymptotic analysis for small values of C in order to evaluate the usefulness of such results. Such an analysis can be quite useful considering that the C parameter cannot assume high values. Table 9.3 presents a comparison between the neutral stability results calculated with the shooting method and those from the asymptotic analysis, considering the zeroth, second and fourth order approximations. Consistent trends are observed.

Table 9.3: Comparison between the Rayleigh number Ra obtained by employing the shooting method and the Rayleigh number obtained by employing the asymptotic analysis for small values of C truncated at zeroth ($\tilde{Ra}_0$), second ($\tilde{Ra}_0 + C^2\,\tilde{Ra}_1$), and fourth ($\tilde{Ra}_0 + C^2\,\tilde{Ra}_1 + C^4\,\tilde{Ra}_2$) orders. The values of the Rayleigh number are obtained for $k = 2$ and $\phi = \pi/2$.

C	Ra	$\tilde{Ra}_0$	$\tilde{Ra}_0 + C^2\tilde{Ra}_1$	$\tilde{Ra}_0 + C^2\tilde{Ra}_1 + C^4\tilde{Ra}_2$
0.001	16.5065313573078	16.5065039553139	16.5066197841567	16.5066197853894
0.01	16.5092450551770	16.5065039553139	16.5180868395888	16.5180991675637
0.05	16.5755829985049	16.5065039553139	16.7960760621851	16.7368123770508
0.1	16.7900117639327	16.5065039553139	17.6647923827987	16.7165734205878

9.6.2 Discussion

In this section the results will be presented and discussed, focusing on the influence of C and ϕ on the instability threshold. The results will be presented in terms of neutral stability conditions and the respective critical conditions. In addition, a discussion about the dominant stability modes is presented as well. Figure 9.5 presents the marginal stability condition in terms of neutral stability curves for different values of ϕ. For every inclination angle, the most unstable curve is demonstrated to be the one relative to the case $C = 0$. For $C = 0$, the unstable region is a semi–infinite region, starting from the neutral stability curve and without limitations above. As the value of C increases, the unstable region limited by these curves starts to become finite and eventually disappears, indicating the appearance of an upper bound for instability. Such a trend is observed for longitudinal, oblique and transverse modes.

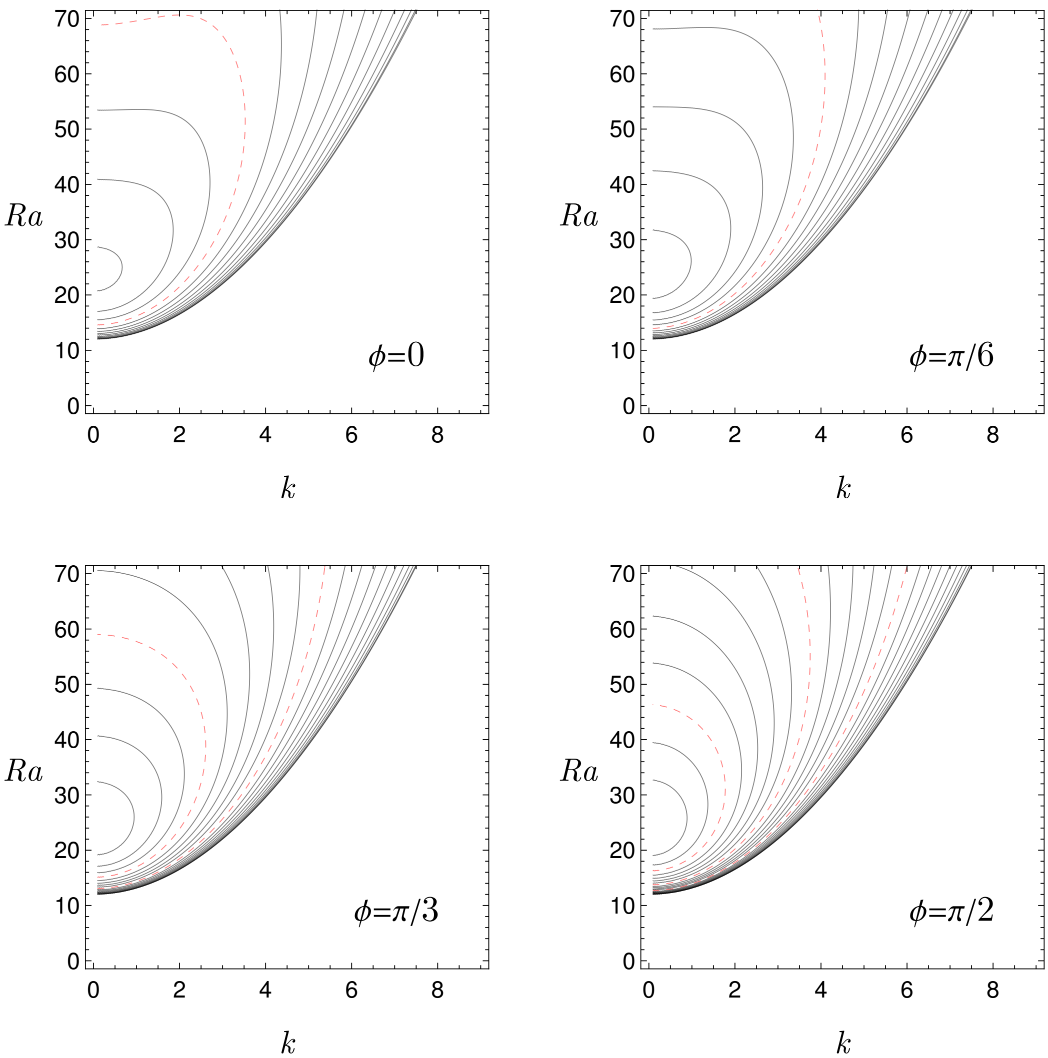

Figure 9.5: Neutral stability curves for different values of C, in steps of 0.02, starting from $C = 0$ up to $C = 0.26$, 0.28, 0.36 and 0.44 for $\phi = 0$, $\pi/6$, $\pi/3$ and $\pi/2$, respectively. Red curves indicate those relative to $C = 0.2, 0.3, 0.4$.

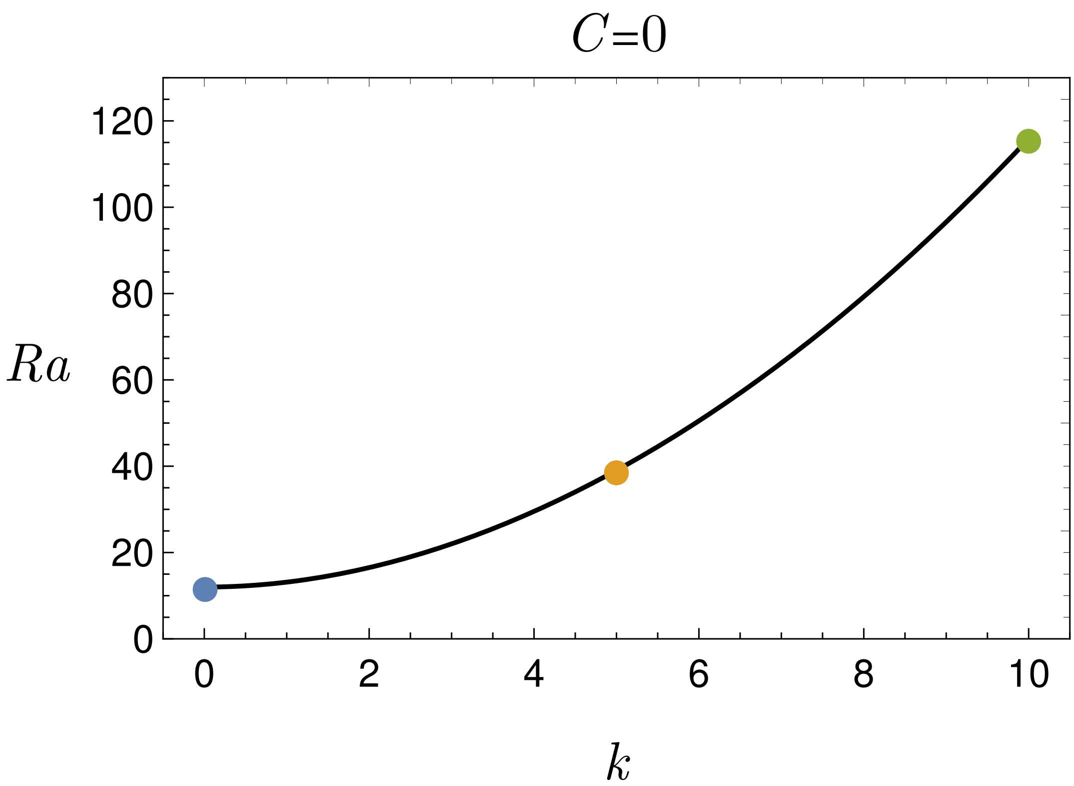

Figure 9.6: Neutral stability curve for $C = 0$. The coloured points define the three wavenumbers, $k = 0.01, 5, 10$, employed in the detailed investigation of the influence of C and ϕ on the neutral stability curve.

Figure 9.6 shows the neutral stability curve for $C = 0$. The case $C = 0$ represents the classical configuration, whose critical condition is known to be $Ra_c = 12$ and $k_c = 0$. For this case, the results do not depend on ϕ since there is no preferred direction for the disturbances.

In order to investigate the role of C and ϕ on the neutral stability condition, three points relative to three different values of k are put in evidence in the Figure 9.6. Figure 9.7 shows the effect of varying C on the the marginal Ra for each one of these wavenumbers for $\phi = \pi/2$. In all three cases, there is a maximum value of C above which no transition is observed. It is possible to see that the maximum C allowed is larger for small values of k, suggesting once again that Ra_c is obtained in the limit as $k \to 0$. Such a result indicates that, as C increases, the unstable region in (k, Ra)–space decreases until it disappears. Such a condition was already expected from the asymptotic analysis for $k \to 0$, which says through Equation (9.33) that, for each value of ϕ, there exists a maximum value of C above which no unstable modes are observed at all.

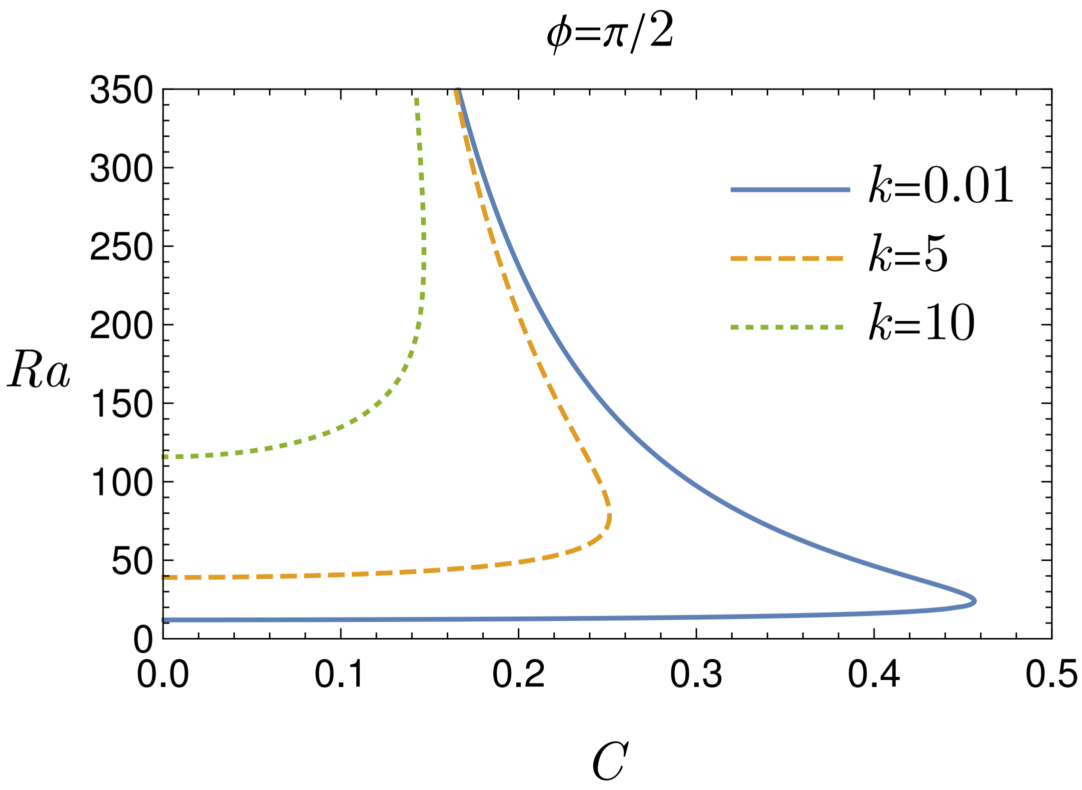

Figure 9.7: Rayleigh number as a function of C for different values of k and $\phi = \pi/2$. Neutrally stable modes are considered.

At this point, Figure 9.8 shows the influence of ϕ on the maximum C allowed for each one of the three wavenumbers marked in Figure 9.6. This figure shows that the maximum value of C monotonically increases with respect to ϕ for all values of k. This is an expected result based on the inequalities presented in Equations (9.34) and (9.35).

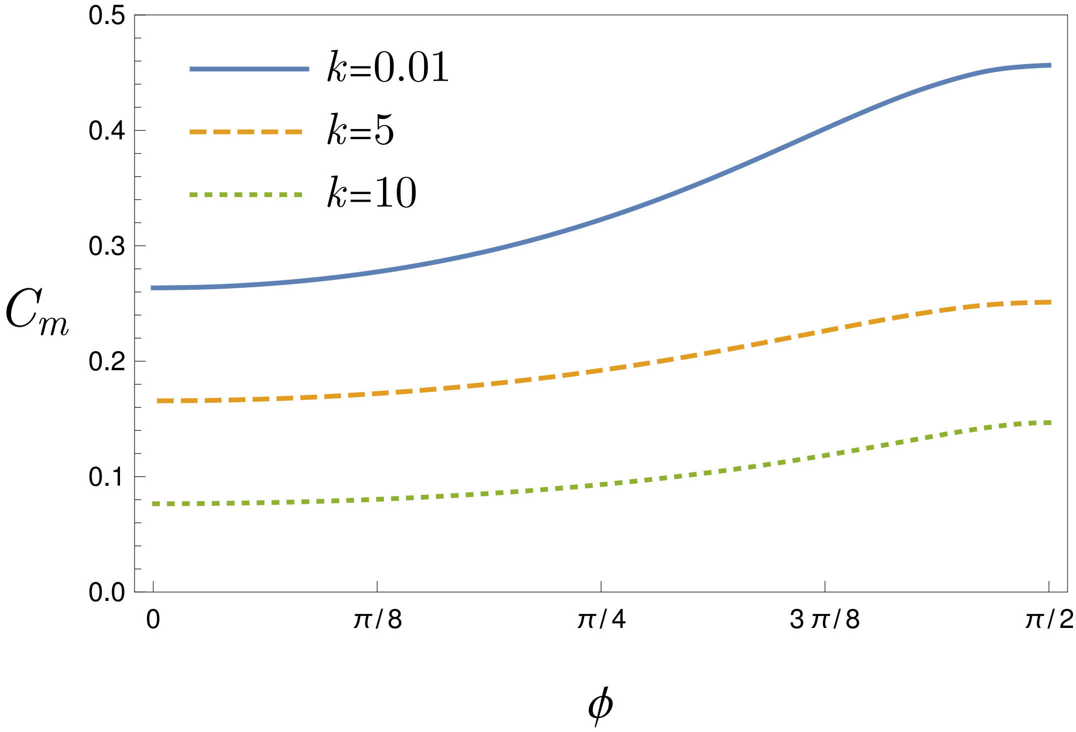

Figure 9.8: Maximum value of C, for fixed k and ϕ, beyond which no neutrally stable modes are possible.

Figure 9.9 shows a three–dimensional map of the most unstable mode (the one with higher growth rate) for $C = 0.1$, containing its growth rate as a function of k and Ra for $\phi = 0$ (left) and $\phi = \pi/2$ (right). It can be seen that the growth rate behaviour is qualitatively different in both cases. While for $\phi = \pi/2$ the behaviour of the growth rate is continuous (as it can be observed from the black line), for all value of k when varying the value of Ra, no such thing occurs for $\phi = 0$. In fact, for $\phi = 0$ there is a discontinuity in the black line that follows the growth rate as varying Ra for a fixed value of k. In order to better understand the reason for this qualitatively different behaviour for different values of ϕ, a cross–section for a fixed value of k in both three-dimensional maps is investigated in detail.

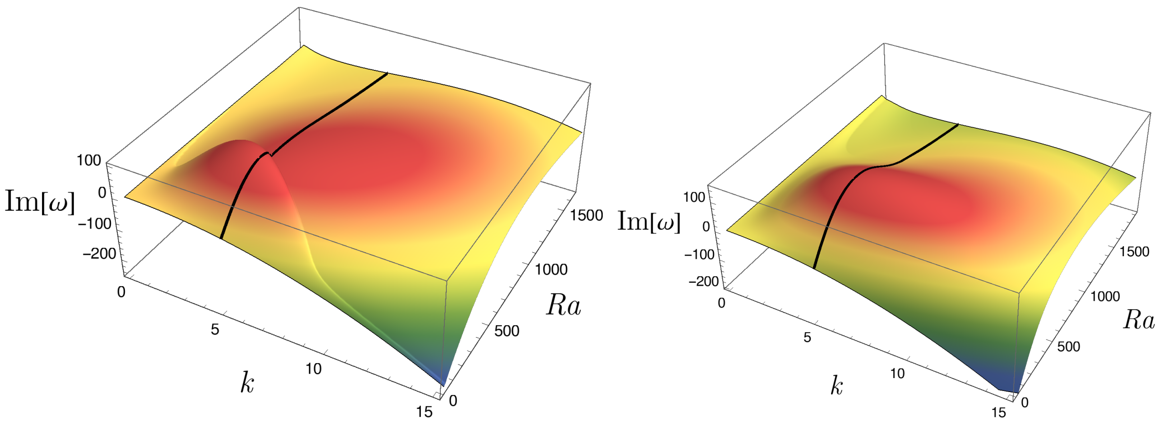

Figure 9.9: Three dimensional map showing the growth rate as a function of the wave and Rayleigh numbers for $C = 0.1$ with $\phi = 0$ (left) and $\phi = \pi/2$ (right).

Figures 9.10 and 9.11 show the data relative to both frequency and growth rate along such a cross–section. For both cases the chosen cross–section is relative to $k = 5$, which is represented by the black line in Figure 9.9.

In Figure 9.10 it can be seen that, as Ra increases, the two most unstable modes merge at a specific value of Ra. Up to this synchronization point, both modes are stationary, as it can be seen in the upper–right frame. Looking at the bottom–frame, it becomes clear what happens. Both modes are stationary for small values of Ra, then, at a specific value of Ra, the two modes collapse and become two modes with the same growth rate and the same absolute value of frequency, but with different sings. In fact, in the bottom–frame of Figure 9.10 these three situation are represented, namely the eigenvalue spectrum is shown for a value of Ra before the merge, another one just after the merge and another one for a higher value of Ra.

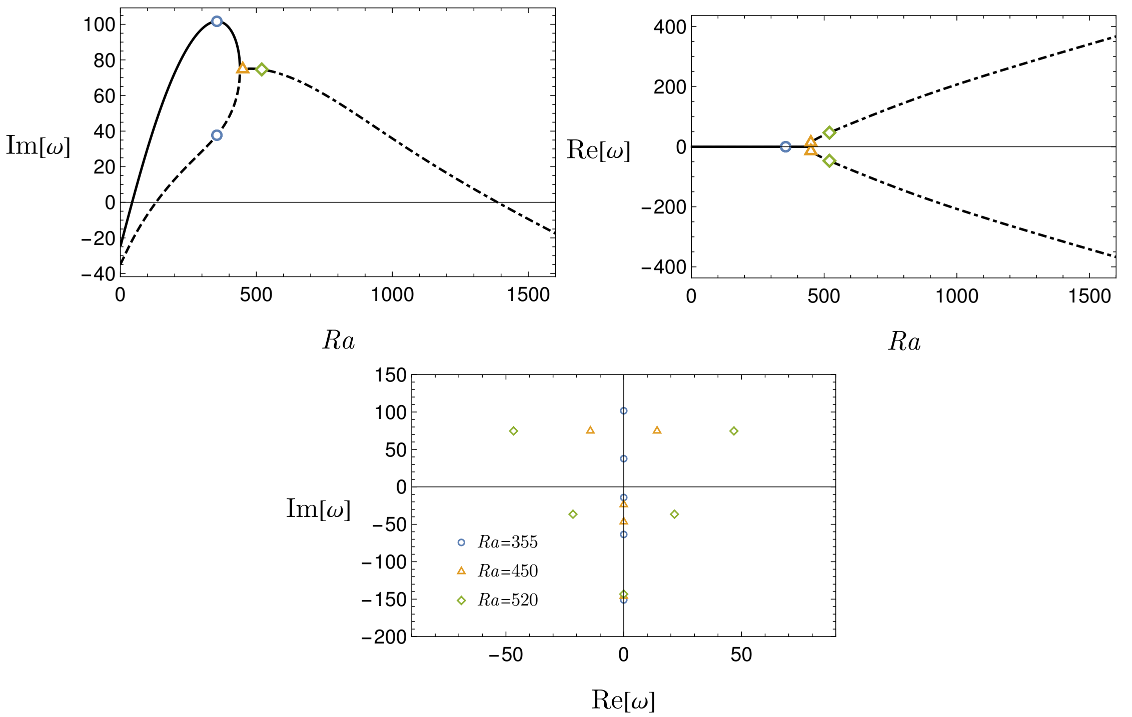

Figure 9.10: Temporal growth rate (top left) and frequency (top right) as functions of Ra as well as the frequency spectra at three different Ra (bottom). Data obtained for $k = 5$, $C = 0.1$ and $\phi = 0$. Solid and dashed lines represent most unstable modes before synchronization at $Ra_m \simeq 438.110$. Dot dashed lines represents both modes beyond this point.

Figure 9.11 shows similar data to Figure 9.10, but for $\phi = \pi/2$. For this case, however, the synchronization is not observed. Both modes have different temporal growth rates, as shown in the upper–left frame of Figure 9.11, and remain stationary for all value of Ra, as shown in the upper–right frame. Nonetheless, it is interesting to note that their temporal growth rates do become quite close for high values of Ra. This behaviour change is summarized in the bottom–frame of Figure 9.11, which shows the spectra at three different Ra within this high Ra region. Thus, synchronization occurs only for transverse modes ($\phi = 0$) but not for longitudinal ones ($\phi = \pi/2$).

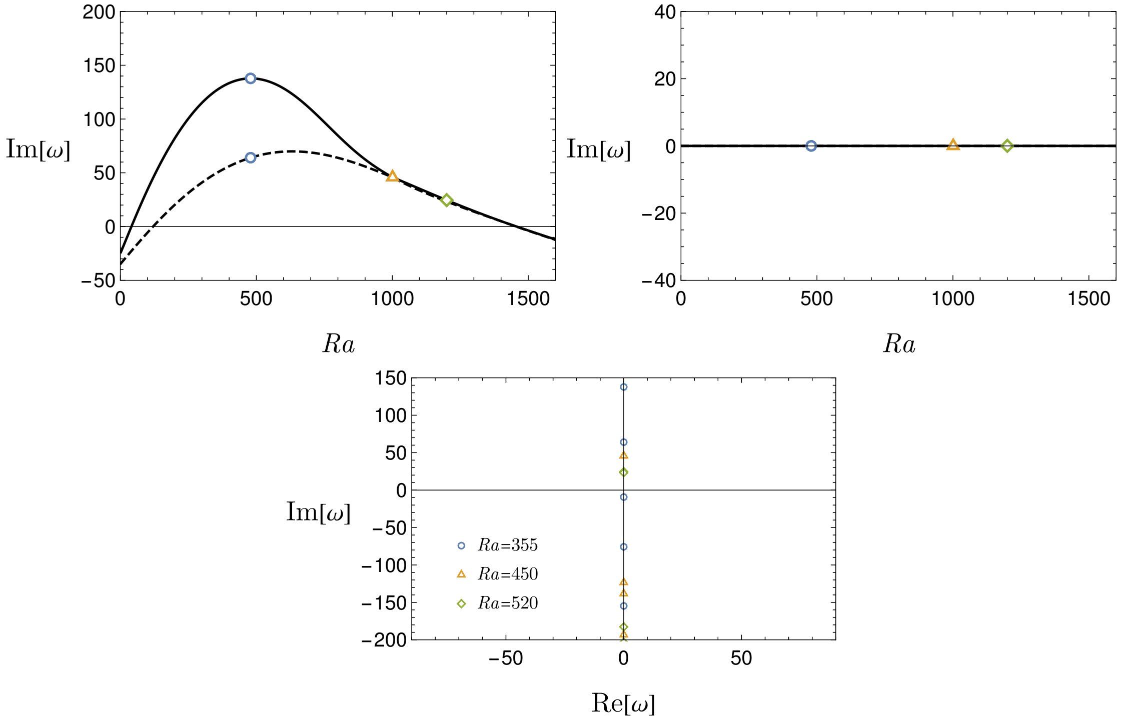

Figure 9.11: Same as Figure 9.10, but for $\phi = \pi/2$. No synchronization occurs.

Now, the investigation can be focused on the influence of C on the stability results. For $C = 0$, there is no preferred orientation of the wave vector. On the other hand, ϕ plays an important role when $C > 0$. Figures 9.12 and 9.13 show neutral stability curves for different values of C for the transverse and longitudinal cases, respectively. The neutral stability curve is represented by the external thick solid lines. At the interior of the neutral stability curve there is the unstable region, that is the region in which disturbances modes with positive values do exist. In that region, positive temporal growth rate isocontours are represented by the thin solid lines. In addition, the synchronization points, that is the points in which the two unstable modes merge, are shown by the thick dashed lines whenever present. Since this finite unstable region exists, there exists also a lower and a upper bound for the critical Rayleigh number. In Figures 9.12 and 9.13 the global maximum growth rates, for each case, is represented by the red dots. The maximum growth rate point is obtained by an optimization process of the original problem with respect to Ra and k very similar to the automatic critical point search employed in a previous work [5]. The additional equations required for this procedure are obtained by taking derivatives of Equations (9.10) with respect of both Ra and k and then imposing $\partial\mathrm{Im}[\omega]/\partial Ra = 0$ and $\partial\mathrm{Im}[\omega]/\partial k = 0$. Further details can be found elsewhere [8, 6].

It is important to note that, even in the presence of upper neutral stability bounds, the lower bound for the critical Rayleigh number always occurs at $k = 0$, which can be analytically determined by Equation (9.30). Another important fact is that all most unstable modes represented by red dots in Figures. 9.12 and 9.13 have finite wavelength, *i.e.* $k > 0$. Thus, based on a linear analysis, it can be said that the nonlinear saturation is unlikely to be reached by the infinite wavelength modes in the supercritical region. However, such an analysis is beyond the scope of the present work. Another important consideration is the fact that the upper bound for the critical Rayleigh number only occurs at $k = 0$ in the limit of high values of C. For these cases, it can be determined by Equation (9.31).

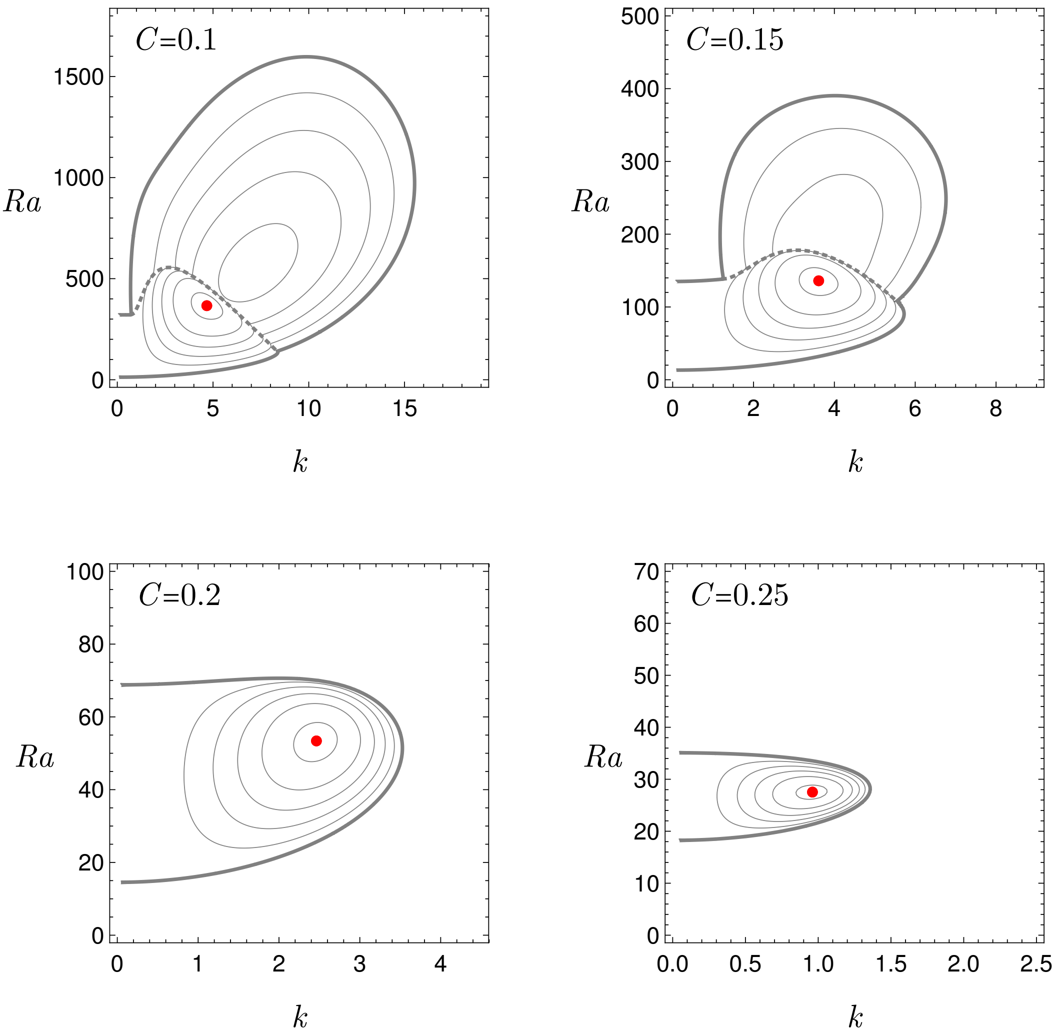

Figure 9.12: Neutral stability curves (thick solid lines) and temporal growth rate isolines (thin solid lines) for different values of C with $\phi = 0$. The red dots identify the maximum temporal growth rate: $\mathrm{Im}[\omega] = 102.298$ at $Ra = 366.298$ and $k = 4.6754$ for $C = 0.1$, $\mathrm{Im}[\omega] = 21.7067$ at $Ra = 135.978$ and $k = 3.61197$ for $C = 0.15$, $\mathrm{Im}[\omega] = 2.58776$ at $Ra = 53.3939$ and $k = 2.46325$ for $C = 0.2$ and $\mathrm{Im}[\omega] = 0.0515489$ at $Ra = 27.5296$ and $k = 0.960554$ for $C = 0.25$.

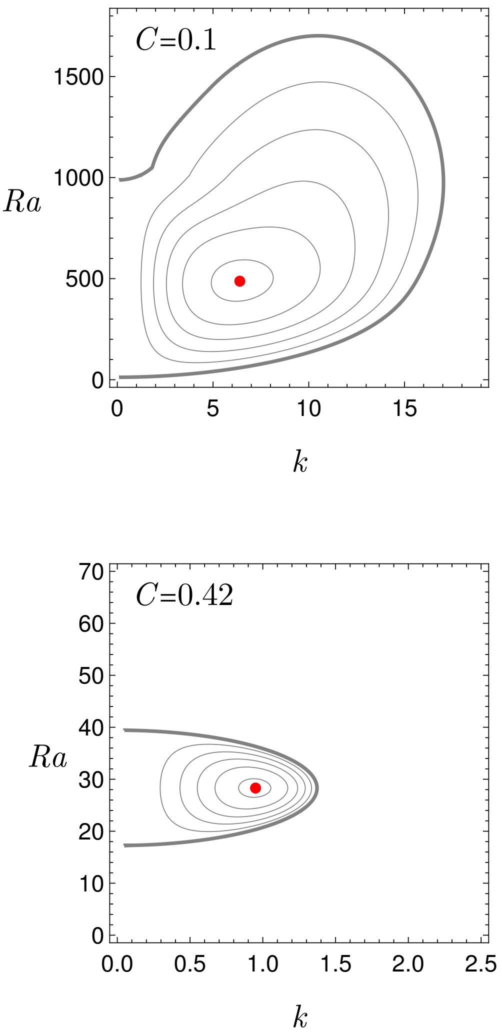

Figure 9.13: Same as Figure 9.12 but for $\phi = \pi/2$. $\mathrm{Im}[\omega] = 144.045$ at $Ra = 487.596$ and $k = 6.39767$ for $C = 0.1$, $\mathrm{Im}[\omega] = 17.9898$ at $Ra = 122.111$ and $k = 3.74012$ for $C = 0.2$, $\mathrm{Im}[\omega] = 0.0782786$ at $Ra = 28.3118$ and $k = 0.950117$ for $C = 0.42$ and $\mathrm{Im}[\omega] = 0.0144728$ at $Ra = 25.8143$ and $k = 0.622522$ for $C = 0.44$.

9.7 Conclusions

The onset of natural convection in a horizontal fluid saturated porous layer bounded by isoflux impermeable boundaries was investigated here. The study of the isoflux Darcy–Bénard instability was investigated from a novel perspective. A one–parameter class of basic states compatible with the imposed boundary conditions was proposed here. The parameter which determines the different states in this class of solutions is the dimensionless horizontal temperature gradient in the x direction, C. The classical conduction basic state is recovered by setting $C = 0$. When $C \neq 0$, the basic states feature infinitely wide Hadley cells with a zero mean horizontal flow rate.

The onset of natural convection has been investigated by means of a linear stability analysis, where the threshold condition has been expressed through neutral stability curves in the parametric (k, Ra) plane. The orientation of the disturbance wave vector relative to the axis x is parametrised by the angle ϕ. Then, $\phi = 0$ describes the longitudinal rolls, a situation where where the normal mode propagates in the x direction. Longitudinal rolls are given by $\phi = \pi/2$ and intermediate values of ϕ describe the oblique rolls. The main features of the present linear stability investigation are the following:

- For $C = 0$, the well–known results for the classical isoflux Darcy–Bénard solution are retrieved. The orientation angle ϕ does not influence the transition to instability for this case. The most unstable modes are stationary and the critical condition is triggered for $k_c = 0$ and $Ra_c = 12$.

- For $C \neq 0$, the longitudinal rolls ($\phi = \pi/2$) are the most unstable modes at the onset of instability, with the critical condition being triggered by infinite wavelength modes ($k_c = 0$). When C is large enough, the upper critical condition is also triggered by infinite wavelength modes for high values of C. For smaller values of C, the upper critical condition is relative to finite wavelength modes $k_c \neq 0$.

- For $C \neq 0$, the neutral stability condition for longitudinal rolls is always given by stationary modes, while oblique and transverse rolls ($0 \leq \phi < \pi/2$) can be either stationary or travelling.

- The lower critical value of Ra_c is determined analytically for every C and is a monotonic increasing function of C. Thus, among all the one–parameter class of basic states, the most unstable one is $C = 0$. On the opposite, the upper critical value of Ra can only be determined analytically for large enough values of C.

Chapter 10

Final discussion

In this thesis, novel results regarding the Darcy–Bénard instability were presented. In order to contribute to a better comprehension of this important field of research, different features that can be relevant for a wide class of applications were considered. The most important information sought here was that regarding the instability threshold and the disturbances pattern selection. The linear stability theory can be the most appropriate choice for the determination of the instability threshold, but it is not always the case. In the present thesis, both the linear and the non linear theories were considered.

Among the important results, it is worth mentioning some specific points. For what concerns vertical throughflow of non–Newtonian fluids in porous media, it can be said that, according to the linear theory and the power–law model for the apparent viscosity, pseudoplastic fluids are more stable than Newtonian fluids for small values of Pe and less stable for high values of Pe. The opposite trend is observed for dilatant fluids. The dominant instability mode on the transition turned out to be always disturbance waves of infinite wavelength. On the other hand, the shape of the vertical sidewall does not affect the instability threshold. However, it affects the linear pattern selection of the instability. In the case of vertical cylinders, it was found that, in the limit of high values of Pe, an asymptotic analysis can be done. Numerical results show that such a solution is reliable from $Pe \simeq 10$. Such a result is important because, as it is known from the literature results, the power–law model for non–Newtonian fluids is more reliable for high values of Péclet number. In fact, in the limit of small values of Pe, the model presents an important singularity, which is expected to impact the stability results. Namely, the model returns a infinite apparent viscosity for pseudoplastic fluids and a zero apparent viscosity for dilatant fluids. Such results are unphysical. For this reason, novel rheological models for apparent viscosity in fluid saturated porous media were proposed, namely Darcy–Carreau and Darcy–Carreau–Yasuda models. By employing these new models, in the limit of vanishing flow rates, the fluid behaves as a Newtonian fluid. Since this is a completely new result, a weakly nonlinear stability analysis is performed for better understand this problem. It was found that the transition from the conductive to the convective state for dilatant fluids is dictated by the linear dynamics. On the contrary, the nature of the bifurcation depends on a parameter that involves the fluid and the porous medium characteristics.

A comparison with theoretical and experimental results for the onset of mixed convection served to confirm that, in the limit of high values of Pe, the proposed model agrees with the power–law behaviour. For high values of Pe, the agreement between experiments and theory was unsatisfactory for both models. On the other hand, for small values of Pe, it can be seen that the present model seems to be a more adequate choice.

Finally, a generalised basic state for the Darcy–Bénard problem heated from below and cooled from above by a constant heat flux was proposed and its instability was investigated. A one–parameter class of basic states was considered, controlled by the dimensionless horizontal temperature gradient C in the direction x. The case $C = 0$ is the well–known basic state for the isoflux Darcy–Bénard case. This is the most unstable between all solutions. In that case, the disturbance rolls have no preferred direction. For $C > 0$, the longitudinal rolls are the most unstable and, at onset of instability they are relative to plane wave disturbances of infinite wavelength. In the case $C \neq 0$, the disturbance modes are always stationary for longitudinal modes, while they can be either stationary or not for oblique and transverse rolls.

10.1 Future perspectives

The present thesis brought important novel results to the understanding of Newtonian and non–Newtonian convection in porous media. This kind of study can be of interest for a wide range of applications. Among others, I can cite here the development of new technologies for building insulation, geophysical engineering and food technology. An accurate modelling of the real world phenomena is a motivation for obtaining useful theoretical results. This work attempted to fill some important gaps in the literature, as the understanding of the influence of complex fluid rheologies as well as of more general equilibrium solutions for the onset of convection in porous media. Among these lines, some further important information can be sought in the future. Here, I mention the study of more complex porous matrices and of more complex fluid models.

In general, a real world system is strongly nonlinear, from the mathematical point of view. For this reason, linear analyses have to be used with care in order to avoid any loss of generality in the real problem. In this sense, nonlinear analyses may be necessary for a better comprehension of complex phenomena. In addition, the characterisation of the instability nature, convective or absolute, is definitely important. Among the future perspectives, I mention the features of these kinds of instability together with the nonlinear analysis. All these topics are important goals to be pursued. The understanding of the disturbance behaviour in the unstable parametric region is a further goal that can be achieved by means of experimental or nonlinear analyses.

Finally, from the results achieved in the present work it is possible to draw some possible investigations that may deserve some attention in the future:

- As discussed extensively in the present work, the power–law model presents a singularity in the limit of vanishing flow–rate. On the other hand, it was concluded in Chapter 5, where the power–law model was considered, that in the limit of small values of flow–rate the critical results can be obtained analytically, what is not true for high values of flow–rate. Such an apparent contradiction deserves to be investigated in the future more carefully.

- The Darcy–Carreau and Darcy–Carreau–Yasuda models proposed in Chapters 7 and 8 were validated by means of the stability results. Nonetheless, a more rigorous experimental validation is needed yet.

- The onset of natural convection for pseudoplastic fluids was found to be subcritical here. However, it was not fully investigated yet, a complete characterization of the transition as well as of the convective patterns arising after the transition is needed. In addition, for a more complete understanding of convection involving dilatant and pseudoplastic fluids, the onset of mixed convection deserves to be investigated by means of nonlinear analyses in the future as well.

- The results from Chapter 9 showed a lower and an upper critical Rayleigh number, indicating a closed unstable parametric region. It should be interest investigating such a closed parametric region from a nonlinear point of view, focusing on the upper neutral stability condition. Another possible important extension could be the investigation of the transition to absolute instability, and how it would be affected by this double neutral stability condition.

Chapter 11

List of publications

1. Brandão, P. V., Celli, M., Barletta, A., Alves, L. S. de B. (2019). Convection in a horizontal porous layer with vertical pressure gradient saturated by a power-law fluid. Transport in Porous Media, 130(2), 613-625.

2. Barletta, A., Celli, M., Brandão, P. V., Alves, L. de B. (2020). Wavepacket instability in a rectangular porous channel uniformly heated from below. International Journal of Heat and Mass Transfer, 147, 118993.

3. Brandão, P. V., Celli, M., Barletta, A., Storesletten, L. (2021). Thermally unstable throughflow of a power–law fluid in a vertical porous cylinder with arbitrary cross–section. International Journal of Thermal Sciences, 159, 106616.

4. Brandão, P. V., Ouarzazi, M. N. (2021). Darcy–Carreau model and nonlinear natural convection for pseudoplastic and dilatant fluids in porous media. Transport in Porous Media, 136(2), 521-539.

5. Brandão, P. V., Ouarzazi, M. N., Hirata, S. C., Barletta, A. (2021). Darcy–Carreau–Yasuda rheological model and onset of inelastic non-Newtonian mixed convection in porous media. Physics of Fluids, 33(4), 044111.

6. Celli, M., Barletta, A., Brandão, P. V. (2021). Rayleigh–Bénard Instability of an Ellis Fluid Saturating a Porous Medium. Transport in Porous Media, 138(3), 679-692.

7. Brandão, P. V., Barletta, A., Celli, M., Alves, L. de B., Rees, D. A. S. (2021). On the stability of the isoflux Darcy–Bénard problem with a generalised basic state. International Journal of Heat and Mass Transfer, 177, 121538.

Bibliography

[1] M. Abramowitz and I. A. Stegun. *Handbook of Mathematical Functions with Formulas, Graphs, and Mathematical Tables*, volume 55. US Government Printing Office, 1948.

[2] Botton V. Allouche, M. H., D. Henry, Usha R. Millet, S., and H. B. Hadid. Experimental determination of the viscosity at very low shear rate for shear thinning fluids by electrocapillarity. *Journal of Non-Newtonian Fluid Mechanics*, 215:60–69, 2015.

[3] L. S. de B. Alves and A. Barletta. Convective instability of the Darcy–Bénard problem with through flow in a porous layer saturated by a power–law fluid. *International Journal of Heat and Mass Transfer*, 62:495–506, 2013.

[4] L. S de B Alves and A. Barletta. Convective to absolute instability transition in the prats flow of a power-law fluid. *International Journal of Thermal Sciences*, 94: 270–282, 2015.

[5] L. S de B Alves, S. C Hirata, and M. N Ouarzazi. Linear onset of convective instability for rayleigh-bénard-couette flows of viscoelastic fluids. *Journal of Non-Newtonian Fluid Mechanics*, 231:79–90, 2016.

[6] L. S. de B. Alves, S. C. Hirata, M. Schuabb, and A. Barletta. Identifying linear absolute instabilities from differential eigenvalue problems using sensitivity analysis. *Journal of Fluid Mechanics*, 870:941–969, 2019.

[7] E. Anderson, Z. Bai, C. Bischof, L. S. Blackford, J. Demmel, J. Dongarra, J. Du Croz, A. Greenbaum, S. Hammarling, A. McKenney, et al. *LAPACK Users' guide*. SIAM, Philadelphia, PA, 1999.

[8] A. Barletta. *Routes to Absolute Instability in Porous Media*. Springer.

[9] A Barletta. Thermal instabilities in a fluid saturated porous medium. In *Heat transfer in multi-phase materials*, pages 381–414. Springer, 2010.

[10] A. Barletta. A proof that convection in a porous vertical slab may be unstable. *J. Fluid Mech*, 770:273–288, 2015.

[11] A. Barletta and D. A. Nield. Instability of Hadley–Prats flow with viscous heating in a horizontal porous layer. *Transport in Porous Media*, 84:241–256, 2010.

[12] A. Barletta and D. A. Nield. Linear instability of the horizontal throughflow in a plane porous layer saturated by a power-law fluid. *Physics of Fluids*, 23(1):013102, 2011.

[13] A. Barletta and D. A. S. Rees. Local thermal non–equilibrium effects in the Darcy–Bénard instability with isoflux boundary conditions. *International Journal of Heat and Mass Transfer*, 55:384–394, 2012.

[14] A. Barletta and L. Storesletten. Onset of convection in a vertical porous cylinder with a permeable and conducting side boundary. *International Journal of Thermal Sciences*, 97:9–16, 2015.

[15] A. Barletta and L. Storesletten. Linear instability of the vertical throughflow in a horizontal porous layer saturated by a power-law fluid. *International Journal of Heat and Mass Transfer*, 99:293–302, 2016.

[16] A. Barletta, E. R. di Schio, and L. Storesletten. Convective roll instabilities of vertical throughflow with viscous dissipation in a horizontal porous layer. *Transport in porous media*, 81(3):461–477, 2010.

[17] A. Barletta, M. Celli, and A. V. Kuznetsov. Heterogeneity and onset of instability in Darcy's flow with a prescribed horizontal temperature gradient. *ASME Journal of Heat Transfer*, 134:042602 (8 pages), 2012.

[18] J. Barrere, O. Gipouloux, and S. Whitaker. On the closure problem for darcy's law. *Transport in Porous Media*, 7(3):209–222, 1992.

[19] J. Bear. *Dynamics of fluids in porous media*. Courier Corporation, 2013.

[20] H. Bénard. Les tourbillons cellulaires dans une nappe liquide [the cellular vortices in a liquid layer]. *Rev Gén Sci Pure Appl*, 11:1261–1271, 1900.

[21] O. Benouared, M. Mamou, and N. A. Messaoudene. Numerical nonlinear analysis of subcritical Rayleigh–Bénard convection in a horizontal confined enclosure filled with non–Newtonian fluids. *Physics of Fluids*, 26(7):073101, 2014.

[22] M. J. Block. Surface tension as the cause of bénard cells and surface deformation in a liquid film. *Nature*, 178(4534):650–651, 1956.

[23] M. Bouteraa, C. Nouar, E. Plaut, C. Métivier, and A. Kalck. Weakly nonlinear analysis of Rayleigh–Bénard convection in shear-thinning fluids: nature of the bifurcation and pattern selection. *Journal of Fluid Mechanics*, 767:696–734, 2015.

[24] J. P. Boyd. *Chebyshev and Fourier spectral methods.* Dover, New York, NY, 2001.

[25] P. V. Brandão, M Celli, A. Barletta, and L. Storesletten. Thermally unstable throughflow of a power–law fluid in a vertical porous cylinder with arbitrary cross–section. *International Journal of Thermal Sciences*, 159:106616, 2021.

[26] P. V. Brandão and M. N. Ouarzazi. Darcy–carreau model and nonlinear natural convection for pseudoplastic and dilatant fluids in porous media. *Transport in Porous Media*, 136(2):521–539, 2021.

[27] P. V. Brandão, M. Celli, A. Barletta, and L. S de B Alves. Convection in a horizontal porous layer with vertical pressure gradient saturated by a power-law fluid. *Transport in Porous Media*, 130(2):613–625, 2019.

[28] P. V. Brandão, A. Barletta, M. Celli, L. S. de B. Alves, and D. A. S. Rees. On the stability of the isoflux darcy–bénard problem with a generalised basic state. *International Journal of Heat and Mass Transfer*, 177:121538, 2021.

[29] P. V. Brandão, M. N. Ouarzazi, S. da C. Hirata, and A. Barletta. Darcy–carreau–yasuda rheological model and onset of inelastic non-newtonian mixed convection in porous media. *Physics of Fluids*, 33(4):044111, 2021.

[30] L. Brevdo. Three-dimensional absolute and convective instabilities at the onset of convection in a porous medium with inclined temperature gradient and vertical throughflow. *Journal of Fluid Mechanics*, 641:475–487, 2009.

[31] L. Brevdo and M. Ruderman. On the convection in a porous medium with inclined temperature gradient and vertical throughflow. Part I. Normal modes. *Transport in Porous Media*, 80:137–151, 2009.

[32] L. Brevdo and M. Ruderman. On the convection in a porous medium with inclined temperature gradient and vertical throughflow. Part II. Absolute and convective instabilities, and spatially amplifying waves. *Transport in Porous Media*, 80:153–172, 2009.

[33] G. O. Brown. Henry darcy and the making of a law. *Water Resources Research*, 38(7):11–1, 2002.

[34] R. L. Burden and J. D. Faires. Numerical analysis, brooks. *Cole, Belmont*, 1997.

[35] R. G. Carbonell and S. Whitaker. Dispersion in pulsed systemsâĂŤii: theoretical developments for passive dispersion in porous media. *Chemical Engineering Science*, 38(11):1795–1802, 1983.

[36] P. J. Carreau. Rheological equations from molecular network theories. *Transactions of the Society of Rheology*, 16(1):99–127, 1972.

[37] M. Celli and A. Barletta. Onset of convection in a non-newtonian viscous flow through a horizontal porous channel. *International Journal of Heat and Mass Transfer*, 117:1322–1330, 2018.

[38] S. Chandrasekhar. *Hydrodynamic and hydromagnetic stability*. Courier Corporation, 2013.

[39] P. Cheng. Heat transfer in geothermal systems. In *Advances in heat transfer*, volume 14, pages 1–105. Elsevier, 1979.

[40] T. Chi, H. S. Tsuei, et al. Thermal instability of a horizontal layer of non–Newtonian fluid heated from below. *International Journal of Heat and Mass Transfer*, 12(9):1173–1178, 1969.

[41] J. M. Chomaz. Absolute and convective instabilities in nonlinear systems. *Physical review letters*, 69(13):1931, 1992.

[42] R. H. Christopher and S. Middleman. Power-law flow through a packed tube. *Industrial & Engineering Chemistry Fundamentals*, 4(4):422–426, 1965.

[43] M. A Combarnous, Paul Bia, et al. Combined free and forced convection in porous media. *Society of Petroleum Engineers Journal*, 11(04):399–405, 1971.

[44] M. Darbouli, C. Métivier, S. Leclerc, C. Nouar, M. Bouteera, and D. Stemmelen. Natural convection in shear-thinning fluids: Experimental investigations by MRI. *International Journal of Heat and Mass Transfer*, 95:742–754, 2016.

[45] H. P. G. Darcy. *Dètermination des lois d'ècoulement de l'eau à travers le sable.* 1856.

[46] A. Delache and M. N. Ouarzazi. Weakly nonlinear interaction of mixed convection patterns in porous media heated from below. *International journal of thermal sciences*, 47(6):709–722, 2008.

[47] A. Delache, M. N. Ouarzazi, and M. Combarnous. Spatio-temporal stability analysis of mixed convection flows in porous media heated from below: Comparison with experiments. *International journal of heat and mass transfer*, 50(7):1485–1499, 2007.

[48] I. Delbende and J. M. Chomaz. Nonlinear convective/absolute instabilities in parallel two-dimensional wakes. *Physics of Fluids*, 10(11):2724–2736, 1998.

[49] R. V. Dharmadhikari and D. D. Kale. Flow of non-newtonian fluids through porous media. *Chemical Engineering Science*, 40(3):527–529, 1985.

[50] H. F. Diaz and R. S. Bradley. The hadley circulation: present, past, and future. In *The Hadley circulation: present, past and future*, pages 1–5. Springer, 2004.

[51] P. G Drazin and William Hill Reid. *Hydrodynamic stability*. Cambridge university press, 2004.

[52] F. Dufour and M. C. Neel. Numerical study of instability in a horizontal porous channel with bottom heating and forced horizontal flow. *Physics of Fluids*, 10(9): 2198–2207, 1998.

[53] J. Dupuit. *Études théoriques et pratiques sur le mouvement des eaux dans les canaux découverts et à travers les terrains perméabls: avec des considérations relatives au régime des grandes eaux, au débouché à leur donner, et à la marche des alluvions dans les rivières à fond mobile*. Dunod, 1863.

[54] G. I. El-Baghdady and M. El-Azab. Chebyshev–Gauss–Lobatto pseudo–spectral method for one–dimensional advection–diffusion equation with variable coefficients. *Sohag Journal of Mathematics*, 3:7–14, 2016.

[55] P. Forchheimer. Wasserbewegung durch boden. *Z. Ver. Deutsch, Ing.*, 45:1782–1788, 1901.

[56] A. V. Getling. *Rayleigh-B nard Convection: Structures and Dynamics*, volume 11. World Scientific, 1998.

[57] A. E. Gill. A proof that convection in a porous vertical slab is stable. *Journal of Fluid Mechanics*, 35(3):545–547, 1969.

[58] W. G. Gray and K. O'Neill. On the general equations for flow in porous media and their reduction to darcy's law. *Water Resources Research*, 12(2):148–154, 1976.

[59] A. Gueye, M. N. Ouarzazi, S. C Hirata, and H. B. Hamed. Onset of primary and secondary instabilities of viscoelastic fluids saturating a porous layer heated from below by a constant flux. *Fluids*, 2(3):42, 2017.

[60] G. Hadley. Vi. concerning the cause of the general trade-winds. *Philosophical Transactions of the Royal Society of London*, 39(437):58–62, 1735.

[61] S. C. Hirata and M. N. Ouarzazi. Three-dimensional absolute and convective instabilities in mixed convection of a viscoelastic fluid through a porous medium. *Physics Letters A*, 374(26):2661–2666, 2010.

[62] S. C. Hirata, L. S. de B. Alves, N. Delenda, and M. N. Ouarzazi. Convective and absolute instabilities in rayleigh–bénard–poiseuille mixed convection for viscoelastic fluids. *Journal of Fluid Mechanics*, 765:167–210, 2015.

[63] S. C. Hirata, G. E. Eny, and M. N. Ouarzazi. Nonlinear pattern selection and heat transfer in thermal convection of a viscoelastic fluid saturating a porous medium. *International Journal of Thermal Sciences*, 95:136–146, 2015.

[64] D. Hlushkou and U. Tallarek. Transition from creeping via viscous-inertial to turbulent flow in fixed beds. *Journal of Chromatography A*, 1126(1-2):70–85, 2006.

[65] J. D Hoffman and S. Frankel. *Numerical methods for engineers and scientists*. CRC press, 2018.

[66] G. M. Homsy and A. E. Sherwood. Convective instabilities in porous media with through flow. *AIChE Journal*, 22(1):168–174, 1976.

[67] C. W. Horton and F. T. Rogers Jr. Convection currents in a porous medium. *Journal of Applied Physics*, 16(6):367–370, 1945.

[68] P. Huerre and P. A Monkewitz. Absolute and convective instabilities in free shear layers. *Journal of Fluid Mechanics*, 159:151–168, 1985.

[69] Wolfram Research, Inc. Mathematica, Version 12. URL `https://www.wolfram.com/mathematica`. Champaign, IL, 2021.

[70] M. Jenny, E. Plaut, and A. Briard. Numerical study of subcritical Rayleigh–Bénard convection rolls in strongly shear-thinning carreau fluids. *Journal of Non-Newtonian Fluid Mechanics*, 219:19–34, 2015.

[71] M. C. Jones and J. M. Persichetti. Convective instability in packed beds with throughflow. *AIChE journal*, 32(9):1555–1557, 1986.

[72] D. D. Joseph. *Stability of fluid motions I*, volume 27. Springer Science & Business Media, 2013.

[73] M. P. Juniper, A. Hanifi, and V. Theofilis. Modal stability theory. *Applied Mechanics Reviews*, 66, 2014.

[74] P. N. Kaloni and Z. Qiao. On the nonlinear stability of thermally driven shear flow heated from below. *Physics of Fluids*, 8(2):639–641, 1996.

[75] P. N. Kaloni and Z. Qiao. Non-linear stability of convection in a porous medium with inclined temperature gradient. *International Journal of Heat and Mass Transfer*, 40:1611–1615, 1997.

[76] M. Kaviany. *Principles of heat transfer in porous media.* Springer Science & Business Media, 1995.

[77] R. E. Kelly. The onset and development of rayleigh–bénard convection in shear flows: a review. *Physicochemical hydrodynamics*, 1:65–79, 1977.

[78] Z. Kemblowski and M. Michniewicz. A new look at the laminar flow of power law fluids through granular beds. *Rheologica Acta*, 18(6):730–739, 1979.

[79] M. C. Kim, S. B. Lee, S. Kim, and B. J. Chung. Thermal instability of viscoelastic fluids in porous media. *International journal of heat and mass transfer*, 46(26): 5065–5072, 2003.

[80] M. C. Kim, S. B. Lee, S. Kim, and B. J. Chung. Thermal instability of viscoelastic fluids in porous media. *International journal of heat and mass transfer*, 46(26): 5065–5072, 2003.

[81] S. Kimura, M. Vynnycky, and F. Alavyoon. Unicellular natural circulation in a shallow horizontal porous layer heated from below by a constant flux. *Journal of Fluid Mechanics*, 294:231–257, 1995.

[82] P. Kolodner. Oscillatory convection in viscoelastic dna suspensions. *Journal of non–Newtonian fluid mechanics*, 75(2-3):167–192, 1998.

[83] E. L. Koschmieder. Bénard convection. *Adv. Chem. Phys*, 26:177, 1974.

[84] E. L. Koschmieder. *Bénard cells and Taylor vortices.* Cambridge University Press, 1993.

[85] Y. A. Kuznetsov. *Elements of applied bifurcation theory*, volume 112. Springer Science & Business Media, 2013.

[86] J. L. Lage. The fundamental theory of flow through permeable niedia from darcy to turbulence. *Transport phenomena in porous media*, 1, 1998.

[87] E. R. Lapwood. Convection of a fluid in a porous medium. In *Mathematical Proceedings of the Cambridge Philosophical Society*, volume 44, pages 508–521. Cambridge University Press, 1948.

[88] S. F. Liang and A. Acrivos. Experiments on buoyancy driven convection in non–Newtonian fluid. *Rheologica Acta*, 9(3):447–455, 1970.

[89] S. Longo, V. Di Federico, L. Chiapponi, and R. Archetti. Experimental verification of power-law non–Newtonian axisymmetric porous gravity currents. *Journal of Fluid Mechanics*, 731, 2013.

[90] A. M. Lyapunov. The general problem of the stability of motion. *International journal of control*, 55(3):531–534, 1992.

[91] R. A. Mahdi, H. A. Mohammed, K. M. Munisamy, and N. H. Saeid. Review of convection heat transfer and fluid flow in porous media with nanofluid. *Renewable and Sustainable Energy Reviews*, 41:715–734, 2015.

[92] D. M. Manole and J. L. Lage. Numerical simulation of supercritical hadley circulation, within a porous layer, induced by inclined temperature gradients. *International Journal of Heat and Mass Transfer*, 38:2583–2593, 1995.

[93] D. M. Manole, J. L. Lage, and D. A. Nield. Convection induced by inclined thermal and solutal gradients, with horizontal mass flow, in a shallow horizontal layer of a porous medium. *International Journal of Heat and Mass Transfer*, 37:2047–2057, 1994.

[94] A. B. Metzner. Heat transfer in non-newtonian fluids. In *Advances in Heat Transfer*, volume 2, pages 357–397. Elsevier, 1965.

[95] A. C. Newell and J. A. Whitehead. Finite bandwidth, finite amplitude convection. *Journal of Fluid Mechanics*, 38(2):279–303, 1969.

[96] X. Nicolas. Bibliographical review on the poiseuille-rayleigh-bénard flows: the mixed convection flows in horizontal rectangular ducts heated from below. *International Journal of Thermal Sciences*, 41(10):961–1016, 2002.

[97] D. A. Nield. Onset of thermohaline convection in a porous medium. *Water Resources Research*, 4(3):553–560, 1968.

[98] D. A. Nield. Convective instability in porous media with throughflow. *AIChE journal*, 33(7):1222–1224, 1987.

[99] D. A. Nield. Convection in a porous medium with inclined temperature gradient and horizontal mass flow. In G. Hetsroni, editor, *Heat Transfer 1990: Proceedings of the Ninth International Heat Transfer Conference, Jerusalem, Israel, vol. 5*, pages 153–158. Hemisphere, 1990.

[100] D. A. Nield. Convection in a porous medium with inclined temperature gradient. *International journal of heat and mass transfer*, 34(1):87–92, 1991.

[101] D. A. Nield. Convection in a porous medium with inclined temperature gradient: additional results. *International journal of heat and mass transfer*, 37(18):3021–3025, 1994.

[102] D. A. Nield. Convection in a porous medium with inclined temperature gradient and vertical throughflow. *International Journal of Heat and Mass Transfer*, 41: 241–243, 1998.

[103] D. A. Nield. A note on the onset of convection in a layer of a porous medium saturated by a non-newtonian nanofluid of power-law type. *Transport in Porous Media*, 87(1):121–123, 2011.

[104] D. A. Nield. A further note on the onset of convection in a layer of a porous medium saturated by a non-newtonian fluid of power-law type. *Transport in porous media*, 88(2):187–191, 2011.

[105] D. A. Nield, D. M. Manole, and J. L. Lage. Convection induced by inclined thermal and solutal gradients in a shallow horizontal layer of a porous medium. *Journal of Fluid Mechanics*, 257:559–574, 1993.

[106] D. A. Nield, A. Bejan, et al. *Convection in porous media*, volume 3. Springer, 2006.

[107] M. N. Ouarzazi, A. Joulin, P. A. Bois, and J. K. Platten. Soret effect and mixed convection in porous media. In *Thermal Nonequilibrium Phenomena in Fluid Mixtures*, pages 428–447. Springer, 2002.

[108] J. P. Pascal and H. Pascal. Nonlinear effects on some unsteady non–Darcian flows through porous media. *International journal of non-linear mechanics*, 32(2):361–376, 1997.

[109] J. R. A. Pearson. On convection cells induced by surface tension. *Journal of fluid mechanics*, 4(5):489–500, 1958.

[110] D. Petrolo, L. Chiapponi, S. Longo, M. Celli, A. Barletta, and V. Di Federico. Onset of Darcy–Bénard convection under throughflow of a shear–thinning fluid. *J. Fluid Mech*, 889:R2, 2020.

[111] M. Prats. The effect of horizontal fluid flow on thermally induced convection currents in porous mediums. *Journal of geophysical research*, 71(20):4835–4838, 1966.

[112] M. Quintard. Introduction to heat and mass transport in porous media. *Porous Media Interaction with High Temperature and High Speed Flows, Von Karman Institute for Fluid Dynamics, Rhode Saint Genese, Belgium*, 2015.

[113] M. Quintard, M. Kaviany, and S. Whitaker. Two-medium treatment of heat transfer in porous media: numerical results for effective properties. *Advances in water resources*, 20(2-3):77–94, 1997.

[114] L. Rayleigh. Lix. on convection currents in a horizontal layer of fluid, when the higher temperature is on the under side. *The London, Edinburgh, and Dublin Philosophical Magazine and Journal of Science*, 32(192):529–546, 1916.

[115] Y. Requilé, S. C. Hirata, M. N. Ouarzazi, and A. Barletta. Weakly nonlinear analysis of viscous dissipation thermal instability in plane Poiseuille and plane Couette flows. *Journal of Fluid Mechanics*, 886:A26, 2020.

[116] J. G. Savins. Non–Newtonian flow through porous media. *Industrial & Engineering Chemistry*, 61(10):18–47, 1969.

[117] P. J. Schmid. Nonmodal stability theory. *Annu. Rev. Fluid Mech.*, 39:129–162, 2007.

[118] P. J. Schmid, D. S Henningson, and DF Jankowski. Stability and transition in shear flows. applied mathematical sciences, vol. 142. *Appl. Mech. Rev.*, 55(3):B57–B59, 2002.

[119] M. Schuabb, L. S. de B Alves, and S. da C Hirata. Two-and three-dimensional absolute instabilities in a porous medium with inclined temperature gradient and vertical throughflow. *Transport in Porous Media*, 132(1):135–155, 2020.

[120] A. V. Shenoy. Non-newtonian fluid heat transfer in porous media. In *Advances in Heat transfer*, volume 24, pages 101–190. Elsevier, 1994.

[121] A. V. Shenoy and R. A. Mashelkar. Thermal convection in non-newtonian fluids. In *Advances in heat transfer*, volume 15, pages 143–225. Elsevier, 1982.

[122] J. C. Slattery. Single-phase flow through porous media. *AIChE Journal*, 15(6): 866–872, 1969.

[123] J. C. Slattery. *Advanced transport phenomena*. Cambridge University Press, 1999.

[124] B. Straughan. *Stability and wave motion in porous media*, volume 165. Springer Science & Business Media, 2008.

[125] S. H. Strogatz. *Nonlinear dynamics and chaos with student solutions manual: With applications to physics, biology, chemistry, and engineering*. CRC press, 2018.

[126] F. M. Sutton. Onset of convection in a porous channel with net through flow. *The Physics of Fluids*, 13(8):1931–1934, 1970.

[127] A. Taleb, H. BenHamed, M. N. Ouarzazi, and H. Beji. Analytical and numerical analysis of bifurcations in thermal convection of viscoelastic fluids saturating a porous square box. *Physics of Fluids*, 28(5):053106, 2016.

[128] L. N. Trefethen, A. E. Trefethen, S. C. Reddy, and T. A. Driscoll. Hydrodynamic stability without eigenvalues. *Science*, 261(5121):578–584, 1993.

[129] L. G. H. Van der Meer. Investigations regarding the storage of carbon dioxide in aquifers in the netherlands. *Energy Conversion and management*, 33(5-8):611–618, 1992.

[130] W. Van Saarloos. Front propagation into unstable states. *Physics reports*, 386 (2-6):29–222, 2003.

[131] J. E. Weber. Convection in a porous medium with horizontal and vertical temperature gradients. *International Journal of Heat and Mass Transfer*, 17(2):241–248, 1974.

[132] S. Whitaker. Advances in theory of fluid motion in porous media. *Industrial & engineering chemistry*, 61(12):14–28, 1969.

[133] S. Whitaker. Flow in porous media i: A theoretical derivation of darcy's law. *Transport in porous media*, 1(1):3–25, 1986.

[134] K. Y. Yasuda, R. C. Armstrong, and R. E. Cohen. Shear flow properties of concentrated solutions of linear and star branched polystyrenes. *Rheologica Acta*, 20 (2):163–178, 1981.

[135] D.Y. Yoon, M. C. Kim, and C. K. Choi. The onset of oscillatory convection in a horizontal porous layer saturated with viscoelastic liquid. *Transport in porous media*, 55(3):275–284, 2004.

[136] Z. Zeng and R. Grigg. A criterion for non-darcy flow in porous media. *Transport in porous media*, 63(1):57–69, 2006.

[137] R. K. Zeytounian. *Convection in fluids: a rational analysis and asymptotic modelling*, volume 90. Springer Science & Business Media, 2009.

[138] C. Zhao, B. E. Hobbs, and A. Ord. *Convective and advective heat transfer in geological systems*. Springer Science & Business Media, 2008.